The Two-Photon Exchange Contribution to Electron-Neutron Elastic Scattering (nTPE) and Extraction of G_M^n at Q^2 = 4.5 GeV^2 in Hall A at Jefferson National Lab

Sebastian Arthur Seeds, PhD

University of Connecticut, 2024

The complexity of the physical world—encompassing stars, planets, life, and matter—originates from its fundamental atomic constituents. At the core of atoms lie protons and neutrons (collectively known as nucleons), whose dynamics are governed by the strong nuclear force, resulting in wonderfully intricate behavior. Nucleons, in turn, are composed of quarks and gluons whose complex interplay gives rise to distinct properties, such as the nucleon charge radius and mass. This interplay can be probed through the study of electromagnetic form factors using electron scattering experiments, which describe the nucleon's electromagnetic structure.

This thesis describes the analysis of commissioning and electron scattering data collected at Jefferson Lab experimental Hall A using the newly constructed Super Bigbite Spectrometer (SBS). SBS is a dual-armed spectrometer composed of many new detector subsystems, including a dedicated Hadron Calorimeter with novel design. The calibration, commissioning, and in-beam performance of this detector, which is intended for use throughout SBS and beyond, are detailed herein. However, the primary aim of this thesis is the analysis of coincident quasielastic data from $h(e,e'p)$, and $d(e,e'N)$ electron scattering events to extract the magnetic form factor of the neutron, G_M^n (experiment E12-019-19, or **GMn**). These measurements employ the so-called ratio method to minimize systematic error by simultaneously detecting quasielastic scattered protons and neutrons from a deuterium target. Preliminary extractions will be presented for negative four-momentum transfer squared Q^2 = 3.0 GeV^2 and Q^2 = 4.5 GeV^2 kinematics over several configurations and independent data sets.

Sebastian Arthur Seeds – University of Connecticut, 2024

Arising from similar experiments on the proton, a discrepancy between the form factor ratio G_E^p/G_M^p as extracted with Rosenbluth separation and polarization transfer techniques, which grows with Q^2, is well documented and can be explained by a significant two-photon exchange contribution to the elastic electron-proton cross section. Owing to the relative difficulty in the extraction of neutron form factors, no similar determination of this discrepancy exists yet for the neutron. During **GMn**, the quasielastic neutron-to-proton cross section ratio was measured at two different values of the virtual photon polarization ε. The analysis status of a Rosenbluth separation to extract G_E^n/G_M^n will be presented.

The Two-Photon Exchange Contribution to Electron-Neutron Elastic Scattering (nTPE) and Extraction of G_M^n at Q^2 = 4.5 (GeV/c)^2 in Hall A at Jefferson National Lab

Sebastian Arthur Seeds

B.A., University of Colorado, 2014

M.S., University of Connecticut, 2020

A Dissertation

Submitted in Partial Fulfillment of the

Requirements for the Degree of

Doctor of Philosophy

at the

University of Connecticut

2024

2024

APPROVAL PAGE

Doctor of Philosophy Dissertation

The Two-Photon Exchange Contribution to Electron-Neutron Elastic Scattering (nTPE) and Extraction of G_M^n at Q^2 = 4.5 GeV^2 in Hall A at Jefferson National Lab

Presented by

Sebastian Arthur Seeds

Major Advisor _____

Andrew Puckett

Associate Advisor _____

Richard Jones

Associate Advisor _____

Arun Tadepalli

University of Connecticut

2024

Acknowledgments

My meandering path through physics has seen a number of significant turns. Many of the choices I've made over the years haven't optimized for time and focus. I'm primarily grateful to my family for helping me to keep my focus on my passions and to see that this meandering path is more valuable and worthwhile to someone like me than the more traditional straight and narrow one. I'll try to give those that I've met along the way the credit they're due, but this task is bound to fail. There are too many people to mention, and I'm not nearly competent enough to adequately articulate my gratitude. Nevertheless, I'll give it a shot.

Throughout my physics career, my oldest friends have always been an island of respite which I take advantage of often and don't acknowledge nearly enough. Kevin Wilson, Christine Fallabell, Tamara and Jeremy Eldridge, Alex Canby, Heather Youngblood, Caitlin Greagor, Ian and Jessica Gudnason-Hellbusch, and Maria Baylon-Guillen have been indispensable in their support and friendship.

My time in undergrad set the tone and pace for my professional life and graduate school. The extraordinary dedication and decency in a field which too rarely sees a marriage of the two from Sam Rubeck, Maithreyi Gopalakrishnan, Shawn Beckman, Sean Braxton, Andrew Berentine, and Jamie Shaw forged enduring friendships and fostered a patience and dedication in me that I won't be able to fully repay.

At UConn, my studies were made considerably easier and more illuminating by my cohort - Provakar Datta, Kaitlin Lyszak, Bren Backhouse, Zoey Harris, Jon Mercedes-Feliz, and Jacob Hastings. I have many fond (in the *type-2 fun* kind of way) memories of countless nights staying up way too late and into the next morning with greasy calzones and beer to cram ten pounds of physics into a five-pound brain-bag. That kind of superposition of fun and pain makes bonds that are hard to break. In Storrs, my friends John Smucker and Chloe Herrera brightened much of my time there and I miss it. I'm especially indebted to Provakar, whose profound insight and loyalty throughout my entire career at UConn and Jefferson Lab played a primary role in shaping my physics intuitions and made a good physicist out of an otherwise mediocre one.

The other primary contributor to my abilities as a physicist is Andrew Puckett. Andrew has been a light in the darkness for this research, and not just for my part in it. His contribution to my understanding of physics along with keeping me professionally on track and productive is impossible to overstate. I am extremely fortunate that he welcomed me into his research group and that he decided to pursue such interesting physics in the space of medium-energy nuclear and electron scattering—the field which I came to graduate school intent on pursuing and still love.

At Jefferson Lab, Mark Jones, Arun Tadepalli, Eric Fuchey, Brian Quinn, Scott Barcus, Dave Mack, Rachel Montgomery, and Juan-Carlos Cornejo were wonderful mentors and instrumental for my understanding of detector design, construction, detector physics, and analysis. They were also supportive and more than accommodating through a time that was unexpectedly stressful owing to the COVID pandemic and well after. Nobody gets a prize for spending time like they did on me—but they should. For my part, I won't forget the sacrifice of their time (and probably their patience).

Finally, my friends and fellow students at Jefferson Lab probably made the largest impact on the content of this dissertation. They are Provakar Datta (again), Casey Morean, Maria Satnik, John Boyd, Anuruddha Rathnayake, Ezekial Wertz, and Cameron Cotton. We were in the trenches together and I've learned a tremendous amount about this research train I'm on from you and even more about how to keep it from flying off the rails.

Contents

List of Figures

List of Tables

1 Introduction

1.1 The Discovery of Nucleon Structure

The goal of this section is to step through the history of nuclear physics starting at the turn of the twentieth century and leading up to modern nuclear physics. It will lay down some concepts used throughout this document and provide broad historical context for the central arguments herein.

1.1.1 Foundational Measurements and Theory

The concept of atoms as indivisible units of matter dates back to ancient Greek philosophers like Democritus, but it wasn't until the 19^{th} century that John Dalton provided the first scientific basis for this idea, when he formulated the first modern atomic theory based on his experiments with chemical reactions[32]. Subsequently, the discovery of the electron by J.J. Thomson in 1897 revealed that atoms were not indivisible, leading to the so-called "plum-pudding" model of the atom[173]. Arguably the first significant leap towards modern understanding came from Ernest Rutherford's gold foil experiment in 1909[150]. By observing the deflection of alpha particles through a thin gold foil, Rutherford concluded that atoms must have a small, dense, positively charged core, which he named the nucleus, surrounded by electrons. This discovery laid the foundation for the modern understanding of atomic structure, marking a pivotal moment in the advancement of quantum theory and nuclear physics.

Building upon the model of the atomic nucleus proposed by Rutherford, further investigations led to the discovery of the proton by Ernest Rutherford himself in 1917[134], and subsequently, the neutron by James Chadwick in 1932[29]. Initially, both protons and neutrons were thought to be point-like and fundamental components of the nucleus. The magnetic moment ($\boldsymbol{\mu}$) in natural units ($c = \hbar = 1$) for these kind of structureless "pure Dirac" particles can be derived from quantum

mechanics and Dirac equation (Paul Dirac, 1928)[51].[1]

$$\boldsymbol{\mu} = \gamma \mathbf{s} \tag{1.1}$$

Here γ is the gyromagnetic ratio and $\mathbf{s}$ is the spin angular momentum of the particle. For a charged particle, where g is the Landé g-factor, q is the charge, and m is the mass:

$$\gamma = g\frac{q}{2m} \tag{1.2}$$

Protons and neutrons are fermions with spin $s = \frac{1}{2}$ and the Dirac equation predicts $g = 2$ exactly. This gives μ for a structureless particle:

$$\boldsymbol{\mu} = \frac{q}{m}\mathbf{s} \tag{1.3}$$

On the point-like assumption, the magnitude of the proton magnetic moment should be the nuclear magneton (μ_N, where along $\hat{z}$, $|\mathbf{s}| = \frac{\hbar}{2}$ or just $\frac{1}{2}$ in natural units) and the magnitude of the neutron magnetic moment should be zero.

$$\text{proton} \rightarrow \mu_p = \mu_N = \frac{e}{2M_p}; \qquad \text{neutron} \rightarrow \mu_n = 0 \tag{1.4}$$

In 1933, Otto Stern measured μ_p and found a significant discrepancy in the expected value for a point-like "pure Dirac" proton, namely $\mu_p \approx 2.79\mu_N$[168]. Similarly, in 1940, while using nuclear magnetic resonance, Luis Alvarez and Felix Bloch measured μ_n and found a significant magnetic moment, $\mu_n \approx -1.91\mu_N$[6]. These results confirmed that the constituents of atomic nuclei (protons and neutrons) are not structureless, point-like particles. Rutherford, Stern, Alvarez, and Bloch all received Nobel prizes for their efforts, although, interestingly, Rutherford received his in Chemistry instead of Physics and for work unrelated to his pivotal discovery[119].

In his gold foil experiments, Rutherford derived a formula to describe the angular distribution

[1] Unless otherwise indicated, natural units will a assumed from here forward.

of alpha particles scattered by a Coulombic (electric) force off gold nuclei. This formula, assuming no target recoil and treated non-relativistically, begins with the Coulomb force (F) between two particles[2]:

$$F = \frac{1}{4\pi\varepsilon_0}\frac{q_1 q_2}{r^2} \tag{1.5}$$

In this equation, r represents the distance between the particles, q_1 is the charge of the scattered alpha particles, q_2 is the charge of the gold nucleus, and ε_0 is the vacuum permittivity. Figure 1 illustrates this scattering process. The diagram shows the impact parameter b, which is related to the scattering angle θ. This angle is crucial for determining the *differential cross section*, a measure of the probability that a particle with a target cross section $\mathrm{d}\sigma$ scatters into a solid angle $\mathrm{d}\Omega$, as shown in figure 2.

$$\mathrm{d}\sigma = 2\pi\, b\, \mathrm{d}b; \qquad \mathrm{d}\Omega = 2\pi \sin\theta\, \mathrm{d}\theta \tag{1.6}$$

This leads to the differential cross section formula:

$$\frac{\mathrm{d}\sigma}{\mathrm{d}\Omega} = \frac{b}{\sin\theta}\left|\frac{\mathrm{d}b}{\mathrm{d}\theta}\right| \tag{1.7}$$

For a fixed target nucleus, $|\mathbf{p}| = |\mathbf{p'}|$, and the change in momentum magnitude experienced by the scattered particle is related to an isosceles triangle, given by:

$$|\Delta\mathbf{p}| = 2p\sin\frac{\theta}{2} \tag{1.8}$$

This change in momentum can also be related to the Coulomb force in the direction of $\mathbf{u}$ (F_u):

$$|\Delta\mathbf{p}| = \int_{-\infty}^{\infty} F_u\, dt \tag{1.9}$$

[2]For this classical derivation of Rutherford scattering, SI units will be used.

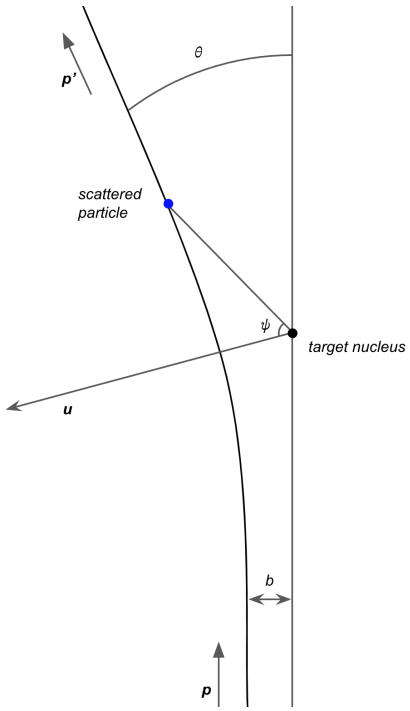

Figure 1: Classical Rutherford scattering of an alpha particle off a target atomic nucleus with no target recoil. The particle path is symmetric about the axis **u**, its position is described via the angle ψ, its initial momentum is **p**, its final momentum is **p'** after scattering, the scattering angle is θ, and b is the impact parameter, which is the perpendicular distance between the initial particle trajectory and the center of the nucleus. For this process, the scattering angle θ is related to ψ by $\theta = \pi - 2\psi_0$, where as $t \to \infty$, $\psi \to \psi_0$, and as time $t \to -\infty$, $\psi \to -\psi_0$. This implies that the angle ψ_0 corresponds to the angle at the point of closest approach to the nucleus.

After changing variables and inserting the force (eq. 1.5) projected on **u**, the integral becomes:

$$\int_{-\infty}^{\infty} F_u \, dt = \int_{-\psi_0}^{\psi_0} F_u \frac{d\psi}{\dot{\psi}} = \int_{-\psi_0}^{\psi_0} \frac{1}{4\pi\varepsilon_0} \frac{q_1 q_2}{r^2} \cos\psi \frac{d\psi}{\dot{\psi}} \tag{1.10}$$

Considering that the angular momentum is related to the impact parameter via the moment of inertia $L = mr^2\dot{\psi} = bp$ (from figure 1) and applying a half-angle identity, another expression for $|\Delta\mathbf{p}|$ can be found:

$$|\Delta\mathbf{p}| = \int_{-\psi_0}^{\psi_0} \frac{1}{4\pi\varepsilon_0} \frac{q_1 q_2}{r^2} \cos\psi \frac{mr^2}{bp} d\psi = \frac{1}{4\pi\varepsilon_0} \frac{2m}{bp} \cos\frac{\theta}{2} \tag{1.11}$$

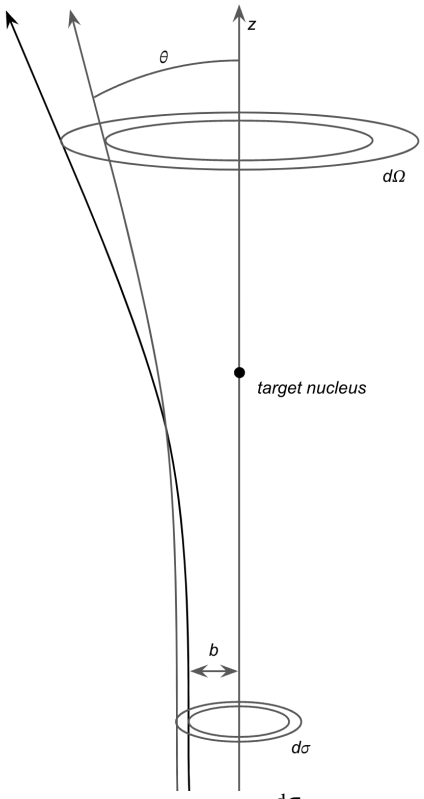

Figure 2: The differential cross section $\frac{\mathrm{d}\sigma}{\mathrm{d}\Omega}$, where the target cross section $\mathrm{d}\sigma$, the solid scattering angle $\mathrm{d}\Omega$, and the impact parameter b are depicted.

Solving for the impact parameter b in terms of the scattering angle θ by equating the two expressions for $|\Delta\mathbf{p}|$ and noting that $p = mv$, we get:

$$2p\sin\frac{\theta}{2} = \frac{1}{4\pi\varepsilon_0}\frac{2m}{bp}\cos\frac{\theta}{2} \quad \rightarrow \quad b = \frac{1}{4\pi\varepsilon_0}\frac{q_1 q_2}{mv^2}\cot\frac{\theta}{2} \tag{1.12}$$

Using equation 1.7, $b(\theta)$, $\mathrm{d}b(\theta)/\mathrm{d}\theta$, and $k = 1/(4\pi\varepsilon_0)$, the Rutherford formula emerges:

$$\frac{\mathrm{d}\sigma}{\mathrm{d}\Omega} = \left(\frac{kq_1 q_2}{4E\sin^2\frac{\theta}{2}}\right)^2 \tag{1.13}$$

In natural units where the charge is equal to that of the electron ($q_1 = q_2 = e$):

$$\frac{\mathrm{d}\sigma}{\mathrm{d}\Omega} = \left(\frac{\alpha}{2E\sin^2\frac{\theta}{2}}\right)^2 \tag{1.14}$$

The Rutherford formula not only serves as a cornerstone for classical scattering theory but, also paved the way for the introduction of more advanced concepts, including quantum scattering theory and the study of nuclear structure discussed later in the chapter.

After the discovery of the proton, it became evident that another force, apart from the known gravitational and electromagnetic forces, must be responsible for the stability of atomic nuclei. The positively charged protons in the nucleus naturally repel each other due to electromagnetic forces, so another mechanism had to exist to keep the nucleus intact. Ernest Rutherford speculated about the existence of a strong force to explain why atomic nuclei did not fly apart under electromagnetic repulsion, and in 1935 Hideki Yukawa proposed the existence of a new particle, which he called a *meson*, that mediated a strong force holding the nucleus together[185]. Yukawa's theory predicted that this particle would be heavier than an electron but lighter than a proton, and it would be responsible for the strong nuclear interaction. Yukawa's meson, later called the pion, was discovered in cosmic ray experiments in the 1940s by Cecil Powell and his colleagues[133]. The discovery of the pion provided the first experimental evidence for the existence of the strong force because the pion shared all the properties predicted by Yukawa for the meson mediating the strong interaction.

Around the same time and with the continuing development of quantum theory, Werner Heisenberg, in 1932, recognized the close similarity in mass between protons and neutrons (see Table 1) and introduced the concept of isospin as an SU(2) symmetry, analogous to quantum spin, to account for this nucleon duality[97]. In this framework, protons and neutrons are not to be regarded as separate particles, but rather two states of a single type of particle known as the *nucleon*. These two states are eigenstates of the isospin operator, characterized by an isospin quantum number $I = \frac{1}{2}$. The third component of isospin, I_3, differentiates the two states: $I_3 = +\frac{1}{2}$ represents the proton state, denoted as $|p\rangle = \left|\frac{1}{2}, \frac{1}{2}\right\rangle$, and $I_3 = -\frac{1}{2}$ represents the neutron state, denoted as $|n\rangle = \left|\frac{1}{2}, -\frac{1}{2}\right\rangle$. These states are analogous to the "up" and "down" components of a quantum spin-1/2 system. The isospin formalism neatly expresses the symmetry in the strong nuclear force, treating the proton and neutron identically in terms of strong interactions.

Propelled by the early formalism of quantum mechanics and Paul Dirac's work with the Dirac

Particle	Mass (MeV)
Proton	938.27
Neutron	939.56

Table 1: Masses of the proton and neutron[125].

equation, Quantum Electrodynamics (QED) was formulated during the 1940s as the quantum field theory of electromagnetism. Developed independently by Richard Feynman, Julian Schwinger, Sin-Itiro Tomonaga, and Freeman Dyson, QED describes how light and matter interact and is the first theory to achieve full agreement between quantum mechanics and special relativity[60, 158, 174, 53]. Central to QED is the explanation of how electromagnetic forces are mediated: it posits that charged particles interact by exchanging *virtual photons*. These photons are the quantized fields representing electromagnetic waves, and their exchange accounts for the electromagnetic forces between particles. This theory provided a comprehensive framework to understand and calculate the electromagnetic interactions of charged particles and the behavior of photons. In 1965, the Nobel Prize in Physics was awarded jointly to Feynman, Schwinger, and Tomonaga "for their fundamental work in quantum electrodynamics, with deep-ploughing consequences for the physics of elementary particles"[121].

1.1.2 Modern Nuclear Physics

Prompted by these findings, subsequent research efforts were directed towards a deeper exploration of the nucleons' internal structure. In the 1950s, Robert Hofstadter's electron scattering experiments at Stanford University provided more insight[100]. These experiments involved bombarding nucleons with high-energy electrons and observing the final states of scattered particles. Since electrons are not subject to the strong nuclear force, they can effectively probe the electromagnetic properties of nucleons, revealing details about their internal charge and magnetization distributions. This led to the introduction of the Sachs form factors, G_E and G_M, to describe these distributions within the nucleon[151]. These quantities, central to the subject of this thesis, along with electron-nucleon (e-N) scattering, will be discussed at greater length later in the chapter. Hof-

stadter was awarded the Nobel prize in 1961 for this work[120].

In the following years, advancements in cosmic ray detection and particle accelerator technologies, including cyclotrons and synchrocyclotrons, led to the discovery of numerous new subatomic particles. This period saw the identification of particles like kaons, known for their peculiar behaviors, and others including lambda, sigma, xi, and omega particles, each with distinct properties that significantly contributed to the study of nuclear forces[77]. These discoveries, characterized by a wide range of masses, charges, and stability, resulted in an extensive and varied collection of particles, famously referred to as the "particle zoo" due to their diversity and complexity.

In 1964, building upon Yukawa's meson concept and aiming to provide a more detailed explanation of the strong nuclear force, Murray Gell-Mann and George Zweig independently proposed the quark model[79, 188]. This model introduced quarks as the fundamental constituents of protons, neutrons, and other particles which are susceptible to the strong interaction. According to the modern formulation of this model, all of these particles (*hadrons*) are comprised of quarks, which come in six flavors: up (u), down (d), charm (c), strange (s), top (t), and bottom (b). Each quark flavor is distinct in its mass and other properties, as summarized in Table 2.

Quark Flavor	Charge	Mass (MeV)	Properties
Up (u)	+2/3	2.16 ± 0.49	Common in protons and neutrons
Down (d)	-1/3	4.67 ± 0.48	Common in protons and neutrons
Charm (c)	+2/3	$1{,}275 \pm 25$	Heavier, found in exotic hadrons
Strange (s)	-1/3	93 ± 9	Contributes to strangeness
Top (t)	+2/3	$172{,}760 \pm 3{,}000$	Heaviest, very unstable
Bottom (b)	-1/3	$4{,}180 \pm 30$	Heavier, found in exotic hadrons

Table 2: General properties of quarks, including their charge, mass with uncertainties, and typical occurrences[127].

Hadrons are divided into two categories based on their quark composition: *baryons* and *mesons*.

- *Baryons*, such as protons and neutrons, are made up of three quarks.
- *Mesons* consist of a quark and an *antiquark* pair.

An antiquark is the antimatter counterpart of a quark — it has the same mass as a quark but opposite electric charge and other quantum numbers. They are denoted by the same flavor symbol, but with

a bar above ($\bar{u}$, for instance). The quark model thus provided a framework for classifying the wide variety of particles discovered in high-energy physics experiments, which were previously difficult to categorize systematically. This greatly simplified the "particle zoo" by showing that the plethora of known particles were just different combinations of a small set of quarks. Tables 3 and 4 provide an overview of the composition of mesons and baryons, respectively. Additionally, a third category exists which contains the electron and muon (among others). These *leptons* are not comprised of quarks and are all considered fundamental. Murray Gell-Mann was awarded the Nobel Prize in Physics in 1969, primarily for his work involving the quark model — generally "for his contributions and discoveries concerning the classification of elementary particles and their interactions"[122].

Meson	Quark Composition
Pion (π^+)	$u\bar{d}$
Pion (π^-)	$\bar{u}d$
Pion (π^0)	$\frac{u\bar{u}-d\bar{d}}{\sqrt{2}}$
Kaon (K^+)	$u\bar{s}$
Kaon (K^-)	$\bar{u}s$
Kaon (K^0)	$d\bar{s}$
Kaon ($\bar{K}^0$)	$\bar{d}s$

Table 3: Examples of mesons. The charge-neutral pion is a superposition of $u\bar{u}$ and $d\bar{d}$ states.

Baryon	Quark Composition
Proton (p)	uud
Neutron (n)	udd

Table 4: Examples of Baryons

Although the quark model effectively simplified the "particle zoo", it initially faced skepticism because quarks, confined within hadrons, could not be directly observed. The decisive evidence for the quark model came from deep inelastic scattering experiments at the Stanford Linear Accelerator Center (SLAC) in the late 1960s. High-energy electron beams were used to probe protons, similar to Hofstadter's method, but at much higher energies. These experiments revealed that protons contained point-like constituents, providing strong evidence for the existence of quarks[36].

For their pioneering investigations concerning deep inelastic scattering (DIS) of electrons on protons and bound neutrons, which have been of essential importance for the development of the quark model in particle physics, Jerome Friedman, Henry Kendall, and Richard Taylor were awarded the Nobel Prize in Physics in 1990[123].

The success of DIS experiments in the late 1960s, which provided compelling evidence for the existence of quarks within protons, set the stage for a more profound theoretical framework. While the quark model explained the composition of hadrons, it did not fully describe the dynamics of how quarks interacted and why they could not be isolated. This gap in understanding led to the development of Quantum Chromodynamics (QCD) in the early 1970s.

QCD emerged as the theory describing the strong interaction, fundamentally explaining how quarks are bound together to form hadrons such as protons and neutrons. This binding is mediated by *gluons*, similar to virtual photons in QED. QCD is characterized by three central concepts: *color charge*, *color confinement*, and *asymptotic freedom*. Color charge, analogous to electric charge, dictates interactions between quarks and gluons within the SU(3) symmetry, encompassing three color states: red, green, and blue[62]. This symmetry framework classifies quark bound states with mesons as singlet $3 \otimes \bar{3}$ states and baryons as singlet $3 \otimes 3 \otimes 3$ states. Protons and neutrons are thus comprised of three *valence* quarks which contribute to the quantum numbers of the nucleon.

In plainer language, QCD describes the strong force such that it becomes stronger as quarks move apart from each other. This leads to color confinement; the phenomenon where quarks and gluons cannot exist in isolation and are always confined within hadrons[88]. This is in stark contrast to, say, electromagnetism, where the force weakens with distance and free charged particles (like electrons) can exist in isolation. When bound quarks are forced apart, as in high-energy particle collisions, the energy between the quarks becomes so great that it spontaneously creates new quark-antiquark pairs — the phenomenon known as *hadronization*[3]. While quarks are confined at larger distances, at very short distances they are almost free. This is the previously mentioned phenomenon of asymptotic freedom[132].

[3] Additional details are important to fully characterize the hadronization process. These are not the focus of this thesis and are left out for brevity.

At time and energy scales bounded by Heisenberg's principle ($\Delta E\,\Delta t \gtrsim 1$), when electrons are accelerated to high energies and used to probe nucleons (such as in deep inelastic scattering), the short interaction time (Δt) within the nucleon corresponds to a large uncertainty in the energy (ΔE) of the interaction. This allows for temporarily "borrowing" of enough energy to create virtual particles, such as quark-antiquark pairs and gluons. These quark-antiquark pairs are analogous to the "pion cloud" model of virtual pion emission and reabsorption by the nucleon. They are more generally referred to as "sea quarks" for these interactions within the nucleon. "Sea gluons" exist in this context as well.

Similar to Heisenberg and isospin before them, the Eightfold Way was developed by Murray Gell-Mann and Yuval Ne'eman which further explores the SU(3) symmetry in classifying hadrons[78, 117]. It arranges these particles into octets and decuplets based on their quark composition, reflecting their bound states. This classification not only simplified the understanding of numerous particles discovered in high-energy experiments but also paved the way for the modern quark model discussed earlier and further detailed in Table 5. In the quark model, each quark is characterized by specific quantum numbers such as a baryon number, which indicates its contribution to a particle's baryonic content, strangeness, and charm. Each of these are essential when describing a particle's behavior during weak interactions. Protons and neutrons, as composites of these quarks, inherit these quantum properties, contributing to their unique characteristics in terms of spin, charge, and mass.

Along with Sheldon Glashow's unification of the weak nuclear and electromagnetic interactions into electroweak theory in 1961, QED and QCD laid the groundwork for the *Standard Model*[81]. This comprehensive theory, which categorizes all fundamental interactions through force carriers and the particles they act upon, remains the most robust framework for explaining natural phenomena (see figure 3). The Standard Model not only encapsulates the known fundamental forces, excluding gravity, but also continues to be the best explanation for nuclear and particle physics as understood today.

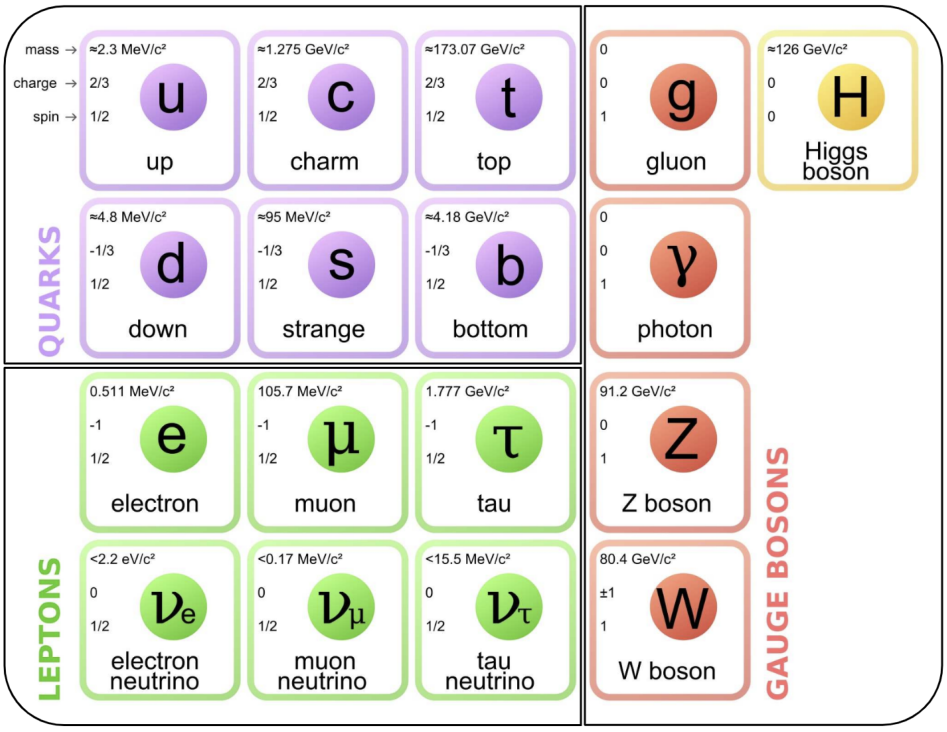

Figure 3: All elementary particles on the standard model with mass, charge, and spin labeled. Leptons and quarks are all fermions. Bosons are labeled. Adapted from [7].

1.2 Elastic *e*-*N* Scattering

Electron scattering experiments like those conducted by Hofstadter provide a powerful and contemporary tool in the field of nuclear physics. In electron-nucleon scattering (*e*-*N*), electrons with varying energy are directed at and scattered off of target nucleons to reveal their structure. To enhance the precision and reliability of these measurements, electrons are collected into beams with high *luminosity*. Luminosity can be defined thus:

$$\mathscr{L} = \frac{I\rho L}{e}, \tag{1.15}$$

where I is the beam current, ρ is the number density of the target, and L is the length of the target[4]. High luminosity allows for a great number of scattering events to be observed, thereby enhancing

[4] $\mathscr{L}$ is often measured in units of $\mathrm{cm}^{-2}\cdot\mathrm{s}^{-1}$

Quark	Charge	Spin	Baryon No.	Isospin (I, I3)	Charm (C)	Strangeness (S)
Up (u)	+2/3	1/2	1/3	(1/2, 1/2)	0	0
Down (d)	-1/3	1/2	1/3	(1/2, -1/2)	0	0
Charm (c)	+2/3	1/2	1/3	(0, 0)	1	0
Strange (s)	-1/3	1/2	1/3	(0, 0)	0	-1
Top (t)	+2/3	1/2	1/3	(0, 0)	0	0
Bottom (b)	-1/3	1/2	1/3	(0, 0)	0	0

Table 5: Quantum Numbers of Quarks

the statistical significance of the data. To probe the structure of the nucleon at various levels, the energies of electron beams are tuned with accelerators. The electron de Broglie wavelength determines how electrons will interact at scale:

$$\lambda_e = \frac{1}{p_e} \tag{1.16}$$

Here λ_e is the electron de Broglie wavelength and p_e is the electron momentum. The energy of the electron is related to its mass and momentum via special relativity:

$$E_e^2 = M_e^2 + p_e^2 \tag{1.17}$$

Here E_e is the energy of the electron, M_e is the mass of the electron, and p_e is the momentum of the electron. Where the velocity of the electron is accelerated to relativistic speeds ($v_e \to c$), $E_e \approx p_e$. As mentioned, the energy of the electron beam determines the scale of the interaction that can be probed with the electron, where higher energy electrons have shorter λ_e and higher frequencies ($\nu_e = 1/\lambda_e$). This allows higher energy electrons to resolve smaller structures within a nucleon of radius r_N in the following manner:

- Where the electron energy is **low** ($\lambda_e >> r_N$), the nucleon appears "point-like," structureless, and spin-less. In this regime, the entire nucleus can be *elastically* scattered by the probe electron.
- Where the electron energy is **medium** ($\lambda_e \sim r_N$), the scattering pattern will reflect the spatial structure of the nucleon's charge distribution and the nucleon appears as an extended charged

object. In this regime, the nucleon within the nucleus can be *quasi-elastically* scattered by the probe electron.

- Where the electron energy is **high** ($\lambda_e < r_N$), the constituents of the nucleon can be resolved, beginning with valence quarks. In this regime, the nucleon is often blown apart which corresponds to *deep inelastic scattering)*.
- Where the electron energy is **very high** ($\lambda_e \ll r_N$), the electron can resolve sea quarks within the nucleon.

In this context, nuclear accelerators produce electrons at medium to high energies to resolve the structure of the nucleon. Figure 4 gives a visual aid for this concept.

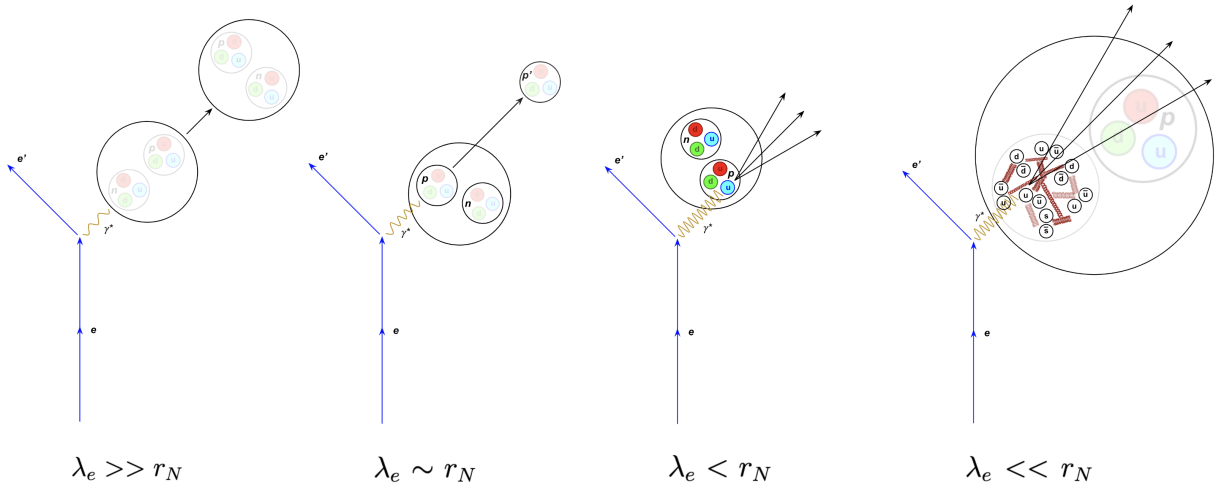

Figure 4: Electron scattering on nuclei. $\lambda_e >> r_N$ (left), elastic scattering of the nucleus is depicted. $\lambda_e \sim r_N$ (left-center), quasi-elastic scattering of nucleons is depicted. $\lambda_e < r_N$ (right-center), inelastic scattering is depicted. $\lambda_e \ll r_N$ (right), sea quarks can be resolved. The primes indicate scattered products and γ^* is the virtual photon that mediates the interaction.

1.2.1 QED Formalism

[5] Quantum Electrodynamics (QED) provides the machinery to calculate cross sections, or interaction probabilities, for the aforementioned (and many other) scattering processes. The simplest of these processes is particle-antiparticle annihilation. To illustrate, consider the annihilation of

[5] This section adapts this work: [129, 92, 35].

two leptons resulting in the production of two more, ($e^+e^- \to \mu^+\mu^-$). In this process, e^- carries momentum $\mathbf{p}$, e^+ carries momentum $\mathbf{p}'$, μ^- carries momentum $\mathbf{k}$, and μ^+ carries momentum $\mathbf{k}'$. With dimensional correction, the general form of the differential cross section for all scattering processes of this kind is given by:

$$\left(\frac{d\sigma}{d\Omega}\right) = \left(\frac{1}{4\pi E_{\text{cm}}}\right)^2 |\mathscr{M}|^2 \tag{1.18}$$

Here E_{cm} is the center-of-mass energy for the interaction and $|\mathscr{M}|$ is the dimensionless quantum amplitude of the process.[6] This amplitude is $|\mathscr{M}|$ cannot be evaluated exactly, but can be expanded perturbatively in α.[7] Direct computation of the probability amplitude requires the interaction Hamiltonian $\mathscr{H}_I$ and, after the first order term vanishes[8], the second order term in the expansion, where the initial state is $|e^+e^-\rangle$ and the final state is $\langle\mu^+\mu^-|$, is of the form:

$$\mathscr{M} \propto \left\langle \mu^+\mu^- \right| \mathscr{H}_I \left|\gamma\right\rangle^{\mu} \left\langle\gamma\right| \mathscr{H}_I \left|e^+e^-\right\rangle_{\mu} \tag{1.19}$$

The contravariant and covariant vector indices are necessary here as the virtual photon which mediates the interaction is a four-vector.[9]

One can depict this process as it appears in the diagram in figure 5. Here k is the muon four-momentum vector, p is the electron's four-momentum vector, and q is the four-momentum transferred between them by the virtual photon such that $q = p + p' = k + k'$. The labels s and r indicate spin states before and after the reaction, respectively. Interpretation of the diagram in terms of the amplitude is straightforward - the muon line is $\langle\mu^+\mu^-|$, the electron line is $|e^+e^-\rangle$, each of the two vertices are the two Hamiltonian terms $\mathscr{H}_I$, and the photon line is $|\gamma\rangle\langle\gamma|$. Via conservation of angular momentum and reference to Klebsh-Gordon coefficients for the remainder, the surviving

[6] This amplitude must not change based on inertial reference frame such that it is Lorentz invariant. It will sometimes be referred to as the *invariant amplitude* for this reason.

[7] α is the fine structure constant which governs the strength of electromagnetic interaction; $\alpha = \frac{e^2}{4\pi} \approx \frac{1}{137}$.

[8] $\mathscr{H}_I$ couples e to μ only via electromagnetic fields, so the direct interaction probability is zero.

[9] Moving forward, bold will denote a traditional three-vector and italic will add time and denote a four-vector

matrix elements correspond to the amplitudes:

$$\mathscr{M}(RL \to LR) = -e^2(1-\cos(\theta)) \tag{1.20}$$

$$\mathscr{M}(LR \to RL) = -e^2(1-\cos(\theta)) \tag{1.21}$$

$$\mathscr{M}(LR \to LR) = -e^2(1+\cos(\theta)) \tag{1.22}$$

where the surviving amplitudes are denoted by the *helicity* of the spin for the configuration. The electron and muon have "right-handedness"("left-handedness") as denoted by R(L) when they have spins fully parallel(anti-parallel) to their momentum vectors. [10] The total amplitude is the average over these states and, after collecting the factors of e into α, the total cross section is:

$$\sigma_{total} = \frac{4\pi\alpha^2}{3E_{cm}} \tag{1.23}$$

Of course, this cross section arises from only the surviving leading-order term in the expansion of the quantum amplitude. In fact, infinite terms exist, but are suppressed at higher orders by a factor of α per order. This represents the relatively weak coupling of the electromagnetic force as compared to the strong nuclear force, for instance.[11]

The diagram in figure 5 represents a powerful methodology for computing amplitudes and, by extension, cross sections. Richard Feynman gave a set of rules to interpret such a diagram. For this case, they dictate the following:

- Draw all possible diagrams where the number of vertices is equal to the order of the expansion.
- For each diagram, write $ig_{\mu\nu}/q^2$ for each internal photon line, which corresponds to $|\gamma\rangle\langle\gamma|$ in the previous expression. This is the *photon propagator*.[12]
- For each diagram, write $-ie\gamma^\mu$ per vertex corresponding to $\mathscr{H}_I$. The Dirac matrix γ^μ couples

[10] More generally, helicity is defined thus: $h = \mathbf{S}\cdot\hat{p}$, where $\mathbf{S}$ is the spin of the particle and $\hat{p}$ is the unit vector pointing in the direction of the momentum of the particle.

[11] The coupling constant for the strong force is denoted as α_s. At energy scales around the Z boson mass, where perturbative methods become viable for QCD, $\alpha_s \approx 0.118$ which is significantly larger than $\alpha = 1/137$.

[12] $g_{\mu\nu}$ is the Minkowski metric tensor.

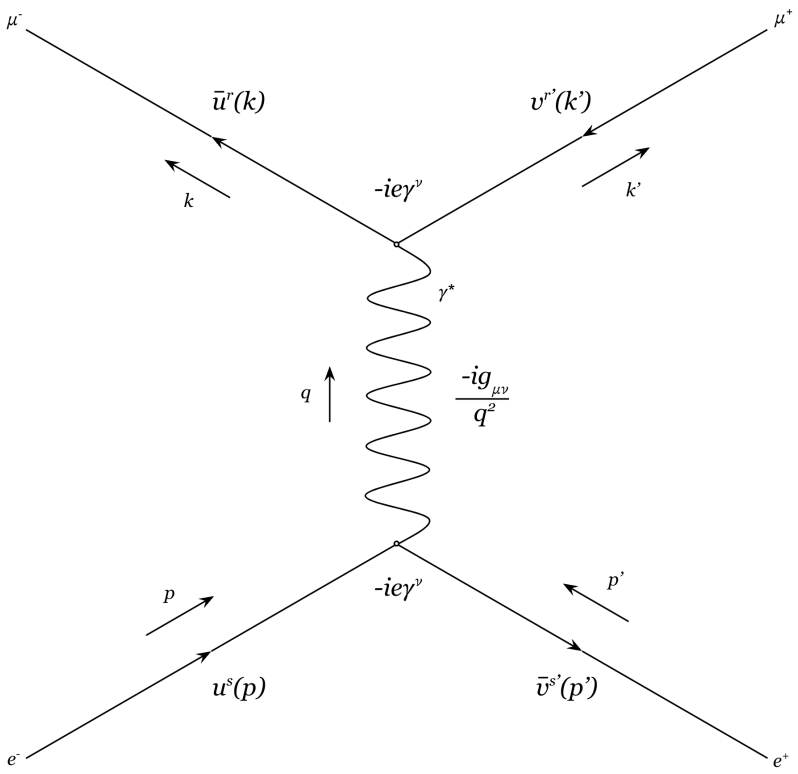

Figure 5: Feynman diagram for lepton annihilation $e^+e^- \to \mu^+\mu^-$ with Feynman rule labels for this process included. The direction of the continuous arrows follows the flow of charge, while the direction of short arrows follows the flow of momentum.

both spin $s = \frac{1}{2}$ particles to the γ vector particle.

- For each diagram, write the appropriate row or column Dirac-spinor (u and v column spinors, $\bar{u}$ and $\bar{v}$ row spinors) corresponding to the initial and final states.

Connecting the initial and final states and written straight from the diagram, the *Feynman diagram* in figure 5 leads to the expression for $\mathscr{M}$[13]:

$$-i\mathscr{M} = \bar{v}^{s'}(p')(-ie\gamma^{\mu})u^{s}(p)\left(\frac{-ig_{\mu\nu}}{q^2}\right)\bar{u}^{r}(k)(-ie\gamma^{\nu})v^{r'}(k') \tag{1.24}$$

$$-i\mathscr{M} = \frac{ie^2}{q^2}\left(\bar{v}^{s'}(p')\gamma^{\mu}u^{s}(p)\right)\left(\bar{u}^{r}(k)\gamma_{\mu}v^{r'}(k')\right) \tag{1.25}$$

It can be shown that this amplitude evaluates to the same cross section as in 1.23. Following the

[13]By convention, the $-i$ can be left off of the left-hand-side (LHS) in the expression.

flow of charge, the factors on either side of the photon propagator correspond to the somewhat more tightly constructed *lepton currents* (or lepton transition currents). In this case:

$$\text{electron} \quad \rightarrow \quad j_e^\mu = -e\bar{v}^{s'}(p')\gamma^\mu u^s(p) \tag{1.26}$$

$$\text{muon} \quad \rightarrow \quad j_\mu^\mu = -e\bar{u}^{r'}(k')\gamma^\mu v^r(k) \tag{1.27}$$

Expressions for currents for other particle types will be discussed later in the chapter. This initial formalism allows for straightforward expressions of the amplitude $\mathscr{M}$ for scattering processes that are more relevant to this thesis given later in the chapter.[14]

There is an important implication of this formalism — each included vertex added to the diagram will add a factor of e to the invariant amplitude, and each photon line adds two factors of e, or one factor of α. It is the strength of the suppression per added virtual photon that leads many cross section calculations to stop at leading order (as has been done here) and rely on the *One Photon Exchange* (OPE) approximation.[15] This approximation will be made throughout the chapter unless otherwise noted.

1.2.2 Mott Cross Section

Now consider the Coulomb field in the interaction Hamiltonian where in e-N scattering, the electron interacts with the Yukawa potential. The interaction Hamiltonian takes the form:

$$H_I = \int d^3x\, e\bar{\psi}\gamma^\mu \psi A_\mu . \tag{1.28}$$

Here $\psi(x)$ is the quantized Dirac field and $A_\mu(x)$ is a generalized classical vector potential (for now).[16] This Hamiltonian describes the interaction between the electron field and the electro-

[14] Many other rules exist for different diagrams not presented here.

[15] Also known as the *Born Approximation*, after Max Born who first formulated it.

[16] As usual, $\psi(x) = \int \frac{d^3p}{(2\pi)^3} \frac{1}{\sqrt{2E_\mathbf{p}}} \sum_{s=1}^{2} \left(a_{\mathbf{p},s} u(\mathbf{p},s) e^{-ip\cdot x} + b^\dagger_{\mathbf{p},s} v(\mathbf{p},s) e^{ip\cdot x} \right)$ where, d^3p represents integration over three-dimensional momentum space, $(2\pi)^3$ is the normalization factor, $E_\mathbf{p}$ is the energy of the particle with momentum $\mathbf{p}$, $a_{\mathbf{p},s}$ and $b_{\mathbf{p},s}$ are the annihilation operators for particles and antiparticles respectively, $a^\dagger_{\mathbf{p},s}$ and $b^\dagger_{\mathbf{p},s}$ are the corresponding creation operators, $u(\mathbf{p},s)$ and $v(\mathbf{p},s)$ are the spinor solutions to the Dirac equation for particles and

magnetic field where the term $e\bar{\psi}\gamma^{\mu}\psi A_{\mu}$ represents the coupling of the electron field ψ with the electromagnetic vector potential A_{μ}, mediated by the gamma matrices γ^{μ}, which encode the spin structure of the interaction. The charge e dictates the strength of this interaction. In the Heisenberg Picture, the evolution operator is time-dependent, often denoted as $U_I(t,t_0)$, and is given by the time-ordered exponential of the interaction Hamiltonian:

$$U_I(t,t_0) = \mathscr{T}\exp\left(-i\int_{t_0}^{t} H_I(t')dt'\right) \tag{1.29}$$

Where $\mathscr{T}$ is the transition matrix. Additionally, the unitary scattering matrix $\mathscr{S}$, which relates the pre-scattering electron initial state $|\mathbf{p}\rangle_{\text{in}}$ to the post-scattering final state ${}_{\text{out}}\langle\mathbf{p'}|$ labeled by the electron momentum vectors, can be related to it:[17]

$$\mathscr{S} = 1 + i\mathscr{T} \tag{1.30}$$

Where:

$$\langle\mathbf{p}'|\mathscr{S}|\mathbf{p}\rangle = {}_{\text{out}}\langle\mathbf{p}'|\mathbf{p}\rangle_{\text{in}} \tag{1.31}$$

Here ${}_{\text{out}}\langle\mathbf{p}'|\mathbf{p}\rangle_{\text{in}}$ is the overlap of incoming and outgoing states of the electron. Computation of the $\mathscr{T}$ matrix element to first order in e yields:

$$\begin{aligned}
{}_{\text{out}}\langle\mathbf{p}'|\mathscr{T}|\mathbf{p}\rangle_{\text{in}} &= \langle\mathbf{p}'|\mathscr{T}\exp\left(-i\int d^4x\mathscr{H}_I\right)|\mathbf{p}\rangle && (1.32)\\
&= \langle\mathbf{p}'|\mathbf{p}\rangle - ie\int d^4x A_{\mu}(x)\langle\mathbf{p}'|\bar{\psi}\gamma^{\mu}\psi|\mathbf{p}\rangle + \mathscr{O}(e^2) && (1.33)\\
&= (2\pi)^4\delta^{(4)}(\mathbf{p}-\mathbf{p}') - ie\bar{u}(\mathbf{p}')\gamma^{\mu}u(\mathbf{p})\int d^4x A_{\mu}(x)e^{i(\mathbf{p}'-\mathbf{p})\cdot x} + \mathscr{O}(e^2) && (1.34)\\
&= (2\pi)^4\delta^{(4)}(\mathbf{p}-\mathbf{p}') - ie\bar{u}(\mathbf{p}')\gamma^{\mu}u(\mathbf{p})\tilde{A}_{\mu}(\mathbf{p}'-\mathbf{p}) + \mathscr{O}(e^2). && (1.35)
\end{aligned}$$

antiparticles, s is the spin state, and $p\cdot x$ is the four-momentum dot product with the space-time point.

[17] The $\mathscr{S}$ elements, $\mathscr{S}_{fi}$ are related to the invariant amplitudes $\mathscr{M}_{fi}$: $S_{fi} = \langle f|S|i\rangle = \delta_{fi} + i(2\pi)^4\delta^{(4)}(p_f - p_i)\mathscr{M}_{fi}$

Where $\tilde{A}_\mu(\mathbf{p}'-\mathbf{p}) = \int d^4x A_\mu(x) e^{i(\mathbf{p}'-\mathbf{p})\cdot x}$ denotes the Fourier transform of the vector potential. Using this result and 1.30, the matrix elements of the $\mathscr{T}$ matrix are given in terms of the vector potential by:[18]

$$\left\langle \mathbf{p}' \right| i\mathscr{T} \left| \mathbf{p} \right\rangle = ie\bar{u}(\mathbf{p}')\gamma^\mu u(\mathbf{p})\tilde{A}_\mu(\mathbf{p}'-\mathbf{p}) \tag{1.36}$$

Now, the cross section for this scattering is just the integral of the probability density as a function of the plane displacement from the potential — or, for consistency, the impact parameter $\mathbf{b}$.

$$d\sigma = \int d^2b P(\mathbf{b}) \tag{1.37}$$

Where the probability density can be written in terms of the initial waveform $|\psi\rangle$ and the electron energy (corresponding to $\mathbf{p}$) as:

$$P = \frac{d^3p}{(2\pi)^3}\frac{1}{2E_\mathbf{p}} \left|{}_{\text{out}}\langle \mathbf{p}|\psi\rangle_{\text{in}}\right|^2 \tag{1.38}$$

The momentum space waveform in terms of $\mathbf{b}$ and the incoming wave momentum states labeled $\mathbf{k}$ is:

$$|\psi\rangle_{\text{in}} = \int \frac{d^3k}{(2\pi)^3}\frac{e^{-i\mathbf{b}\cdot\mathbf{k}}}{\sqrt{2E_k}}\psi(\mathbf{k})|\mathbf{k}\rangle, \tag{1.39}$$

With a suitable expression for the wavefunction and with equation 1.31, the probability term can be evaluated:

$$\left|{}_{\text{out}}\langle \mathbf{p}|\psi\rangle_{\text{in}}\right|^2 = \int \frac{d^3kd^3k'}{(2\pi)^6}\frac{1}{\sqrt{4E_\mathbf{k}E_{\mathbf{k}'}}}\psi(\mathbf{k})\psi^*(\mathbf{k}')_{\text{out}}\langle \mathbf{p}|\mathbf{k}\rangle_{\text{in}}\,{}_{\text{out}}\langle \mathbf{p}|\mathbf{k}'\rangle^*_{\text{in}} e^{-i\mathbf{b}\cdot(\mathbf{k}-\mathbf{k}')} \tag{1.40}$$

$$= \int \frac{d^3kd^3k'}{(2\pi)^6}\frac{1}{\sqrt{4E_\mathbf{k}E_{\mathbf{k}'}}}\psi(\mathbf{k})\psi^*(\mathbf{k}')\langle \mathbf{p}|i\mathscr{T}|\mathbf{k}\rangle\langle \mathbf{p}|i\mathscr{T}|\mathbf{k}'\rangle^* e^{-i\mathbf{b}\cdot(\mathbf{k}-\mathbf{k}')} \tag{1.41}$$

Since $A_\mu(x)$ is time dependent, the transition amplitude can be written in terms of the invariant

[18] In fact, one can adopt the Feynman rule for this step — an electron transition current coupled to a vector potential $A_\mu \to -ie\gamma^\mu\tilde{A}_\mu(\mathbf{q})$. Note that the lowest order term that survives still corresponds to OPE where the second factor of e is supplied by the form of the Yukawa potential.

amplitude and a delta function of energy:

$$\left\langle \mathbf{p}' \right| i\mathscr{T} \left| \mathbf{p} \right\rangle \equiv i\mathscr{M} \cdot (2\pi)\delta\left(E_f - E_i\right) \tag{1.42}$$

So, the probability term can be carried further:

$$|_{\text{out}}\langle \mathbf{p}|\psi\rangle_{\text{in}}|^2 = \int \frac{d^3k\, d^3k'}{(2\pi)^6\sqrt{2E_k 2E_{k'}}} \psi(\mathbf{k})\psi^*(\mathbf{k}')\, |i\mathscr{M}|^2\, (2\pi)^2 \delta(E_p - E_k)\delta(E_p - E_{k'}) e^{-i\mathbf{b}\cdot(\mathbf{k}-\mathbf{k}')} \tag{1.43}$$

Now one can evaluate the cross section with equation 1.37 and perform contractions over many delta functions.[19]

$$d\sigma = \frac{d^3p}{(2\pi)^3 2E_{\mathbf{p}}} \int \frac{d^3k}{(2\pi)^3 2E_{\mathbf{k}} v} |\psi(\mathbf{k})|^2\, |i\mathscr{M}|^2 (2\pi)\delta(E_{\mathbf{p}} - E_{\mathbf{k}}) \tag{1.44}$$

Where the momentum is localized the expression may be simplified:[20]

$$d\sigma = \frac{d^3p}{(2\pi)^2} \frac{1}{4E_{\mathbf{p}}E_{\mathbf{k}}v} |\mathscr{M}|^2 \delta(E_{\mathbf{p}} - E_{\mathbf{k}}) \tag{1.45}$$

For the full differential cross section, integrate over the magnitude of $\mathbf{p}$:

$$\frac{d\sigma}{d\Omega} = \int \frac{dp\, p^2}{(2\pi)^2} \frac{1}{4E_{\mathbf{p}}E_{\mathbf{k}}v} |\mathscr{M}|^2 \delta(E_{\mathbf{p}} - E_{\mathbf{k}}) \tag{1.46}$$

$$= \frac{q}{(4\pi)^2} |\mathscr{M}(k,\theta)|^2 \tag{1.47}$$

Where the integral is evaluated with the delta function which fixes only the magnitudes of the momentum vectors $|\mathbf{p}| = |\mathbf{k}|$. This requires that the invariant amplitude depend on the momentum $|\mathbf{k}|$ and the scattering angle θ only.

The specific form of the Yukawa potential in momentum space (where $\mathbf{q} = \mathbf{p} - \mathbf{k}$ and Z is the

[19] The notation gets a little messy, but the integration over the impact parameter is evaluated thus: $\int d^2b\, e^{-i\mathbf{b}\cdot(\mathbf{k}-\mathbf{k}')} = (2\pi)^2\delta^{(2)}(\mathbf{k}_\perp - \mathbf{k}'_\perp)$; and the other two deltas thus: $\delta(E_{\mathbf{k}} - E_{\mathbf{k}'}) = \frac{E_{\mathbf{k}}}{k_\parallel}\delta(k_\parallel - k'_\parallel) = \frac{1}{v}\delta(k_\parallel - k'_\parallel)$ where $|\mathbf{v}| = v = v_\parallel$

[20] Note that for a normalized wave packet, $\int \frac{d^3k}{(2\pi)^3} |\psi(\mathbf{k})| = 1$

total number of particles in the nucleus with charge e) is:

$$A^0(\mathbf{q}) = \frac{Ze}{|\mathbf{q}|^2} \tag{1.48}$$

$$= \frac{Ze}{|\mathbf{p}-\mathbf{k}|^2} \tag{1.49}$$

From Feynman rules for this process where the energy of the electron E may change, the invariant amplitude is:

$$i\mathscr{M}(k,\theta) = ie\bar{u}(p')\gamma^\mu \tilde{A}_\mu(\mathbf{q})u(p) \tag{1.50}$$

For this unpolarized case, the initial electron spin states are averaged and the probability is the sum over final electron spin states. After evaluation of the sum with trace technology to reduce steps, the form of the probability is more manageable:[21]

$$\frac{1}{2}\sum_{\text{spin}}|\mathscr{M}|^2 = \frac{1}{2}\sum_{\text{spin}}\left|\bar{u}(p')(-ie\gamma^\mu\tilde{A}_\mu)u(p)\right|^2 \tag{1.51}$$

$$= \frac{e^2}{2}\sum_{\text{spin}}\text{Tr}\left[\bar{u}(p')u(p)\gamma^\mu u(p)\bar{u}(p')\gamma^\nu\right]\tilde{A}_\mu\tilde{A}_\nu \tag{1.52}$$

$$= \frac{e^2}{2}\text{Tr}\left[(\not{p}'+m_e)\gamma^\mu(\not{p}+m_e)\gamma^\nu\right]\tilde{A}_\mu\tilde{A}_\nu \tag{1.53}$$

$$= 2e^2\left[2EE' + p'\cdot p + m_e^2\right]\left(\frac{Ze}{|\mathbf{q}|^2}\right)^2 \tag{1.54}$$

The differential cross section in terms of the invariant amplitude here is given by 1.47 and momentum conservation requires that the form of the Yukawa potential depends only on the angle between the vectors **p** and **k** and the magnitude:

$$\frac{Ze}{|\mathbf{q}|^2} = \frac{Ze}{|\mathbf{p}-\mathbf{k}|^2} = \frac{Ze}{4|\mathbf{p}|^2\sin^2(\theta/2)} \qquad \text{and} \tag{1.55}$$

$$\frac{d\sigma}{d\Omega} = \frac{1}{(4\pi)^2}\left(\frac{1}{2}\sum_{\text{spin}}|\mathscr{M}(k,\theta)|^2\right) = \frac{1}{(4\pi)^2}|\overline{\mathscr{M}}(k,\theta)|^2 \tag{1.56}$$

[21] Standard Feynman slash notation is employed here and moving forward, namely $\not{p} \equiv \gamma^\mu p_\mu$

Where the bar indicates that the amplitude is averaged over the initial spin states and summed over the final spin states. Simplifying where, for the electron, $m \approx 0$, $E \approx |\mathbf{p}|$, $Z = 1$, and substituting for α:

$$\frac{d\sigma}{d\Omega} = \frac{1}{(4\pi)^2} \frac{2e^2(EE' + \mathbf{p}' \cdot \mathbf{p} + m^2)Z^2e^2}{\left(4|\mathbf{p}|^2 \sin^2(\frac{\theta}{2})\right)^2} \tag{1.57}$$

$$= \frac{1}{(4\pi)^2} \frac{e^4(2EE' - |\mathbf{p}|'|\mathbf{p}|(1 - \cos(\theta)))}{8|\mathbf{p}|^4 \sin^4(\frac{\theta}{2})} \tag{1.58}$$

$$= \frac{1}{(4\pi)^2} \frac{e^4(2EE' - 2EE' \sin^2(\frac{\theta}{2}))}{8|\mathbf{p}|^4 \sin^4(\frac{\theta}{2})} \tag{1.59}$$

$$= \frac{1}{(4\pi)^2} \frac{e^4 EE'(1 - \sin^2(\frac{\theta}{2}))}{4E^4 \sin^4(\frac{\theta}{2})} \tag{1.60}$$

$$= \frac{\alpha^2 E' \cos^2(\frac{\theta}{2})}{4E^3 \sin^4(\frac{\theta}{2})} \tag{1.61}$$

This is the differential cross section that arises from a point source potential and at the relativistic limit and is equivalent to the *Mott cross section* which describes the point-like component of the electron-nucleon differential cross section which will be discussed in the next section.[22]

$$\left[\frac{d\sigma}{d\Omega}\right]_{\text{Mott}} = \frac{\alpha^2 E' \cos^2(\frac{\theta}{2})}{4E^3 \sin^4(\frac{\theta}{2})} \tag{1.62}$$

Again, this expression also assumes only the lowest order in α. In the nonrelativistic limit with a fixed target ($E = E'$) where $|\mathbf{p}|/E = \beta$, the Rutherford formula derived at the beginning of this chapter is recovered (equation 1.14).[23]

1.2.3 Rosenbluth Formula

The last step through QED formalism is to discuss the relativistic electron elastic scattering cross section for a continuously charged object with target recoil, such as the proton or the neutron. The Feynman diagram for this process, at lowest surviving order in α (OPE), is given in figure 6. From

[22] As usual, $\beta = \frac{v}{c}$, or just $\beta = v$ in natural units.

[23] Often $\left[\frac{d\sigma}{d\Omega}\right]_{\text{Mott}}$ is simply written as σ_{Mott}.

the Feynman rules for this process, the invariant amplitude is:

$$-i\mathscr{M} = \bar{u}(k')(ie\gamma^{\mu})u(k)\left(\frac{-ig_{\mu\nu}}{q^2}\right)\bar{v}(p')(-ie\Gamma)u(p) \tag{1.63}$$

The first two terms are straightforward — the first arises from the electron spinors and vertex, and the second arises from the photon propagator. However, as discussed, baryons are composite objects whose non-trivial internal structure arises from strong interactions between quarks and is not calculable from first principles. As such, the vertex factor is more complex. Nevertheless, the general structure of this factor can be understood. The nucleon vertex factor Γ^{ν} can be expressed in terms of the bilinear covariants of the Dirac equation which survive parity conservation:[24]

$$\Gamma^{\nu} = K_1\gamma^{\nu} + iK_2\sigma^{\nu\alpha}(p'-p)_{\alpha} + iK_3\sigma^{\nu\alpha}(p'+p)_{\alpha} + K_4(p'-p)^{\nu} + K_5(p'+p)^{\nu} \tag{1.64}$$

Here $\sigma^{\nu\alpha}$ is the commutator of gamma matrices, defined by $\sigma^{\nu\alpha} \equiv \frac{i}{2}[\gamma^{\nu},\gamma^{\alpha}]$, p and p' are the four-momenta of the incoming and outgoing fermions, respectively, and the K_i are structure factors which are functions of the square of the momentum transfer $q^2 = (p'-p)^2$ to preserve Lorentz invariance. Each of the structure factors K_i are introduced to account for the effects that cannot be explained by the Dirac equation alone, such as the finite size of the particles and higher-order corrections. In composite objects like hadrons, they are phenomenological parameters that need to be determined by experiment. In the case of fundamental point-like particles, the K_i terms reduce to the charge of the electron and the anomalous magnetic moment, which are related to the Landé g-factor discussed previously. Evaluating the tensor terms reduces the expression to three form factors, labeled with F_i:[25]

$$\Gamma^{\nu} = F_1\gamma^{\nu} + i\frac{F_2}{2M}\sigma^{\nu\lambda}q_{\lambda} + F_3\frac{p'^{\nu}-p^{\nu}}{M} \tag{1.65}$$

[24] Parity is conserved in elecromagnetic interactions.

[25] Namely, applying anti-commutation ($\{\gamma^{\mu},\gamma^{\nu}\} = 2g_{\mu\nu}$) and Dirac equation for free particle spinors ($(\gamma^{\mu}p_{\mu} - m)u = \bar{u}(\gamma^{\mu}p_{\mu} - m) = 0$), then grouping like terms.

Here M refers to the mass of the nucleon.[26] This, at first glance, is a suitable form of the *baryon current* defined analogously to the lepton current as:

$$J^{\mu'} = e\bar{v}(p')(-\Gamma^{\mu})v(p) \tag{1.66}$$

$$= -e\bar{v}(p')\left(F_1\gamma^{\nu} + i\frac{F_2}{2M}\sigma^{\nu\lambda}q_{\lambda} + F_3\frac{p'^{\nu} - p^{\nu}}{M}\right)v(p) \tag{1.67}$$

If it is a current, it must be conserved ($q_{\mu}J^{\mu} = 0$). This requirement forces $F_3 = 0$ and the resulting expression of the invariant amplitude is:

$$\mathscr{M} = j^{\mu}\frac{g_{\mu\nu}}{q^2}J^{\nu} \tag{1.68}$$

$$= \frac{e^2}{q^2}\bar{u}(k')\gamma^{\mu}u(k)g_{\mu\nu}\bar{v}(p')\left[F_1(q^2)\gamma^{\nu} + F_2(q^2)\frac{i\sigma^{\nu\lambda}q_{\lambda}}{2M}\right]v(p) \tag{1.69}$$

F_1 and F_2 are known as the *Pauli* and *Dirac* form factors, respectively, and they encode information about the electromagnetic distribution of the nucleon within them.

As discussed previously, the de Broglie wavelength relates directly to the resolving power of a scatterer. More precisely for *e*-*N* scattering, the de Broglie wavelength of the virtual photon represents the resolving power of the nucleon structure. This wavelength is related to the momentum transfer q:

$$\lambda_{\gamma^*} = \frac{1}{Q}, \tag{1.70}$$

where $Q^2 \equiv -q^2$ and $Q \equiv \sqrt{|q^2|}$. In this context, as $Q \to 0$, the cross section of the nucleon must reduce to a point charge with appropriate magnetic moment. These conditions imply the vertex factor for the nucleon is like that of a point-like particle ($\Gamma^{\nu} \to \gamma^{\nu}$), and the constraints for protons and neutrons:

$$\text{proton} \quad \to \quad F_1^p(0) = 1, \quad F_2^p(0) = \kappa_p \tag{1.71}$$

$$\text{neutron} \quad \to \quad F_1^n(0) = 0, \quad F_2^n(0) = \kappa_n \tag{1.72}$$

[26] Unless otherwise noted, M always refers to the nucleon mass while m refers to the electron mass.

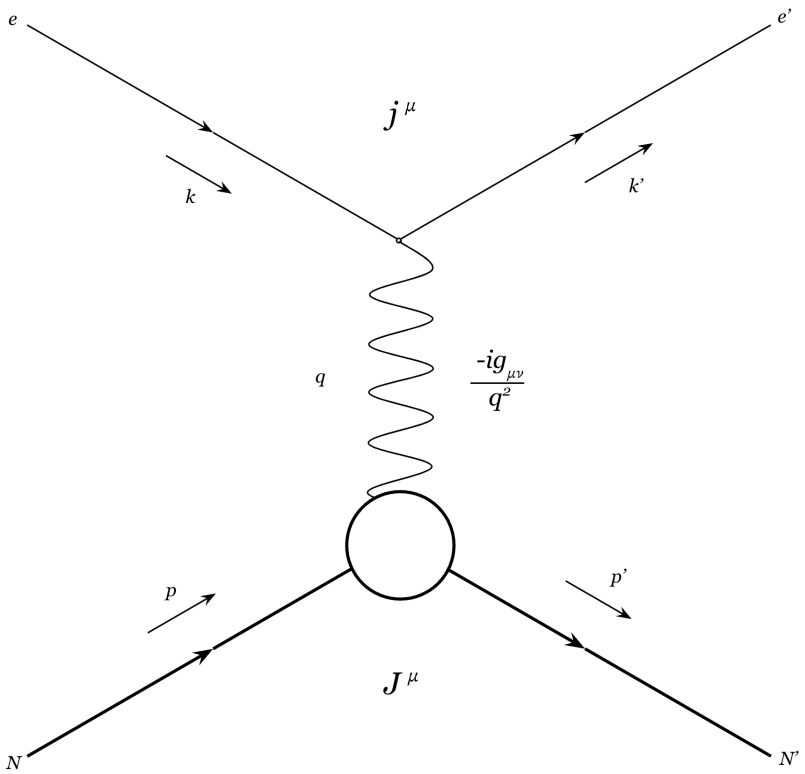

Figure 6: Feynman diagram for electron-nucleon scattering $e+N \to e+N$ with invariant current components labeled, including the lepton and baryon currents j^μ and J^μ respectively.

With this limiting behavior, the differential cross section can be evaluated in the lab frame from the invariant amplitude in terms of the lepton and baryon currents, assuming initial nucleon at rest:

$$\frac{d\sigma}{d\Omega} = \sigma_{\text{Mott}} \left[\left(F_1^2 + \frac{Q^2}{4M^2} F_2^2 \right) + \frac{Q^2}{2M^2} (F_1 + F_2)^2 \tan^2 \left(\frac{\theta}{2} \right) \right] \tag{1.73}$$

Here, θ is the electron scattering angle, κ is the anomalous magnetic moment of the nucleon, and m is the mass of the nucleon.[27] When $Q^2 \to 0$, the Mott cross section is recovered, as expected. By reparameterizing the Dirac and Pauli form factors and adding the scaling variable $\tau = \frac{Q^2}{4M^2}$ and longitudinal polarization of the virtual photon $\varepsilon = 1/(1+2(1+\tau)\tan^2(\frac{\theta}{2}))$, the $F_1 F_2$ cross term

[27] In the literature, κ is often absorbed into the definition of F_2.

can be removed and a much more manageable expression can be determined:[28]

$$\frac{d\sigma}{d\Omega} = \frac{\sigma_{\text{Mott}}}{\varepsilon(1+\tau)}\left(\varepsilon G_E^2 + \tau G_M^2\right) \tag{1.74}$$

This is the *Rosenbluth Formula* which relates the differential cross section to the *Sachs form factors* G_E and G_M. The Sachs form factors in terms of the Pauli and Dirac elastic form factors are as follows:

$$G_E \equiv F_1 - \frac{Q^2}{4M^2}F_2 \tag{1.75}$$

$$G_M \equiv F_1 + F_2 \tag{1.76}$$

G_M is the Sachs magnetic form factor and G_E is the Sachs electric form factor and the set of two exist for both the proton (G_M^p, G_E^p) and the neutron (G_M^n, G_E^n) independently. In the Rosenbluth formula, these represent a set of terms which can be separated and measured more easily than F_1 and F_2, but contain the same exclusively empirical information about the nucleon.

It is often useful to further reduce the Rosenbluth formula to absorb the common Mott term into the differential cross section thus:

$$\sigma_r = \tau G_M^2(Q^2) + \varepsilon G_E^2(Q^2) \tag{1.77}$$

Here σ_r is the *reduced cross section* and the form factors are represented with their Q^2 dependence explicitly.

1.2.4 Two Photon Exchange

As mentioned before, higher-order terms, suppressed by each additional pair of photon vertices, exist to characterize these cross sections. It follows, then, that the next largest contributions to the invariant amplitude come from processes at the same order in α, including two-photon-exchange (TPE) processes, vertex corrections, bremsstrahlung, and vacuum polarization (among others).

[28] See Appendix A for list of useful expressions.

TPE effects are unique among these effects owing to the model-dependence of their calculations[29]. The next-to-leading order Feynman TPE "box" diagrams are depicted in figures 7 and 8. To interpret the scattering amplitude for these processes, the so-called Mandelstam variables come into play. They are as follows:

$$s = (k+p)^2 = (k'+p')^2, \quad t = (k-k')^2 = q^2, \quad u = (p-k')^2 = (p'-k)^2 \tag{1.78}$$

where $s+t+u = 2M^2 + 2m^2$. Here, s (the total center of mass energy of the system), t, and u are all invariant under Lorentz transformations. Figure 6 depicts the t-channel diagram (OPE). Figure 7 depicts the s-channel diagram where the vertices couple the incoming momentum states and the outgoing momentum states. The u-channel "crossed-box" (figure 8) diagram and contribution arise from the coupling of the initial and final momentum states, which are interchanged (electron to nucleon and vice versa) compared to the "box" diagram. In both diagrams, the intermediate hadronic state R exists inside the "box," between the vertices of the two virtual photons depicted.

The contribution to the invariant amplitude from two photon exchange can be written in terms of the hadronic and leptonic tensors ($H^{\mu\nu}$ and $L^{\mu\nu}$, respectively). The hadronic tensor is formed from R and can be written thus:

$$H^{\mu\nu} = \bar{u}_N(p')\Gamma^{\mu\alpha}_{R\to\gamma N}(p+q_1,-q_2)S_{\alpha\beta}(p+q_1,M_R)\Gamma^{\beta\nu}_{\gamma N\to R}(p+q_1,q_1)u_N(p) \tag{1.79}$$

Here the hadronic transition current operator, represented by $\Gamma^{\mu\alpha}_{R\to\gamma N}$ and $\Gamma^{\mu\alpha}_{\gamma N\to R}$, accounts for both incoming and outgoing momenta of the virtual photons q_1 and q_2, and $S_{\alpha\beta}(p+q_1,M_R)$ is the hadronic state propagator for R. The leptonic tensor:

$$L^{\mu\nu} = \bar{u}_e(k')\gamma^\mu S_F(k-q_1,m)\gamma^\nu u_e(k) \tag{1.80}$$

[29]So-called "hard" TPE effects are referenced here, where the momentum and energy of the exchanged photons are higher than "soft" TPE processes which can be calculated and whose effects can be corrected for in a model-independent manner.

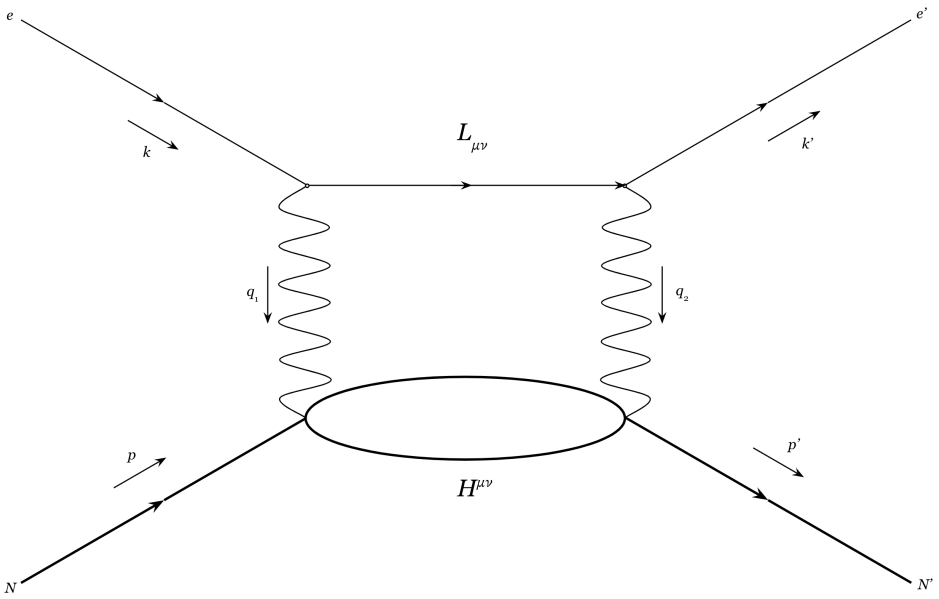

Figure 7: Feynman s-channel "box" diagram depicting two-photon exchange. Note that the lepton and hadron currents are non trivial represented as tensors.

Where the electron propagator is necessary to account for the intermediate state and is given by:

$$S_F(k, m_e) = \frac{(\not{k} + m)}{k^2 - m^2 + i\varepsilon'} \tag{1.81}$$

ε' is an infinitesimally small term consistent with "Feynman's $i\varepsilon$ prescription"[178].[30]

If we include the tensors which describe the electron and hadron components, the contribution to the TPE box amplitude from R can be written as:

$$\mathscr{M}_{\gamma\gamma}^{\text{box}} = -ie^4 \int \frac{d^4 q_1}{(2\pi)^4} \frac{L_{\mu\nu} H_R^{\mu\nu}}{(q_1^2 - \lambda^2)(q_2^2 - \lambda^2)}, \tag{1.82}$$

Here, λ^2 is another infinitesimally small term introduced now to remove infrared (IR) divergences associated with the emission of low-energy (long-wavelength) photons (the $q_1 = 0$ and $q_2 = 0$ poles) and ensuring the integral converges. The "crossed-box" term ($M_{\gamma\gamma}^{\text{xbox}}$) can be derived from

[30] Without this term, the contour integral over the complex plane blows up at $k^2 = m^2$. This term shifts the pole off of the real axis and the sign of $i\varepsilon'$ preserves causality.

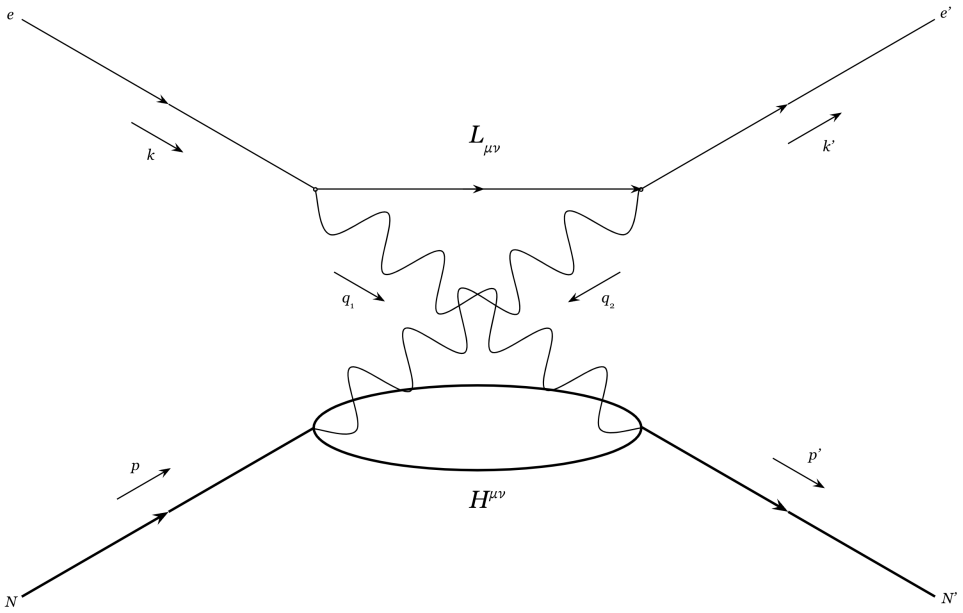

Figure 8: Feynman u-channel "crossed-box" diagram depicting two-photon exchange. Note that the lepton and hadron currents are non trivial represented as tensors.

the "box" term ($M_{\gamma\gamma}^{\text{box}}$) via application of crossing symmetry.[31] In terms of these contributions, it can be shown that the relative TPE correction to the reduced cross section can be written as the interference term between the OPE and TPE amplitudes:[32]

$$\delta_{\text{TPE}} = \frac{2\text{Re}(M_{\gamma}^{*} M_{\gamma\gamma})}{|M_{\gamma}|^2} \tag{1.83}$$

Typically, the vanishingly small momentum transfer factors of q_i (the "soft" components which are the same for point-like particles and responsible for IR divergences) are encapsulated in model-independent *radiative corrections*, which account for the emission of a real bremsstrahlung photon in *e-N* scattering processes. These corrections are subtracted from the overall TPE correction to leave only the part of q_i which are model-dependent and probe the hadronic structure (the "hard" components). This entails that $\delta_{\text{TPE}} = \delta_{\text{soft}} + \delta_{\text{hard}}$ and the total correction to the reduced cross section is the sum of these terms and the real bremsstrahlung emission term δ_{brem}.

[31] ie. $M_{\gamma\gamma}^{\text{xbox}}(u,t) = -M_{\gamma\gamma}^{\text{box}}(s,t)\big|_{s\to u}$ (unpolarized case).

[32] By adding each of the box amplitudes *coherently*: $M_{\gamma\gamma} = M_{\gamma\gamma}^{\text{box}} + M_{\gamma\gamma}^{\text{xbox}}$. See [11].

Prominently, the IR corrections contributed by Mo and Tsai are used for this correction, including the IR divergent "soft" contribution[116]:[33]

$$\delta_{\mathrm{IR}}(\mathrm{MoT}) = -\frac{2\alpha}{\pi}\left[\log\left(\frac{E}{E'}\right)\log\left(\frac{2M\sqrt{EE'}}{\lambda^2}\right) - \mathrm{Li}_2\left(1-\frac{M}{2E}\right) + \mathrm{Li}_2\left(1-\frac{M}{2E'}\right)\right] \tag{1.84}$$

Where Li_2 is the dilogarithm function. The radiative-corrected TPE correction is given by:

$$\delta_{\gamma\gamma} \equiv \delta_{\mathrm{TPE}} - \delta_{IR}(\mathrm{MoT}) \tag{1.85}$$

With these corrections, the measured reduced cross section is related to the reduced cross section from OPE by:

$$\sigma_r^{\mathrm{meas}} = \sigma_r(1+\delta_{\gamma\gamma}) \tag{1.86}$$

Generally, the measured discrepancy between measurement methods sensitive to TPE contributions (measuring σ_r) and those that aren't (measuring σ_r^0) can be expressed in a similar way:

$$\delta_{\gamma\gamma}^{meas} = \frac{\sigma_r}{\sigma_r^0} - 1 \tag{1.87}$$

Different measurement methods will be discussed later in the chapter.

1.2.5 Nuclear Effects

The formalism governing elastic $e-\mu$ scattering and elastic $e-N$ scattering was outlined previously. Practically, electron scattering from a proton or neutron target requires an electron beam and a stationary target. Often in practice, and for this work, cryogenic targets filled with liquid hydrogen (LH2) or liquid deuterium (LD2) are used.[34] In the prior case, hydrogen contains a single proton in its nucleus which provides an essentially free proton target. In the latter case, deuterium contains a single proton and a single neutron in its nucleus which provides a simultaneous

[33] More recently, the calculation by Maximon and Tjon have improved on these radiative corrections by omitting approximations used in Mo and Tsai's original work[110].

[34] More on targets in chapter 2.

quasi-free proton and quasi-free neutron target. In both cases, the target is kept in a liquid phase to increase particle density and promote scattering rate.[35]

When scattering from deuterium, as has been performed for this work, the protons and neutrons are part of a bound nucleus. This introduces a number of *nuclear effects* which broaden the momentum distribution of scattered nucleons:

1. **Fermi Smearing**: The broadening (or smearing) of the nucleon momentum distribution due to its Fermi motion inside the nucleus.

2. **Binding Energy**: The energy required to remove a nucleon from the nucleus affects the energy balance of the scattering process and must be accounted for. For LD2, this value is close to 2.2 *MeV*.

3. **Nuclear Medium Effects**: These include modifications to the properties of nucleons when they are bound in a nucleus compared to when they are free, such as changes in mass and size (nucleon swelling), as well as the density-dependent effects on nucleon interactions.

4. **Final-State Interactions (FSI)**: After a nucleon is struck and before it exits the nucleus, it may interact with other nucleons. This can change the energy, momentum, and even the identity of the particles detected.

5. **Meson Exchange Currents (MEC)**: Contributions to the scattering amplitude from processes where mesons (like pions) are exchanged between nucleons within the nucleus during the interaction.

6. **Short-Range Correlations (SRC)**: Nucleons within the nucleus can form short-range correlated pairs with high relative momentum, leading to deviations from the mean field behavior.

7. **Shadowing and Anti-shadowing**: At small Bjorken-x values in deep inelastic scattering, the structure function can be suppressed (shadowing) or enhanced (anti-shadowing) due to the overlap of nucleon parton distributions.

[35] Details in chapter 3.

8. **Nuclear Deformation and Excitations**: The shape of the nucleus and the potential for exciting nuclear states can alter the scattering cross section.

In principle, all of these effects influence the final state momentum distributions of scattered protons and neutrons from a nucleus with more than one nucleon ($Z > 1$). For this reason *quasi-elastic* scattering is distinct from elastic scattering. It refers to a scattering process where a projectile (such as an electron) interacts with a target nucleon in such a way that the nucleon is ejected from the nucleus, with the nucleus remaining in a state near its ground state, and the overall reaction appears similar to elastic scattering on a free nucleon (such as in elastic scattering from hydrogen). In general, the strength of these effects increases with Z. For those experiments which aim to measure form factors of the neutron, such as in this work, there exists no free neutron target. As such, the deuteron is a prime candidate for these measurements, but entails corrections which address these nuclear effects. [36]

1.3 Sachs Form Factors

Where each of the Pauli and Dirac form factors parameterize aspects of both the electric and magnetic distributions within the nucleon in both the relativistic and non-relativistic scattering cases, the electric Sachs form factors have a neater interpretation at low Q^2 ($Q^2 \ll M_N^2$):

$$G_E(Q^2) = \int \rho(\mathbf{x}) e^{-i\mathbf{q}\cdot\mathbf{x}} d^3\mathbf{x}, \tag{1.88}$$

where $\rho(\mathbf{x})$ is the charge distribution within the nucleon. A similar expression can be shown for G_M, defined in terms of the magnetization instead of the charge density. In the limit where $Q^2 \to 0$

[36] See section 1.4.3 and chapter 3 for additional details.

with equations 1.71, 1.72, 1.75, and 1.76:[37]

$$\text{proton} \quad \rightarrow \quad G_E^p(0) = 1, \quad G_M^p(0) = \mu_p \tag{1.89}$$

$$\text{neutron} \quad \rightarrow \quad G_E^n(0) = 0, \quad G_M^n(0) = \mu_n \tag{1.90}$$

In this limit, the namesake of each of the form factors becomes obvious as they reduce to the charge and magnetic moments of the proton and neutron.

An interesting application of low Q^2 Sachs form factors arises from this relationship when electric and magnetic spatial distributions are used to approximate the radii of nucleons. As $Q^2 \rightarrow 0$, $\tau \rightarrow 0$ and $\frac{d\sigma}{d\Omega}$ are dominated by G_E. Expansion of G_E in the small $\mathbf{q}$ with equation 1.88 for a spherically symmetric charge density $\rho(r \equiv \mathbf{x})$ gives:

$$G_E = \int \rho(\mathbf{x}) \left(1 + i\mathbf{q}\cdot\mathbf{x} - \frac{(\mathbf{q}\cdot\mathbf{x})^2}{2} + \mathscr{O}(\mathbf{q}^3)\right) d^3x \tag{1.91}$$

$$= \int_0^\infty \rho(r) r^2 dr \int_0^\pi \sin\theta d\theta \left(1 + i|\mathbf{q}| r\cos\theta - \frac{1}{2}\mathbf{q}^2 r^2 \cos^2\theta + \mathscr{O}(\mathbf{q}^3)\right) \tag{1.92}$$

$$= 1 - \frac{1}{6}\mathbf{q}^2 \int |\mathbf{x}|^2 \rho(|\mathbf{x}|) d^3x + \mathscr{O}(\mathbf{q}^3) \tag{1.93}$$

$$= 1 - \frac{1}{6}\mathbf{q}^2 \langle r^2 \rangle + \mathscr{O}(\mathbf{q}^3) \tag{1.94}$$

After differentiating the last term with respect to $\mathbf{q}^2$ and sending $\mathbf{q} \rightarrow 0$:

$$\langle r^2 \rangle = -6 \frac{dG_E}{d\mathbf{q}^2}\bigg|_{\mathbf{q}^2 \rightarrow 0} \tag{1.95}$$

This expectation value is the RMS charge radius of the nucleon — of significant interest in many sub-fields of physics and astrophysics.

[37] The magnetic moment of the proton can be expressed as the sum of its Dirac magnetic moment (which is 1 nuclear magneton by definition) and its anomalous magnetic moment, $\mu_p = 1 + \kappa_p$. The neutron, being electrically neutral, does not have a Dirac magnetic moment. Its total magnetic moment is solely due to its anomalous magnetic moment and $\mu_n = \kappa_n$. From experimental measurements, the magnetic moments of the proton and neutron are $\mu_p = 2.793\,\mu_N$ and $\mu_n = -1.913\,\mu_N$, respectively, where μ_N is the nuclear magneton.

1.4 Techniques

As has been shown in previous sections, through elastic form factors, one can relate the charge and magnetic structure of the nucleon to their cross sections. These cross sections can be measured in the lab. In the lab frame, quasi-elastic scattering is depicted in figure 9. For this scattering, it is convenient to introduce some definitions in terms of lab-frame variables. The squared four-momentum transfer Q^2 can be defined in terms of the incident electron (beam) energy E and the scattered electron energy E' thus:

$$Q^2 = 4EE' \sin^2\left(\frac{\theta_e}{2}\right) \tag{1.96}$$

The invariant mass of the final hadronic system W can be defined thus:

$$W^2 = M^2 + 2M\nu - Q^2 \tag{1.97}$$

Here, ν is the energy transferred from the beam electron to the nucleon, M is the rest mass of the nucleon, and Q^2 is the four-momentum transfer. When $W > M$, the scattering is inelastic. Inelastic processes include cases where the nucleon is excited to a higher energy state or resonance (such as the Δ resonance) and deep inelastic scattering (DIS) where the nucleon is broken apart. For elastic and quasi-elastic scattering processes, the scattered nucleon remains intact, and $W = M$. Figure 10 gives an estimated depiction of the $e-N$ cross sections for these and other scattering processes at low to medium Q^2.

For quasi-elastic scattering, a convenient measure is θ_{pq}, which is the angular difference between the detected nucleon four-vector p' and the calculated q four-vector. Where the scattering event obeys elastic kinematics, the recoil nucleon direction aligns with the direction of q.

Through analysis of the scattered electron and nucleon from many events, the cross section and cross section ratio at a fixed Q^2 can be determined with precision. Various techniques exist to perform this kind of extraction.

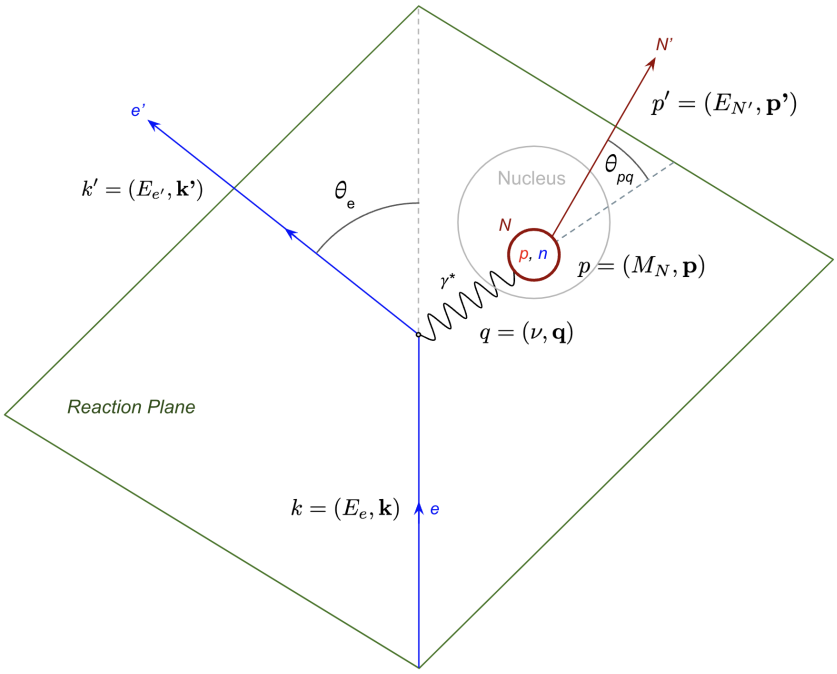

Figure 9: Depiction of electron-nucleon scattering in the lab frame. k is the initial four-momentum of the beam electron, k' is the final four-momentum of the scattered electron, p is the four-momentum of the nucleon at rest, p' is the final four-momentum of the scattered nucleon, θ_e is the electron scattering angle, θ_{pq} is the angle between q and p', q is the four-momentum of the virtual photon, and ν is the energy transferred from the electron to the nucleon during scattering.

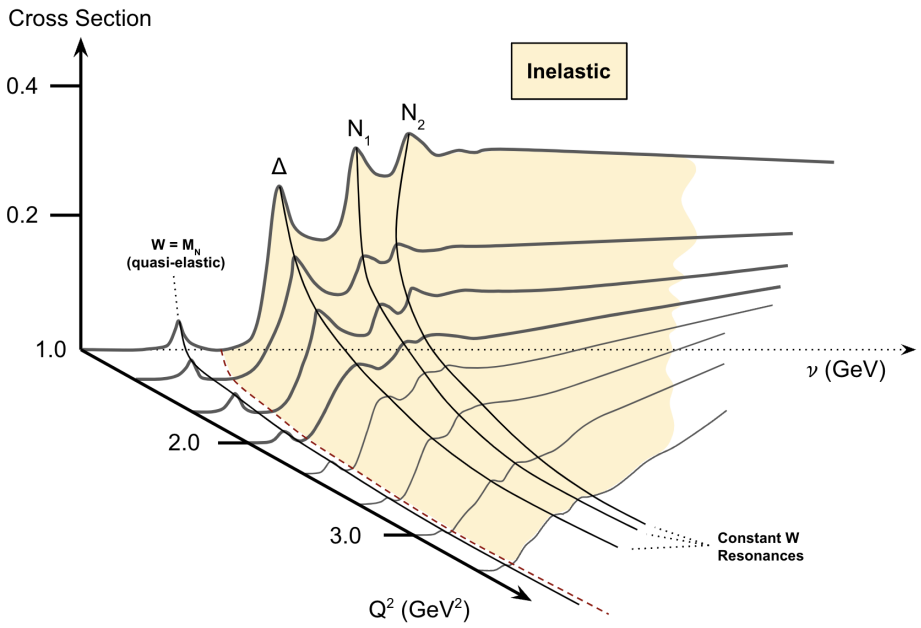

Figure 10: The interaction e-N cross section as a function of the energy transfer from beam electrons ν and momentum transfer Q^2. Δ and the N_i resonances correspond to nucleon excited states. Note that the quasi-elastic cross section drops quickly as a function of Q^2. Adapted from [187].

1.4.1 L/T separation

Early $H(e,e',p')$ measurements of form factors exploited the product of G_E and ε in the OPE reduced cross section σ_r to disambiguate the Sachs form factors G_M and G_E.[38] One can rewrite equation 1.77 in the following way:

$$\sigma_r = \tau G_M^2(Q^2) + \varepsilon G_E^2(Q^2) = \sigma_T + \varepsilon \sigma_L, \tag{1.98}$$

where $\sigma_T(Q^2) = \tau G_M^2(Q^2)$ and $\sigma_L(Q^2,\theta_e) = G_E^2(Q^2)$. Due to the unique dependence of the longitudinal polarization of the virtual photon ε on the electron scattering angle θ_e, the scattering angle can be varied experimentally while holding Q^2 fixed to produce different measurements of σ_r whose difference depends only on $G_E^2(Q^2)$. Figure 11 depicts the linear nature of the reduced cross section's dependence on ε for a fixed Q^2 where G_M^2 is the y-intercept and G_E^2 is the slope[149].

[38] The notation $H(e,e',p')$ indicates that the electron (e) was scattered from hydrogen (H) and both the final state electron e' and the final state proton p' are detected.

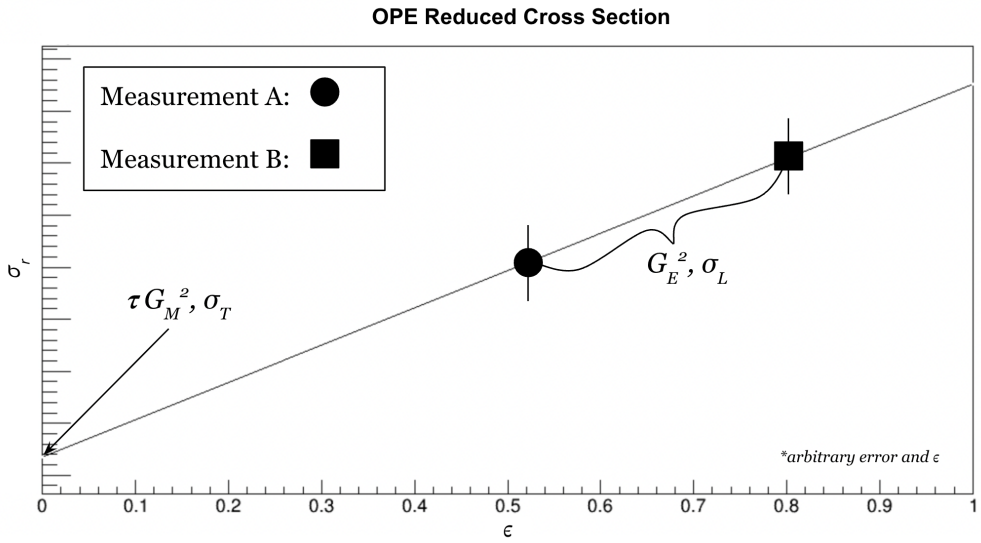

Figure 11: Depiction of Rosenbluth slope from two mock experimental points (labeled A and B) at two arbitrary values of ε. On Born approximation, the relationship is linear and both the longitudinal and transverse components of the cross section can be disambiguated.

Practical L/T separation measurements of the Sachs form factors measure σ_r for at least two values of ε then can extrapolate back to the y-intercept to extract G_M and evaluate the slope to extract G_E. Because the term containing σ_L vanishes as $\varepsilon \to 0$, this component of the reduced cross section is considered the longitudinal contribution to the reduced cross section and σ_T (what's left after σ_L vanishes) is considered the transverse contribution to the reduced cross section. It is important to note that, because Q^2 depends on beam energy (figure 1.96), each measurement must adjust both the scattering angle θ_e and beam energy E to vary ε while keeping Q^2 fixed[149].

When examining the dependence of the *form factor ratio* (or FFR) G_E/G_M on Q^2, it is convenient to factor out the Sachs magnetic form factor from the right hand side of the OPE reduced cross section:

$$\sigma_r = \sigma_T + \varepsilon\sigma_L \tag{1.99}$$

$$= \tau G_M^2(Q^2) + \varepsilon G_E^2(Q^2) \tag{1.100}$$

$$= G_M^2(Q^2)\left(\tau + \frac{\varepsilon RS(Q^2)}{\mu_N^2}\right) \tag{1.101}$$

This introduces the *Rosenbluth slope*, *RS*, defined as:

$$RS(Q^2) = \left(\frac{\mu_N G_E(Q^2)}{G_M(Q^2)} \right)^2 \tag{1.102}$$

Where μ_N is the magnetic moment of the nucleon included to ensure *RS* is dimensionless.[39]

L/T separation, or the *Rosenbluth method*, has seen widespread use in the field since the early years of form factor measurements. However, the structure of the reduced cross section leads to the dominance of G_M over G_E at high Q^2 (or more specifically $\tau \gg 1$) where $0 \leq \varepsilon \leq 1$. As a result, the relative error of G_E in the high Q^2 regime grows quickly beyond the relative error in σ_r. Owing to this shortcoming, polarization transfer methods were developed which measure FFRs with polarization observables which have better sensitivity at higher momentum transfers.

Because L/T separations are dependent on the Rosenbluth formula, and OPE by extension, their radiative corrections omit hard two photon exchange contributions. At low Q^2, TPE effects are expected to be minimal, but scale with τ such that higher Q^2 measurements of the FFR become increasingly contaminated[20]. For example, an estimate of the corrected Rosenbluth slope (*RS*) in terms of the contaminated Rosenbluth slope ($\widetilde{RS}$) which approximates the slope in ε by averaging over all TPE corrections is:

$$RS = \frac{\widetilde{RS} - \mu_N^2 \tau \frac{b}{a}}{1 + \overline{\varepsilon} \frac{b}{a}} \tag{1.103}$$

Here, b and a are linear fit parameters to σ_r of the form $a + b\varepsilon$, and $\overline{\varepsilon}$ is the average longitudinal polarization of the virtual photon over the fit range. Note the dependence of the correction on τ where $RS = ((\mu_N G_E)/G_M)^2$ is the square of the dimensionless FFR[11].

1.4.2 Polarization Transfer

Polarization transfer (PT) methods measure the elastic FFR via polarization observables instead of absolute cross sections or cross section ratios. Traditionally, this involves methodologies where either the beam is polarized and the target is unpolarized or both are polarized. The former case,

[39] Often in the literature, the Rosenbluth slope is plotted in terms of $\sqrt{RS} = \frac{\mu_N G_E}{G_M}$.

a longitudinally polarized electron beam scattering from an unpolarized target ($\vec{e}+p \rightarrow e+\vec{p}$), is depicted in figure 12[103].[40] With the Born approximation, in terms of lab-frame variables, the important polarization observables are related to the form factors thus:

$$I_0 P_L = \frac{(E+E')}{M}\sqrt{\tau(1+\tau)}G_M^2(Q^2)\tan^2\left(\frac{\theta_e}{2}\right) \tag{1.104}$$

$$I_0 P_T = -2\sqrt{\tau(1+\tau)}G_E(Q^2)G_M(Q^2)\tan\left(\frac{\theta_e}{2}\right) \tag{1.105}$$

Here P_L and P_T are the longitudinal and transverse polarization observables and I_0 is a normalization factor, defined as:

$$I_0 = G_{E_p}^2(Q^2) + \frac{\tau}{\varepsilon}G_{M_p}^2(Q^2). \tag{1.106}$$

The final state nucleon polarization is measured with a recoil polarimeter which gives simultaneous measurements of the longitudinal component (P_L) and the transverse component (P_T) of the scattered nucleon momentum (the normal component, P_N, vanishes on OPE).[41] With equations 1.104 and 1.105, the FFR can be solved for:

$$\frac{\mu_N G_E}{G_M} = -\frac{P_T}{P_L}\frac{\mu_N(E+E')}{2M}\tan\left(\frac{\theta_e}{2}\right) \tag{1.107}$$

The left-hand-side of this expression is equivalent to the square root of the FFR term represented in 1.103. For polarization transfer methods which use a polarized beam and polarized target ($\vec{e}+\vec{p} \rightarrow e+\vec{p}$), so-called *double polarization*, the measurement varies, but the information is essentially the same[11].[42]

Because polarization methods measure the ratio of polarized and unpolarized cross sections, most radiative effects cancel. The TPE correction to the OPE cross section can be expressed in terms of the Mo and Tsai corrections in equation 1.84 to each component of the polarization

[40] Here the vector symbol (as in $\vec{p}$) indicates that the particle is polarized. This convention will persist for the rest of the document.

[41] Parity and time-reversal symmetry demand that P_N vanish to leading order in α. See [103].

[42] For details extracting the FFR from polarization asymmetry measurements, see [128].

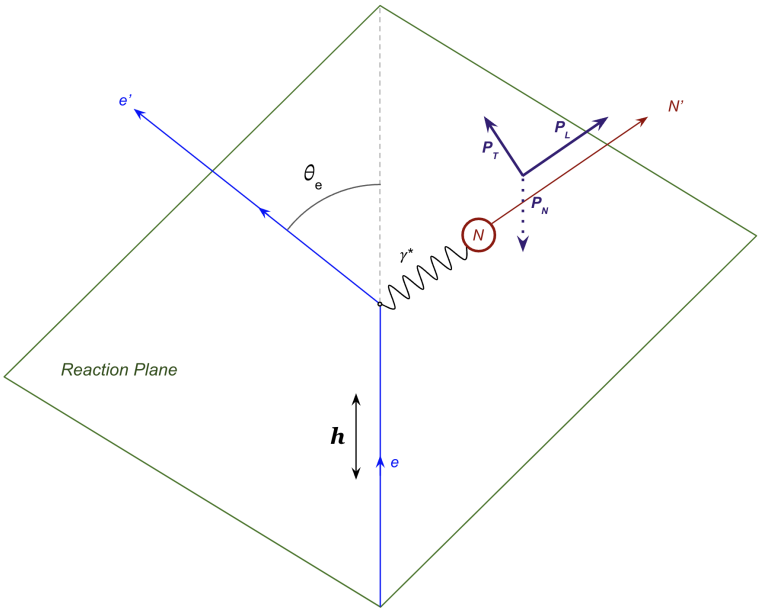

Figure 12: Schematic diagram depicting the polarization transfer from a polarized incident electron e with helicity $\mathbf{h}$ to an unpolarized nucleon final state N'. The longitudinal polarization component $\mathbf{P}_L$ is aligned along the momentum transfer direction $\mathbf{q}$, the transverse polarization component $\mathbf{P}_T$ lies in the reaction plane perpendicular to $\mathbf{q}$, and the normal polarization component $\mathbf{P}_N$ is perpendicular to the reaction plane. This setup illustrates how the spin state of the nucleon is influenced by the spin state of the incident electron in the scattering process.

observables P_L and P_T:

$$\bar{\delta}_{L,T} = \delta_{L,T} - \delta_{IR}(MoT) \tag{1.108}$$

With these corrections, the dimensionless FFR $\widetilde{R}$ contaminated by TPE can be expressed in terms of the dimensionless FFR R:

$$\widetilde{R} = R\left(\frac{1+\bar{\delta}_T}{1+\bar{\delta}_L}\right) \tag{1.109}$$

The scaling of the correction with τ is gone when compared to equation 1.103, and the correction for TPE is very small relative to that of L/T separation methods. Figure 13 demonstrates this difference. For this reason, PT methods are considered to be largely insensitive to TPE effects relative to L/T separation methods.

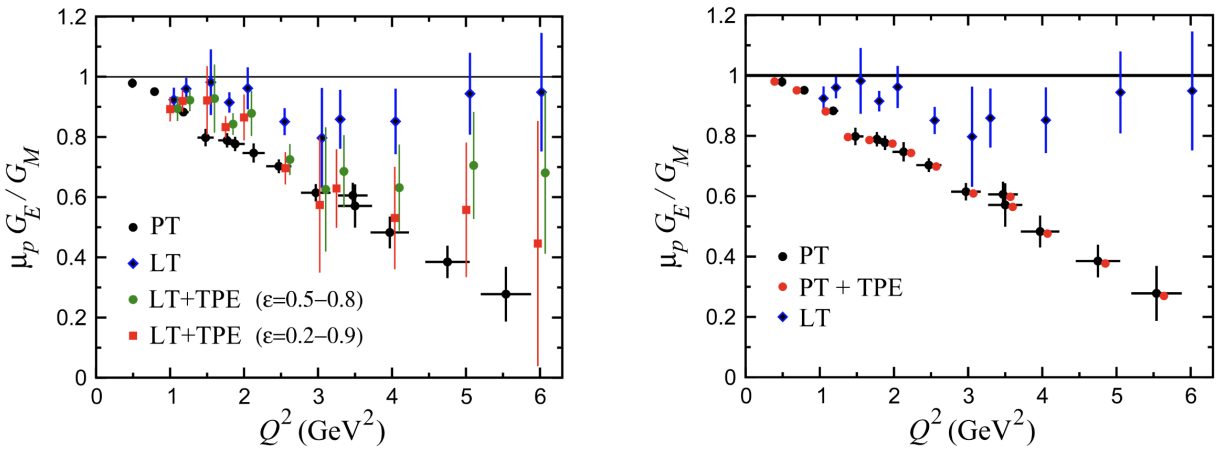

Figure 13: FFR ratio data plotted along with corrections for TPE effects. (*Left*) Data plotted with L/T corrected points. (*Right*) Data plotted with PT corrected points. Note that PT corrections are significantly suppressed relative to L/T corrections. Plots from [11].

1.4.3 Ratio Method

Many sources of systematic errors exist for quasi-elastic $e-N$ scattering experiments. While these are ultimately apparatus dependent, some sources of error common in these kinds of experiments are:[43]

- Target thickness, density, and polarization
- Beam intensity, position, and polarization
- *Data acquisition* (DAQ) deadtime
- Electron trigger efficiency and acceptance
- Electron track reconstruction and efficiency
- Magnetic field settings for the electron arm
- Nuclear effects

In principle, these errors pose significant challenges to achieving precision measurements, especially for neutrons.

The *ratio method*, also known as the "Durand technique", is a measurement strategy where the nucleon cross section is measured over both isospin states simultaneously (protons and neutrons)[52].

[43] See chapter 3 for detailed systematic errors for this work.

Nominally, for a deuterium target, this ratio is $d(e,e'n)p/d(e,e'p)n$, or:[44]

$$R'' = \frac{\frac{d\sigma}{d\Omega}\Big|_{d(e,e'n)}}{\frac{d\sigma}{d\Omega}\Big|_{d(e,e'p)}} \tag{1.110}$$

Here the cross sections in the ratio account for specific nuclear effects unique to each of $d(e,e'n)$ and $d(e,e'p)$ reactions. In this ratio, common factors such as the electron beam characteristics, detector efficiencies, and most systematic uncertainties cancel out, isolating the effects of neutron and proton structure. This measurement technique significantly reduces the uncertainties associated with experiments involving multiple setup changes.

The ratio method relies on a comparable treatment of protons and neutrons for each detection event. For example, if a proton is detected in a given event, it must also be true that a corresponding neutron would have been detected under the same conditions. If this cannot be guaranteed, then additional nucleon-dependent systematic errors can affect the ratio.

While nuclear effects are not fully cancelled in the ratio, for a deuterium target, only a small correction is necessary to account for the differences in the interactions and motion of protons and neutrons. These corrections primarily affect final-state interactions (FSI) and Fermi smearing (ε_{nuc}). After application of this calculable correction for each cross section, the resulting "pure" cross section ratio (R') of neutrons to protons is:

$$R' = \frac{R''}{1+\varepsilon_{nuc}} = \frac{\frac{d\sigma}{d\Omega}\Big|_{n(e,e)}}{\frac{d\sigma}{d\Omega}\Big|_{p(e,e)}} \tag{1.111}$$

With a precise knowledge of the proton cross sections at various experimentally fixed values of Q^2, this method has been used to extract much more precise measurements of neutron form factors, otherwise unavailable via neutron-exclusive measurements.[45]

[44] For electron-deuteron scattering, the ratio is sometimes denoted equivalently: ${}^2H(e,e'n)p/{}^2H(e,e'p)n$

[45] See "proton-subtraction" and "proton-tagging" techniques which have had success at lower Q^2 [72].

1.5 World Data

The global efforts to measure electromagnetic form factors have significantly advanced our understanding of nucleon structure. Current high-precision data across various Q^2 ranges have been collected from several experiments, offering detailed insights into both proton and neutron form factors.

1.5.1 Proton

Early measurements, such as those done by R. Hofstadter, supported the OPE approximation and L/T separation methodology in electron-proton $(e-p)$ scattering by showing a linear dependence of σ_r to ε. Later tests of linearity up to $Q^2 = 3\,GeV^2$ indicate that form factors follow the so-called *dipole form factor*[180]:

$$G_D \equiv \frac{1}{\left(1+\frac{Q^2}{\Lambda^2}\right)^2} \quad \text{with} \quad \Lambda^2 = 0.71\,GeV^2 \tag{1.112}$$

This form is so named because its Q^2 dependence has the same form as the Fourier transform of a spatially exponential charge distribution, similar to a dipole in momentum space. Due to the similarity between the dipole form and G_M^p and G_E^p, it is a standard comparison for proton form factors[9].[46]

$$G_D \approx G_E^p \approx \frac{G_M^p}{\mu_p} \tag{1.113}$$

From this comparison, $\mu_p G_E^p/G_M^p \approx 1$ over these Q^2 ranges, the OPE approximation was applied to extract proton form factors from LH2 targets at higher Q^2 via elastic cross section analysis under the assumption that $RS \approx 1$. [47]

However, for $Q^2 > 1\,\text{GeV}^2$, PT methods began to show a strong deviation from the dipole form in the ratio G_E^p/G_M^p (reflected in figures 14 and 15). These measurements indicate that G_E^p falls

[46] For a spatial charge distribution of the form $\rho(r) \propto e^{-\lambda r}$, where λ is related to Λ, the Fourier transform translates the spatial decay into the Q^2 dependence seen in G_D in momentum space the same way.

[47] The superscript in the Sachs form factors indicates the isospin state of the nucleon, p for proton and n for neutron.

off more rapidly with increasing Q^2 compared to G_M^p, leading to a decreasing ratio G_E^p/G_M^p with increasing Q^2[103, 143].

As detailed in previous sections, methods that aim to measure the neutron with precision often employ the ratio technique. The viability of this method for neutron form factor extraction relies on the precision of independent proton world data. The free proton in hydrogen eliminates nuclear corrections, reducing sources of systematic error and allowing for more precise determination of proton form factors. For $Q^2 < 10\,\mathrm{GeV}^2$, ample proton world data are available, supporting the use of the ratio method effectively [10].

1.5.2 Form Factor Ratio Puzzle

In figure 14, data for $Q^2 \geq 1,\mathrm{GeV}^2$ show a significant disagreement between L/T separation methods and polarization transfer (PT) methods. This discrepancy is known as the *form factor ratio puzzle* (FFRP). Within the Standard Model, the only known mechanism to explain this discrepancy is hard two-photon exchange (TPE), which is not corrected for in L/T separation data that relies on the one-photon exchange (OPE) approximation and the consequent linearity of σ_r in ε [11, 28].

Figure 13, discussed in a previous section, suggests that at least some of the difference can be explained with model-dependent TPE corrections to the OPE reduced cross section[20]. Figure 16 depicts the effectiveness of such corrections up to $Q^2 = 4.1,\mathrm{GeV}^2$. The discrepancy becomes more difficult to reconcile with these model-dependent corrections at higher Q^2, commensurate with the fact that radiative corrections become more pronounced in this regime [128].

1.5.3 Neutron

Precision neutron form factor measurements are much more difficult to make than those of the proton owing, as mentioned, to the lack of sufficiently dense free neutron targets. Nevertheless, current neutron measurements make use of liquid deuterium and the ratio method to extract precision cross sections. From the current data, G_D describes G_M^n well up to about $Q^2 = 4.5\,GeV^2$ such

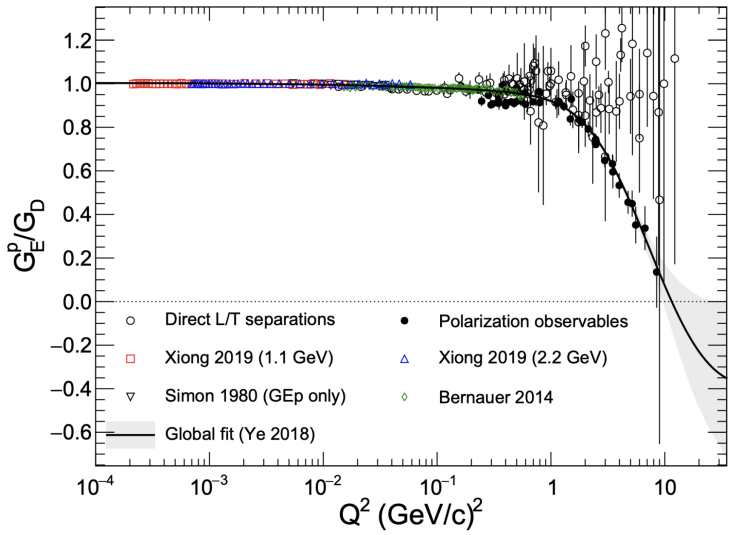

Figure 14: Approximate world data for G_E^p normalized by the dipole form G_D. G_D approximates the world data well where $Q^2 \leq 1\,GeV^2$ and the ratio is unity. No hard TPE corrections are applied to L/T data. Note the growing difference between open circles which indicate L/T separation measurements and the solid circles which indicate PT measurements. Ye global fit to the data is in gray. World data and plot from [87].

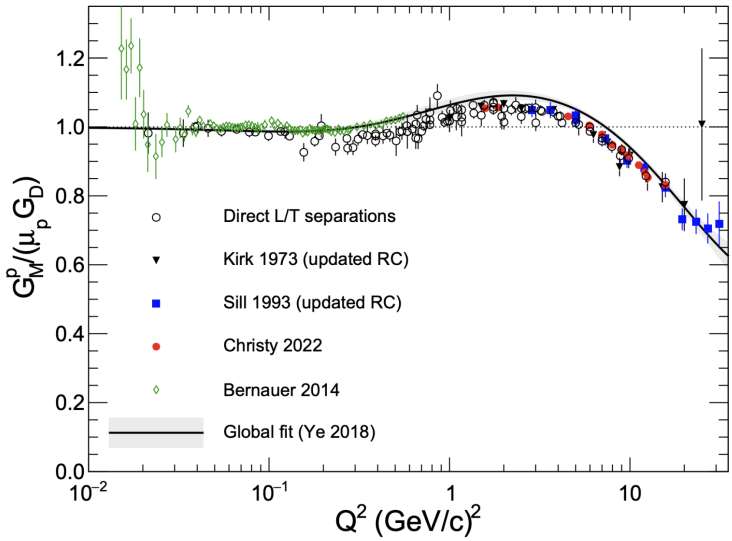

Figure 15: Approximate world data for G_M^p normalized by the dipole form G_D. G_D approximates the world data well where $Q^2 \leq 1\,GeV^2$ and the ratio is unity. Ye global fit to the data is in gray. World data and plot from [87].

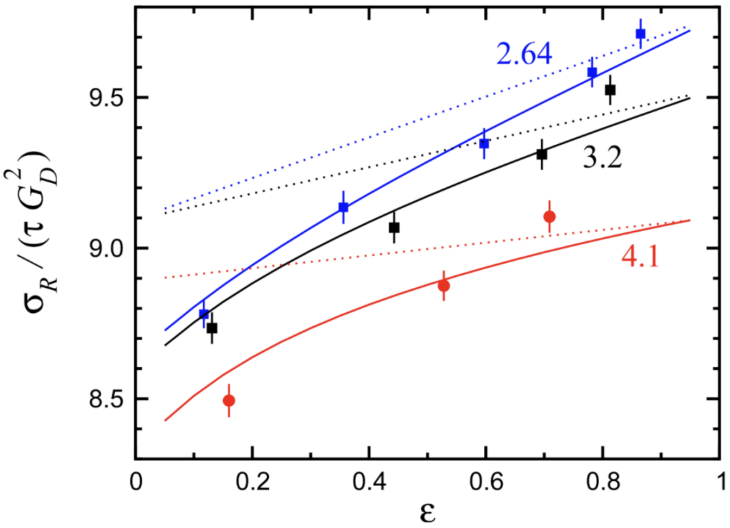

Figure 16: Rosenbluth slope (dotted line) and TPE corrected Rosenbluth slope (solid line) with JLab PT data at $Q^2 = 2.67 - 4.1\,GeV^2$[11].

that:

$$G_D \approx \frac{G_M^n}{\mu_n} \tag{1.114}$$

For G_E^n, the dipole form isn't expected due to the net charge neutrality of the neutron ($G_E^n(0) = 0$). The deviation for the neutron magnetic form factor from the dipole form factor is also apparent, deviating around $Q^2 = 4.5\,GeV^2$. Figure 18 summarizes the world data for G_M^n and figure 17 summarizes the world data for G_E^n.

Of note is that, to date, no L/T separation has been performed on the neutron. As such, an adequate measurement of the difference between L/T separation methods and PT methods for the neutron has not been made. While this difference is well documented for the proton, giving rise to the form factor ratio puzzle, an opportunity exists to measure the TPE contribution to the elastic electron-neutron cross section for the first time[148, 109].

1.5.4 Theory and Models

Parametrized fits to G_M^n, G_E^p, and G_M^p along with a separate parametrization for G_E^n provide quasielastic cross sections for $d(e,e'N)$ events in simulations[165] used in this work. The Riordan parametrization[148]

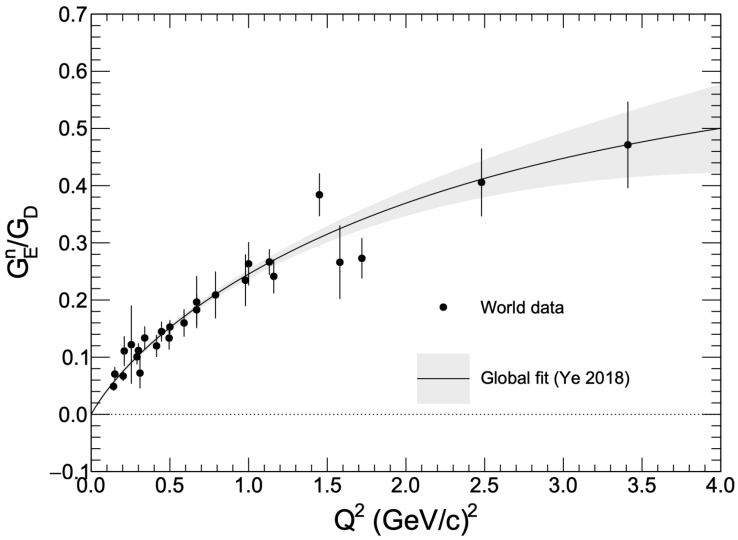

Figure 17: World data for G_E^n from [87].

to G_E^n world data utilizes parametrized expansions in τ_n with coefficients a_i and b_i of the form:

$$G_E^n(\tau_n) = G_D \cdot \frac{a_1\tau_n + a_2\tau_n^2 + a_3\tau_n^3}{1 + b_1\tau_n + b_2\tau_n^2 + b_3\tau_n^3}$$

where G_D is the dipole form factor and $\tau_n = Q^2/(4M_n^2)$ is evaluated for the neutron. Kelly parametrizations[104] are similarly constructed for both neutrons and protons and cover the remaining form factors, utilizing expansions in τ_N and coefficients α_i, β_i, α_i' and β_i'. For G_E:

$$G_E(\tau_N) = \frac{\alpha_1 + \alpha_2\tau_N}{\beta_1 + \beta_2\tau_N + \beta_3\tau_N^2 + \beta_4\tau_N^3},$$

and for G_M:

$$\frac{G_M(\tau_N)}{\mu_N} = \frac{\alpha_1' + \alpha_2'\tau_N}{\beta_1' + \beta_2'\tau_N + \beta_3'\tau_N^2 + \beta_4'\tau_N^3},$$

where μ_N is the magnetic moment of the nucleon in question[48].

To extract the quasielastic cross section of the neutron from data, the quasielastic cross section of the proton can be evaluated from Arrington07 and Ye parametrizations[10, 184]. The Arrington07 parametrizations used for the proton cross section are "TPE corrected," where the influence

[48]Coefficients used in this section can be found in Appendix B.

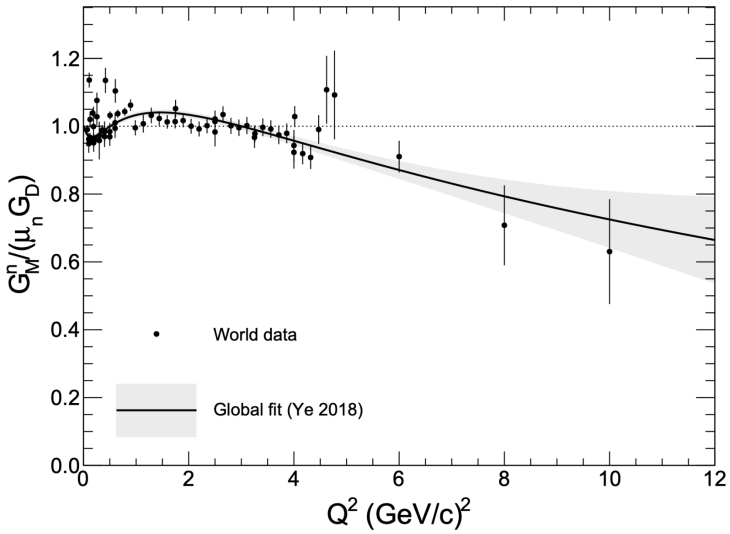

Figure 18: World data for G_M^n from [87].

of polarization transfer on the fit is mitigated. They can be expressed with coefficients A_i and B_i for both G_E and G_M in this way:

$$G(\tau_p) = \frac{1 + A_1\tau_p + A_2\tau_p^2 + A_3\tau_p^3}{1 + B_1\tau_p + B_2\tau_p^2 + B_3\tau_p^3 + B_4\tau_p^4 + B_5\tau_p^5}$$

Errors on G_E^p and G_M^p data points are provided in tables in [10] and can be interpolated for a given Q^2 value. Departing from τ, the Ye parametrization for G_E^n utilize a different set of expansion parameters:

- $z = \frac{\sqrt{t_{\text{cut}}+Q^2} - \sqrt{t_{\text{cut}}-t_0}}{\sqrt{t_{\text{cut}}+Q^2} + \sqrt{t_{\text{cut}}-t_0}}$, where $t_{cut} = 4M_\pi^2$ and $t_0 = -0.7$[49]
- $x = \begin{cases} 1e-8 & \text{if } Q^2 = 1 \\ \log_{10}(Q^2) & \text{otherwise} \end{cases}$

With these and coefficients c_i, G_E^n from the fit is as follows:

$$G_E^n(z) = \sum_{i=0}^{10} c_i \cdot z^i,$$

[49] M_π is the charged pion mass, 0.13957 GeV and t_0 is the cut-off value[172, 184].

and with coefficients d_i the error on the fit is:

$$G^n_{E,err}(x, G_D) = 10^{\left(\Sigma_{i=0}^{14} d_i \cdot x^i\right)} \cdot G_D,$$

where z and x are defined above and G_D is the dipole form factor[184].

1.6 This Work

Neutron form factor measurements at $Q^2 > 4\,GeV^2$ are sparse for G^n_M and non-existent for G^n_E over the same range. In the Fall of 2021 through the Winter of 2022, experiment E12-09-019 (*Precision Measurement of the Neutron Magnetic Form Factor up to* $Q^2 = 18.0\,(GeV/c)^2$ *by the Ratio Method*) took simultaneous proton and neutron cross section data on a liquid deuterium target from $Q^2 = 3.0$ GeV^2 to $Q^2 = 13.6$ GeV^2. The analysis employs the ratio (Durand) technique to reduce systematic uncertainties on the measured quasielastic neutron to proton cross section ratio. After corrections, this ratio enables the extraction of G^n_M. These extractions, detailed in chapter 4, rely upon world data fits for the proton (for G^p_E and G^p_M). The Kelly parametrizations for G^p_M, G^p_E, and G^n_M and Riordan parametrization for G^n_E are used to evaluate the proton and neutron cross section event-by-event in Monte Carlo to generate simulated data, used in the analysis. Figure 19 shows the projected Q^2 coverage of the experimental run. Henceforth, experiment E12-09-019 will be referred to simply as **GMn**, unless otherwise noted.

As noted, an L/T separation has not yet been performed for the neutron and no neutron RS world data yet exists. At the same time as experiment E12-09-019, experiment E12-20-010 (*Measurement of the Two-Photon Exchange Contribution to the Electron-Neutron Elastic Scattering Cross Section*), took simultaneous proton and neutron cross section data at $Q^2 = 4.5\,GeV^2$ and two values of ε, $\varepsilon = 0.52$ and $\varepsilon = 0.80$, to extract the Rosenbluth slope for the neutron at this momentum transfer. These results will be compared to the PT world data for G^n_E to evaluate the difference and the expected hard TPE contribution to the elastic electron-neutron cross section. The current state of this analysis is part of the work presented here. Henceforth, experiment E12-20-010 will

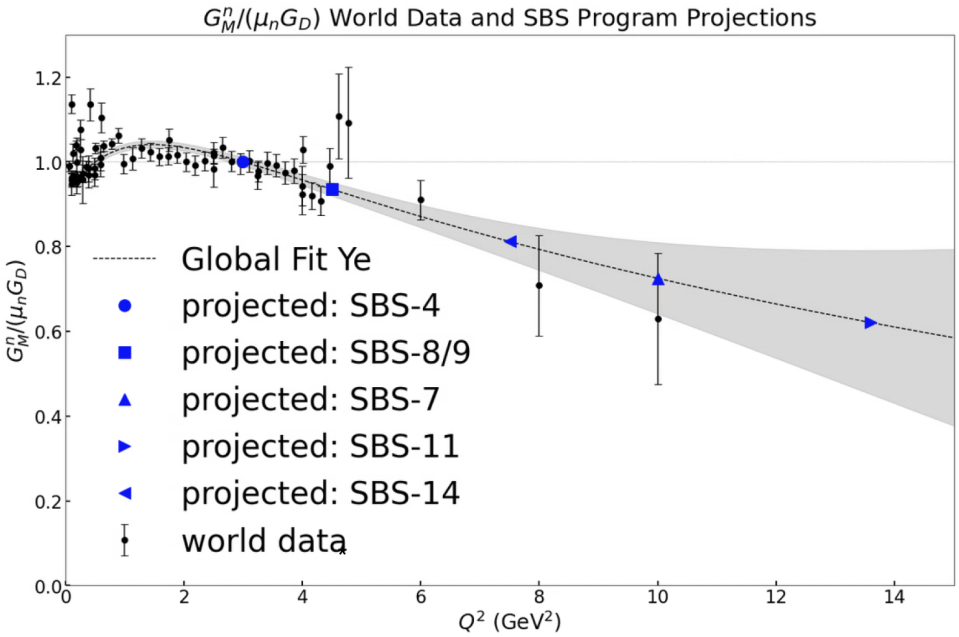

Figure 19: World data and fits along with **GMn** projected Q^2 points. Projected **GMn** points are located arbitrarily on the Ye et al. global fit.

be referred to simply as **nTPE**, unless otherwise noted.

2 Apparatus

2.1 Strategy

The aim of the experiments outlined in this work is to measure the neutron to proton cross-section ratios. These measurements are facilitated by the Continuous Electron Beam Accelerator Facility (CEBAF) and the Super Bigbite Spectrometer (SBS). Together, they enable high-precision measurements of neutron form factors across wide and unprecedented Q^2 regimes (see Table 6). CEBAF delivers high energy electrons in a continuous beam at high current into experimental hall A to scatter from a fixed liquid hydrogen (LH2) or liquid deuterium (LD2) target with high luminosity, where SBS resides.[50]

SBS is a two arm apparatus configured for **GMn** and **nTPE** with a single electron-arm event trigger. Each arm is exclusive in purpose — the electron arm (beam left) is designed to detect quasi-elastic scattered electrons and the hadron arm (beam right) is designed to detect their corresponding quasi-elastic scattered hadrons.

Kine	Q^2 (GeV/c)^2	E_{beam} (GeV)	θ_e	θ_N	E' (GeV)	p_N (GeV)	ε
4	3.0	3.73	36.0°	31.9°	2.11	2.35	0.719
8	4.5	5.98	26.5°	29.4°	3.59	3.20	0.798
9	4.5	4.03	49.0°	22.0°	1.63	3.20	0.514
14	7.4	5.98	46.5°	17.3°	2.00	4.83	0.466
7	9.9	7.93	40.0°	16.1°	2.66	6.13	0.497
11	13.5	9.89	42.0°	13.3°	2.67	8.11	0.412

Table 6: **GMn** Kinematics and Details

Over the kinematics settings in table 6 (labeled *kine*), SBS measured the neutron to proton cross section ratio via the ratio method. From these data, **GMn** will extract G_M^n for all kinematic settings and **nTPE** will evaluate the neutron RS from kinematics 8 and 9 (*SBS-8* and *SBS-9* respectively) where Q^2 is similar, but ε varies commensurate with scattering angle and beam energy.[51] See figure 20 for an illustration of **GMn**'s Q^2 coverage and **nTPE** points.

[50] For other SBS experiments, a polarized Helium-3 target is also utilized.

[51] Moving forward, reference to kinematics will adopt this convention, where kinematic i will be referred to as SBS-i.

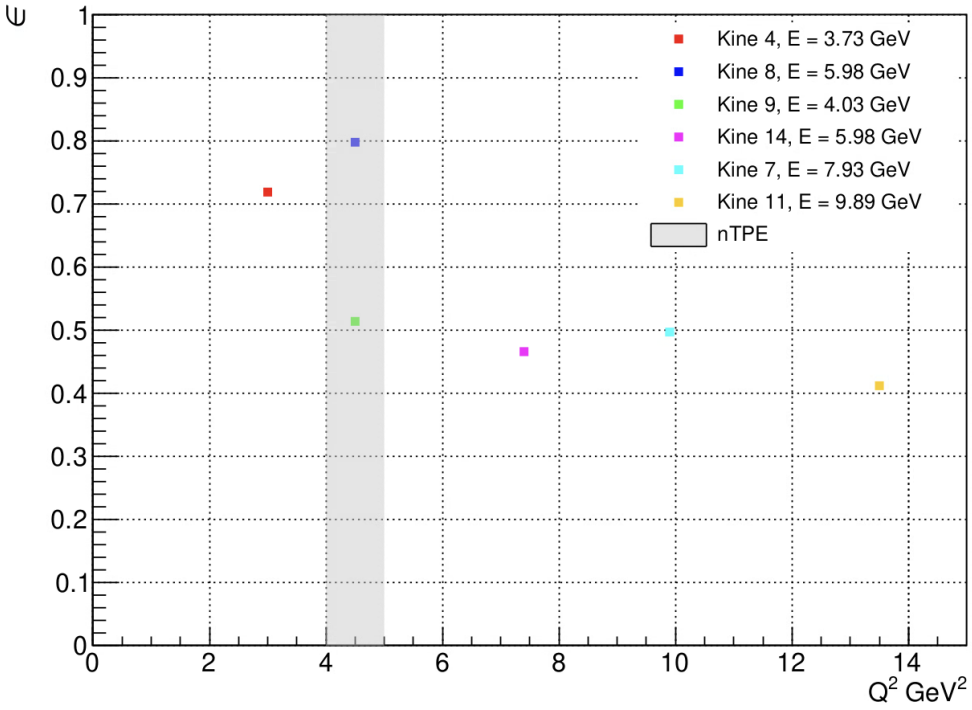

Figure 20: ε vs Q^2 depicting the **GMn** run group kinematics, including **nTPE** points.

Making several high Q^2 measurements poses a number of experimental challenges.

- As Q^2 grows, the quasi-elastic $e-N$ cross section drops rapidly. High luminosity and continuous running is important to address the low relative quasi-elastic yield as compared to similar experiments at lower Q^2.
- Minimizing systematic errors requires large hadron acceptance and a powerful magnet to separate protons and neutrons for simultaneous measurement of both.
- With several fixed Q^2 points, optimizing acceptance (and yield by extension) requires a spectrometer capable of taking a "big bite" of the momentum.
- Optimizing the acceptance for several Q^2 points also entails movement of both arms independently in both θ (with respect to the beamline) and r (with respect to the target chamber).

For these reasons and others, a novel spectrometer was constructed. SBS is a temporary installation, intended to carry out its experimental program over roughly 6 years of running (see figure 7 for experiment name and extracted form factor). Note that the **GMn** run group (which includes

nTPE) was the first experimental run of the SBS experimental group.

Experiment	Form Factor	Q^2 Range	Time Frame
GMn (E12-09-019)	G_M^n	up to 13.5 GeV^2	Oct. 2021 - Feb. 2022
GEn-II (E12-09-016)	G_E^n	up to 9.7 GeV^2	Oct. 2022 - Oct. 2023
GEn-rp (E12-17-004)	G_E^n (PT)	4.5 GeV^2	April 2024 - May 2024
GEp-V (E12-07-109)	G_E^p	up to 12 GeV^2	Oct. 2024 - May 2025

Table 7: Timeline of Super Bigbite Spectrometer (SBS) Nucleon Form Factor Program.

For accurate evaluation of systematics and to extract cross sections from quasielastic yields, all of the relevant geometry in SBS has been translated into Geant4 and, coupled with several Monte Carlo (*MC*) particle event generators (including the SIMC event generator which includes nuclear and radiative corrections), constitutes *G4SBS*. G4SBS allows for accurate simulation of scattering events during the **GMn** run group, albeit with fits to nucleon form factor world data baked in. With data in hand, comparisons to MC allows for extraction of quasielastic cross sections, and extraction of form factors.

While this work entails the preliminary analysis of **GMn** and **nTPE**, it is not limited to these physics. Because SBS is a new spectrometer and installation, many of the preliminary goals of the first experimental run are to adequately characterize the various detector subsystem performance for later experimental runs in the SBS run group. Owing to this focus, special attention is paid to the SBS spectrometer and the Hadron Calorimeter (HCal) in particular.

2.2 The Continuous Electron Beam Accelerator Facility

The Continuous Electron Beam Accelerator Facility (CEBAF) at Jefferson Lab (or JLab) is located in Newport News, Virginia. It consists of two parallel linear accelerators (linacs) connected by recirculation arcs on either side designed to bend electrons from one linac to the other (the "race-track"), an electron injector, and several experimental halls. Each linac is composed of several cryomodules containing superconducting Niobium cavities which resonate in radio frequencies (SRF cavities). Niobium superconducts in superfluid Helium, at around 2 K, which reduces the

heat load generated by the cavities by a factor of 3 and improves accelerator efficiency[94].

In 2017, JLab completed an upgrade of the accelerator improving its electron energy reach to 12 GeV. After the 12 GeV upgrade, there are now 52 and 1/4 cryomodules with eight SRF cavities per cryomodule operating in both linacs. Each linac is capable of imparting 1090 MeV to electrons moving through it which are kept on track by several arcs of magnets that can handle the high momentum of 12 GeV electrons[94]. Figure 21 depicts CEBAF.

The accelerator is capable of delivering polarized or unpolarized electrons into the experimental halls after production in the injector. This production results from near infrared ($\lambda = 780$ nm), polarized laser light impinging on Gallium Arsenide (GaAs) photocathodes under a high negative potential. The resulting electron current arising from the photoelectric effect is directed into the accelerator at $E_{injector} = 123$ MeV[99]. Each pass through the pair of linacs is a single "pass," where the electron picks up energy such that:

$$E_{beam} = E_{injector} + N_{pass}(E_{northlinac} + E_{southlinac}) \tag{2.1}$$

The full reach of beam energy reached for **GMn** and **nTPE** can be seen in figure 20, with maximum of $E_{beam} = 9.89$ GeV for SBS-11. These electrons are high-duty and effectively continuous wave (CW), delivered to the experimental halls in bunches at 250 MHz or 499 MHz (configurable). CEBAF delivered electrons to Hall A at 250 MHz (4 ns bunches) for both **GMn** and **nTPE**[112].

Figure 21 includes the locations of all four experimental halls at JLab, each with a different focus. From table 8, experimental halls A and C are the high current halls, receiving up to 100 μA of current[112]. Between these, hall C contains the High Momentum Spectrometer (HMS) and Super High Momentum Spectrometer (SHMS), leaving Hall A the only hall with no active permanent spectrometer installation. In 2021, SBS was installed there and will continue its operation until it is expected to be removed in 2025 at the conclusion of the current form factor program to make room for the upcoming MOLLER experiment. The SBS apparatus will continue to see use in later experiments after the conclusion of the form factor program.

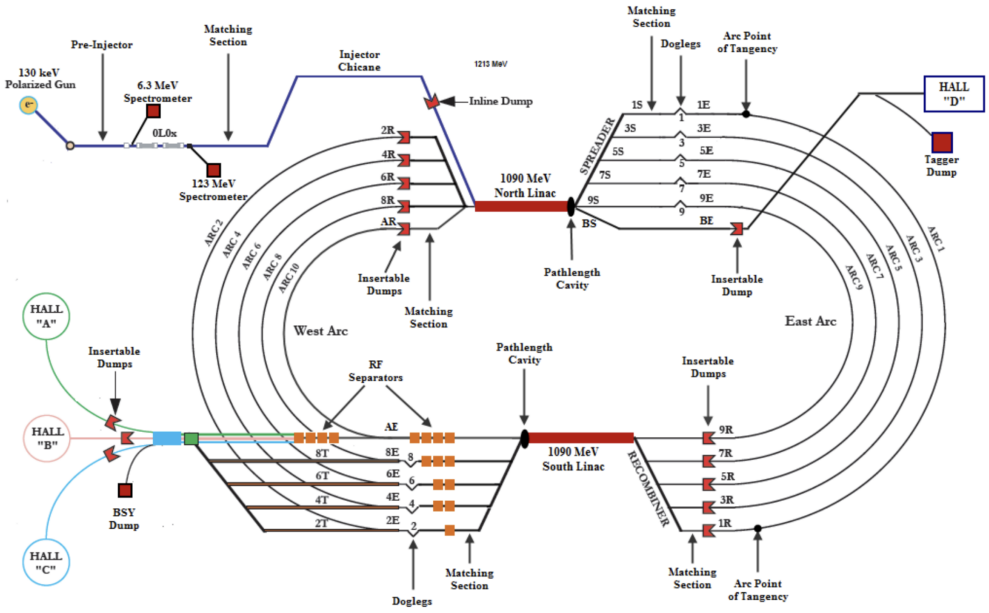

Figure 21: Schematic of CEBAF after the 12 GeV upgrade. Reproduced from [181].

Hall A	Hall B	Hall C	Hall D
precision	hermeticity	precision	polarized photons
11 GeV beamline			$E_\gamma \sim 8.5 - 9$ GeV

Table 8: Capabilities of the Jefferson Lab Halls[94].

2.2.1 Hall A Beamline and Diagnostics

The hall A beamline contains several components both upstream of the target and downstream of the target. Upstream of the target, the beam diagnostic monitors are in-line with the evacuated beam pipe (containing the electron beam) leading up to the target chamber. The now defunct High Resolution Spectrometers (HRS, left and right) are moved out of the way for the SBS installation downstream of the target. On beam left is the Bigbite Spectrometer and on beam right is the hadron arm. Positioned behind the left HRS is the DAQ bunker housing the many crates, high voltage supplies, and computing hardware necessary to record data on all detector subsystems. Figure 22 shows two views of the hall with dimensions not to scale.

While the ratio method employed for both experiments cancels uncertainties related to the beam current and position, it was necessary to monitor them for the health of the targets and to

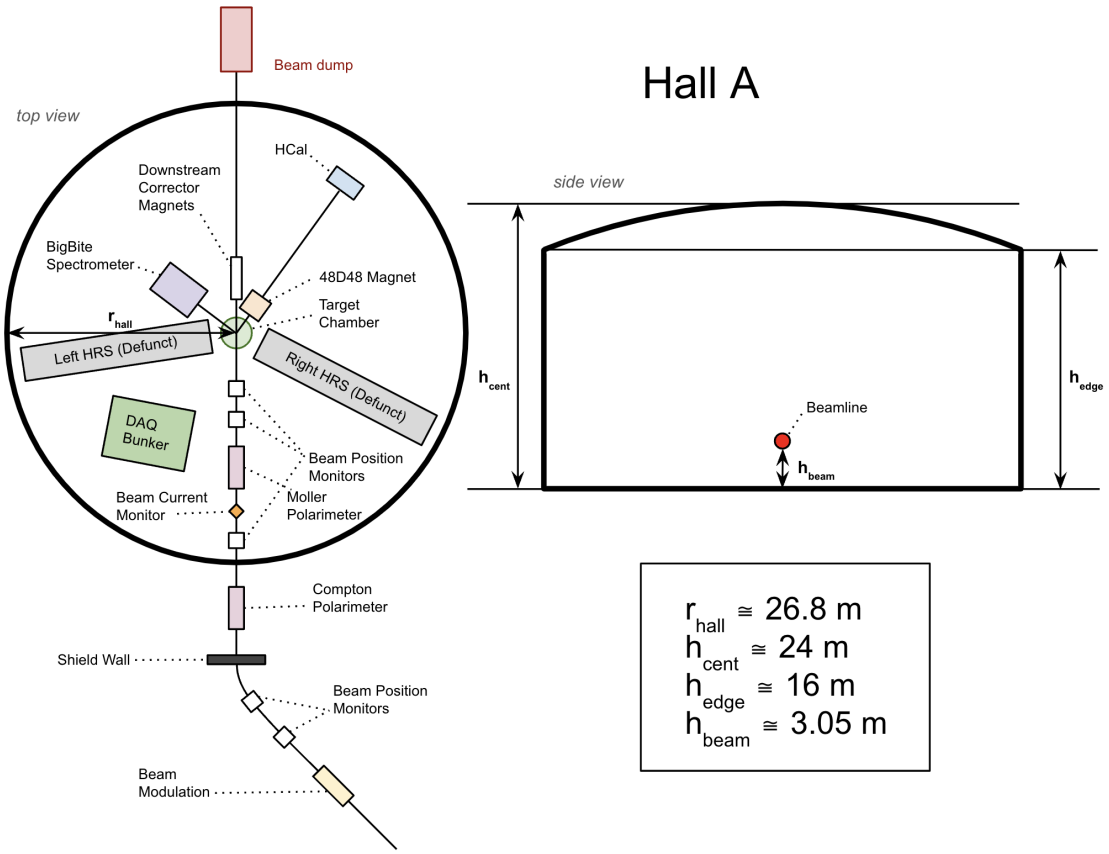

Figure 22: Top-down and side views of experimental Hall A at JLab. The side view is along the beamline. Dimensions are not to scale.

ensure statistics goals were met. The Beam Charge Monitors (BCM) system located roughly 25 m upstream of the target makes use of two thermally and magnetically shielded mechanisms to garner an accurate measurement of the current delivered into the hall.

The first of these BCM systems is a parametric current transformer called an "Unser," which generates a wire current proportional to the electron beam passing by it. This proportionality constant is calibrated and the beam current can be determined from the Unser wire current. This tool is used largely as a diagnostic and absolute reference for the second BCM mechanism due to the short signal drift timescale inherent to the technique.

The second method uses two RF resonant cavities, each tuned to 1497 MHz, placed on either side of the Unser monitor. When the beam passes through these cavities, they generate a voltage signal proportional to the beam current. This signal is amplified and converted from an RMS

value to a DC value using a 1 MHz RMS-to-DC converter over a 1-second collection time. The analog signal is then read by a voltmeter and digitized for continuous monitoring of the beam current. The digital signal is converted to a frequency and sent to scalers for readout by the CEBAF Online Data Acquisition system (CODA) every 2-5 seconds. These signals are also sent to the Experimental Physics Industrial Control System (EPICS) for recording. Figure 9 shows the total charge accumulated over all kinematics using EPICS data[186].[52]

The beamline is also checked by Beam Position Monitors (BPMs). These instruments are installed along the Hall A beamline upstream of the target to accurately monitor the position and direction of the particle beam without disturbing it. Positioned strategically after beam steering magnets and other focusing elements, BPMs utilize four antennae, arranged diagonally at the corners of the beamline, to detect the beam's presence. These antennae, running parallel to the beamline, induce currents as the beam passes, allowing for the calculation of the beam's position based on the difference in the signals they receive. See figure 23 for reference.

The computation of the beam's position involves a calibration constant C and employs the formulae:

$$x_{\text{rot}} = C\left(\frac{X_p - X_m}{X_p + X_m}\right) \tag{2.2}$$

$$y_{\text{rot}} = C\left(\frac{Y_p - Y_m}{Y_p + Y_m}\right), \tag{2.3}$$

where X_p, X_m, Y_p, and Y_m represent the ADC signals from the antennae induced by the beam, and $C = 18.76\,\text{mm}$ acts as the calibration constant. This formulation enables the determination of the beam's position in a rotated coordinate system, which is then transformed into the

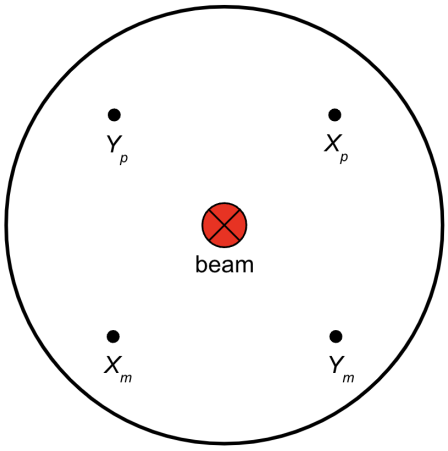

Figure 23: BPM antenna array.

[52]The fundamental frequency of the accelerator is set to 1497 MHz, matching the BCM RF cavities, to produce configurable beam bunch frequencies of 250 MHz or 499 MHz.

Kinematic	Target	SBS Mag (A)	Total Charge (C)
4	LD2	0	0.022407
4	LD2	630	0.050238
4	LD2	1050	0.006716
7	LD2	1785	0.534710
8	LD2	0	0.169141
8	LD2	1050	0.092791
8	LD2	1470	0.758027
8	LD2	2100	0.174146
9	LD2	1470	2.554209
11	LD2	0	0.117723
11	LD2	2100	9.471579
14	LD2	1470	1.516005
4	LH2	0	0.022230
4	LH2	630	0.035021
4	LH2	1050	0.010209
7	LH2	1785	0.310150
8	LH2	0	0.204514
8	LH2	1050	0.030475
8	LH2	1470	0.416299
8	LH2	2100	0.205330
9	LH2	1470	0.675756
11	LH2	0	0.122969
11	LH2	2100	3.349326
14	LH2	0	0.168349
14	LH2	1470	0.630457

Table 9: Aggregated Charge Data for LD2 and LH2 Targets. Only "good" runs are counted for these data. No zero field data was taken for SBS-14. The maximum current on the 48D48 "SBS" magnet is 2100 A. Refer to table 6 for more information.

standard laboratory coordinates by rotating around the beam direction by $\theta = 45^{\circ}$, ensuring the positions align with the lab's frame of reference[186].

The BPMs provide real-time feedback for beam steering adjustments via the calculation of the beam's position to within 100 μm for currents above 1 μA and was instrumental for initial beam-steering procedures to bring beam into the hall before each kinematic. Absolute positioning, necessary for detailed studies, is achieved through additional calibration using wire scanners, which interact directly with the beam to offer a precise location. The dual recording method—averaging positions over short intervals and logging detailed event-by-event data—ensures comprehensive monitoring and control over the beam's trajectory. Additional BPM measurements are made by the *Machine Control Center* (MCC) on the accelerator-side of operations for further confirmation of beam alignment. Hall A BPM real-time data is read into EPICS for further analysis.

If the beam is misaligned, it can impinge on its enclosure, the target, or other obstructions which can lead to a host of significant failure modes, not least of which is rapid unscheduled disassembly of the target. As a failsafe, *ion chambers* are installed periodically in the hall to monitor background radiation.[53] In the event of a beam excursion or other out-of-control radiological event, a nearby ion chamber will register count rate above threshold and initiate a *Fast ShutDown* (FSD) of the accelerator to prevent and limit fallout from the event. While MCC responds quickly to ramp beam current back to nominal, these occurrences are frequent (up to 20/hour during **GMn**) in the 12 GeV era and the lower data collection rate associated with ramp time becomes significant over frequent occurrences. Due to presence of fringe fields, corrector dipole magnets located downstream of the target in Hall A are necessary to refocus the beam and to prevent beam excursions which trigger FSD from these ion chamber systems.

Even when the beam is well controlled and located, it is necessary to spread the energy deposited by the beam out over the target cell to prevent damage or rupture. Field coils positioned roughly 23 m upstream of the target bend the beam into a *raster* pattern, effectively tracing the transverse position of the beam through a configurable shape of a configurable size. This results

[53] Ion chambers are devices that measure ionizing radiation by detecting the electrical current created when radiation ionizes the gas within a sealed container, with the current strength indicating the amount of radiation present.

in a somewhat distorted, but effectively spread out beam shape at the target. For an intrinsic beam size on the order of 100 μm, this is necessary for all cryotargets used in during **GMn** and **nTPE**. The **GMn** run group made use of a 2 x 2 mm^2 square shaped raster. Figure 24 depicts the raster common to the run group.

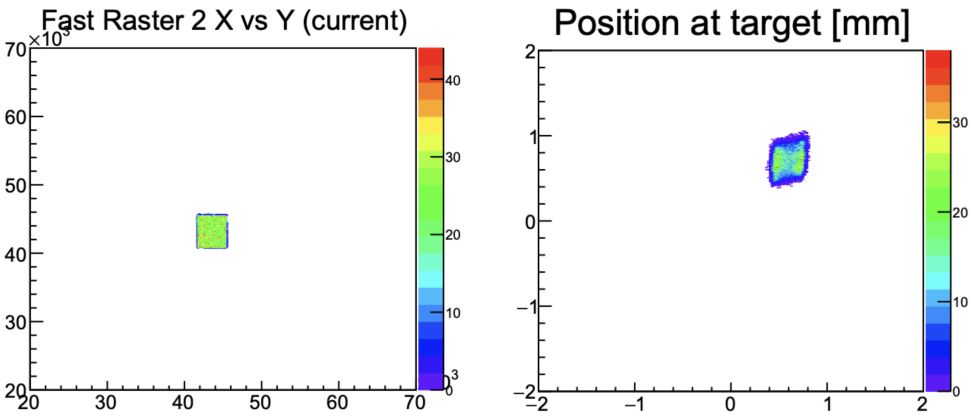

Figure 24: (*left*) Fast raster at raster in uncalibrated raster units. (*right*) BPM pattern at the target in mm. Typical for **GMn** running group, but taken from Panguin data quality plots, run 13792 SBS-9.

2.3 Targets

The two cryotargets used to obtain proton and neutron yields and calibrations were liquid hydrogen (LH2) and liquid deuterium (LD2). Each were located on a "ladder" designed to move a desired target into the path of the beam by remote control in the *counting house* (or experimental control room located above the hall). The other targets located on the ladder, carbon foils and carbon hole, were used for beam and rate diagnostics, beam steering, and BPM calibrations.

2.3.1 Cryotargets and Reference Cell

Each of the Hall A cryotargets is contained within an aluminum "beer-can" cell, which is cooled with a continuous flow of liquid helium. Figure 25 depicts several cells on the "target ladder." This ladder can be remotely moved to place a desired target into the electron beam. When the electron beam is directed at a cryotarget target, significant heating occurs due to the energy deposited within

the liquid by the beam (measured as $-dE/dx$ in MeV/g/cm^2). To prevent phase transitions within the cell, it must be continuously cooled. However, to account for the heat difference between beam-on and beam-off conditions and the corresponding energy deposition in the cell, the return coolant lines must also be heated to maintain a stable temperature and prevent freezing of the return lines. Generally speaking, reducing the helium flow rate via the Joule-Thomson (JT) valve decreases the power draw of the heater at a calculable rate. See Table 10 for cryotarget details, including the energy loss of electrons, which will be revisited in later sections[89].

Figure 25: Image of the cryotarget ladder in Hall A during **GMn**. Picture credit [37].

Cryo	Holding T	Freezing T	Boiling T	Density	-dE/dx
LH2	19 ± 0.01 K	13.8 K	22.2 K	0.0723 g/cm^2	4.8 MeV/g/cm^2
LD2	22 ± 0.01 K	18.7 K	25.3 K	0.167 g/cm^2	2.4 MeV/g/cm^2

Table 10: Temperatures of LH2 and LD2 in 15 cm cells[38].

The heaters operate on a closed power loop such that the JT valve must be tuned to maintain the holding temperature within the reserve power limitations of the heater, especially where experimental halls A and C share this reserve power (for **GMn** run group, 75 W). Additionally, a 2x2 mm^2 raster must be on when the cryotarget is in operation to prevent damage to the cell. For these reasons, the cryotarget requires a constant monitoring during operations (both with and without beam) to ensure that the temperature stays within holding parameters and failure modes are addressed immediately.

The effect of the aluminum endcap "windows" on either end of the cell on the measured proton and neutron cross sections cancels on the ratio of form factors and, for absolute measurements, can be mitigated with sufficient cuts on the vertex position of the scattering event evaluated with e' tracks formed in the electron arm. See figure 26 for cryotarget position and dimensions. Regardless, a reference (or "dummy") target is also maintained on the ladder to enable systematics analysis and, where necessary, subtraction of endcap contributions to the measured cross sections. This reference target consists of two aluminum foils that duplicate the dimensions of the upstream and downstream Aluminum cryotarget cell endcaps.

2.3.2 Carbon Foils and Carbon Hole

The primary purpose of carbon foils is to serve as extended optics targets for vertex reconstructions during optics tuning. Each foil is a plane oriented orthogonally to the beam direction with a thickness of 0.044 ± 0.001 g/cm^2, arranged in line with the beam direction. For the **GMn** run group, 4-foil and 5-foil carbon (99.95% C) targets were available on the target ladder for coarse and fine tuning of optics parameters [113]. A sieve plate, featuring numerous regularly spaced holes and situated between the target chamber and the tracking arm (the Bigbite stack), allowed for the precise mapping of electron rays through these holes from each vertex position on the foils into the tracking arm (see figure 27). This setup enabled the construction of an optics matrix that accurately provides electron track information at the target from electron track information in the Bigbite detector stack, accounting for the deflections from the electron arm magnet. See Table 11

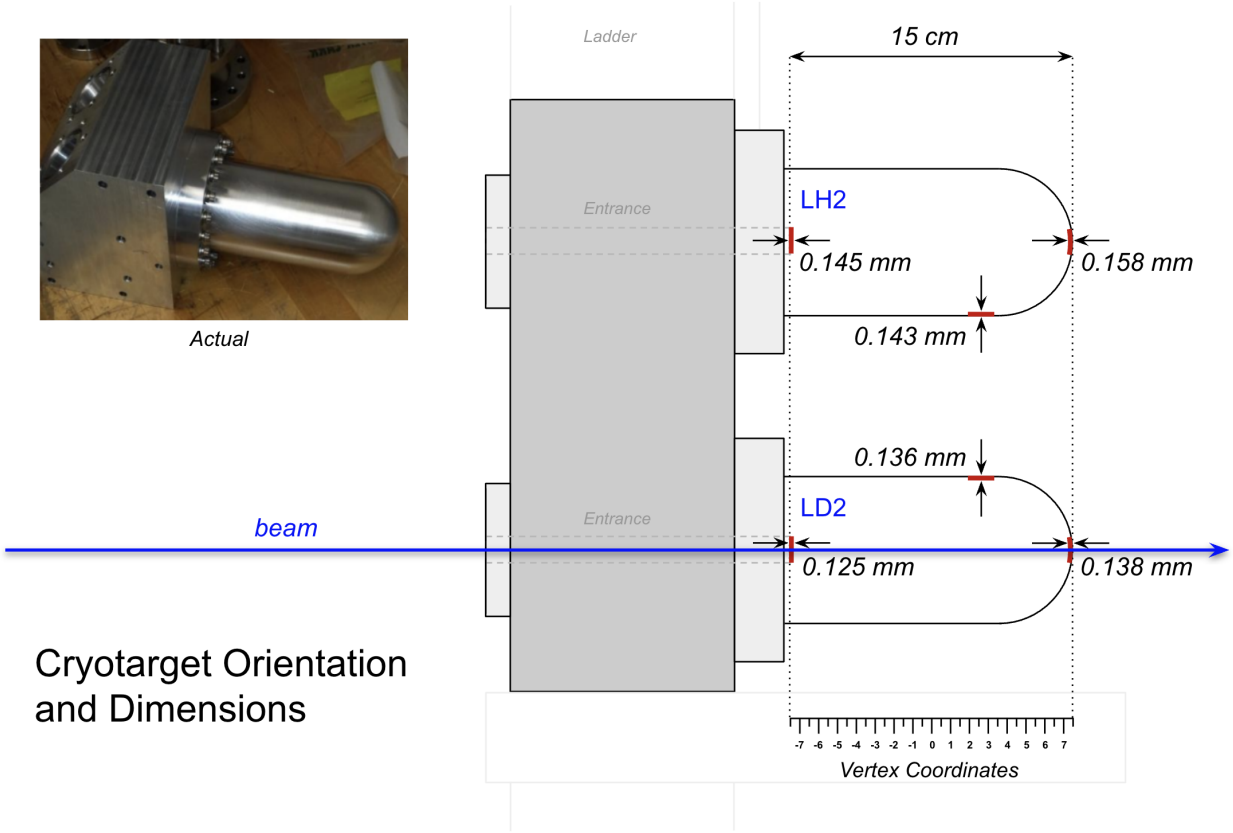

Figure 26: The LH2 and LD2 cryotargets are positioned longitudinally with the beam on the target ladder, with relevant dimensions provided. Vertex coordinates in the lab frame are consistent with the analysis. All measurement tolerances are bounded by ± 0.012 mm, except for the cryotarget overall length, which is 150 ± 0.26 mm. Figure 25 is adapted from [91] and is not to scale for Hall A targets.

for vertex locations of foil targets.

Carbon hole targets (5 mm and 2 mm diameter) were also available on the target ladder to calibrate beam positions during beam steering operations and beam calibrations before each SBS setting. These operations were necessary after long downtime periods, usually after SBS configuration changes and significant hall operations.

2.4 Super Bigbite Spectrometer

SBS is designed with a tracking spectrometer, the Bigbite Spectrometer, on beam left designed to detect elastic and quasi-elastic electrons. On beam right is the SBS (or 48D48) magnet and Hadron

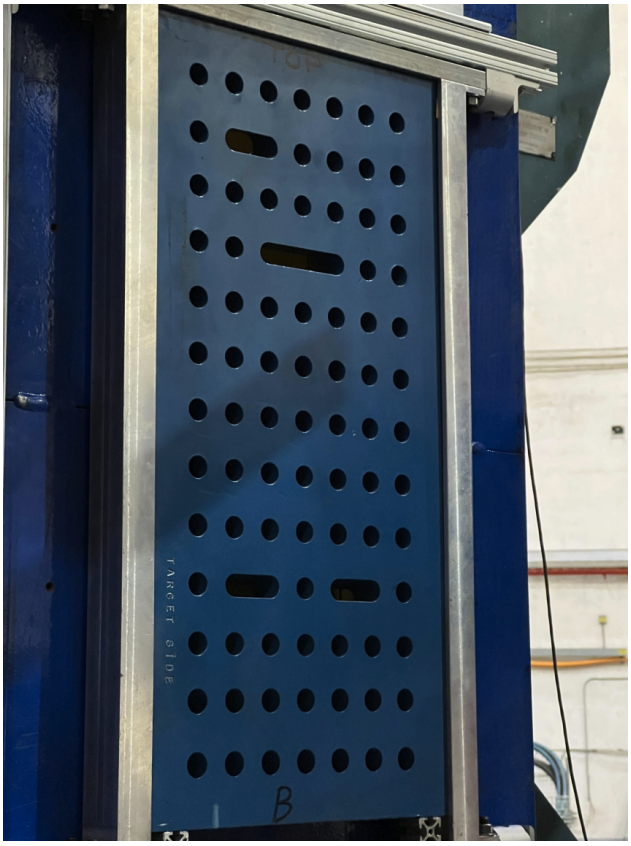

Figure 27: The sieve plate used to calibrate optics in the GMn run group. Vertical and horizontal asymmetries along with many holes allow for particles passing through the sieve and detected in Bigbite to be reconstructed back to the target.

Calorimeter (HCal) designed to detect elastic and quasi-elastic protons and neutrons. The Bigbite Spectrometer is the electron arm of the experiment and the beam-right subsystems are the hadron arm. Figure 28 is a visualization of the entire SBS spectrometer in the SBS Geant4 package, G4SBS[65].

The Bigbite Spectrometer stack consists of many detector subsystems. A sum-over-threshold in the electromagnetic calorimeter (an *EM-Cal* named "BBCal") located in this arm constitutes the single-arm trigger for the experiment. On each event, the electron track can be reconstructed from BBCal and hits in the 5 Gas Electron Multiplier (GEM) layers back to the vertex position in the target. A timing hodoscope (or simply "hodo") provides precision time-of-flight measurements for the electron and the Gas Ring Imaging Cherenkov (GRINCH) provides Particle ID (*PID*) for the

Target	Foil locations in z [cm]				
	1	2	3	4	5
5 Foils	-10	-5	0	5	10
4 Foils	-7.5	-2.5	2.5	7.5	

Table 11: Carbon foil locations for 5-foil and 4-foil setups. z positions (longitudinal with beam) in vertex coordinates.

electron, which allows for pion rejection. In order proceeding from the target chamber outward, the subsystems are: the Bigbite dipole, four GEM layers (the "Front Tracker"), the GRINCH, the fifth GEM layer (the "Back Tracker"), the BBCal preshower, the timing hodoscope, and finally the BBCal shower. The entire stack is oriented 10° from horizontal to optimize acceptance for upbending electron tracks. Figure 30 depicts the Bigbite spectrometer stack and magnet. These subsystems will be discussed at greater length in the following sections[65].

On each trigger, HCal registers many hits (in principle). From the details of the reconstructed electron track, a straight line projection from the vertex can be drawn to the face of HCal (the "neutron hypothesis"). The difference between the expected location of a hit in HCal from the neutron hypothesis and the actual hit in both the dispersive direction (vertical, X in transport coordinates) and non-dispersive direction (horizontal, Y in transport coordinates) can be calculated per event. This "delta" variable along with the 1.6 T·m SBS magnet enables the separation of proton and neutron distributions in HCal. HCal is discussed in a later section. Analysis of yield data and delta distributions are in chapter 3.

2.5 Interactions of Radiation in Media

Detection of charged particles is generally easier than the detection of neutral particles because charged particles interact electromagnetically as they travel through a medium, leaving behind a trail of ionization that can be readily detected. The SBS experiments employ gas-filled chambers for its GEMs (Gas Electron Multipliers), which detect charged particles through ionization radiation. Charged particles interact with plastic scintillators primarily through the processes of ionization and excitation. Plastic scintillators are composed of organic polymer materials doped

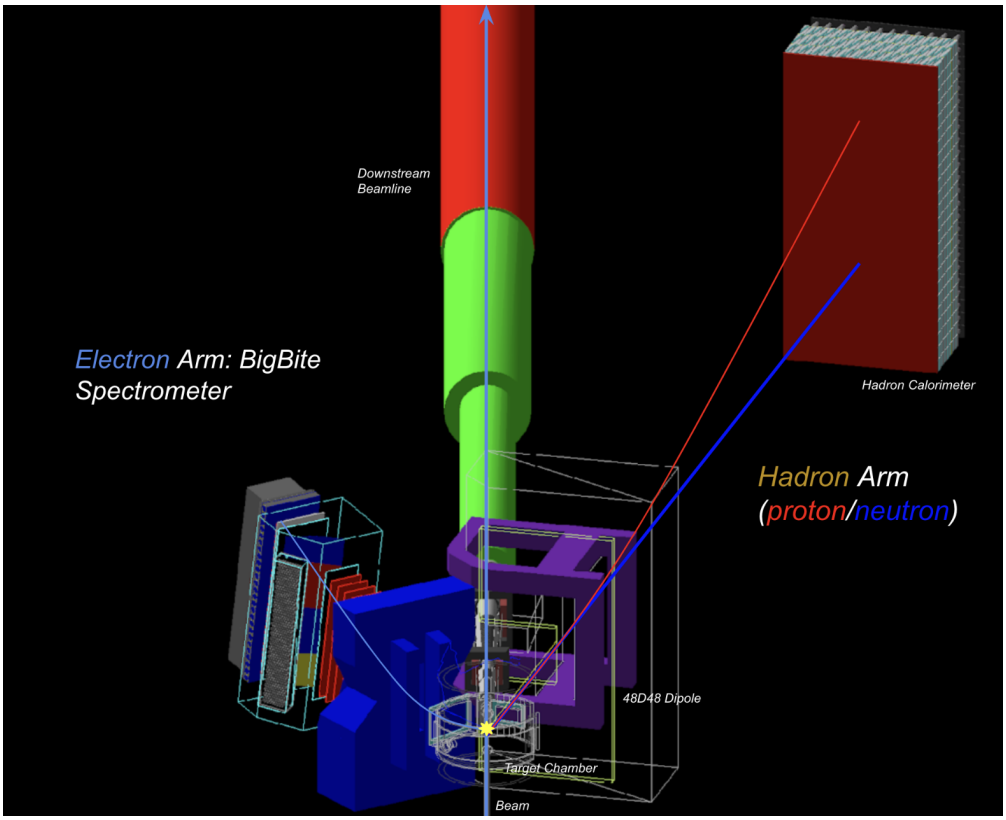

Figure 28: Wide view of the Super Bigbite Spectrometer installed at JLab, experimental hall A. Various detection paths for possible scattered particles are included for reference. Visualization in SBS Geant4 (G4SBS).

with small amounts of fluorescent compounds (the molecules of which are called *fluors*) [108]. When a charged particle, such as an electron or proton, passes through the scintillator material, it interacts with the electrons of the atoms and fluors in the plastic, causing two main effects: ionization and excitation [105].

- **Ionization** occurs when the incoming charged particle has enough energy to remove an electron from an atom in the scintillator, creating ion pairs. These initial charged particles see minimal energy loss as a function of distance through media and are commonly referred to as *MIPs* (Minimum Ionizing Particles) [108]. After collision, the MIP directly ionizes the scintillator material's molecules, leading to the formation of free electrons and positively charged ions. These products may readily interact with other atoms in the scintillator.
- **Excitation** involves a charged particle transferring energy to the electrons in the scintillator

molecules without necessarily ionizing them. This energy promotes electrons in the fluor to excited energy states which include vibrational sub-levels (for excited state S1, vibrational sub-levels S11, S12, S13, etc.). The vibrational states are transferable between neighboring fluors and, after a characteristic time, these vibrational modes equalize between many fluors, returning many fluor molecules to the base electronic energy state (S1, S2, S3, etc.). When these excited electrons return to their ground state, they emit photons within a tight emission spectrum constrained by these base excited states [105]. This light emission process is known as fluorescence. Figure 29 shows fluorescence along with other emission processes. Scintillation detectors detect the light emitted by excited states of atoms and molecules and do not directly detect ionization.

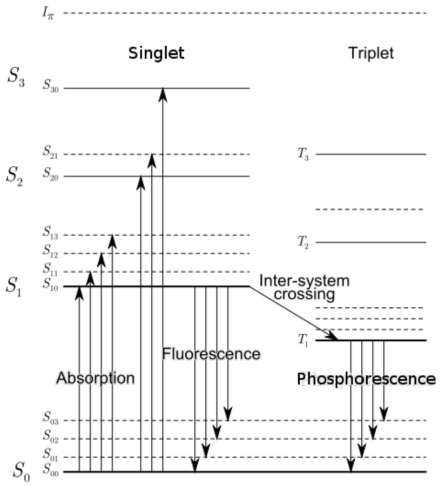

Figure 29: Jablonski diagram depicting electronic excited states with vibrational fine structure and fluorescent emission[163, 105].

The fluorescent compounds added to the scintillator material are chosen for their ability to efficiently convert the absorbed energy into light and for their tight emission spectrum, which needs to be well matched to the peak sensitivity of photomultiplier tubes (PMTs) [105]. Wavelength shifters and waveguides help to match scintillated light to peak PMT sensitivities at high collection efficiency, after which PMTs convert light into an analog pulse for processing [108]. The amount of light produced is generally proportional to the energy deposited by the charged particle, as is

shown by Birk's Law [105]:

$$\frac{d\mathscr{L}}{dx} = \mathscr{L}_0 \frac{dE/dx}{1 + k_B \cdot dE/dx} \tag{2.4}$$

$$d\mathscr{L} = \frac{S \cdot dE}{1 + k_B \cdot dE/dx} \tag{2.5}$$

where the luminescence (or light yield) $\mathscr{L}$ is related first to the luminescence at low specific ionization density $\mathscr{L}_0$ and Birk's constant k_B which governs the quenching or saturation of the organic fluor [108]. The formula can be made more practical by introducing the scintillation efficiency S after integration in equation 2.5 and more readily demonstrates the dependence of light emission on energy deposited [105].

In addition to ionization and excitation, two secondary radiation phenomena, Cherenkov and bremsstrahlung radiation, significantly impact the detection and characterization of high-energy charged particles [108, 105]:

- **Cherenkov radiation** occurs when a charged particle moves through a dielectric medium at a speed greater than the phase velocity of light in that medium, emitting electromagnetic radiation (typically visible as a blue glow)[108].
- **Bremsstrahlung radiation**, also known as braking radiation, is produced when a charged particle is decelerated or deflected by the electric field of a nucleus, emitting a broad spectrum of electromagnetic radiation. This process is a significant consideration in the design and interpretation of experiments, especially for high-Z materials like lead in calorimeters [105].

Lead glass calorimeters like BBCal utilize Cherenkov radiation for energy measurement of electromagnetic particles. The high refractive index of lead glass makes it an efficient medium for Cherenkov radiation production. As high-energy particles traverse the lead glass, they emit Cherenkov radiation, which is then focused and collected in PMTs, providing a precise measure of the particle's energy [108, 105].

Like scintillators, charged particles interact with gas-filled detectors primarily through ionization and excitation. However, unlike scintillators, gas-filled detectors do not rely on fluorescence

but rather on ionization and electric potentials as their principal mechanism. In a Gas Electron Multiplier (GEM), for instance, the interaction of a charged particle with the gas results in the formation of electron-ion pairs. These pairs are generated when the charged particle ionizes gas molecules within the chamber [154].

Each electron and its corresponding positive ion are accelerated by a potential difference maintained between an anode and cathode, leading to the collection of charges and their conversion into analog signals at the electrodes. As the particle moves through the gas, it gains energy from the electric field and can cause additional ionization events. This process of gas amplification, known as a *Townsend avalanche*, is described by an exponential law [175, 105]:

$$I = I_0 e^{\alpha \cdot d} \tag{2.6}$$

where I is the current at the anode, I_0 is the initial current (or charge) generated by the primary ionization event, α is the first Townsend coefficient (representing the number of ionizations per unit length per electron), and d is the distance over which the avalanche occurs [108, 175].

Some gaseous detectors, like the GEMs, enhance the gas-amplification process by using a design that concentrates electric fields along the path of the electrons to the terminal anode or cathode (known as the *readout plane*). The readout plane in GEMs is the terminal anode, which collects electrons after they have undergone gas amplification. The gas amplification factor in GEMs, for example, is designed to safely reach values as high as 8000 over three main amplification stages under SBS operating conditions[154].

Neutral particles are also detectable, but generally more difficult to do so. For neutrons the detection mechanism is complicated by the fact that excitation interactions in scintillator must first be mediated by nuclear interactions which produce showers of detectable particles. To promote these nuclear interactions, absorbers, or dense (often iron) materials, can be strategically placed in proximity to scintillator. When neutrons penetrate an absorber, they can be absorbed by heavy nuclei or cause spallation, leading to the emission of secondary particles. Spallation occurs when

the incident projectile has enough energy—typically several hundred MeV to a few GeV—to overcome the binding energy of the nucleons in the target nucleus [108, 126]. Upon impact, the kinetic energy of the projectile is transferred to the target nucleus, causing it to become highly excited and, as a result, eject several nucleons and possibly light fragments (like deuterons and alpha particles). Secondary particles from spallation reactions, including charged pions and protons, propagate the shower by further interacting with the absorber material, creating additional particles. This process involves *multiple scattering* and is known as a *hadronic shower* [19][54].

The hadronic shower comprises both charged and neutral particles. As the shower develops, it produces a mixture of particles that can interact with a subsequent detection medium, such as plastic scintillator [108, 105]. The complexity of this process leads to significant energy loss from the initial particle. This loss comes in two central forms: the generation of neutral particles and secondary electromagnetic radiation (such as emission, Cherenkov, and bremsstrahlung) which can pass out of the detector volume without interacting with scintillator; and excitations which result in the increase in the kinetic energy of atoms and molecules. From the former process, some of the energy of the incident particle is not deposited inside the detector volume. This energy is *missing energy*. From the latter process, only *some* of the energy deposited within the detector volume is sampled by scintillators. This fraction of energy sampled to incident particle energy is the *sampling fraction*[19].

Electromagnetic radiation, composed of photons, is similarly neutral in charge. It interacts with matter primarily through three mechanisms, each with its distinct energy dependence and significance — the photoelectric effect, Compton scattering, and pair production.

- **The photoelectric effect** describes the absorption of the energy of a photon by an atom, leading to the ejection of an electron when the photon's energy exceeds the electron's binding energy. This effect is most significant at lower photon energies and in materials with high Z, where it exhibits a strong dependency on the atomic number (Z^3 to Z^4 dependence), decreasing with increasing photon energy [126, 108].

[54] It is worth mentioning that any massive hadron can produce such a shower, including protons.

- **Compton scattering** describes the inelastic scattering of a photon by an electron, resulting in a lower energy photon and an ejected electron. This mechanism is most relevant for photon energies from a few hundred keV to several MeV and is relatively independent of the atomic number of the material, relying instead on electron density [126, 108].
- **Pair production** occurs when the energy of a photon surpasses twice the rest mass of the electron (approximately 1.022 MeV), leading to the creation of an electron-positron pair in the vicinity of a nucleus. This process becomes increasingly probable with higher photon energies and is the dominant interaction mechanism for photons in the several MeV to GeV energy range, with its likelihood rising with the material's atomic number [126, 19].

The absorption of photons in a medium follows an exponential law:

$$I_{ab} = I_0 e^{-\mu \cdot x} \tag{2.7}$$

where I_0 represents the incident photon flux in $\mathrm{cm}^{-2}\ \mathrm{s}^{-1}$, and x is the depth of the media in cm. The linear attenuation coefficient μ, given by [105]:

$$\mu = \mu_{PE} + \mu_C + \mu_{PP} \tag{2.8}$$

This coefficient encompasses the contributions from the photoelectric effect (μ_{PE}), Compton scattering (μ_C), and pair production (μ_{PP}). In all of these processes, photons carrying energy create energetic charged particles which may be detected via scintillators or gas-filled chambers [108, 105, 19].

The mean rate of energy loss (stopping power) for a charged particle in both SBS scintillators and SBS gaseous detectors is given by the *Bethe-Bloch* formula[105]:

$$-\frac{dE}{dx} = Kz^2 \frac{Z}{A} \frac{1}{\beta^2} \left[\frac{1}{2} \ln \frac{2m_e c^2 \beta^2 \gamma^2 T_{\max}}{I^2} - \beta^2 - \frac{\delta(\beta\gamma)}{2} \right] \tag{2.9}$$

Here, $-\frac{dE}{dx}$ represents the energy loss per unit distance, while K is a proportionality constant that

factors in the electron density of the medium. The charge number of the incoming particle is denoted by z, and Z and A represent the atomic number and atomic mass of the medium, respectively. The particle's velocity relative to the speed of light is expressed as β, with the corresponding Lorentz factor given by $\gamma = \frac{1}{\sqrt{1-\beta^2}}$. The maximum kinetic energy transferable to a free electron in a single collision is $T_{\max}$, and I refers to the mean excitation potential of the medium. The term $\delta(\beta\gamma)$ accounts for the density effect, correcting the stopping power for the polarization of the medium at high particle velocities. The Bethe-Bloch formula describes ionization losses, which are dominant at lower energies and for heavy charged particles [108, 105].[55]

For highly relativistic electrons, however, the dominant energy loss mechanism is bremsstrahlung. Bremsstrahlung losses occur when a high-energy electron is decelerated in the electric field of a nucleus, emitting radiation in the process. The rate of energy loss due to bremsstrahlung is given by:

$$-\frac{dE}{dx} \approx \frac{E}{X_0} \tag{2.10}$$

where X_0 is the *radiation length*, a material constant that characterizes the distance over which a high-energy electron loses a significant portion $(1/e)$ of its energy through bremsstrahlung [126]. With this definition, the Molière radius (R_M) describes the lateral spatial distribution of secondary particles generated by electromagnetic showers in the material. For complex materials, the Molière radius is defined thus[126]:

$$\frac{1}{R_M} = \frac{1}{E_s}\sum_j \frac{w_j E_{cj}}{X_j} \tag{2.11}$$

Here E_s is the scale energy, approximately 21 MeV, which is a characteristic of these media. The variables w_j, E_{cj}, and X_j represent the weight fraction, the critical energy, and the radiation length of the j-th element in the material, respectively. The sum is over all elements present in the material, accounting for their individual contributions to the electromagnetic shower development. The critical energy E_{cj} refers to the energy at which the losses due to ionization and bremsstrahlung are equal for the j-th element, and the radiation length X_j is the distance over which a high-energy

[55] See Appendix A for a detailed breakdown of these variables.

electron loses a significant portion $(1/e)$ of its energy through interactions with the j-th element. For uniform media, the equation reduces to[108]:

$$R_M = \frac{E_s}{E_c} X_0 \tag{2.12}$$

This radius is calculable for lead glass and other materials and used to determine the design parameters for calorimeters in SBS[108, 105].

2.6 The Bigbite Spectrometer

The purpose of the electron arm is to measure the position and momentum of scattered electrons. Bigbite is so named due to its large angular and momentum acceptance for scattered electrons. With precision e' position over several planes and precise e' momentum per event, e' tracks can be reconstructed back to the target vertex position in the target from analysis of many possible combinations of hits across tracking subsystems in Bigbite. To accurately reconstruct particle tracks, an optics model must be calculated for each kinematic setting, sensitive to the position of the Bigbite spectrometer, particularly its distance to the target. This model follows the JLab Hall A/C convention, adopting an independent *transport* coordinate system for each spectrometer arm and an independent vertex coordinate system for the target. After proper calibration using a sieve plate, the optics model calculates event coordinates in the vertex system from those measured in the focal plane system. In this system, the focal plane is defined at the beginning of the first GEM layer for the Bigbite spectrometer. The transport coordinate convention is consistent across all subsystems, with the fixed origin for each subsystem located on the face of each detector element.[56]

After selection of the most probable track by event, the track provides the means to calculate kinematical quantities for scattered electrons in Bigbite. From these quantities, like track momentum and e' vector components, constraints on quasi-elastic protons and neutrons can be placed and the scattered nucleon expected position can be determined. With these quantities, one can also

[56] e.g., for the BBCal preshower plane, $\hat{z}ps = 0$ is on the face of the calorimeter, and $\hat{x}ps$ points towards the floor in hall coordinates.

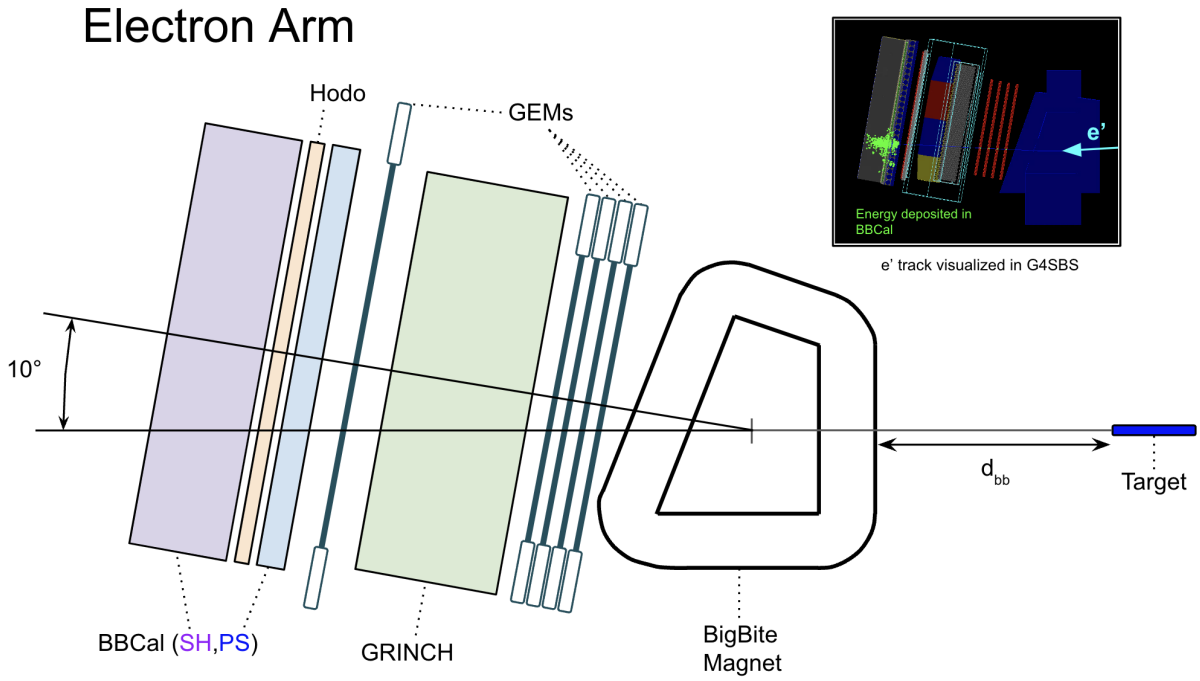

Figure 30: The Bigbite Spectrometer with electron detection event. Visualized in SBS Geant4 (G4SBS).

select elastic events (via LH2) and quasi-elastic events (via LD2) in the hadron arm (Section E).

2.6.1 Bigbite Magnet

The Bigbite magnet bends charged particles into different dispersive trajectories to enable momentum selections on scattered electrons in the Bigbite spectrometer. The Bigbite electromagnet is a dipole capable of 0.9 T·m field integral, which was run at 100% field (750 A) for all kinematics. Behind the magnet, the Bigbite detector stack is positioned with a 10% grade relative to the field (and lab frame horizontal) close to the target to optimize the acceptance (designed to a provide solid angle aperture up to 75 msr) for quasi-elastic electrons across their momentum spectrum.

2.6.2 Gas Electron Multipliers

GEMs are charged particle tracking detectors which consist of several polymer foils with a high density of small perforations (order tens of μm in diameter). These foils are made of copper-

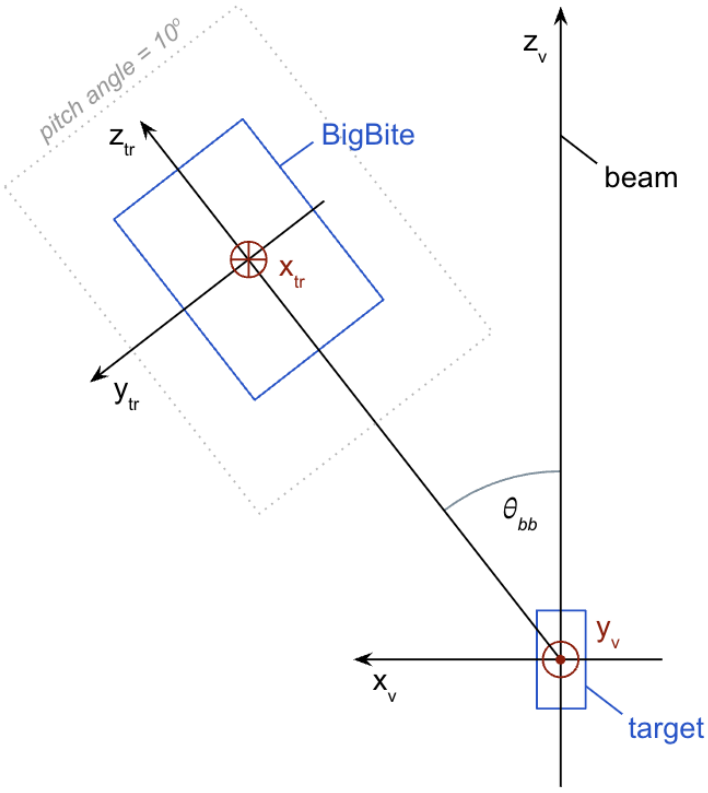

Figure 31: Vertex (or "hall", denoted here with subscript "v") coordinates and transport (or "spectrometer", denoted here with subscript "tr") coordinates. The transport coordinates follow the Bigbite's central ray, rotated with the same 10° angle as the detector stack (see figure 30). θ_{bb} is the Bigbite angle with respect to the downstream beamline.

polyimide-copper sandwiches and are separated by a few mm, forming cells. Each cell is filled with 75%/25% Argon/CO_2 which is placed under a strong potential between the anode and cathode (each copper layer describing the cell, at roughly 4 kV)[24, 154, 82].

When a charged particle passes through the detector, it ionizes many molecules of the heavy gas mixture, producing free electrons which undergo a Townsend avalanche, producing many additional ionized electrons. The concentrated fields within the perforations of the GEM foils allow the free passage of electrons and promote additional ionization in the gas. After passage through several cells defined by three foils, each foil providing a gain factor of 20, the avalanche electrons reach the readout plane.

At the readout plane, the avalanche electrons induce signals on the strips. These strips are

conductive traces on the readout plane and are responsible for detecting the induced charge. The signal from these strips is then read out by APVs (many-channel analog-to-digital converters), which convert the analog signals into digital data for further analysis. The relatively heavy noble gas Argon provides for the primary ionization, while CO_2 is included to stabilize the avalanche process. Figure 32 depicts one such event on a single GEM[24].

Via COMPASS results, GEMs are capable at event rates as high as 25 kHz/mm^2. By design, the expected position resolution for each GEM is 70 μm. In principle, they are designed to handle the very high luminosities that CEBAF is capable of[24].

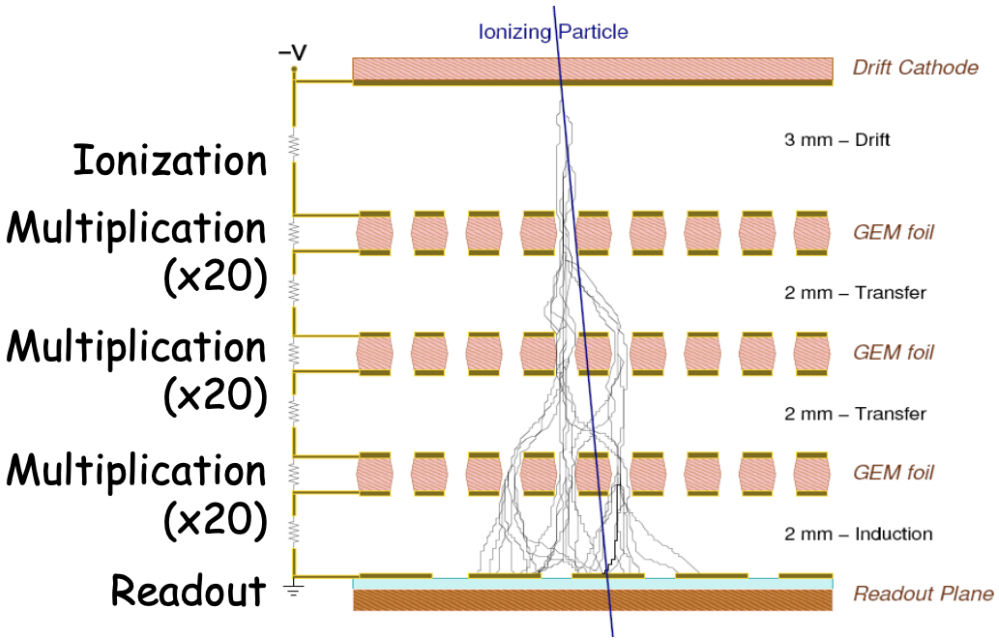

Figure 32: Slice of one GEM depicting ionization event with SBS standard three foil construction. Depiction of gem foils and geometry from [154].

In SBS, GEMs were developed by the University of Virginia (UVA) and Istituto Nazionale di Fisica Nucleare (INFN). SBS GEMs contain strips oriented either $\pm$ 30° (u/v, figure 33) or 90°/0° (x/y) with respect to the transverse direction. With hits on more than one strip, the precise location of a MIP passing through the plane of a GEM can be determined. These strips cover an active area of 40 x 150 cm^2 with very high segmentation (roughly 42k readout channels). On each signal over threshold at the readout plane, a single strip reads out to an APV for amplification and pulse shaping and then to an MPD for digitizing[24].

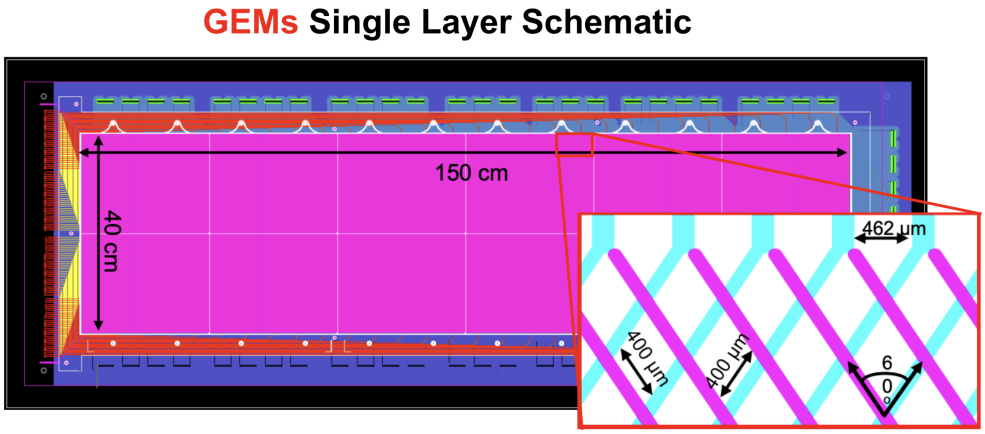

Figure 33: Active area of a UVA GEM with u/v strip layout. Image adapted from [83].

The dense segmentation in the GEMs leads to very high rates, which can pose challenges for data acquisition and track reconstruction. To improve efficiency, it is essential to handle the GEM pedestal data accurately and apply common-mode corrections.

In the context of GEM detectors, the ”pedestal” refers to a constant offset unique to each channel (physical readout strip connected to an APV). The GEM pedestal data, acquired through dedicated runs typically without beam and with full readout, is used to determine the mean value of this constant offset and the RMS deviation from the mean (random noise). These runs allow for precise calibration of each channel.

During online data processing, the pedestal values are automatically subtracted from all the APV samples before any other processing steps. This ensures that the constant offsets are removed, enabling accurate signal measurement. Each sample is measured in ADC counts and has a specific width in nanoseconds, determined by the sampling rate of the APV.

Following the pedestal subtraction, common-mode corrections are applied. Common-mode noise refers to the correlated fluctuations in the baseline signal that affect multiple channels similarly. By assessing these fluctuations across all channels of an APV, a correction factor is calculated and applied to each sample to mitigate this effect. Figure 35 illustrates the common-mode offsets before and after corrections. After applying these corrections, the pedestal-subtracted and common-mode-corrected signals can then be processed further.

The APVs digitize the analog signals from the GEM strips. These digitized signals are then sent to a MPD (Multi-Purpose Digitizer), which further processes the data. The combination of APV and MPD functions as an ADC (Analog-to-Digital Converter), converting the analog signals from the GEM strips into digital data that can be analyzed[154].

This online zero suppression, which rejects signals below a certain threshold set by the pedestal, can be enforced in the crate before data reaches the ROC (Read-Out Controller), ensuring that only significant signals are recorded and processed.

The GEMs' primary utility is for e' track reconstruction. On any given trigger, the GEM window contains 6 samples, each 24 ns apart. Within this time window, many strips may, and often do, read over the threshold on every layer.

After zero suppression, 1D clustering is performed: each strip that fires (i.e., has a signal over the threshold) is checked for neighboring fired strips that are consistent in time with the central maximum ADC value[57]. Next, 2D hit associations are formed by combining 1D clusters from each of the two non-parallel readout strip directions. These 2D hits are further filtered based on ADC/time correlations and other quality parameters.

The track-finding algorithm then proceeds by forming all possible 2D hit combinations from 1D clustering results, consistent with the active area and external detector constraints. Each tracking layer is divided into a 2D uniform rectangular grid. Hits are looped over in the front layer, forming straight lines to a back constraint point, typically a calorimeter cluster. An error matrix, calculated from grid bin and back constraint widths, defines the region of interest in the back layer. This significantly reduces combinatorial complexity.

For each allowed combination of grid bins in the front and back layers, straight-line projections are made to all intermediate layers. For each allowed combination of grid bins in the front and back layers, straight-line projections are made to all intermediate layers. Hits that fall within a certain edge tolerance of neighboring bins are also considered. This ensures that hits near the boundaries of bins are included in the track reconstruction process, improving the efficiency of identifying

[57] Additional details exist which account for overlapping peaks in 1D clusters. See [142].

the correct particle tracks. The best chi-squared per degree of freedom for a straight-line fit in 3D is found, considering timing, ADC correlation, and other hit quality metrics. This process starts by requiring hits in all N layers, then $N-1$, $N-2$, down to a minimum of 3 hits, treating all combinations of layers equally in each iteration.

Gain matching across APV channels ensures that signals are consistent across different channels, improving tracking efficiency. As indicated, a constraint region, determined from the Bigbite calorimeter and target vertex projection, provides additional handles on reducing combinatorics before tracks are calculated[183][142].

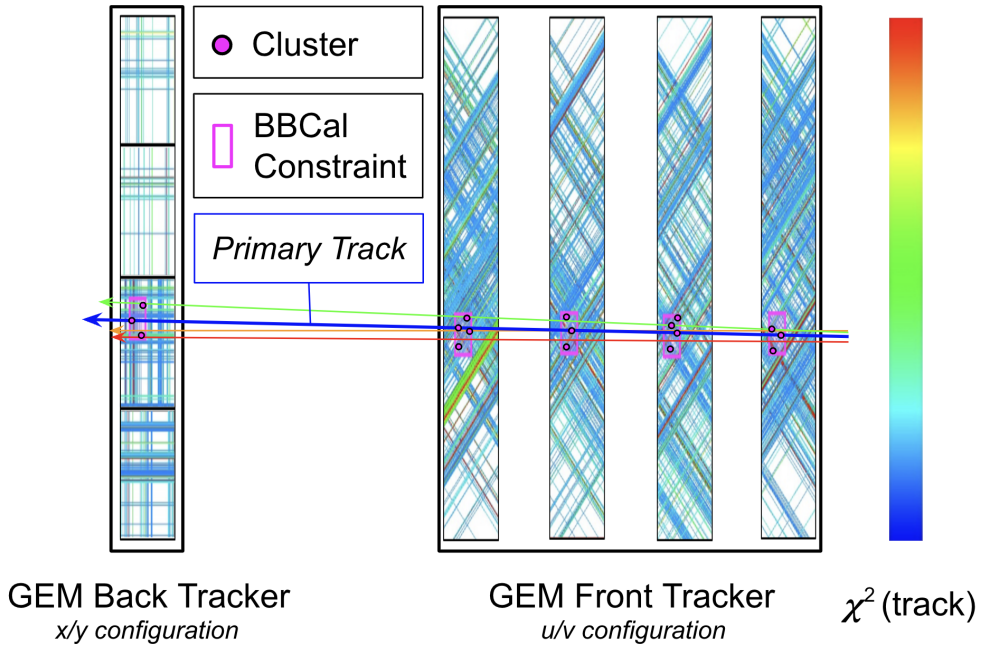

Figure 34: Bigbite stack with GRINCH, Hodoscope, and BBCal omitted. Tracks minimize χ^2 for straight line tracks from the calorimeter constraint, through surviving clusters, and back to the vertex position in the target. Optics parameters account for the effects of the Bigbite magnetic field. Placement not to scale. Adapted from [137].

Due to the high segmentation and rates in the GEMs, concerns about digital crosstalk and signal pileup were investigated during **GMn**. Signal pileup can occur on single APV channels where multiple hits are measured together. The resulting APV sum can result in tracking efficiency losses. Time deconvolution techniques were developed and investigated during data reconstruction to enhance signal reconstruction per event. However, they were ultimately found to be ineffective

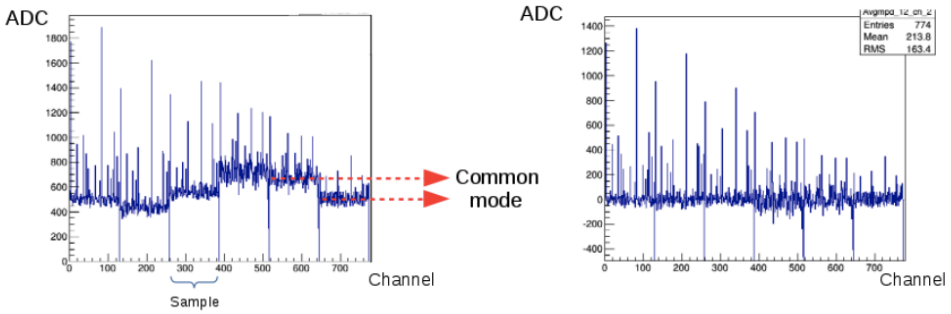

Figure 35: Plots depicting APV samples before(after) common mode corrections on the left(right). Plot from [70].

for improving performance in **GMn** and were therefore not used[147]. Digital crosstalk arises from a mismatch between timing and signal routing and results in APV signals from adjacent channels erroneously counted together. Digital crosstalk can give rise to spurious signals in GEM layers and false tracks. While methods were developed to reduce digital crosstalk occurrences, these occurrences were ultimately determined to have negligible impact on quasielastic yields after track selection and these methods were not implemented for **GMn** data reconstruction[25].

2.6.3 The Bigbite Calorimeter

The Bigbite Calorimeter is a lead glass electromagnetic calorimeter designed to measure the energy of charged particles moving through it primarily via the process of Cherenkov radiation. It is divided into two planes, the preshower (PS) and shower (SH), with e' tracks first encountering the PS and then the SH as they pass through the detector stack. The PS has 52 lead glass blocks, stacked in a 26 row by 2 column grid with their long dimension perpendicular to the central Bigbite ray. Each PS block is 9 x 9 x 29.5 cm. The SH has 189 lead glass blocks, stacked in a 27 row by 7 column grid with the long dimension oriented longitudinal with the central Bigbite ray. Each SH block is 8.5 x 8.5 x 34 cm. Each of these blocks in both the PS and SH is coupled to a photomultiplier tube (PMT) whose analog signals are made into two copies. One copy is sent to fADCs located in the DAQ bunker and the other processed in the *front-end* electronics (FE) where the Bigbite trigger is formed and sent to the DAQ bunker. Each of the lead glass blocks were

designed such that electromagnetic showers are contained within two rows of the PS and a 3 x 3 block section of the SH (each section $\approx 3\ R_M$). Figure 36 depicts the calorimeter in the detector stack[17, 171].

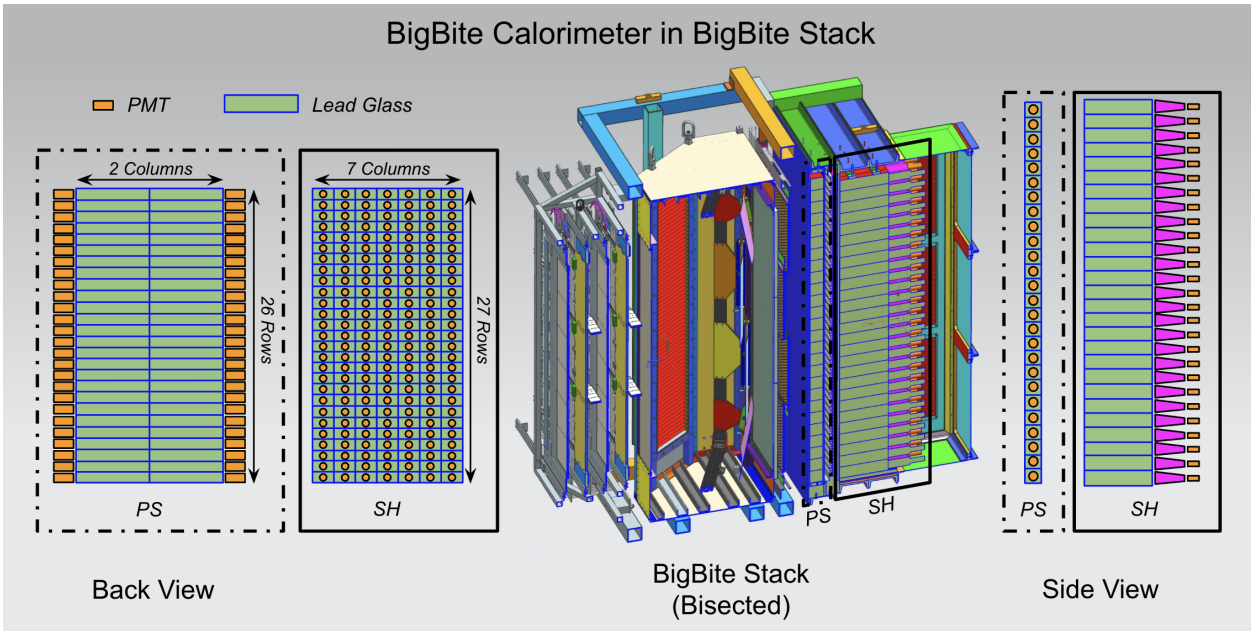

Figure 36: BBCal situated in the Bigbite stack. The shower (SH) and preshower (PS) planes are shown. Exploded view not to scale.

The primary purpose of BBCal is to absorb and measure the total energy of electrons. Via cuts on the energy deposited in the PS, pions can be rejected during analysis. The energy resolution of BBCal is given by:

$$\text{Energy Resolution} = \frac{\sigma_E}{E} = \frac{a}{\sqrt{E}} \oplus b \oplus \frac{c}{E} \tag{2.13}$$

Here a, b, and c are constants, E is the energy in GeV, and $\oplus$ denotes a quadrature sum. Within the sum, a/$\sqrt{E}$ represents the stochastic term related to statistical fluctuations in the particle shower development, b is the constant term related to systematics and calibration errors, and c/E represents the noise term, including electronics and readout noise. Typically for electromagnetic calorimeters, the stochastic term tends to dominate the others[85]. BBCal is designed to operate with energy resolution $\sigma_E/E \approx 6\%$[39].

Analog sums over these blocks (PS and SH) which pass threshold constitute the main single-

arm trigger for the experiment. This threshold is remotely configurable and tuned to ensure that the trigger is efficient for the events of interest (elastic and quasi-elastically scattered electrons) while also maintaining an event trigger rate that does not significantly reduce the live time of the data acquisition (DAQ).[58]

2.6.4 The Gas Ring Imaging Cherenkov Detector

GRINCH is designed to provide offline particle identification (PID), specifically for pion rejection. It consists of a 88.9 cm deep tank filled with heavy gas containing four cylindrical mirrors. As charged particles pass into the heavy gas (C_4F_8 is the heavy gas deployed for the GRINCH), they emit Cherenkov light which these mirrors focus onto an array of 510 PMTs arranged in a honeycomb pattern. Each of these PMT signals is processed by a front end (FE) NINO card imposing an analog threshold. For PMTs with signals above threshold, the NINO card generates a logic pulse with a width of 10 ns, which is read out by a dedicated VETROC TDC channel recording leading edge (LE), trailing edge (TE), and time-over-threshold (TOT) information[65].

Figure 37 depicts an electron emitting Cherenkov radiation. When the electron passes into the GRINCH volume, it begins emitting cones of Cherenkov light consistent with the expression:

$$\cos\theta_c = \frac{c}{nv} \tag{2.14}$$

Here θ_c is cherenkov propagation angle, n is the index of refraction for the heavy gas, and v is the velocity of the electron. Scattering from the target at SBS Q^2 values produces many negatively charged pions projected into the acceptance of the electron arm with momenta similar to that of quasielastic electrons.[59] However, due to their larger mass, pions with similar momenta are moving with less velocity than quasielastic electrons. Since the cone angle θ_c depends only on the velocity, selection of sufficiently large clusters from GRINCH provides electron selection and pion rejection.

[58] The DAQ event rate limit during **GMn** was 5 kHz.

[59] The Bigbite magnet bends most π^+ below the detector stack, but many π^- continue into the acceptance.

Operation of GRINCH in SBS is best characterized as a threshold Cherenkov. The threshold for pions to produce signals in GRINCH (p_{th}) is given by:

$$p_{th} = \frac{m_\pi}{n^2 - 1}, \tag{2.15}$$

where m_π is the mass of the pion and n is the refractive index of the gas in the chamber. Calculation of this threshold for C_4F_8 leads to the GRINCH pion thresholds:

$$p_{th} \approx 2.72 \quad \text{GeV} \quad (\pi^+ \text{ and } \pi^-), \tag{2.16}$$

above which pions will begin creating signals in the GRINCH[60].

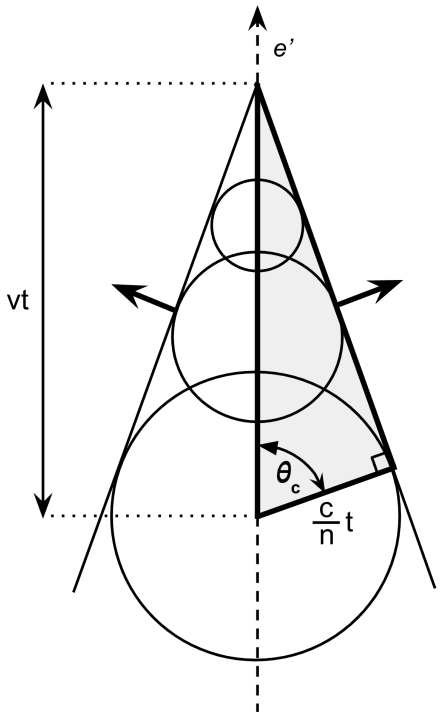

Figure 37: Schematic of Cherenkov light propagation in a medium with index of refraction n. θ_c is the Cherenkov propagation angle, e' is a scattered electron, v is the electron's velocity, t is a reference time, and c is the speed of light.

The segmentation of GRINCH also opens the door to additional tracking assistance in offline analysis where primary cluster positions in GRINCH can be matched with tracks as they pass through the GRINCH acceptance to reject accidentals[153][61]. Inversely, selecting the primary cluster with a track matched requirement improves the PID capabilities of the detector[62]. That said, heavy gas was not introduced to GRINCH until the later in the run group (SBS-8, SBS-9, and part of SBS-14), before which the chamber was filled with CO_2. This sub-optimal state of the GRINCH chamber limits the effectiveness of the detector in the early kinematics. Consequently, analysis of earlier kinematics contained in this thesis uses GRINCH variables only for SBS-8 and SBS-9. Figure 38 depicts the detector.

[60] For C_4F_8, n=1.00132 and the mass of the charged pion m_{π^+,π^-}=139.6 MeV.

[61] In practice, a GRINCH constraint on tracking is not applied, but could be in principle.

[62] Selection of GRINCH clusters with tracking information is active in reconstruction for GMn where applicable[155].

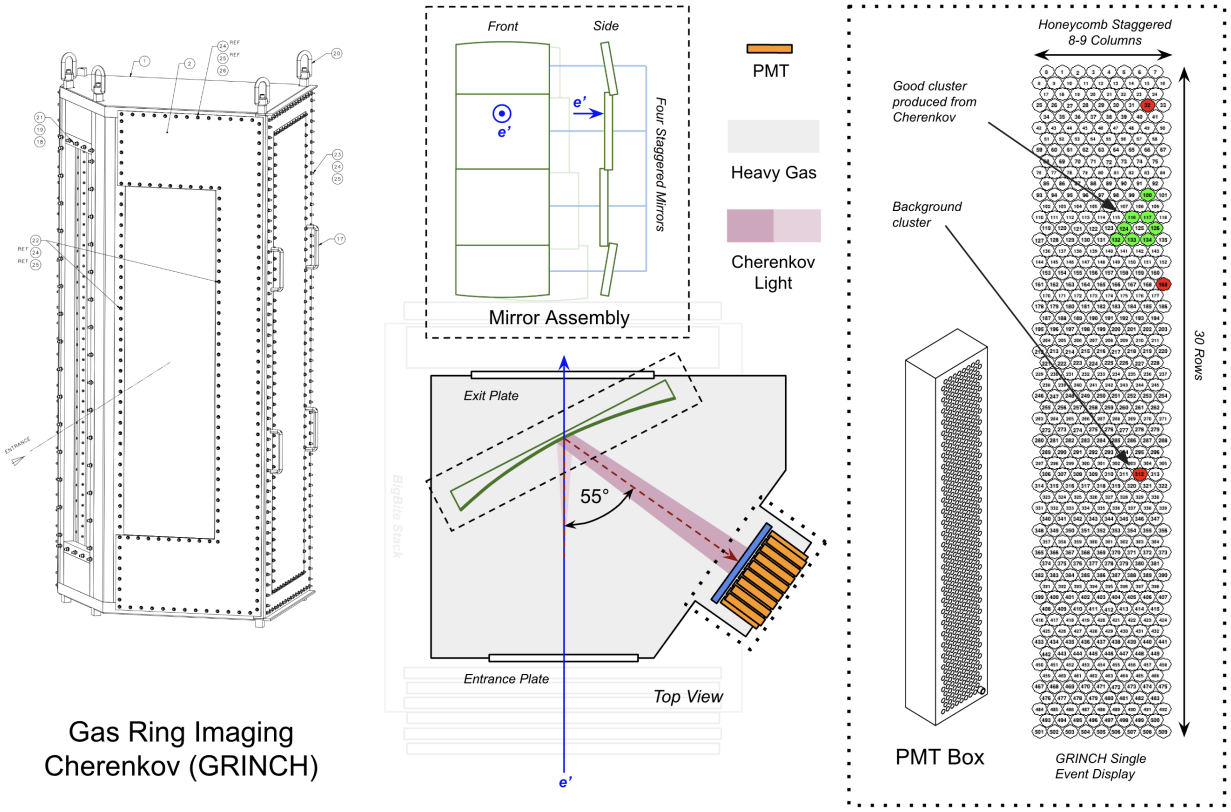

Figure 38: The GRINCH. The design is optimized to reject pions within the momentum range of scattered electrons accepted in Bigbite via Cherenkov light.

2.6.5 The Timing Hodoscope

The hodoscope consists of 89 scintillator bars arranged perpendicular to the dispersive direction in the Bigbite stack and read out by a PMT on each end (178 total channels). Each of these PMTs is read out by a CAEN 1190 Time to Digital Converter (*TDC*) which records leading edge (*LE*) and trailing edge (*TE*) timing information. The hodoscope FE has a similar setup as the GRINCH, where analog signals from PMTs are processed by NINO cards which apply an analog threshold for good hits before sending signals to TDC channels. Due to the high timing precision, the hodoscope is intended to provide event reference time for timing signals used in other detectors, especially the HCal and its associated time of flight (*TOF*) measurement for scattered elastic and quasielastic nucleons.

With accelerator RF corrections, timing resolution of 200 *ps* is expected[93]. While the seg-

mentation of the hodoscope is low relative to the GEMs in the Bigbite stack, it can provide additional position constraints on good e' tracks in the electron arm. Dispersive (vertical) position information is made available by this segmentation. The time difference between signals in both PMTs attached to the same bar along with parameterization of the bar's light propagation speed allows for the unambiguous determination of the transverse (horizontal) position. This requires sufficient in-beam calibrations made by matching hit positions with electron track position information primarily from the GEMs.

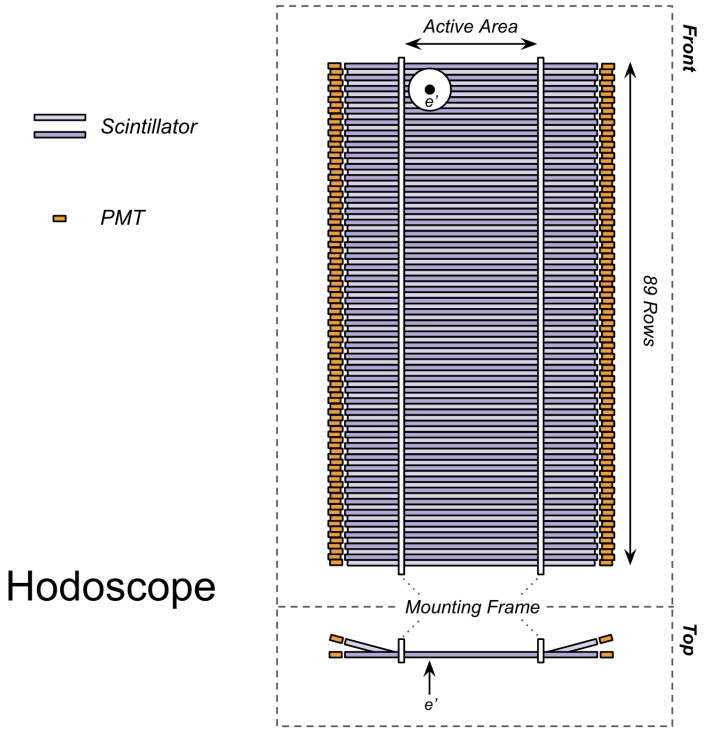

Figure 39: The timing hodoscope consisting of 89 organic plastic scintillator bars mounted perpendicular and transverse to the e' central ray with PMTs on each end.

2.7 The Hadron Arm

The hadron arm consists of the SBS magnet and HCal and detects recoil elastic and quasielastic nucleons. With e' track information from the Bigbite spectrometer, the q-vector for recoil nucleons can be obtained and applied to compare with cluster position information on HCal. This compar-

ison is ultimately used to measure quasielastic $e-p$ and $e-n$ nucleons. Without detection of the spectator nucleon in $d(e,e'n)p$ and $d(e,e'p)n$ events, separation of protons and neutrons in the SBS magnetic field is necessary.

2.7.1 SBS Magnet

The SBS dipole magnet operates at a maximum of 2100 A producing a 1.6 T·m magnetic field integral. This magnetic field bends the trajectory of scattered quasielastic protons from LD2 and elastic protons from LH2 and provides the only means of separating scattered neutrons and protons. The field volume accommodates and matches the full acceptance of HCal and effectively sweeps charged background particles of energy < 1.3 GeV out of the acceptance across all kinematics, with better rejection at higher field strength[65].

2.7.2 Hadron Calorimeter

The Hadron Calorimeter (HCal) is positioned in line with the SBS magnet following the central ray of quasielastic nucleons from the target. It is designed to resolve the positions, energies, and timing from these scattered protons and neutrons. Since HCal is the subsystem focus in this work, details are included in a dedicated chapter (chapter 3).

2.8 Trigger and DAQ

Data acquisition in SBS is a complex, multiple-step process which begins with the trigger, proceeds to signal acquisition at the many digitizing converters, continues through data collection and real-time processing, goes to storage of these data on tape, and proceeds to decoding and reconstruction. Figure 40 depicts this workflow.

Due to the high rate of scattering from the target chamber producing signals in all detectors, data collection must be restricted to a subset of signals which are more likely to correspond to quasielastic events. In addition to the design and configuration of the spectrometers to optimize the acceptance for quasielastic particles, an analog trigger is employed such that outside of a trigger

window, data is not collected. For the **GMn** run group, this trigger is the BBCal sum over threshold trigger.

Due to the separation of the PS and SH in space and accounting for the mismatch in row dimensions between the SH and PS, an overlapping regions map which maps 2 row PS cluster regions to 2 row SH cluster regions is made[63]. From this map, an analog sum over possible sum cluster regions is implemented at the FE where signals that pass a tuned threshold constitute the main trigger for the DAQ. This threshold is determined per experimental configuration to optimize GEM performance and DAQ livetime. Figure 41 shows this map.

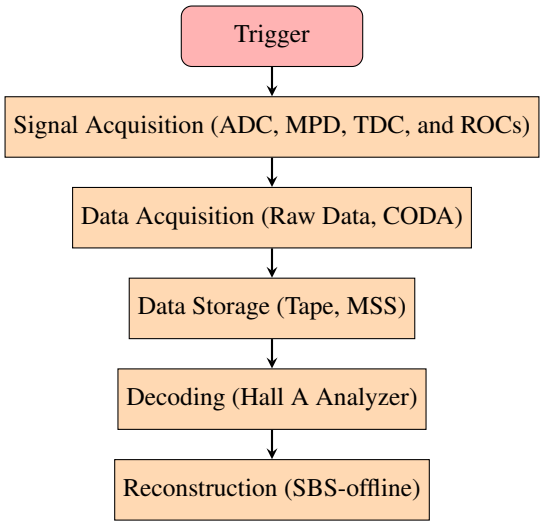

Figure 40: Workflow of data processing in SBS. Systems involved in each process are included in parentheses.

All analog signals in the PS and SH are continuously summed and sent to the discriminators "BBCAL LOW" and "BBCAL HIGH" where they are checked against a remotely configurable threshold value to register a trigger. After the trigger signal is sent from the FE to the *trigger interface* (TI) at the DAQ bunker, a signal is sent from an integrated *trigger supervisor* (TS) to the many crates which hold fADCs, TDCs, and MPDs across all subsystems[64]. This begins data collection within time windows and latencies configurable by crate.[65] This setup, along with judicious remote setting of the trigger threshold at the FE, allows for a drastic reduction of DAQ rates.[66] Figure 42 shows the front-end configuration of the trigger signal flow where "BBCAL HIGH" (indicating a

[63]Sometimes 2 row PS cluster regions are mapped to 3 row SH cluster regions to account for the segmentation geometry.

[64]These fADCs, TDCs, and MPDs, were located in the DAQ bunker for all electronics except the MPDs, which were located in a small shielding bunker near Bigbite.

[65]For example, a fADC window could be configured to be 160 ns wide with a latency of 100 ns for one channel. This configuration would be done with FE processing time, cable lengths and material compositions, and signal delays accounted for.

[66]For the highest Q^2 kinematics, the un-discriminated background rate from detectors was sometimes several hundreds of MHz.

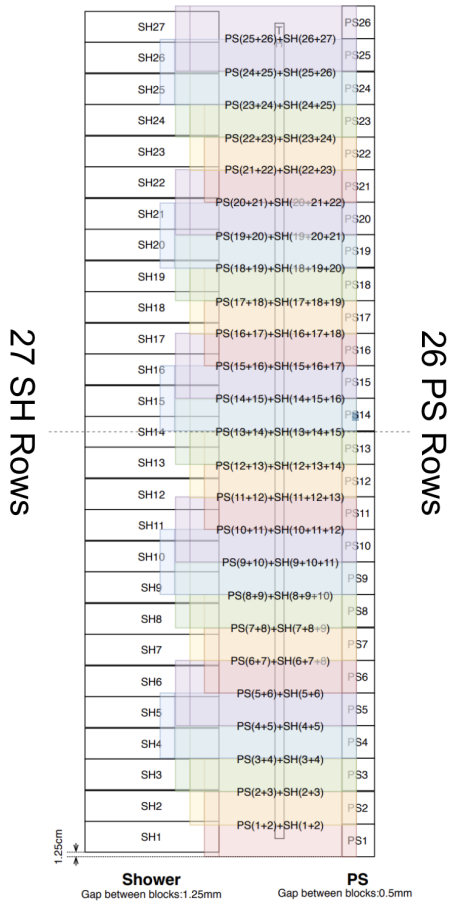

Figure 41: BBCal SH/PS trigger groups. Each of the colored boxes indicates the overlap from row regions in PS to SH to account for the difference in segmentation geometry between them. Image adapted from [17].

higher threshold) was used for in-beam data collection.

In practice, many trigger signals are input to the TS which makes any combination of them available to begin data collection. These available triggers are configurable in the *counting house* (a control room where the experiment is administered, monitored, and data is quality checked) with *prescales*, where each prescale value PS_N cuts the rate written by the DAQ by a factor given by[90]:

$$\text{Prescale Factor} = \frac{1}{2^{PS_N - 1} + 1} \tag{2.17}$$

A PS_N of -1 corresponds to disabling the trigger and a PS_N of 0 corresponds to no data reduction by the DAQ. Each event written corresponds to a trigger source, written into the data by a ded-

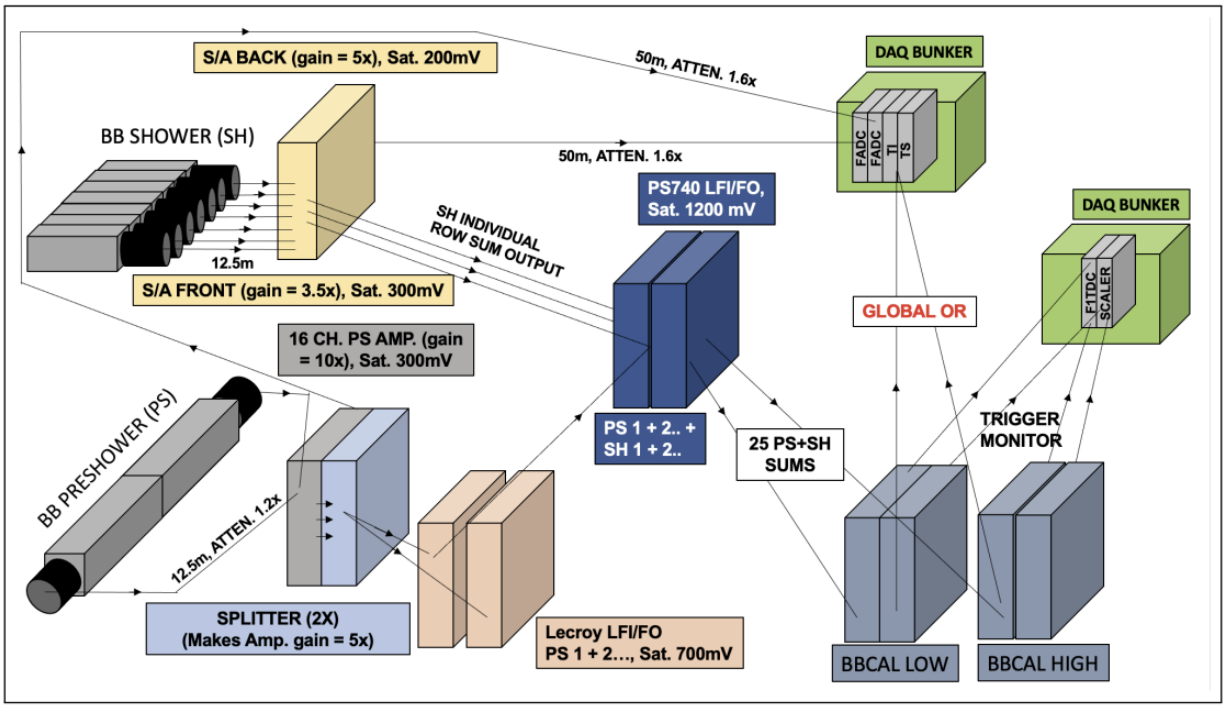

Figure 42: BBCal to FE to DAQ bunker signal flow diagram[42].

icated TDC. Table 12 gives a list of all triggers available during the experimental run and their correspondence to the TDC channel they were on, both in hardware and eventually written to the output data tree.

Signal	TDC Channel #
HCal	0
BBCal Lo	1
BBCal Lo vetoed by BBCal Hi	2
EDTM Pulser	3
RF Time	4
BBCal Hi (main)	5

Table 12: Trigger TDC Channels and Contents

Restricting the data rate to the DAQ is critical to reduce DAQ dead time. This occurs when the data acquisition software cannot process data fast enough to manage the data sent to it (the *datastream*). This dead time is monitored by comparing incoming triggers to accepted triggers in CODA. In order to monitor the electronic deadtime rate, a signal is injected into the datastream. This signal comes from a configurable pulser called the *Electronic Dead Time Monitor* (EDTM)

pulser. By comparing the total number of events sent by the pulser to the total number of events written by the DAQ, the electronic dead time can be evaluated. For the **GMn** run group, the EDTM pulser was set to 20 Hz and included in data collection with the primary trigger (BBCal Hi). To monitor the subsystem rates directly in the counting house, a parallel analog to digital system consisting of scaler electronics was also available. Scaler events are inserted into the datastream and made available to encoding during the experiment. These data are available on the *scaler tree* in output data files after data reconstruction. For the SBS DAQ, 5 kHz is the maximum data rate set by the bandwidth limitations of the MPD pipeline.

Data acquisition, including trigger type via prescale, is controlled with *CEBAF Online Data Acquisition*, or CODA. The TS determines the written data format based on the trigger type. This format encodes all digitized data from all sources available on a trigger in terms of a data structure consisting of an array of 32-bit words (EVIO format)[56]. This structure begins with a "header" which categorizes the remaining words. The rest of the structure encodes the raw data. The data structure includes metadata such as run number, trigger information, event type, etc. It also includes the raw data via access to the various crates holding ADC, TDCs, and MPDs — the *Read-Out Controllers* (or ROCs)[34].

Data from systems not included in the TS, or in the SBS spectrometer by extension, is managed and recorded using the *Experimental Physics and Industrial Control System* (EPICS). By polling several Input/Output Controllers (IOCs) which monitor critical systems on average once per two seconds, these values can be monitored in the counting house and optionally sent into the datastream for record. These critical systems are myriad and include HV settings for all subsystems, but among them BCM data was put into the datastream and made available for encoding by CODA[34].

2.8.1 Threshold and SBS Field Effects

Due to the influence of the strong SBS fringe field on BBCal PMTs, it was observed that gain matching and BBCal high voltage changes were necessary to remove bias in the trigger. With-

out these operations, sections of the acceptance artificially produce more events than others and quasielastic events may fail to be recorded. Between GMn kinematics, often during beam steering operations, cosmic runs were taken with the BBCal trigger and magnets on to gain match across PMTs and optimize high voltage settings prior to production data collection. The main advantage of using cosmic data for this purpose is that high-energy cosmic rays are relatively unaffected by the SBS and Bigbite magnetic fields. Additionally, cosmic rays are always available and do not require running the CEBAF to collect data, which makes them efficient for initial calibration. Cosmic rays also populate all channels of BBCal and have MIP-like energy deposits, allowing for the estimation of energy deposit without the benefit of PID cuts and prior to having a good initial calibration. These steps prevent both trigger bias and PMT saturation. Table 13 gives the threshold conversion factors derived from each high voltage setting across kinematics in GMn[67].

Table 13: e' Trigger Parameters

Kinematic	Q^2 **(GeV^2)**	$E_{e'}$ **(GeV)**	$E_{e'}$ **Range (GeV) Low/High**	Th_{CF} **(mV/MeV)**	Th **Range (mV) Low/High**
4	3.0	2.12	1.88/2.39	0.28	-425/-500
9	4.5	1.63	1.43/1.86	0.35	-428/-609
8	4.5	3.58	3.09/4.14	0.14	-405/-478
14	7.4	2.00	1.75/2.31	0.28	-500/-525
7	9.9	2.66	2.27/3.15	0.21	-380/-450
11	13.6	2.67	2.29/3.25	0.21	-400/-480

Table 14: e' trigger parameters where the Q^2 and $E_{e'}$ are the central values. The conversion factor for use with remote threshold controls derived from the updated HV settings is Th_{CF}. $E_{e'}$ range is bounded by the BBCal row and expected quasielastic electron energy expected there. The threshold range Th is bounded by the lowest value and highest value used during the kinematic. For all settings, the most common setting is on the high end[43].

2.9 Geant4, SIMC, and G4SBS

In order to understand the complex impacts that various materials and physical processes have on collected data, to design and plan for expected results, and ultimately to benchmark key physical

[67]Ensuring that Bigbite and SBS magnets were on for these gain matching procedures accounted for the noticeable fringe field effects from these magnets on BBCal PMTs. Due to the increased distance between Bigbite and SBS magnets and HCal, no *in situ* gain matching was necessary for HCal.

observables, G4SBS simulations were used. G4SBS first includes a set of particle generators which produce events from a target vertex position with physical parameters defined via repeated random sampling (Monte Carlo methods where physical limits are configurable). After a single particle generator is chosen and event generation limits are configured, all produced radiation is tracked through a configurable and accurate model of SBS (including geometry and material properties) utilizing the Geant4 framework. Each SBS model corresponds to a single configuration including the placement of the spectrometer arms (see 6). Each model may also be configured with many other options including the target type, SBS and Bigbite magnet field settings, sieve plate and photon shield settings, beam current, etc.

Geant4 is a toolkit for simulating the passage of particles through matter using Monte Carlo methods. These methods provide a statistical approach to tracing the history of a large number and variety of particles as they interact with matter, capturing complex processes in a detailed and probabilistic manner [73, 74]. Geant4 includes an extensive repository of physics models and interaction cross sections, covering a broad energy range from eV to TeV[69, 74]. This makes it highly suitable for simulating a wide array of physical phenomena, including the quasielastic events in experiments like the Super Bigbite Spectrometer (SBS) at Jefferson Lab. Geant4 is adequate for modeling the passage of nucleons through matter, with reliable physics models down to thermal energies (approximately 0.025 eV), ensuring accurate proton and neutron transport and interaction simulations [46, 69]. G4SBS uses several Geant4 physics lists to track radiation through detectors.

- **G4DecayPhysics**: Handles the decay processes of particles, including beta decay, muon decay, and hadron decays [67].
- **G4EmStandardPhysics**: Standard electromagnetic physics processes such as ionization, bremsstrahlung, Compton scattering, photoelectric effect, and pair production [68].
- **G4EmExtraPhysics**: Includes additional electromagnetic processes like synchrotron radiation, gamma conversion to muons, and the generation of optical photons [69].
- **G4HadronElasticPhysics**: Deals with elastic scattering processes for hadrons, providing

models and cross-sections for the elastic scattering of protons, neutrons, and other hadrons [67].

- **G4IonPhysics**: Manages physics processes related to ions, including ion-ion interactions and ionization in various materials [67].
- **G4NeutronTrackingCut**: Applies tracking cuts specifically for neutrons to limit their tracking below certain energy thresholds, enhancing simulation performance [67].
- **G4HadronPhysicsFTFP_BERT**: Handles hadronic interactions using the FTFP (Fritiof) and Bertini cascade models, covering a wide energy range [67].
- **G4StoppingPhysics**: Manages stopping processes of particles, particularly the capture of stopped muons and pions, including the processes occurring when these particles come to rest [67].
- **G4OpticalPhysics**: Includes processes related to optical photons, such as scintillation, Cerenkov radiation, absorption, Rayleigh scattering, and boundary processes [67].
- **G4StepLimiterPhysics**: Imposes a limit on the step size of particles during tracking to ensure accuracy, especially in regions with high gradients of fields or material properties [67].

There are many event generators to choose from in G4SBS. Among them, the proton gun generator, neutron gun generator, elastic generator, inelastic generator, and the adapted SIMC generator are of particular use in this analysis[68]. The proton and neutron gun generators produce protons or neutrons across a configurable energy range and acceptance. The elastic and inelastic generators produce elastically and inelastically scattered particles (respectively) which result from scattering into a configurable acceptance, target, and beam energy range. The SIMC generator produces quasielastic protons and neutrons from a configurable target and beam energy, like the last two generators, but also includes important added nuclear and radiative effects[65, 165].

SIMC in SBS uses a modified version of the base Hall C software version with the same name. The Hall C SIMC calculates the acceptance functions for Hall C spectrometers for $(e, e'p)$

[68] It is important to note that SIMC is a standalone package used to simulate electron scattering events in both Hall A and Hall C.

reactions, among others, but does not include $(e,e'n)$. By default, SIMC simulates scattered protons from $d(e,ep)$ and $h(e,e'p)$ reactions and accounts for the following[166]:

- Initialization of generation limits. This includes acceptance and energy limits.
- Vertex generation within cryotarget geometry and beam energy generation.
- Generation of $d(e,e'p)$ scattering kinematics including $\theta_{e'}$, θ_p, $\phi_{e'}$, ϕ_p, $p_{e'}$, and p_p with the application of the deuteron spectral function.
- Modification of kinematics with radiative corrections including the generation of hard photons.
- Further modification of kinematics with Coulomb corrections using the *Effective Momentum Approximation* (EMA) which modifies the initial energy and momentum of the electron to account for nuclear effects which occur before the primary scattering event.
- Generation of background processes including the kaon electroproduction and pion production channels.

The updated version adapts the event generation to G4SBS geometry with many changes. Among them[40]:

- Box geometries were added to SIMC to bound the acceptance of produced particles in SIMC.
- An interface was constructed to enable G4SBS to interpret the output of SIMC.
- $(e,e'n)$ reaction was added to the SIMC generator, with masses corrected for the neutron, an updated fit to world data for elastic form factors, the same spectral function as the proton, and radiative corrections applied to the incoming and outgoing electron.[69]
- Creation of updated output tree variables which includes vertex information and the creation of log files which includes generation volume, number of events tried, and luminosity important for normalization during analysis.
- The AV18 deuteron wavefunction model is used to determine the spectral function.

As mentioned, the SIMC event generator addresses two important characteristics of quasielastic scattering. First, Fermi motion is included which accounts for the intrinsic motion of nucle-

[69]The spectral function for $(e,e'p)$ is a good approximation for $(e,e'n)$, as the deuteron is a very weakly bound nucleus. The form factors were updated to the Kelly fit for both protons and neutrons.

ons within the bound deuteron nucleus. The effect of this motion is to smear out measured momenta and positions for scattered electrons and nucleons. Second, radiative corrections including bremsstrahlung and vertex corrections are addressed. Bremsstrahlung occurs due to the proximity of the scattering electron to a nuclear Coulomb field and produces both internal Bremsstrahlung (radiation of a photon due to interaction with nucleus participating in the primary scattering event) and external Bremsstrahlung (radiation of a photon arising from other nuclei). Photons emitted in this way can be real or virtual and modify the interaction cross section for quasielastic events. Vertex corrections are higher order virtual photon effects which modify the interaction vertex in the presence of a nuclear Coulomb field. These effects can modify the effective charge and magnetic moment of scattered particles, affecting the quasielastic cross section. Both must be accounted for in order for MC to accurately model quasielastic scattering in SBS[65].

After the primary scattering event is simulated by SIMC, G4SBS takes over to handle the tracking of final-state particles through the experimental geometry and to simulate the detector response. These interactions are managed using specialized response algorithms and designated detector components that accurately model how the detectors interact with the particles. The SIMC generator is used for all G_M^n and FFR extractions.

The raw G4SBS output does not match the data structure of decoded data. In order to achieve a clean comparison between data and MC, digitization libraries and a reconstruction database which enable the encoding and decoding of MC data were constructed[65]. With this, simulated data which matches experimental data, including any potential effects from decoding and reconstruction of the data, is achieved[65, 155]. Unless otherwise noted, the terms Monte Carlo (MC), simulation, or G4SBS will be used interchangeably and generally refer to the generated, digitized, and reconstructed output of G4SBS and SIMC.

3 The Hadron Calorimeter

The SBS Calorimeter consists of 288 (24 rows by 12 columns) of single energy-sampling modules. Each 15cm x 15cm x 1m module can be referred to as a separate *channel* or *block* and consists of 40 layers of interleaved steel and scintillator. The steel acts as an absorber for incoming hadrons and promotes hadronic showers which deposit energy from a single event potentially into many adjacent modules. The electromagnetic energy contained in these showers is sampled by the interleaved scintillator (PP0 2,5-Diphenyloxazole) and transduced into light. This light is channeled into a wavelength shifter (St. Gobain BC-484) and then into a waveguide which directs scintillated light into a single PMT on the end of the module (Photonis XP2262 or XP2282)[130]. The signal from each module is amplified (10x) and split with half sent to a dedicated ADC channel (fADC250) and half sent to both trigger logic and a dedicated TDC channel (F1TDC). In addition to front-end (FE) trigger logic, HCal is equipped with a pulsed LED system to monitor quantum efficiency and cosmic paddles (2x on both top and bottom of HCal). HCal itself is offset vertically from beam height by 75 cm. Behind HCal, a two floor mezzanine houses front-end electronics. Figure 43 is a front and side view of the HCal apparatus. Figure 44 depicts the detector in detail.

HCal is not intended to undergo any internal configuration changes to the hardware. The detector is, however, moved between kinematics to optimize acceptance matching between HCal and the electron arm (Bigbite) and to achieve different central values of ε for nTPE. See table 15 for **GMn** HCal configurations. The distance is with respect to the target and the angle is with respect to the downstream beamline in the target (or hall) coordinates.

Configuration Setting	Kinematics						
	1	4	7	11	14	8	9
HCal Distance (m)	13.5	11.0	14.0	14.5	14.0	11.0	11.0
HCal Angle (deg)	33.5	31.9	16.1	13.3	17.3	29.4	22.0

Table 15: HCal information for **GMn** Kinematics. See 6 for more information.

Figure 43: The front and side of HCal pictured from the downstream beampipe. The mezzanine containing front-end electronics can be seen behind HCal.

3.1 Modules

Modules in HCal are a modified COMPASS design. Each module is constructed with interleaved steel and scintillator plates flanking a perpendicular wavelength shifting (WLS) panel (St. Gobain BC-484). The WLS panel has a peak absorption at 375 nm, a peak emission at 484 nm, and bisects the module along the long dimension in order to promote the absorption for fluoresced light. Each 1.5 cm thick steel plate acts as an absorber to create hadronic showers with incoming hadrons. These showers produce charged particles and electromagnetic radiation whose energy is sampled (sampling fraction $\approx 8\%$ via MC) by interleaved 1.0 cm scintillator plates. This PPO 2,5-Diphenyloxazole scintillator fluoresces at a peak wavelength of 385 nm with a very fast decay time (between 1.4 and 2.5 ns)[15].

Each module's scintillator and steel panel stacks is offset by one panel on either side of the WLS

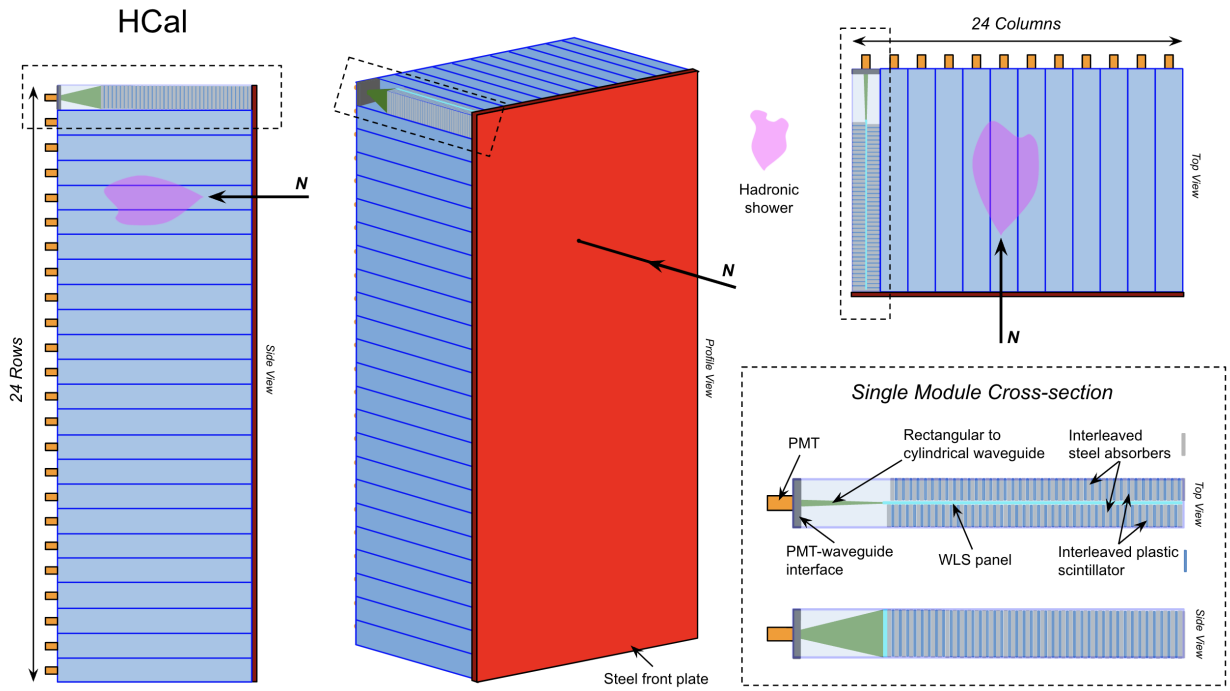

Figure 44: HCal with incident nucleon (N) and cross section of module. 12 x 24 blocks (288 in total).

panel to reduce saturation of the scintillator and to optimize light collection. The total number of panels and dimension of each panel is equal to 40 on each side and the same between modules to eliminate potential bias in detection efficiency.

The PMTs at the end of the module signal chain have peak efficiency close to 500 nm. As such, each interleaved scintillator panel is epoxied to a perpendicular WLS panel with very fast decay time (around 3ns) which absorbs this light and fluoresces at 484 nm. The WLS panel is then epoxied to a rectangular-to-cylindrical waveguide designed to efficiently direct all scintillated light into a PMT. This waveguide is coupled to the PMT with optical grease.[70]

The PMTs are of two different types. The first is a 12-stage Photonis XP2262 with base construction by Carnegie Melon University. The moniker used for this PMT type is “CMU” and there are 192 of these deployed in HCal. All CMU PMTs occupy columns 1-4 and 9-12. The second is an 8-stage Photonis XP2282 with base construction by Jefferson Lab. This type is called “JLab” and there are 96 deployed in HCal. All JLab PMTs occupy columns 5-8.

[70] See Appendix B for light collection optimization procedures regarding PMT/waveguide coupling in HCal.

For many modules, the gain profiles after cosmic calibrations do not match well with PMT types with similar numbers of dynodes. The trend in these modules is towards lower gain and is consistent with the assumption that structural compromise exists between light-guide and WLS or between scintillator and WLS. This will be discussed further in the next chapter.

3.2 Cosmic Paddles

Located on the top and bottom of HCal are two pairs of scintillator panels designed to detect cosmic rays in coincidence. They are composed of plastic scintillator and wrapped in aluminized Mylar to improve internal reflection. Each panel is epoxied to curved light guides which direct scintillated light into coupled PMTs. These PMTs are configured to be read out by four dedicated fADC channels. Figure 45 depicts the paddle setup separated from HCal.

Figure 45: Cosmic paddles used for cosmic muon triggers in HCal. There are two paddles and PMTs per set, the larger of which is situated on the top of HCal in Hall A for SBS experiments.

Optimized for rate, the pair with the larger surface area are placed on the top of the detector and the pair with the smaller surface area are placed on the bottom. The observed cosmic muon

rate with top and bottom coincidence triggers through HCal is about 300 Hz.

Cosmic muons produce fluorescence in scintillators throughout HCal with an average energy sampled through the detector of about 14 MeV.[71] With expected energy from cosmic muons, gain-matching can be accomplished across all channel PMTs[72].

3.3 Pulsed LED Array

HCal is augmented with a pulsed LED array. This array distributes many different brightness settings directly to PMTs from within modules via 18 optical fibers per LED control box. Each of these control boxes serves a 3 column by 6 row region on HCal and is mounted on the side of the detector closest to the PMT region that it serves. There are 16 total LED control boxes. These control boxes are powered in pairs by power distribution boxes located on the upper mezzanine behind HCal. Figure 46 depicts the layout of the pulsed LED system with HCal.

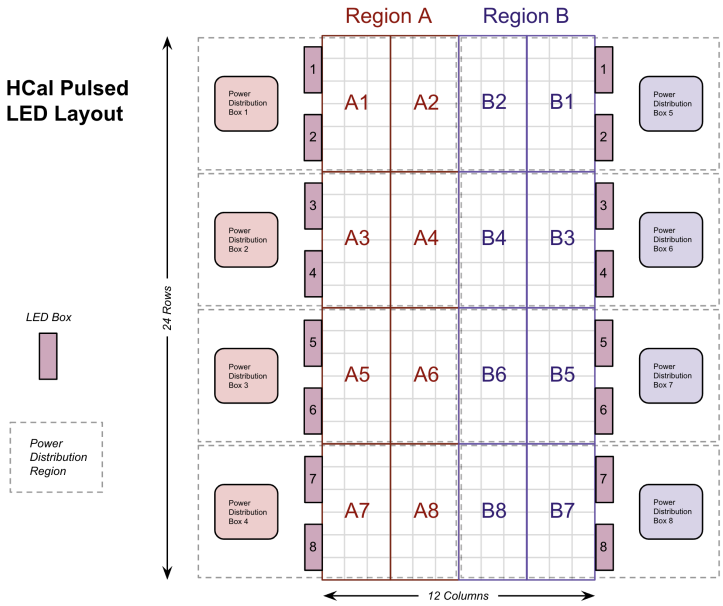

Figure 46: HCal LED distribution schematic; view from behind. Figure adapted from [146].

Each LED control box contains six LEDs, numbered from 1 to 6. The brightness of each sub-

[71] This figure can be calculated with the Bethe-Bloch formula and application of a 10% sampling fraction.
[72] See chapter 3 for HCal cosmic calibration information.

sequent LED doubles that of its predecessor, allowing for a range of combined brightness settings. These settings can deliver illumination to photomultiplier tubes (PMTs) that vary from 1 to 64 times the brightness of the first LED[146].

The LEDs emit pulses in the form of square waves, each lasting approximately 20 nanoseconds. Users can activate multiple LEDs simultaneously and with a suitable sequence to achieve various brightness levels and patterns. The pulse array sequence is configurable by flags file located in the readout controller for the lower HCal crate. This sequence allows for configuration of N steps with individual brightness settings. The frequency of these pulses is determined by a dedicated pulser channel (DVCS) which can be controlled via prescale setting in CODA.

The construction of the LED control boxes is precise, with fiber optics and LEDs positioned delicately for optimal performance. Therefore, opening the control boxes is strongly discouraged. Once opened, it is unlikely that the box can be reassembled to achieve the original efficiency. The internal components are fragile and sensitive to displacement.

The pulsed LED array enables extraction of HCal PMT alpha parameters and gain plateau regions, important for calibrations. Additionally, the LED array may be configured to run parasitically throughout experimental run periods with a consistent brightness setting sequence, providing a dataset which may be analyzed to determine gain stability through time. Throughout GMn, the pulse sequence was consistent and the frequency set to 10 Hz.

3.4 Front End

The front end consists of cabling for all channels and electronics for analog signal processing. These electronics are positioned on the second floor of a two floor mezzanine situated behind HCal. The first floor of the mezzanine provides access to PMTs located in the bottom half of HCal. The top floor of the mezzanine provides access to PMTs located in the top half of HCal, HCal front-end electronics, cosmic paddles, and LED power supplies.

3.4.1 fADC, TDC, High Voltage, and Cabling

All fADCs and TDCs are located in 2 VXS crates in the DAQ bunker. These crates house 16 fADC250 modules with 16 channels each and 5 F1TDC modules with 64 channels each[57, 59]. VTP read out controllers were installed after the end of GMn running (on 7/26/2022) to enable FPGA trigger formation at the crate level with HCal ADC and TDC information[160].

The fADC250s are analog to digital converters which have a sampling rate of 250 MHz, resulting in 4 ns sample widths[59]. Each fADC was configured in mode 1 to record full waveforms and the time window set to 180 ns for GMn. All fADC250 configurations are performed in each crate's read out controller.

The F1TDCs are multi-hit, rolling time to digital converters. On each trigger, the F1TDCs may record multiple hits over minimum threshold on a configurable time window within an 800 ns buffer. The time window is configured to 300 ns width for GMn. Similar to the fADC250s, all configurations are made in the F1TDC read out controller, located in its VXS crate.

Due to DAQ instability, many latencies were necessary throughout the run for both ADC time and TDC time to center the signal within the first third of the window. This positioning improves centering of the overall signal pulse, with the rising edge constituting the hit and the trailing edge occurring sometime afterwards. Necessary latency adjustments sometimes were large enough that, without them, the signal was shifted outside of the window. Some ADC data losses were incurred during GMn running where latencies were unexpectedly needed to recenter data within the window and adjustments were performed later, after the issue was discovered by shift crews or HCal support. The TDC window was large enough that no data losses on TDC data were incurred.

High voltage is provided with two LeCroy-1458 crates. Each of these crates is controlled with raspberry pi controller, designated rpi20(rpi21) powering the bottom(top) half of HCal. Dedicated software controls were provided by an HVS program configured and operated on the dedicated "enpcamsonne" computer located in the hall, accessed via SSH protocol. These software controls have been updated and hosted in the counting house after the end of the GMn experimental run.

Cabling for HCal uses a series of six carts where spare signal cable is coiled and stored. These

carts enable the movement of HCal for different configuration settings without substantial repositioning of cables and while keeping the length of all cables similar between configurations. Signal cables are routed down from the second floor of the mezzanine to the ground, through each of the six carts behind HCal, over a cable tray support frame, along the downstream beamline, under the left HRS pivot, and then directed into the DAQ bunker on the side farthest from the beamline. Each of the signal cables (RG58 and RG59 are used) is 100 m in length. HV cables (RG58 RP SHV 5000V) are bundled and routed directly to the downstream beamline where they follow a parallel path to the DAQ bunker. In total, approximately 69 km of cables weighing nearly 2500 kg is needed and was laid out to operate HCal.

Hardware	**Purpose**	**Specification**
Module	Facilitate hadron showers, provide segmentation for position	40 layers alternating steel/scintillator, 1 WLS, 1 custom light guide, 1 PMT (15cm x 15cm x 1m)
Scintillator	Transduce hadron kinetic energy to gamma radiation	PPO 2,5-Diphenyloxazole: fluor, peak at 385nm
Wavelength Shifter (WLS)	Shift gamma to PMT peak detection efficiency	St. Gobain BC-484: 3ns decay; peak absorption 375nm; peak emission 484nm
PMT	Transduce gamma to signal	192 12-stage “CMU” Photonis XP2262, 96 8-stage “JLAB” Photonis XP2282 (center third columns)
ADC	Analog-to-digital conversion (per module)	fADC250: 2V dynamic range; 250 MHz (4 ns samples)
TDC	Time-to-digital conversion (per module)	F1TDC: Multi-hit; 800 ns dynamic range

Table 16: Specifications and Purposes of Detector Hardware

3.5 Front End to DAQ Signal Chain

Raw PMT signals are routed into PS776 dual-output amplification modules which amplify the raw PMT signal by a factor of ten (10) and shape the signals. Signals output by this device are inverted pulses. A mixing scheme is used to prevent signals from adjacent PMTs from entering amplifiers on adjacent channels to mitigate potential cross-talk. One output is routed via patch panel and 100 m cable to the DAQ bunker for fADC250 processing.

Signals from the other output are divided with a 50/50 analog splitter. One half of the signal is routed through a PS706 discriminator (threshold -10 mV), then via patch panel and 100 m cable to the DAQ bunker for F1TDC processing. The threshold for this discriminator was tuned to the minimum possible value which recovered expected signals during commissioning. The other half of the signal is sent to a UVa-120 modified summing module which sums all signals from a 4x4 channel region (each of G1-G18). This summing module outputs a summed signal to a UVa-133 modified summing module which sums all signals from a 4x4 overlapping region (each of r1-10). This sum is sent to a modified PS706 discriminator equipped with a remote threshold control. Signals over threshold are converted to logic pulse and sent via patch panel and 100 m cable to the DAQ bunker for processing at the TS. A diagram of the front-end logic can be found in figure 47.

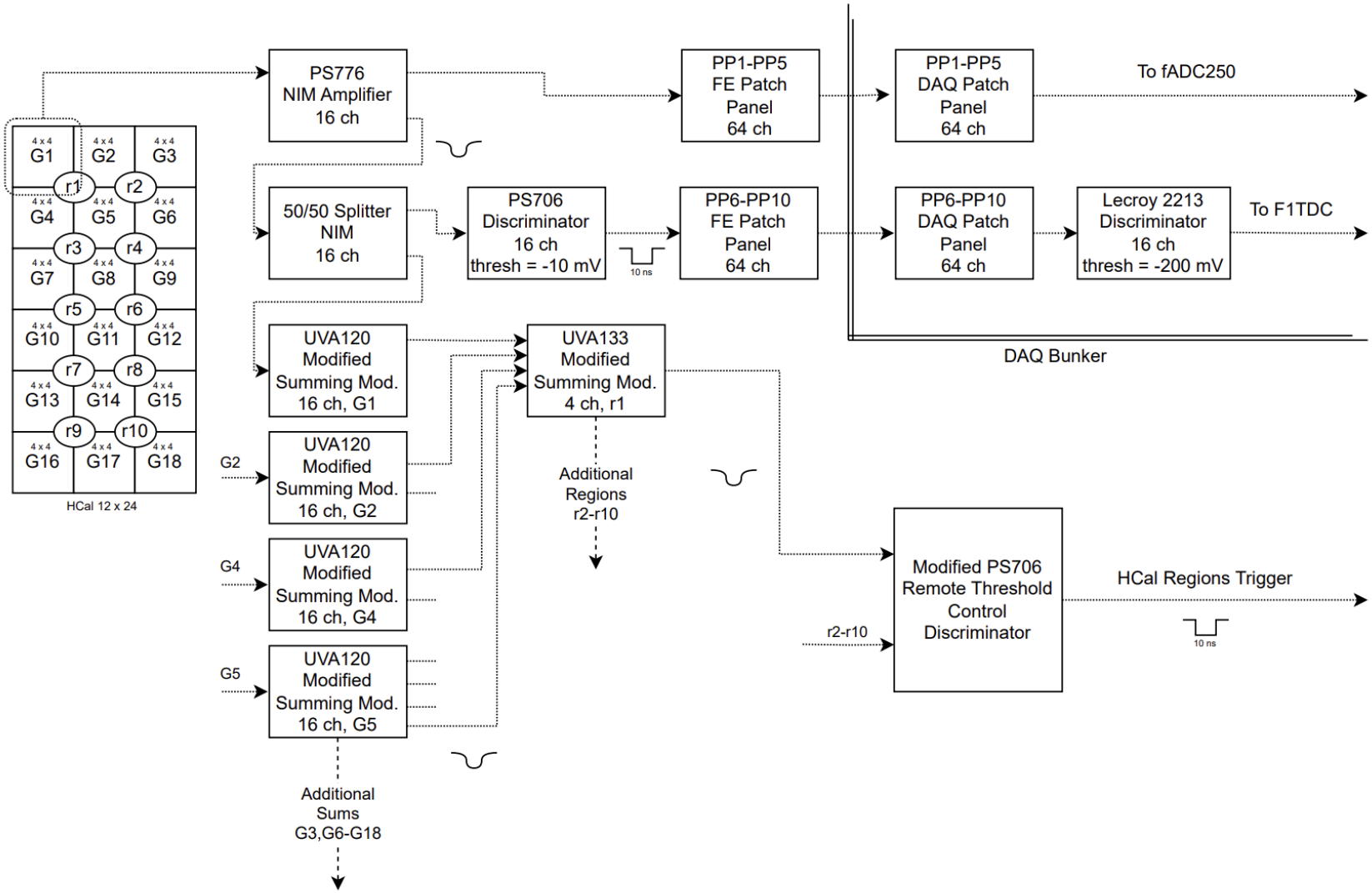

Figure 47: HCal front-end logic.

HCal has reserved fADC250 channels for each of the regions r1-r10 and the sum over sums. These signals are recorded after reconstruction on the branch `sbs.trig.*`.

3.6 Triggers

HCal is equipped with three independent triggers, each of which as been discussed in previous sections. They are as follows:

- Cosmic paddles: coincident signal over threshold in cosmic paddle sums creates trigger at the front-end. Signals are sent via patch panel and 100m cable to the DAQ bunker.
- DVCS Pulser: the DVCS pulser sends signals to the front end which produce LED light directed into PMTs. Signals created by the DVCS pulser originating in the DAQ bunker are delayed to be coincident with response signals from PMTs, then routed into the TS for processing.
- Overlapping regions: HCal is partitioned into 4x4 block regions (G1-G10, see figure 47) from which all signals are summed. Each of these sums participates in at least one addition sum of sums (r1-r10). A sum over threshold set in the counting house produces a trigger sent via patch panel and 100 m cable to the DAQ bunker and TS for processing.

3.7 Thresholds

Each signal chain contains several threshold discriminators designed to prevent various sources of noise and backgrounds from being promoted to signal in the DAQ. Each of these discriminator settings are configured with different goals in mind.

- Along the ADC path, the trigger energy threshold (TET) was disabled in the fADC250 (the only discriminator on this path) in order to assess pedestal and full waveform data per event accurately.
- Along the TDC path, a primary discriminator set to -10 mV is applied to remove low amplitude noise from the analog signal. The output of this discriminator is as square wave logic signal sent over 100 m long cables and discriminated again in the DAQ bunker. This sec-

ond stage is performed to remove parasitic RF and reflections on the long cables which may cause random TDC signals. It is set to -200 mV where the lowest expected amplitude of logic signals from the front end (after long cable attenuation) are roughly -300 mV[73].

- Along the trigger path, the sum trigger signal is discriminated using a variable threshold, which is adjusted based on the expected rates and nucleon energies for each kinematic setting.

The HCal overlapping regions trigger can be configured remotely in the counting house via GUI. The conversion factor between mV input to the discriminator and effective scintillator-deposited energy threshold in MeV used for the majority of the experiment is given by:

$$6.914 \text{ MeV/mV} \tag{3.1}$$

This conversion factor is extracted via cosmic ray analysis detailed in Chapter 4. Since GMn operated with a single-arm Bigbite trigger, no set HCal trigger thresholds are reported here[74].

[73] See Appendix C for a detailed attenuation study of HCal signal cables.

[74] This conversion factor depends on PMT HV settings and differs slightly for a fraction of runs taken during SBS-4 with different HCal HV settings.

4 Analysis

4.1 Data Reconstruction

All reconstructed data follows a common Root nomenclature strategy, which describes each variable accessed from a TTree (or just tree) within a generated .root file. The tree contains detector information per event organized into many branches, allowing for the selection of data per detector subsystem. Variables from detectors are named following a convention that includes the spectrometer arm, the detector, and the specific variable. For example, `bb.ps.e` represents the BigBite calorimeter preshower primary cluster energy. Additionally, branches in the tree provide information for tracks and kinematic variables reconstructed using multiple BigBite detector subsystems. These variables have their own branch naming structure. Table 17 lists the branches with definitions used in this analysis, but many additional branches exist for each subsystem, which are necessary for detector calibrations and analysis.

Detector/type	**Top-Level**	**Sub-branch**	**Contains**
BigBite track	`bb`	`tr`	BigBite reconstructed track variables
BBCal Preshower	`bb`	`ps`	BigBite Calorimeter Preshower variables
BBCal Shower	`bb`	`sh`	BigBite Calorimeter Shower variables
GEM track	`bb`	`gem.track`	GEM reconstructed track variables
GRINCH TDC cluster	`bb`	`grinch_tdc.clus`	GRINCH cluster
Hodoscope Cluster	`bb`	`hodotdc.clus`	Hodoscope bar cluster variables
HCal Primary	`sbs`	`hcal`	Hadron Calorimeter channel variables
HCal Cluster	`sbs`	`hcal.clus`	Hadron Calorimeter all cluster variables
HCal Cluster Block	`sbs`	`hcal.clus_blk`	Hadron Calorimeter primary cluster all block variables
Kinematic	`e`	`kine`	Reconstructed kinematic variables

Table 17: Data Branch Mapping for Detector Subsystems.

The available variable data depends on the detector subsystem and readout method. Energy and amplitude measurements by channel originate in analog to digital converters - ADCs in the calorimeters and the GEMs[75]. Timing measurements by channel can originate in both analog to digital and time to digital converters, adding TDCs to available readout methods[76]. Each leaf on

[75]The GRINCH also has some ADC readout, but these aren't used during data analysis. The combination of APV and MPD constitute an ADC for GEMs.

[76]Surrogate integrated ADC values can also be obtained via time-over-threshold measurements on the assumption

the tree is encoded as either a variable-sized array, a fixed-sized array, or a single value. Additional data per event can refer to different data sources, such as multiple energy measurements across many clusters or many blocks within a single cluster. A more comprehensive list of these variables is documented in the SBS wiki and in the github repository for SBS-offline[155, 157].

4.1.1 Calorimeter ADC and TDC

The fADC250 uses a circular memory buffer to continuously sample analog signals. When a trigger signal is received at the ROC, the ADC looks back into a circular memory buffer based on a configured latency per ROC to identify relevant samples. These latencies are configured based on the observed location of the signal peak and set such that signals appear within the first third of the window. The readout window, whose width is also configured, captures ADC samples around the trigger event signal, providing detailed waveform information per channel.

Energy variables are the product of pedestal-subtracted, integrated ADC values given in pC and gain coefficients which convert pC to GeV. Integrated ADC in pC is reconstructed from samples in mV over sample widths in ns with a 50 Ohm resistance per channel. ADC amplitudes, where available on the tree, are given in mV[77]. Full integrated ADC values on the tree are the sum over pedestal-subtracted ADC samples within a window width configured at the ROC per crate. Pedestals are obtained from the minimum between the average of the first four ADC samples and the average of the last four ADC bins per event. The gain coefficients are extracted per detector and per voltage setting with dedicated energy calibration procedures.

Timing variables are available from buffered TDCs, with a reference time provided by the trigger. For multi-hit TDCs, a ”good time cut” is applied based on the observed difference between the signal time and the trigger time to choose the hit closest to the expected signal time. Timing variables are also available from ADC signals where the difference between the beginning of the ADC window, opened by the trigger, and the estimated ADC signal over threshold provides ADC

of regular signal waveform shape and linearity between integrated signal and signal amplitude. Such is the case for GRINCH cluster ADC values on the tree.

[77] ADC raw output can also be accessed with ADC amplitude measured in raw ADC units (RAU) and integrated ADC in summed raw ADC units (sRAU)

time. The finite rise-time and linearity of the rising-edge evident in ADC signals is exploited to extract a timewalk corrected timing via linear interpolation between the peak ADC location and the first ADC sample prior to the peak below threshold.

4.1.2 Calorimeter Clustering

The calorimeter variables used in this analysis generally derive from clusters reconstructed by SBS-offline. On each event, all blocks over the threshold form a list which is sorted by descending energy. Clustering begins with the first (highest energy) block on the list and attempts to associate additional blocks to the cluster based on distance and timing criteria.

In the clustering algorithm, once the first block is added to a cluster, the algorithm loops over every block that has already been added to the cluster. For each block in the cluster, it considers all unused blocks in the list. Two quantities are checked for each block under consideration:

- The distance between the current block and the nearest block already in the cluster.
- The ADC time difference between the current block and the nearest block already in the cluster. The intrinsic timing resolution for calorimeters improves with detected particle energy, which informs this value[78].

Both criteria must be met for the block to be added to the current cluster. If the block passes both checks, it is added to the cluster and removed from the block list. This process repeats, considering all blocks in the cluster, until no more blocks can be added. Then, a new cluster is formed from the next highest energy block on the list, and the process repeats until no blocks remain in the list. Table 18 gives these cut values for GMn kinematic settings.

4.1.3 Cluster Selection

This default reconstruction methodology does *not* always identify the primary cluster (with index 0, the first added to the cluster list) as the highest energy cluster arising from quasielastic hadrons. While clustering employs a timing cut between blocks for internal cluster consistency, it does not

[78] Proper alignment of HCal timing over ADC channels is necessary to make this feature effective.

Kine	Central $p_{e'}$ (GeV)	Central $p_{N'}$ (GeV)	e' ADC Δt max (ns)	N ADC Δt max (ns)	HCal Δcentroid max (cm)	BBCal SH Δcentroid max (cm)
4	2.11	2.37	10	12	30	15
7	2.67	6.13	10	10	30	15
8	3.58	3.20	10	12	30	15
9	1.63	3.20	10	12	30	15
11	2.66	8.11	10	10	30	15
14	2.00	4.83	10	10	30	15

Table 18: Cluster Inclusion Cuts for GMn Kinematic Settings. See 6 for more information.

apply a timing cut for the cluster as a whole to account for time-of-flight values expected from elastic scattering events. Fortunately, all cluster information is available for analysis per event, and selection from among available clusters is possible from the default reconstructed data[79].

After reconstruction, when selecting clusters with the highest probability of being caused by an elastically scattered nucleon, a wide cut on the difference between the ADC time of the highest energy block in the HCal cluster and the BBCal primary cluster ADC time (the coincidence signal peak) removes random events that arrive too early or too late to HCal[80]. From among these clusters, the highest energy cluster can be selected and promoted to the primary cluster for analysis, thereby removing background events. This method was used for all analyses presented here.

4.1.4 BigBite Tracks

GEM hits over threshold on strips read out by APV/MPDs provide position information for ionizing particles passing through each plane of the detector[49]. Each particle forms a Townsend avalanche shared by several strips. These strips are oriented in two directions (either U-V or X-Y configuration, see Apparatus) to provide independent position information for the ionization cluster in two-dimensions. Signals from adjacent, parallel strips are grouped together to form 1D clusters in each dimension. A constraint region defined by the primary cluster footprint in the BBCal shower provides an e' tracking constraint. Within this constraint, 2D clusters are formed per

[79] After pass-2 calibrations, the primary cluster has been updated to be the highest sum energy cluster among available clusters per event.

[80] This ADC time cut is kept large to allow for tuning coincidence timing cuts done later. For more information, see Appendix B for cluster selection algorithms.

layer combining information from each of the two strip orientations. The position of each cluster is the signal-weighted centroid of each cluster [137].

Per event, many track candidates are reconstructed from the many 2D cluster centroids available in all five GEM planes, starting from the outermost GEM layers to the innermost layer. From these centroids, straight lines are fit through all possible combinations leading to many possible tracks on most triggers. The track which minimizes χ^2/ndf is selected per event. The aim of tracking is to optimize the efficiency of finding good tracks while minimizing the number of false positives ("fake tracks"). Achieving these goals often involves a trade-off between efficiency and the purity (accuracy) of track-finding.

Other cuts can be placed at the clustering level to improve tracking efficiency, including "hit quality," which measures the ADC and time correlation per hit, fiducial cuts that restrict hits to well-defined geometric regions of the detector to avoid edge effects and dead zones, and tighter optics constraints. Additionally, placing cuts on the number of participating hits among GEM planes can reduce the number of false positives, although it may decrease overall tracking efficiency. To maintain integrity of the tracking process, the tracking algorithm prioritizes tracks with the largest possible number of hits during track finding. During reconstruction, only events with at least one track that passes all cuts are retained for further analysis. Further track quality cuts may also be applied to enhance the purity of the reconstructed tracks.

Other cuts can be placed at the clustering level to improve tracking efficiency, including "hit quality," which measures the ADC and time correlation per hit, fiducial cuts that restrict hits to well-defined geometric regions of the detector to avoid edge effects and dead zones, and tighter optics constraints, which will be discussed momentarily. Additionally, placing cuts on the number of participating hits among GEM planes can reduce the number of false positives, although it may decrease overall tracking efficiency. The tracking algorithm prioritizes tracks with the largest possible number of hits. During reconstruction, only events with at least one track that passes all cuts are reconstructed for analysis. Further track quality cuts may also be applied to enhance the purity of the reconstructed tracks.

Detailed optics are required to reconstruct tracks back to the vertex position, where the primary scattering event occurred. The process uses a transport-matrix to map tracks in BigBite (the "focal plane") back to the target frame vertex using a power series expansion of each target variable in terms of all the focal-plane variables up to second-order. Carbon foil targets discussed in the previous section provide known target-frame z coordinates to reconstruct. A sieve plate placed between the target chamber and the BigBite magnet allows for reconstruction of target-frame x and y coordinates with e' tracks which pass through the holes in the sieve[81].

Reconstructed track information on the tree is provided in target frame variables for analysis (see table 17). The track momentum is given by its Cartesian components and vertex positions are given by their Cartesian components. Table 19 gives e' track variables and their descriptions. Figure 31 gives the orientation of the BigBite coordinates and 26 describes the target z-coordinate system at the vertex and within the target.

e' variable	**leaf**	**Description**
$\|\mathbf{p}\|$	p	Magnitude of the momentum of the primary e' track
p_x	px	x-component of the e' track momentum in target coordinates
p_y	py	y-component of the e' track momentum in target coordinates
p_z	pz	z-component of the e' track momentum in target coordinates
v_x	vx	x position of the e' track vertex in target coordinates
v_y	vy	y position of the e' track vertex in target coordinates
v_z	vz	z position of the e' track vertex in target coordinates

Table 19: Kinematic Variables for the Primary Electron Track

4.1.5 Track Energy Loss in Target

As scattered electrons leave the target, they lose energy by excitation and ionization of target materials described by the Bethe formula 2.9. The amount of energy lost (E_{loss}) to these processes can be estimated using the central BigBite angle θ_{bb}, the target density ρ_{tar}, the collisional stopping power of the target $\left(\frac{dE}{dx}\right)_{\text{tar}}$, and the radius of the target cell r_{cell}[82]:

$$E_{\text{loss}} = \frac{r_{\text{cell}}}{\sin(\theta_{\text{bb}})} \cdot \rho_{\text{tar}} \cdot \left(\frac{dE}{dx}\right)_{\text{tar}} \tag{4.1}$$

[81] For additional information, see [170]

[82] The cryotarget cells used in **GMn** were 2 inches in diameter[89].

The reconstructed energy from the primary BigBite track is dominated by the momentum of the track due to the negligible mass of the electron compared to the central momenta at all kinematics, such that:[83]

$$\mathrm{E}_{e'} = \sqrt{\mathbf{p}_{e'}^2 + m_e^2} \approx |\mathbf{p}_{e'}|. \tag{4.2}$$

As such, this estimated energy loss is added back to the primary track momentum per event, resulting in $\mathrm{p}_{\mathrm{recon}} = |\mathbf{p}_{e'}| + \mathrm{E}_{\mathrm{loss}}$. The reconstructed four-momentum of the electron becomes:

$$p^{\mu}_{\mathrm{recon}} = \left(\mathrm{E}_{\mathrm{recon}}, p_x \cdot \frac{\mathrm{p}_{\mathrm{recon}}}{|\mathbf{p}|}, p_y \cdot \frac{\mathrm{p}_{\mathrm{recon}}}{|\mathbf{p}|}, p_z \cdot \frac{\mathrm{p}_{\mathrm{recon}}}{|\mathbf{p}|}\right), \tag{4.3}$$

where $\mathrm{E}_{\mathrm{recon}} = \sqrt{\mathrm{p}_{\mathrm{recon}}^2 + m_e^2}$. The e' angles can be reconstructed with the momentum components $\mathbf{p}_{\mathrm{recon}} = (p_{\mathrm{x,recon}}, p_{\mathrm{y,recon}}, p_{\mathrm{z,recon}})$:

$$\theta_{e'} = \arccos\left(\frac{p_{\mathrm{z,recon}}}{\mathrm{p}_{\mathrm{recon}}}\right), \tag{4.4}$$

$$\phi_{e'} = \arctan\left(\frac{p_{\mathrm{y,recon}}}{p_{\mathrm{x,recon}}}\right). \tag{4.5}$$

Unless otherwise stated, all further analysis relying on e' momentum uses this correction. The parameters used for this calculation can be found in table 20 [118][84].

Material	ρ (g/cc)	dE/dx (MeV $\cdot$ cm^2/g)
LH2	0.0723	5.74
LD2	0.169	5.81
Aluminum	2.7	2.1

Table 20: Material Properties for Energy Loss Calculations

4.2 Delta Variables

So-called *delta variables* arguably represent the central tool used in SBS analysis. Delta variables use detailed position information for quasielastic nucleons detected in the hadron arm and elastic

[83] See 6 and note that $m_e = 0.511$ MeV.

[84] Additional corrections can be made for the air outside of the scattering chamber, the scattering chamber exit window, and 1/8" Al shield present for later kinematics (SBS-8 and SBS-9), but are not included in this analysis.

projections from e' tracks in the electron arm to build distinct distributions for both protons and neutrons. These position data enable the extraction of quasielastic yields and extractions of nucleon cross section ratios.

In order to define each of the delta variables, dx and dy, pure elastic kinematics must be assumed for each primary track in BigBite. With this assumption, an expected location for an elastically scattered neutron can be determined on HCal. However, not all of these events will correspond to quasielastic events from the primary scattering event. Elastic selection will be discussed later in this chapter to address this issue.

4.2.1 Nucleon Projections

Per event, the primary track reconstructed in BigBite is assumed to be from an elastic electron. The target is assumed to be at rest and the beam electron carries energy given by the beam energy. With this information and assumptions, the nucleon momentum vector can be reconstructed.

The $\mathbf{q}$-vector is first reconstructed with the beam electron momentum and the reconstructed e' momentum:

$$\mathbf{q} = \mathbf{p}_{\text{beam}} - \mathbf{p}_{\text{recon}}, \tag{4.6}$$

where $|\mathbf{p}_{\text{beam}}| \approx \text{E}_{\text{beam}}$ for relativistic electrons. When e' is detected in BigBite, there is no information to identify the scattered nucleon from BigBite information alone.

The energy transfer q^0 can be defined as:

$$\text{q}^0 = \text{E}_{\text{beam}} - \text{E}_{\text{recon}}, \tag{4.7}$$

forming the four-momentum transfer q^μ as:

$$q^\mu = (\text{q}^0, \mathbf{q}). \tag{4.8}$$

From the four-momentum transfer q^μ, the expected elastic nucleon four-momentum can be ex-

tracted:

$$p_N^\mu = q^\mu + p_{\text{target}}^\mu, \tag{4.9}$$

where $p_{\text{target}}^\mu = (M_N, 0, 0, 0)$, with M_N being the average of the proton and neutron masses ($M_N = (M_p + M_n)/2$) to account for the lack of scattered nucleon information[85].

The invariant mass of a generic four-momentum vector is defined as:

$$M^2 = |p^\mu|^2 = \mathrm{E}^2 - \mathbf{p}^2, \tag{4.10}$$

such that Q^2 and W^2 can be extracted, where they represent the invariant masses squared of the four-momentum transfer vector q^μ and the expected elastic nucleon four-momentum vector p_N^μ, respectively. The energy transferred from the beam electron to the nucleon, ν, is the energy component of the q^μ vector.

A similar approach is possible which reconstructs the nucleon four-momentum $\mathbf{p}_N$ using the track angles as an independent quantity. This approach is sometimes favorable given the high GEM angular resolution relative to track momentum resolution depending on e' momentum. Per event, the momentum of an elastically scattered electron can be calculated from the measured scattering angle and the known beam energy as follows:

$$p_{\text{calc}} = \frac{E_{\text{beam}}}{1 + \left(\frac{E_{\text{beam}}}{M_N}\right)(1 - \cos(\theta_{e'}))}. \tag{4.11}$$

From the calculated e' momentum, the energy transfer ν and magnitude of the nucleon can be calculated. Additionally, the expected magnitude of the elastic nucleon momentum can be obtained from ν:

$$|\mathbf{p}_N| = \sqrt{\nu^2 + 2 \cdot M_N \cdot \nu} \tag{4.12}$$

For deuterium, the average over the nucleon masses (M_N) provides an adequate approximation. Assuming coplanarity for quasielastic scattering, the angles which define $\mathbf{p}_N$ in the target frame

[85] The mass of the proton (neutron) $M_p(M_n) = 0.938(0.940)$ GeV. The average M_N is 0.939 GeV.

can be extracted:

$$\phi_N = \phi_{e'} + \pi, \tag{4.13}$$

$$\theta_N = \arccos\left(\frac{E_{\text{beam}} - p_{\text{calc}} \cdot \cos(\theta_{e'})}{|\mathbf{p}_N|}\right) \tag{4.14}$$

The unit vector defined by the nucleon scattering angles can be reconstructed:

$$\hat{\mathbf{p}}_N = (\sin(\theta_N)\cos(\phi_N), \sin(\theta_N)\sin(\phi_N), \cos(\theta_N))\,. \tag{4.15}$$

With these quantities in hand, the scattered nucleon four-vector can be reconstructed in the target frame:

$$p_N^\mu = (\nu + M_N, |\mathbf{p}_N|\hat{p}_{N,x}, |\mathbf{p}_N|\hat{p}_{N,y}, |\mathbf{p}_N|\hat{p}_{N,z})\,. \tag{4.16}$$

Per event, p_N^μ can be used to define the expected location of an elastically scattered nucleon from the e' track reconstructed in BigBite.

4.2.2 HCal Expected

In order to project this elastic nucleon vector to HCal, HCal coordinates must be defined relative to the target-frame coordinates. This can be done with the HCal central angle with respect to the downstream beamline θ_{HCal} and vector operations. These operations for HCal axes follow:

- z-axis: Defined by a clockwise rotation about the target-frame y-axis,

$$\hat{z}_{\text{HCal}} = (\sin(-\theta_{\text{HCal}}), 0, \cos(-\theta_{\text{HCal}})) \tag{4.17}$$

- x-axis: Defined as the negative y-axis of the target coordinate system,

$$\hat{x}_{\text{HCal}} = (0, -1, 0) \tag{4.18}$$

- y-axis: Defined by taking the cross product of the z-axis and x-axis and normalizing,

$$\hat{y}_{\text{HCal}} = \frac{\hat{z}_{\text{HCal}} \times \hat{x}_{\text{HCal}}}{\|\hat{z}_{\text{HCal}} \times \hat{x}_{\text{HCal}}\|} \tag{4.19}$$

The HCal origin in HCal coordinates is defined with the distance to HCal d_{HCal}:

$$\mathbf{O}_{\text{HCal}} = d_{\text{HCal}} \cdot \hat{z}_{\text{HCal}} + d_v \cdot \hat{x}_{\text{HCal}} \tag{4.20}$$

where d_v is the vertical offset required to match coordinate positions in data to the actual position of HCal in the hall[86].

With these axes defined, the expected nucleon position is extracted by calculating the intersection of the nucleon's trajectory with the HCal plane. First, the intersection distance, $s_{\text{intersect}}$, along the nucleon's path is determined by projecting the vector from the vertex, $\mathbf{v}$, to the HCal origin, $\mathbf{O}_{\text{HCal}}$, onto the HCal's z-axis, $\hat{z}_{\text{HCal}}$[87]. This is given by:

$$s_{\text{intersect}} = \frac{(\mathbf{O}_{\text{HCal}} - \mathbf{v}) \cdot \hat{z}_{\text{HCal}}}{\hat{p}_N \cdot \hat{z}_{\text{HCal}}}$$

where $\hat{p}_N$ is the unit vector in the direction of the nucleon's momentum defined earlier. The intersection point, $\mathbf{r}_{\text{HCal}}$, is then reconstructed by extending the direction vector from the vertex by this distance:

$$\mathbf{r}_{\text{HCal}} = \mathbf{v} + s_{\text{intersect}} \cdot \hat{p}_N$$

The x and y coordinates of the expected position on the HCal are obtained by projecting this intersection point onto the HCal's x- and y-axes, $\hat{x}_{\text{HCal}}$ and $\hat{y}_{\text{HCal}}$, respectively:

$$x_{\text{exp}} = (\mathbf{r}_{\text{HCal}} - \mathbf{O}_{\text{HCal}}) \cdot \hat{x}_{\text{HCal}}$$

[86] For data reconstructed post pass-2 position calibrations, no offset parameter is necessary (d_v=0).

[87] For all elastic projections, $\mathbf{v} = (0, 0, v_z)$ is a good approximation for this analysis. It is noteworthy that target energy-loss isn't necessary for the scattered nucleon.

$$y_{\text{exp}} = (\mathbf{r}_{\text{HCal}} - \mathbf{O}_{\text{HCal}}) \cdot \hat{y}_{\text{HCal}}$$

These coordinates, x_{exp} and y_{exp}, define the expected position of the nucleon on the HCal plane in the HCal coordinate system. Figure 48 depicts the HCal coordinate system and the target-frame coordinate system together.

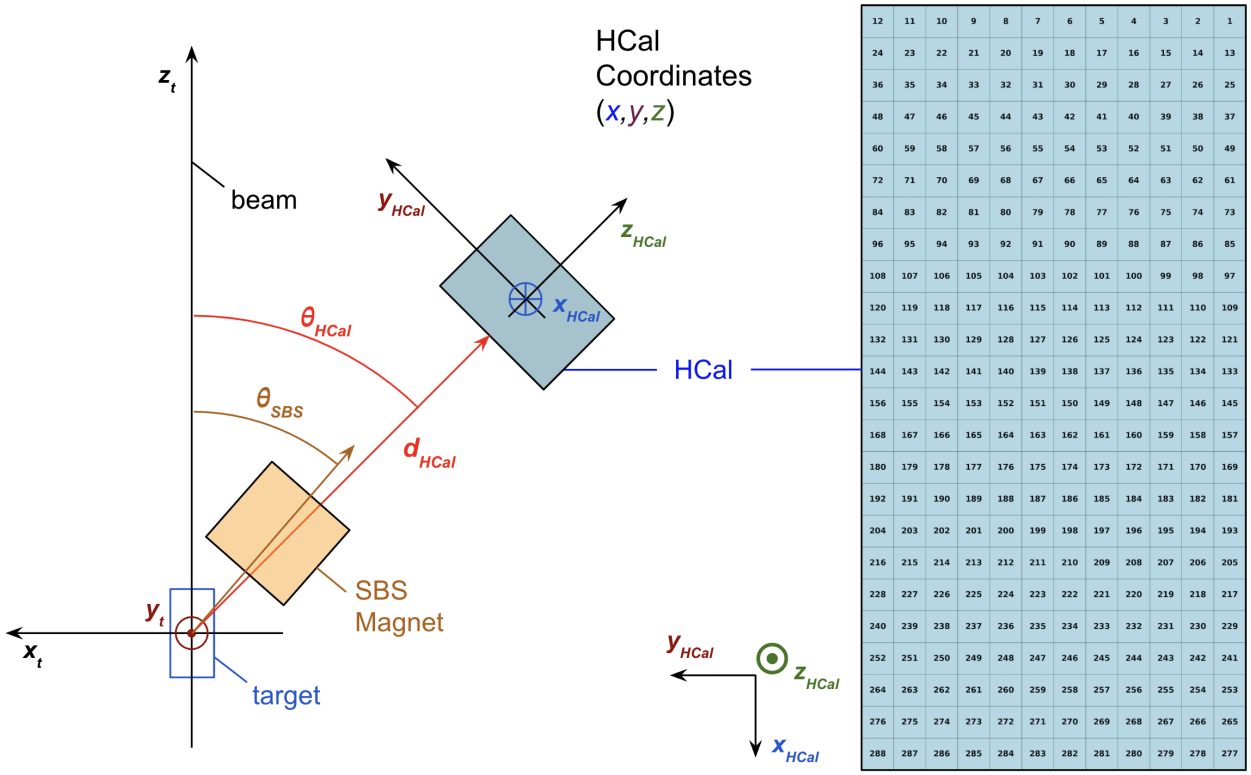

Figure 48: HCal coordinate system $(x_{\text{HCal}}, y_{\text{HCal}}, z_{\text{HCal}})$ relative to the target-frame coordinates (x_t, y_t, z_t). The SBS (48D48) magnet central angle θ_{SBS} and HCal central angle θ_{HCal} may be configured independently per kinematic. The distance to HCal from the target-frame origin (d_{HCal}, also configurable) is depicted. The right hand side of the figure depicts HCal rotated into face-on view with block indices for reference.

4.2.3 The Neutron Hypothesis

These expected locations are the result of *straight-line* projections. Of course, the presence of the SBS magnetic field produces a deflection angle for charged particles passing through it. As a result, the method outlined here details the so-called "neutron hypothesis," where x_{exp} and y_{exp} indicate the expected position of an elastic *neutron* only.

The deflection distance for scattered protons may be calculated per event using the field integral and $\mathbf{p}_N$. The proton deflection distance, d_{deflect}, is given by:

$$d_{\text{deflect}} \approx \tan\left(\theta_{\text{deflect}}\right) \cdot \left(d_{\text{HCal}} - \left(d_{\text{SBS}} + \frac{d_{\text{gap,SBS}}}{2}\right)\right),$$

where the deflection angle θ_{deflect} is:

$$\theta_{\text{deflect}} = \frac{0.3 \cdot BdL}{|\mathbf{p}_N|},$$

BdL is the field integral in T·m, $|\mathbf{p}_N|$ is the magnitude of the proton's momentum in GeV, d_{HCal} is the distance to the HCal, d_{SBS} is the distance to the SBS, and $d_{\text{gap,SBS}}$ is the gap in the SBS dipole magnet. This deflection distance can be used to reconstruct the expected positions of scattered protons as they traverse the SBS magnetic field by adjusting their trajectory based on the calculated deflection.

The expected x and y positions on the HCal plane can be determined by projecting the altered trajectory onto the HCal's x and y axes. This results in:

$$x_{\text{exp,p}} = \left(\mathbf{r}_{\text{HCal}} + \theta_{\text{deflect}} \cdot \hat{x}_{\text{HCal}} - \mathbf{O}_{\text{HCal}}\right) \cdot \hat{x}_{\text{HCal}}$$

$$y_{\text{exp,p}} = \left(\mathbf{r}_{\text{HCal}} + \theta_{\text{deflect}} \cdot \hat{x}_{\text{HCal}} - \mathbf{O}_{\text{HCal}}\right) \cdot \hat{y}_{\text{HCal}}$$

While these coordinates, $x_{\text{exp,p}}$ and $y_{\text{exp,p}}$, define the expected position of the proton on the HCal plane in the HCal coordinate system, practical SBS analysis of deuterium usually omits this adjustment to produce delta-x (dx) plots with pronounced and separated peaks.

4.2.4 Delta Variables

The measured dispersive location (x_{HCal}) and measured transverse location (y_{HCal}) of the presumed scattered nucleon in HCal is reconstructed from many ADC signals in HCal. More specifically, the energy-weighted centroid of the primary cluster provides these measured coordinates after cluster

selection per event. With these measured values and the projected elastic nucleon HCal positions detailed earlier, delta-x is simply defined:

$$dx = x_{\text{HCal}} - x_{\text{exp}}, \tag{4.21}$$

and represents the difference between the expected dispersive HCal position of the scattered nucleon and the detected dispersive HCal position of the presumed scattered nucleon. A similar calculation defines the transverse delta-y:

$$dy = y_{\text{HCal}} - y_{\text{exp}}. \tag{4.22}$$

Figure 49 demonstrates the per-event calculation of delta variables.

The dispersive dx variable plotted for a given kinematic and SBS field setting on deuterium will reveal two distinct peaks, one corresponding to detected protons and one corresponding to detected neutrons. Figure 50 depicts a typical dx vs dy distribution - this one from Q^2 = 4.5 GeV^2 with a deuterium target and with SBS magnetic field at 70% of maximum. The "spot" which emerges at $dx = dy = 0$ corresponds to events where the HCal primary cluster centroid is very close to the "neutron hypothesis" projection from BigBite. This peak corresponds to quasielastically scattered neutrons. The second "spot" which emerges at $dx = -0.9$ m and $dy = 0$ exhibits an offset introduced by the deflection from the SBS field. This peak corresponds to quasielastically scattered protons whose trajectories are bent vertically upward where positive $\hat{x}$ in HCal coordinates points vertically downward. The relative size of each peak is due to several factors which can be controlled for, but mainly (and crucially) due to the cross section difference between neutrons and protons.

The same variables can describe proton detections from hydrogen as well. Relative to proton distributions from deuterium, elastically scattered proton distributions are much more sharply peaked. The Fermi motion describing the target proton momentum in deuterium has the effect of "smearing out" measurements of protons and neutrons, whose at-rest momentum imparts greater

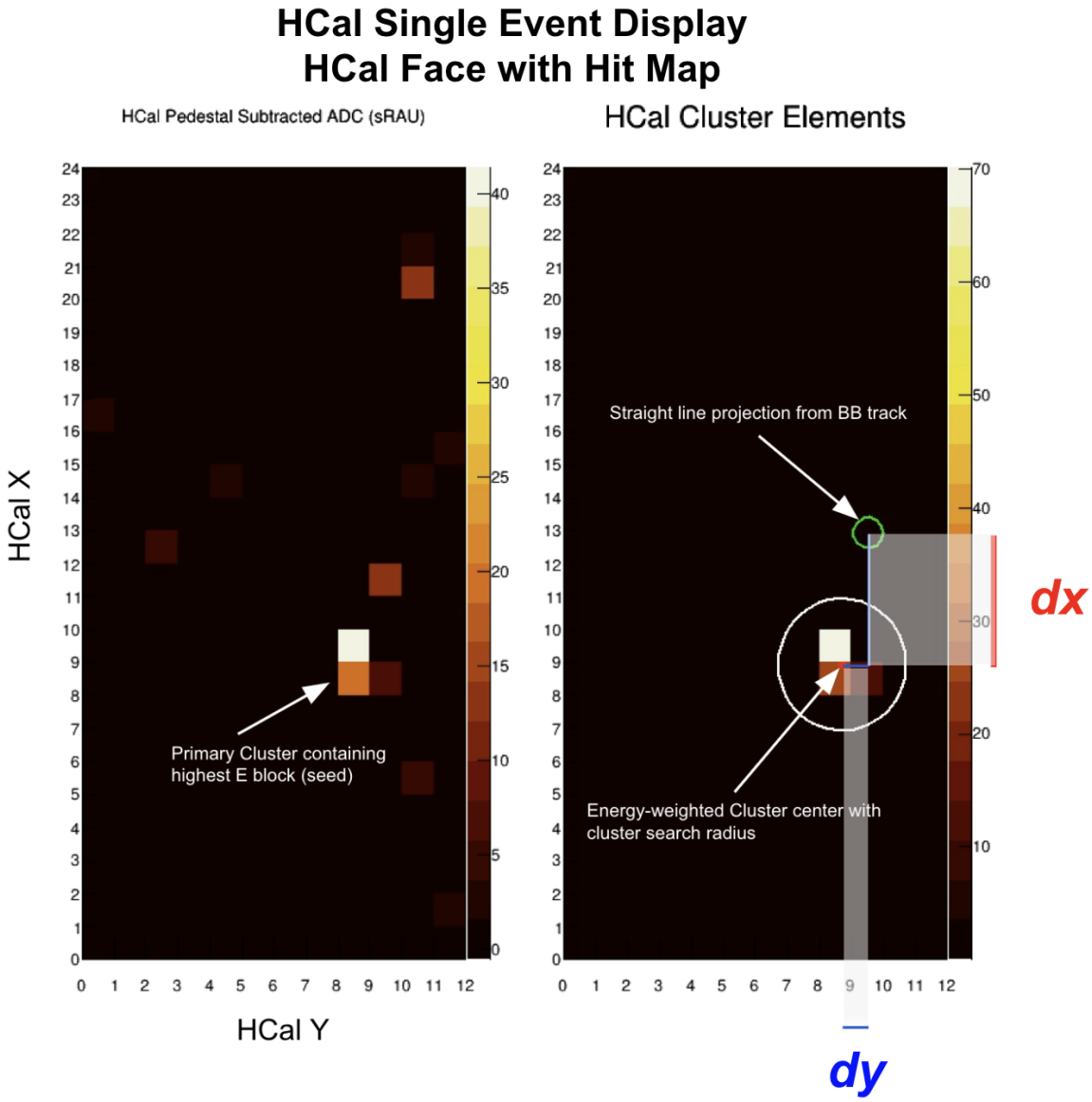

Figure 49: A single triggered event in HCal where the signals above pedestal are represented on the z-axis in integrated ADC units (sRAU). The primary cluster centroid is depicted as a red dot, the cluster block search region used during cluster reconstruction is depicted as a white circle, and the expected nucleon position is circled in green. *dx* and *dy* are shown relative to their components.

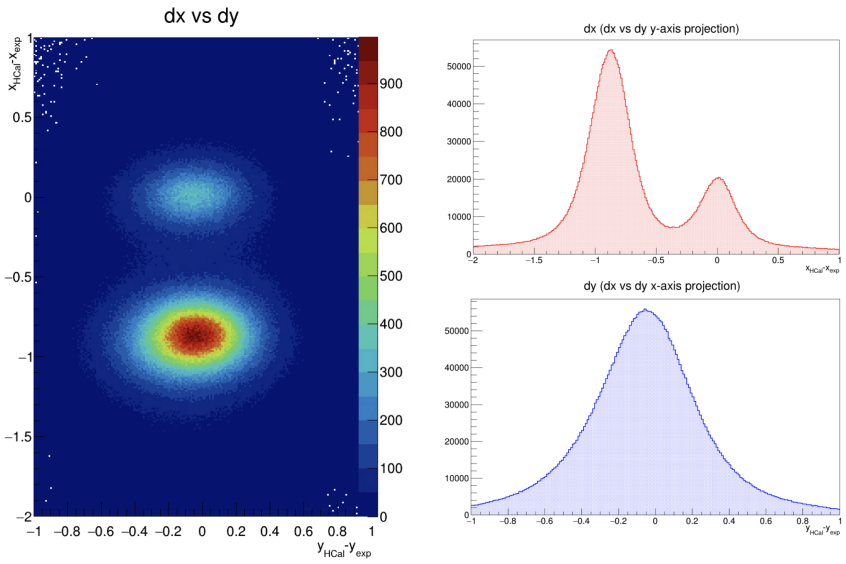

Figure 50: The delta variables, dx and dy, at $Q^2 = 4.5$ GeV^2 (SBS-8, 70% field) using the "neutron hypothesis" plotted for a deuterium target (LD2) against each other and separately in meters. The neutron "spot" emerges at the origin and proton "spot" emerges with a deflection in the dispersive direction at $dx = -0.9$ m and $dy = 0.0$ m. Data taken at SBS-8 with liquid deuterium at SBS field 70%. In HCal coordinates, positive $\hat{x}_{HCal}$ points towards the floor in the hall resulting in the proton "spot" located beneath the neutron "spot." Elastic cuts (discussed in the next section) reduce backgrounds in these distributions.

error to the elastic assumptions used to reconstruct them. The improved position precision (measured using delta variables) and other quantities are exploited to better calibrate several subsystems, including HCal. Figure 51 depicts a dx vs dy distribution from $Q^2 = 4.5$ GeV^2 with a hydrogen target and with the SBS magnetic field at 70% of maximum.

Whereas dx resolves the proton and neutron, dy does not have the power to distinguish between quasielastically scattered nucleons. However, dy is useful for making broader selections of quasielastically scattered nucleons. Selecting events within ellipses drawn around nucleon peaks in dx can effectively distinguish between protons and neutrons, but these cuts have the potential to introduce bias when integrating relative nucleon events due to the overlap of their distributions between the peaks in dx. In contrast, dy offers a single selection criterion for quasielastic scattered nucleons with no nucleon bias, where the dy peak corresponding to both protons and neutrons. Inelastic events appear outside of the peak location and can be cut.

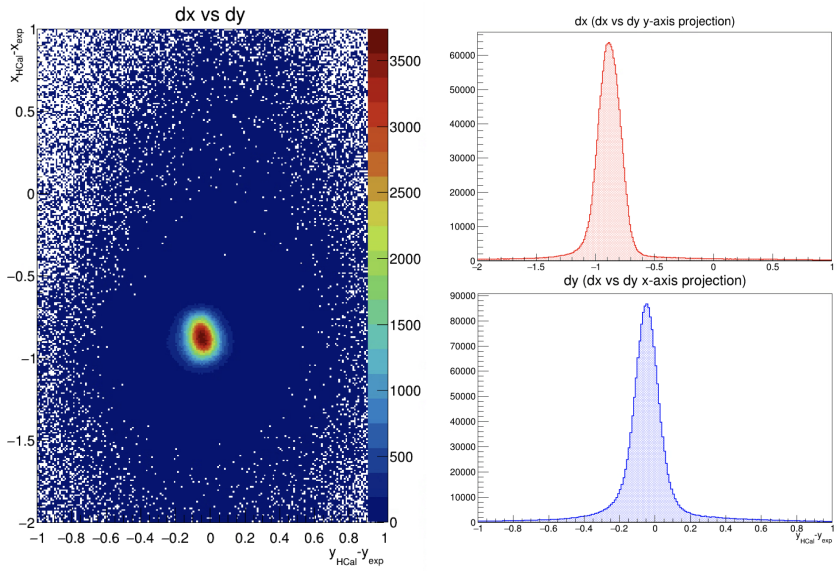

Figure 51: The delta variables, dx and dy, at Q^2 = 4.5 GeV^2 (SBS-8, 70% field) using the "neutron hypothesis" plotted for a hydrogen target (LH2) against each other and separately in meters. The proton "spot" emerges with a deflection in the dispersive direction at $dx = -0.9$ m and $dy = 0.0$ m, same as in deuterium. Data taken at SBS-8 with liquid deuterium at SBS field 70%. Elastic cuts (discussed in the next section) reduce backgrounds in this distribution.

4.3 Elastic Selection

The design of SBS and its single arm BigBite trigger promotes triggers on elastic electron tracks and assists in removing backgrounds. For example:

- The vertical pitch angle of the BigBite detector stack (10°) optimizes the acceptance for upbending, negatively charged particles.
- The energy threshold required to create a trigger in BigBite provides another trigger-level selection on elastic events by suppressing low-energy particles which are produced at much higher rates than elastically scattered electrons.
- In the hadron arm, the strong SBS magnetic field (1.6 T·m at full strength) sweeps low energy charged particles from the target chamber out of the HCal acceptance, reducing the chance of random coincidence events.

Despite these advantages, many triggers which do not correspond to elastic scattering are present

in the data.

In order to extract elastic form factors with the ratio method, the elastic $(e,e'n)$ and elastic $(e,e'p)$ events must be distinguished from those events which arise from inelastic scattering, randoms, and other backgrounds. Several subsystems are often involved in rejection of undesired events from each source.

4.3.1 Sources of Backgrounds

Among particles, pions make up the largest kind of background in **GMn**. While positively charged pions are mitigated, but not eliminated, by the BigBite design, neutral and negatively charged pions (π^0 and π^- respectively) from several sources produce triggers in BigBite[88]. Two subsystems in BigBite provide means to reject these triggers:

- GRINCH operating as a threshold Cherenkov with a charged pion threshold p_{th} = 2.72 GeV provides selection on electrons with a cut on cluster block multiplicity greater than 2. Application of this cut rejects pions that do not create signals in GRINCH below threshold.
- BBCal preshower can reject pions similarly with a cut on sufficiently large energy deposition. This cut is set around 200 MeV for all kinematics.

Cutting on these two subsystems constitutes the primary particle ID (PID) cuts on the electron arm. A demonstration of the efficacy of these subsystem cuts can be found in figure 52. Each of the colored cuts are *anticuts*, or cuts with their logic inverted to select on what they're meant to cut out. In the case presented, the anticuts select on pions. With both PID anticuts applied, no apparent quasielastic W^2 signal at the nucleon mass remains and only the pion contamination remains. Pions that are not produced in the target can also be detected, although for the trigger thresholds used, this source of background does not constitute a significant source of triggers.

Thresholds placed on the calorimeters remove many low energy backgrounds. In BBCal, a remote controllable discriminator allows for the configuration of the threshold for the e' trigger.

[88] Among these sources are exclusive pion electroproduction ($e^- + n \to e' + p + \pi^-$), resonant pion production ($e^- + n \to e' + \Delta^0 \to e' + p + \pi^-$), deep inelastic scattering ($e^- + N \to e' + X$), photoproduction ($\gamma + N \to N' + \pi$), other secondaries, and background interactions. Many triggers corresponding to π^0 tracks exist in the BigBite acceptance, especially at high Q^2.

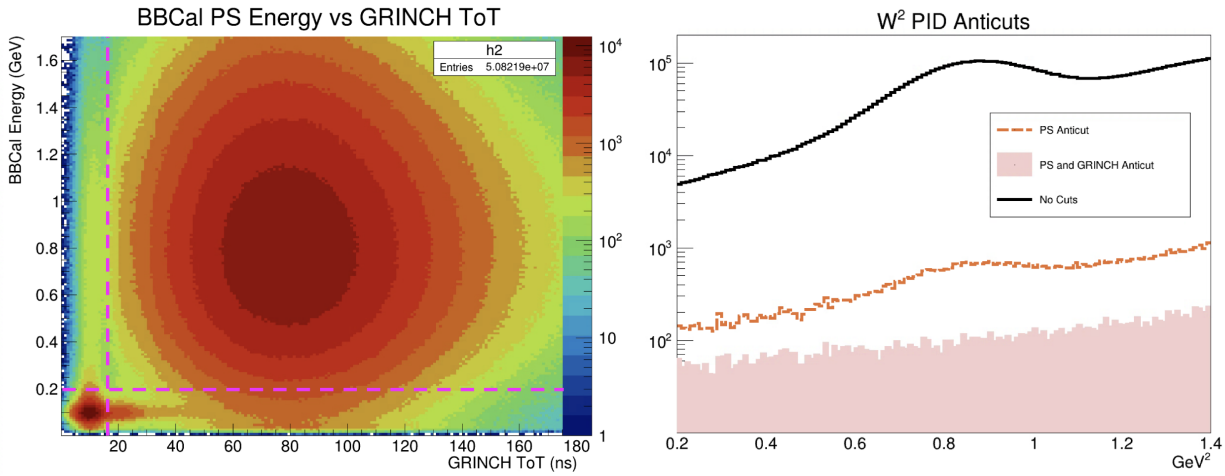

Figure 52: (**left**) BBCal preshower energy vs GRINCH ToT (ADC analog) showing electron spot and pion bands. Cuts (magenta dotted lines) mark the lower limits for acceptable electron events. (**right**) A demonstration of the efficacy of pion selection using BBCal preshower and GRINCH. The top black curve is the W^2 distribution without cuts, the middle red curve is the same with a BBCal preshower pion anticut (preshower energy 200 MeV) and the last solid curve includes both the preshower anticut and a GRINCH pion anticut (GRINCH cluster block multiplicity 2). All data from Q^2 = 4.5 GeV^2 (SBS-8) with a deuterium target.

While this threshold is set as high as possible consistent with a high efficiency for elastic and quasi-elastic scattering events (live time was kept above 95% throughout GMn), the threshold in BBCal is necessary to prevent triggers on events caused by low energy particles which do not correspond to quasielastic events [89].

Many triggers arise from events that do not correspond to quasielastic scattering in the target. Selection of events around the real coincidence peak in the difference between BBCal and HCal ADC time (the coincidence time, or *coin* for short) subtracts many background events. Figure 53 demonstrates the emergence of the real coincidence timing peak before and after cuts for Q^2 = 4.5 GeV^2 and zero SBS field. Isolation of the coincidence time peak demonstrates the efficiency of quasielastic selection at this Q^2 (4.5 GeV^2) independent of coincidence timing cuts and the reduction of the peak after elastic cuts demonstrates the efficacy of elastic selection in reducing

[89] In HCal, the overlapping regions trigger is equipped with a similar threshold control to prevent triggers on background events which originate largely from the target chamber and downstream beampipe. Recall that the HCal trigger was not used in GMn.

background events.

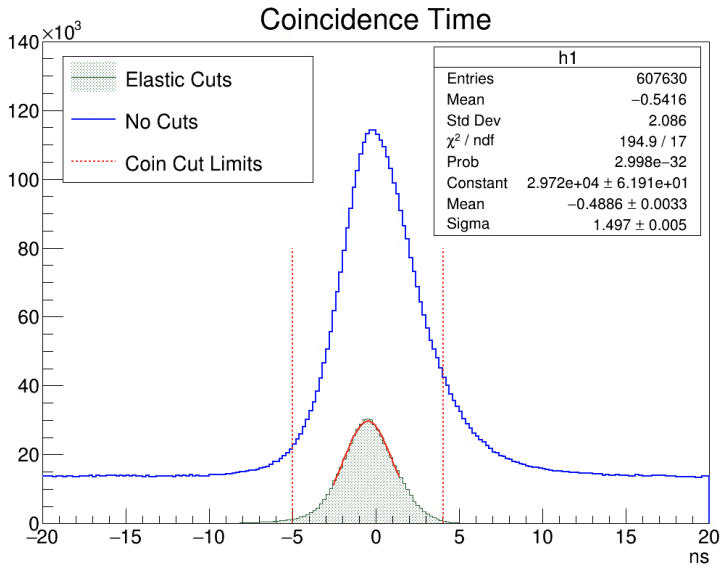

Figure 53: Coincidence time from SBS-8 at zero SBS field is depicted with Gaussian fit parameters on the "Elastic Cuts" distribution. Elastic cuts include PID, vertex, W^2, and nucleon spot selection in HCal. Cut limits for demonstration are set at 3σ of the signal peak, taking only data between the cuts. The peak occurs close to 0 ns only after timing offset calibrations in both BBCal and HCal.

Exploiting the track vertex resolution and additional tracking information provides another handle to reject backgrounds arising from "bad tracks".[90] Regarding the vertex information, a cut on the target-frame z position of the track vertex to require the scattering event originated within the target effectively excludes background events which originate outside of the target volume. Figure 54 demonstrates the primary track distribution in the direction longitudinal with the beam (track vertex z) and example cuts. Further cuts include requiring minimum hits on track among GEM planes (recall that there are 5 in total) and maximum χ^2 for track fit quality. Table 21 gives several possible cuts with descriptions[91].

Even after suppressing pion-induced triggers, there are still many events whose primary tracks correspond to inelastic events (see 10). A cut on the squared invariant mass (W^2) around the squared nucleon mass selects events whose kinematics match elastic scattering. For quasi-elastic

[90] The vertex resolution from track reconstruction is roughly 2 mm / $sin(\theta_e)$, where θ_e is the BigBite central angle.
[91] See Appendix B for more information on optics validity cuts.

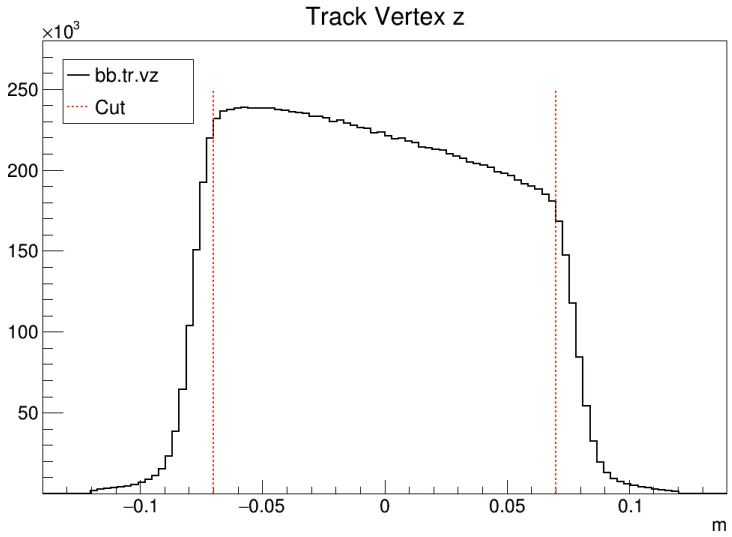

Figure 54: Track vertex position distribution in m. This distribution describes the beam-longitudinal position of the scattering event within the target. Example cuts (red dotted lines, at ± 0.07 m) describe example limits between which events are required to be within the target proper (cryotargets are 15 cm long, see 26).

scattering, this cut will not remove all inelastic contamination from the signal.

Further cuts on kinematic correlations dx and dy can improve selection on quasielastic events by removing those events whose detection location in HCal differs greatly from the location of a quasi-elastically scattered nucleon. These so-called "spot" cuts can be equivalent to cuts on θ_{pq}, though θ_{pq} cuts can be made in lieu of spot cuts if desired from tree variables. Figure 55 demonstrates a proton spot for hydrogen data at $Q^2 = 4.5$ GeV^2. Figure 56 depicts the invariant mass without cuts, with elastic cuts, with spot cuts, and with θ_{pq} cuts.

An advantage of using spot cuts is that they can be easily decomposed into Cartesian cuts on x and y in HCal coordinates. Because dx and dy distributions are symmetric in these coordinates, spot cuts are natural for nucleon selection, where the major and minor axes of an ellipse (defining the cut region) can be informed by the spread of the dx and dy distributions. For the purposes of cross-section extractions in **GMn**, overall yields in the dispersive direction (dx plots) are used, making cuts on this variable less useful. However, with judicious cuts on dy alone, many inelastic and background events can be removed from these dx distributions, reducing systematic uncertain-

Variable(s)	Example Cut	Cut Requirement
bb.tr.vz	abs(bb.tr.vz) < 0.07	Primary track vertex position within target
bb.gem.track.nhits	bb.gem.track.nhits > 3	Minimum number of GEM planes have clusters on primary track
bb.gem.track.chi2ndf	bb.gem.track.chi2ndf < 30	Maximum placed on primary track reconstruction fit chi2/ndf
bb.tr.rx, bb.tr.rth	abs(bb.tr.rx - 0.9 * bb.tr.rth) < 0.3	Track vertical projection to BigBite midplane within BigBite acceptance (optics validity)
bb.tr.ry, bb.tr.rph	abs(bb.tr.ry - 0.9 * bb.tr.rph) < 0.1	Track horizontal projection to BigBite midplane within BigBite acceptance (optics validity)

Table 21: Track Cuts for BigBite Spectrometer

ties.

4.3.2 e' E/p and Minimum Energy

The e' E/p ratio is utilized to identify electrons by comparing the energy deposited in the calorimeter ($E_{e'}$) to the momentum measured by the BigBite spectrometer ($p_{e'}$). Electrons typically exhibit an E/p ratio close to 1. This ratio is used to verify the calibration quality of BBCal and partially suppresses backgrounds when used as a cut. The cut is usually defined as a 3 σ window around $E/p = 1$.

Minimum energy cuts on the calorimeters also effectively cut out randoms and background. By setting a threshold below which energy depositions are ignored, low-energy noise and spurious signals are excluded. This improves the signal-to-noise ratio by isolating genuine physical events that deposit more energy.

Figure 57 illustrates the E/p distribution, showing a clear peak at $E/p = 1$ for electrons. By applying the cut, contamination from non-electron events can be reduced. The cut depicted is at $\pm$ 3σ about the mean.

4.3.3 HCal Acceptance and Aggregate Elastic Selection

Due to the nature of hadronic showers, an acceptance cut is typically employed in HCal. This cut removes all events where the primary cluster position (the energy-weighted centroid) lies near

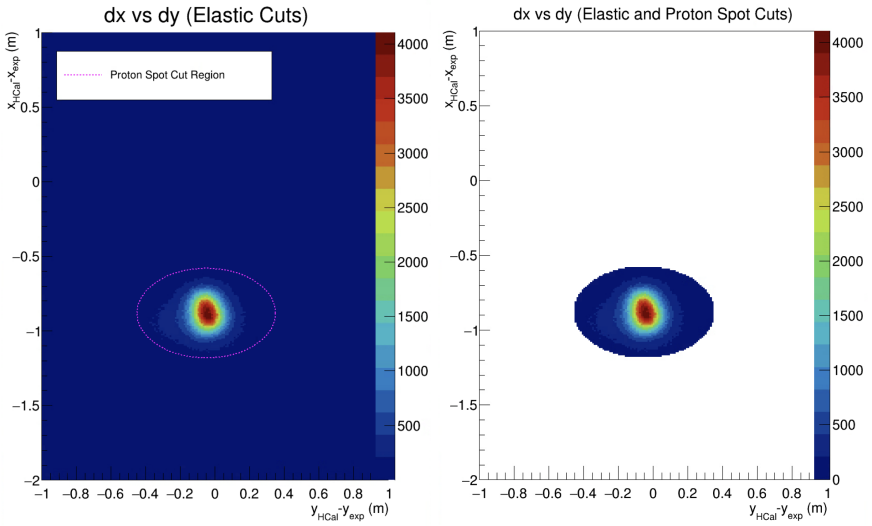

Figure 55: Demonstration of nucleon spot cuts on kinematic correlation plots from hydrogen at Q^2=4.5 GeV^2 (SBS-8). This spot cut is not optimized. The dx vs dy distribution with elastic cuts is plotted on the left. The magenta dotted line defines the spot cut region with different major (dy, 0.4 m) and semi-major (dx, 0.3 m) axes. The same distribution is plotted on the right with added spot cut.

the periphery of HCal. For these events, some of the shower is disproportionately lost out of the HCal volume and data contain relatively unreliable energy, timing, and position reconstruction from HCal variables. Figure 58 demonstrates this effect for protons on hydrogen data. A practical cut removing one block from the periphery of HCal, defining the HCal *active area*, is used in this analysis.

Figure 59 puts all of these concepts together and demonstrates elastic selection on deuterium data taken with Q^2=4.5 GeV^2 (SBS-8). What remains after these cuts is as pure a quasielastic signal as is currently possible, modulo refined cut value selections. The quasielastic cross section ratio and yield ratio can be extracted with lower systematic uncertainty from the final bottom (black) distribution after removal of randoms and reduction of backgrounds.

4.4 Monte Carlo

Up until this point in the analysis, nuclear and radiative effects have largely been ignored. The effects of fermi motion in kinematic correlations dx and dy are manifest and spot cuts whose

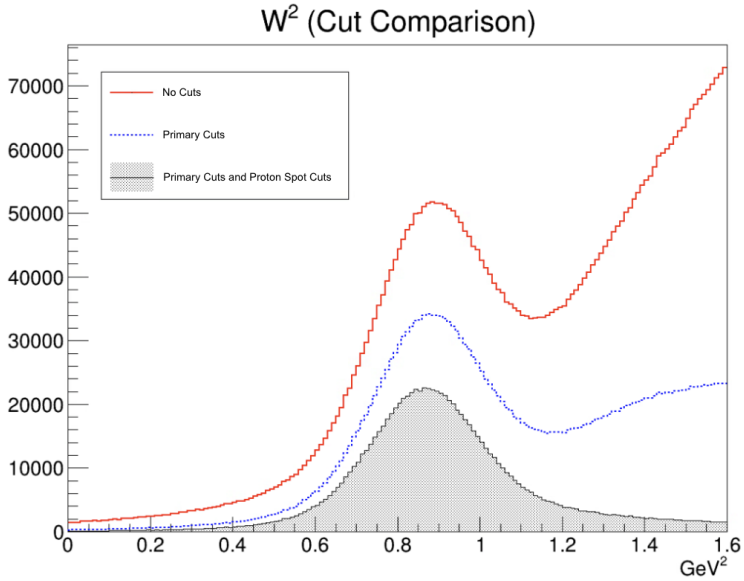

Figure 56: W^2 distribution from hydrogen at Q^2=4.5 GeV^2 (SBS-8). Primary cuts cover vertex position, track hits and χ^2, preshower energy, PID, and coincidence time. The addition of the spot cut removes much of the inelastic contamination revealing the quasielastic peak in W^2 expected at M_p^2 = 0.88 GeV^2.

size are determined by the spread of the data are sensitive to this effect, but the fact that pure elastic scattering does not well describe the quasielastic process under scrutiny has not yet been addressed. The many nuclear effects which affect quasielastic scattering and are present in the data have been described in chapter 2, along with their relative importance in the analysis informed by their respective cross sections at this Q^2 range. To correct for these effects in data, simulated, digitized, and reconstructed data are of paramount importance.

4.4.1 Data/MC Comparisons

Simulations used in extraction of cross sections include a set of data branches which includes all of those that exist for reconstructed real data. These branches include digitized output that reconstructs detector response from physics variables available in raw simulated data from G4SBS. The reconstruction methods which are employed for clustering, tracking, and branch construction are identical between real data and simulated data after digitization and replay. This enables a direct comparison between expected distributions and real data distributions unencumbered by

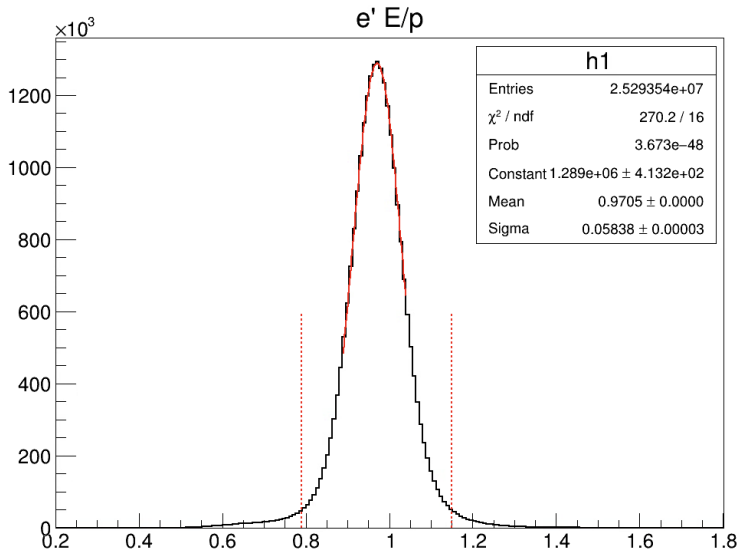

Figure 57: Distribution of e' E/p for tracks in BigBite. The region bounded by dashed red lines indicates the selected range for electron identification, effectively isolating the electron peak near E/p = 1. These data are from hydrogen at Q^2 =4.5 GeV^2.

systematics arising from data reconstruction.

G4SBS is designed to reproduce the detector response at each kinematic setting under the same experimental conditions in the hall. It replicates analysis variables and distributions, including kinematic correlations dx and dy. Simulation results are used to benchmark HCal calibrations, background rates, nucleon detection efficiencies, and cross-section extractions. Importantly, it can distinguish between protons and neutrons and between quasielastic and inelastic events.

Practical use of the simulation requires the installation of several interrelated software systems (discussed in Chapter 2) and the configuration of several generation macros[92]. For each kinematic setting, the following event generation parameters must be configured for SIMC:

- Number of events generated
- Beam energy
- Beam energy variation
- Electron arm momentum
- Electron arm angle

[92]For an installation guide, see [164]

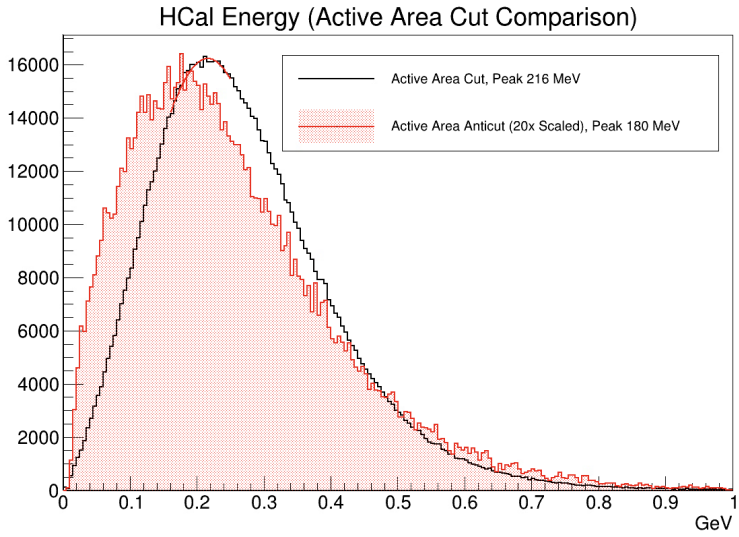

Figure 58: HCal energy spectrum for hydrogen data at Q^2=4.5 GeV^2. Both spectra include cuts over vertex position, track hits and χ^2, preshower energy, PID, W^2, proton spot, and coincidence time. The active area cut removes all events whose primary cluster centroids are within one block of the periphery of HCal. The difference between the active area cut and active area anticut is consistent with the loss of energy in periphery clusters out of the HCal volume.

- Proton arm momentum
- Proton arm angle
- Target type
- Target density
- Random seed configuration

SIMC is a completely separate Monte Carlo event generator which provides input for G4SBS. Additionally, for each kinematic setting, the following experimental parameters must be configured for G4SBS to accurately represent the state of the hall and track radiation through each detector:

- Experiment geometry
- Target type and length
- Generator type (inelastic, SIMC, etc.)
- Hadron type (to select SIMC input)
- HCAL distance and vertical offset

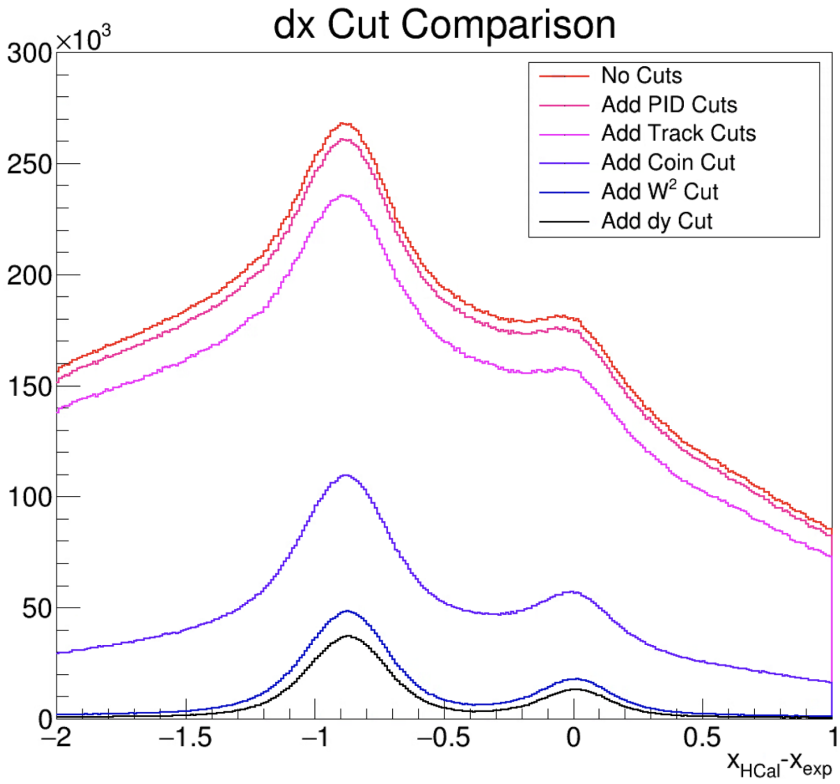

Figure 59: Elastic selection comparison with dx is depicted from hydrogen at Q^2=4.5 GeV^2 (SBS-8). The caption describes cuts placed on the data in sequential order where each cut corresponds with the distribution from the top to the bottom.

- Beamline configuration
- Magnet field settings (BigBite and SBS magnets)
- Scattering chamber shielding

These parameters are used to generate many quasielastic Monte Carlo events using rejection sampling with phase space limited by the configuration macros and weighted by interaction cross sections and the nucleon spectral function. Quasielastic protons and quasielastic neutrons from $d(e,e'N)$ events are generated separately, resulting in two separate sets of data. Both sets resulting from the SIMC generator are pure quasielastic, with a third set of data generated separately for inelastic events. All output is written to raw output simulation files in ROOT format.

Due to the large difference in relative weights per event, rejection sampling at SIMC event generation improves the simulation efficiency tremendously. After configuring the simulation pa-

rameters for SIMC and G4SBS independently, a sample set of events generated by SIMC (roughly 500k events) is sufficient to empirically determine the weight limits ($\text{weight}_{\text{max}}$, in ub/MeV/sr^2) for events in SIMC. These weight limits are determined by the maximum event weight which occurs within the acceptance and optimize the performance of the rejection sampling. Figure 60 depicts empirical cuts on these weights, where the greater between the two nucleons is taken as a general rejection sampling limit (RS limit) on SIMC event generations per kinematic. Configuring SIMC to use rejection sampling will prevent full simulation of events whose weights do not make the cut (in red) and prevent their tracking through G4SBS. This improves the data space efficiency and the processing time by roughly a factor of 100[44].

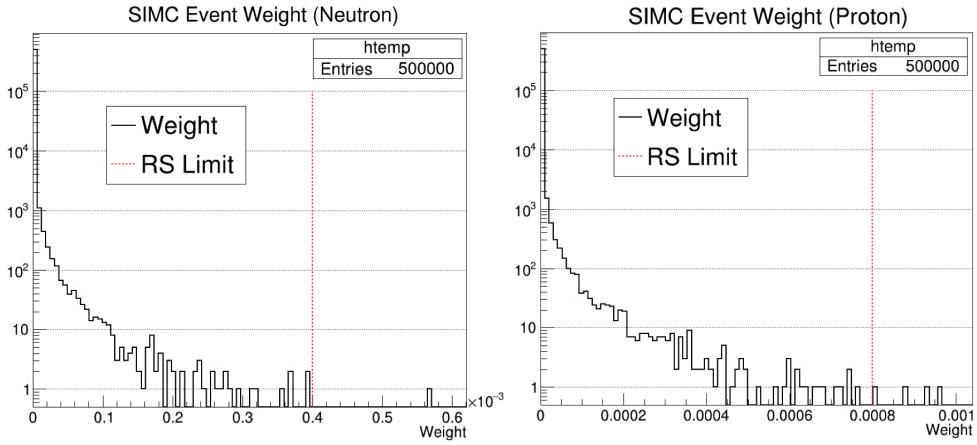

Figure 60: SIMC event weights for Q^2 = 4.5 GeV^2. The empirical limits (red dotted lines) are set at minimum weight beyond which negligible data appears.

With rejection sampling enabled, simulated distributions must be weighted after generation with a single factor to properly interpret the output. Normalization factors (the weights) are of the form[93]:

$$\text{norm} = \text{weight}_{\text{max}} \cdot \mathscr{L} \cdot V_{\text{gen}} / N_{\text{tried}}, \tag{4.23}$$

where $\text{weight}_{\text{max}}$ is the maximum weight in units of $\mu b/\text{MeV}$, $\mathscr{L}$ is the integrated luminosity in μb^{-1}, V_{gen} is the generation volume in MeV $\cdot$ sr^2, and N_{tried} is the number of attempts made to generate events. The values are available after configuration in the output of the simulation.

[93]This definition applies after the implementation of rejection sampling.

The raw simulation files produced by G4SBS are ready for higher level analysis, even without digitizing and reconstructing the data. Many important parameters, such as background rates, energy deposition, and time of flight can be evaluated from these data. After digitization and reconstruction, the final MC data trees match those reconstructed from real data, are complete with accurate detector response, and are ready for real data comparison. These comparisons can be made on physics variables reconstructed from detector output, with an important caveat: timing variables are not yet reliable in simulation. This shortcoming does not significantly impact the analysis where quasielastic events are already distinct from inelastic events in simulation. Figure 61 shows the data processing pipeline for simulated events[94].

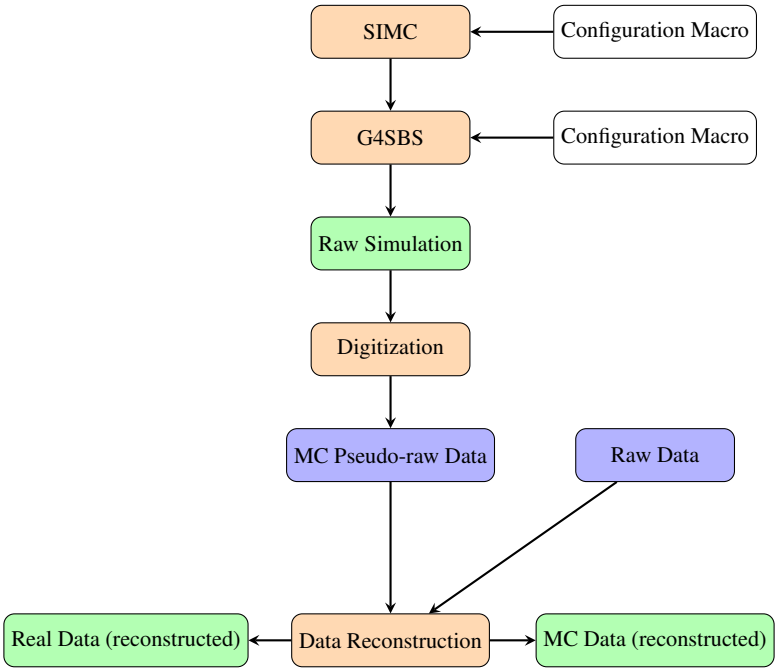

Figure 61: Flowchart of the SBS MC Data Processing Pipeline. Macros are in white, programs are in orange, data are in blue, and data ready for analysis are in green. Final reconstructed data (real and MC) are ultimately compared in analysis.

With similar cuts placed on the simulation and real data, direct comparisons for nearly any quantity of interest can be made and inform the results of analysis. Fits to data which include scaled versions of simulated distributions are used to extract information which is present in simulation,

[94]To improve the efficiency of this process, a set of shell scripts have been jointly developed to streamline generation of simulated events. See [45] for code and more information.

but not in real data. Figure 62 demonstrates the ability of the simulation to reproduce real data dx distributions where additional event information can be accessed with simulation files (like nucleon type and true physics properties prior to transduction by detector subsystems).

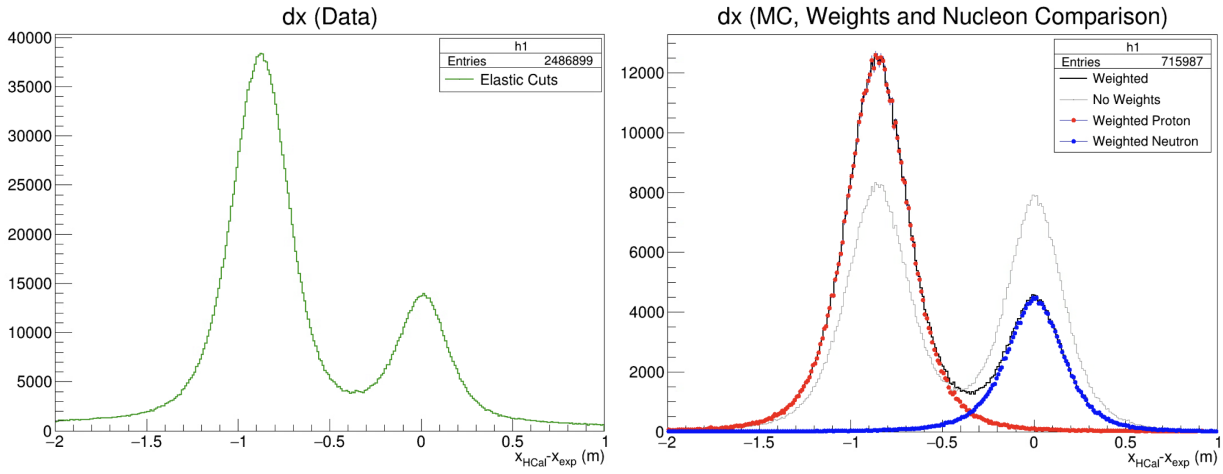

Figure 62: (left) dx distribution after electron track quality cuts, coincidence time cuts, and aggressive elastic cuts from Q^2 = 4.5 GeV^2 data in green. Some inelastic background persists in the signal. (right) Simulated quasielastic dx proton(neutron) distributions with red(blue) markers produced with the SIMC generator with default weights. The sum of both protons and neutrons is in black and the unweighted versions of these peaks are superimposed in gray. These distributions include radiative and nuclear corrections.

4.4.2 Inelastic Background and Efficiency

While the quasielastic generator used in simulation models all known relevant physical processes comprehensively and accurately, the inelastic generator is constrained to single pion production models[95] . To first order, single pion channels dominate the $d(e,e'N)$ inelastic cross section at these Q^2. Figure 63 demonstrates the ability of the combined SIMC and inelastic generator to reproduce W^2 distributions at Q^2 = 3.0 GeV^2. The strong agreement between W^2 data and MC signal (quasielastic) strengthens the extraction methodology where aggressive elastic selection promotes

[95] At the time of this work, the inelastic generator in G4SBS does not include an accurate cross section model for single pion electroproduction. It takes the inclusive structure function and assumes the hadronic final state is always pion-nucleon, leading to an overestimation of the single-pion electroproduction cross section.

high dx signal to background[96]. With high signal to background, simulated quasielastic signal can be fitted to the data and model backgrounds can be used to fit any remaining inelastic contamination.

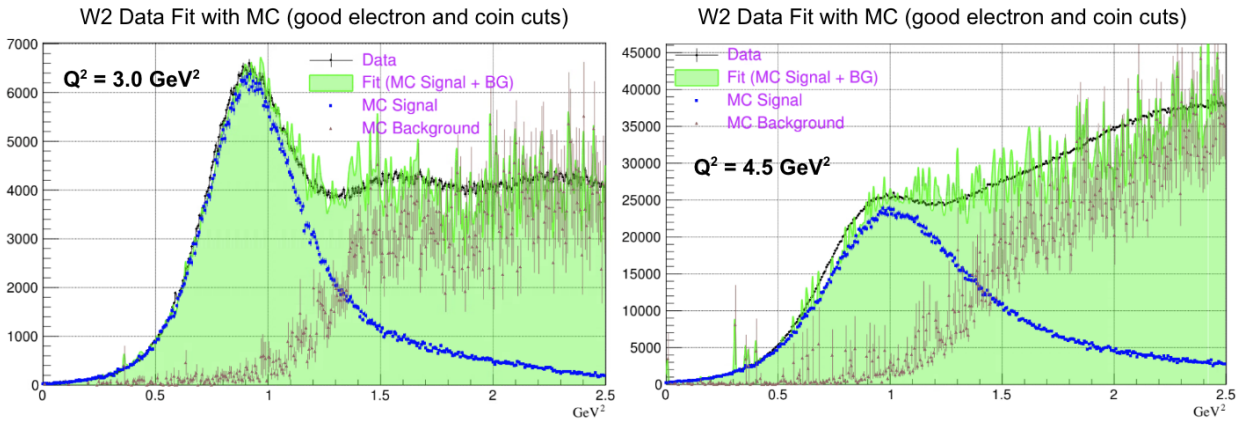

Figure 63: $Q^2 = 3.0(4.5)$ GeV^2 (deuterium, SBS-4(SBS-8), left(right)) data in black fitted with SIMC quasielastic signal and inelastic background. Each of the signal and background are allowed an arbitrary scale to match the data. The data are presented with good electron and coincidence time cuts. The relative paucity of inelastic data manifest in these plots is related to the the relatively small fraction of simulated inelastic events that survive the cuts.

Despite the strong qualitative agreement, there remains an opportunity to improve the simulation with a more accurate inelastic generator. This is especially true for related MC data to be used in dx distributions where they can be used to subtract backgrounds and ultimately for G_M^n extraction.

Due to the good, but imperfect nature of elastic selection techniques previously outlined, inelastic contamination in the quasielastic signal is one of the primary sources of systematic uncertainty. With the shape of the elastic signal from MC and efficiency of quasielastic selection, matching many backgrounds with the MC signal will be used to estimate the systematic contribution to the uncertainty. The methodology for this will be outlined later in this chapter.

The other primary source of systematic error arises from nucleon detection efficiency. Owing to the construction of HCal, the neutron to proton efficiency ratio is expected to be very high and

[96]Note that all analysis requires a cut on W^2 placed at most at 1.4 GeV^2.

close to unity, mitigating this source of systematic error.

4.5 HCal Analysis

This section outlines the methods and results of HCal analysis, both for the purposes of characterizing the detector and to extract important physics parameters needed for the analysis. HCal analysis began before the beginning of the experimental run in the Test Lab on Jefferson Lab campus and continued through **GMn** running. The end of the section will conclude with notes on the ongoing HCal analysis effort.

4.5.1 Test Lab LED Setup and Process

A typical HCal LED analysis run consists of several cycles. Each cycle consists of 1000 events at each of 5 LED settings. LED setting 0 corresponds to LEDs OFF. Pedestals over all channels are determined using this setting. ADC distributions with this setting are fit with a Gaussian and the mean is taken to be the pedestal per cycle. With extracted pedestals, 1000 events are taken with LEDs 1-4 (LED setting 1-4) without combinations to produce pedestal-subtracted ADC amplitude distributions in raw ADC units (RAU). To prevent saturation, the brighter LEDs are not used for this analysis (LED settings >4).

Due to the consistent ADC profile for energy deposition in scintillator, ADC amplitude and integrated ADC (raw units sRAU) are observed to be strongly correlated within HV regions with stable gain[97]. Additionally, ADC amplitude in RAU has the benefit that saturation occurs at the maximum ADC value set by 12 bit precision (RAU_{sat}=4095) such that saturation can be easily determined by event. For these reasons, ADC amplitude is used to extract alpha parameters.

Many analysis runs are taken, each corresponding to an individual set of HV settings. Consecutive analysis run HV changes do not exceed 50V on each PMT. Two types of PMTs exist in HCal and are tested. The first set are 8-stage Photonis XP2282 "JLab" PMTs. These occupy the center four columns over all 12 column x 24 row HCal channels. The second set are 12-stage Photonis

[97] Landau distributions are used and model this ADC profile well.

XP2262 “CMU” PMTs. These occupy all other columns.

For the bottom half of the detector (channels 144-288, starting from 1), averages over JLab and CMU PMTs analyzed for the top half were used to assess alpha parameters and plateau regions. Technical issues with the test setup and time constraints prevented full LED analysis before the start of GMn.

4.5.2 Alphas and Plateaus

Alpha parameters were extracted from plots of average raw ADC units, $\langle \text{RAU} \rangle$, vs HV setting using an exponential fit of the form:

$$\text{fit} = P_0 \frac{X}{P_1}^{\alpha}, \tag{4.24}$$

where X is the HV value (in V), P_0 is the observed lowest ADC mean (in RAU), P_1 is the lowest HV value (in V), and α is the PMT gain parameter[98]. When constrained to stable gain regions in HV, the alpha parameter per PMT can be used to set HV by solving for X in 4.24.

Due to the difference in the number of dynodes between CMU and JLab PMTs, the gain profile and alpha parameters from each are dissimilar. All alpha parameters are extracted individually with the same fit function 4.24. Figure 64 depicts example fits to both PMT types. All extracted alpha parameters can be found in Appendix C, table **??**.

Regarding assessment of PMT plateau regions, or regions in HV with stable gain, the number of photoelectrons (npe) can be determined from ADC data per LED setting with the following formula:

$$\text{npe} = \left(\frac{\langle RAU \rangle}{\sqrt{\langle RMS \rangle^2 - \langle RMS_{\text{ped}} \rangle^2}} \right)^2 \tag{4.25}$$

Here, $\langle RAU \rangle$ is the mean ADC amplitude, $\langle RMS \rangle$ is the RMS of the ADC amplitude distribution, and $\langle RMS_{\text{ped}} \rangle$ is the RMS of the ADC pedestal distribution. Plotting npe vs HV enables extraction of stable gain regions in HV per channel per LED setting. These regions are defined by a minimum

[98] This parameter can be represented by $n_d \cdot \alpha'$ where n_d is the number of dynodes and α' is a more generalized PMT gain parameter. This process extracts α by PMT individually for all channels, so this detail is omitted from analysis.

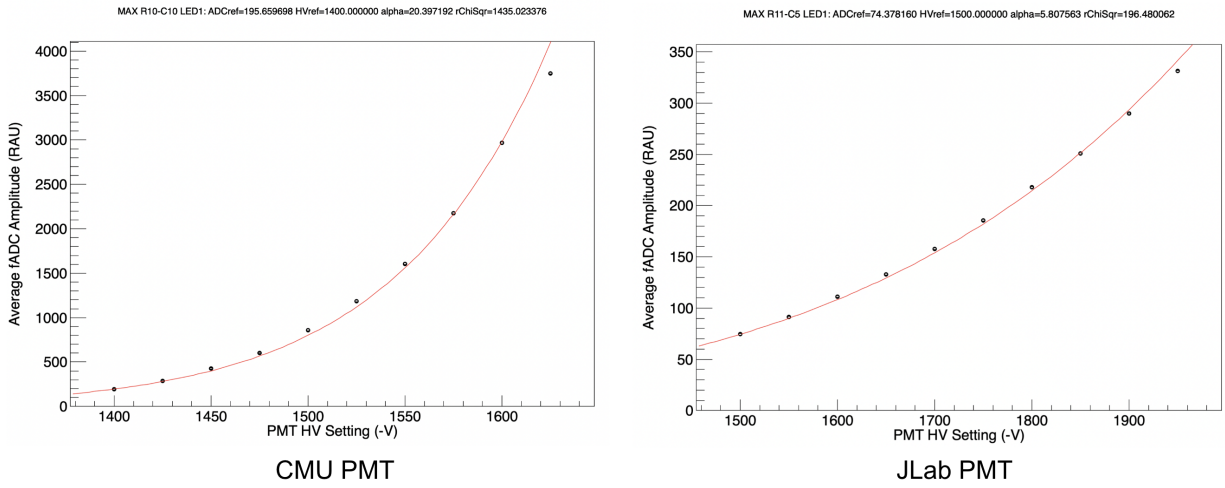

Figure 64: CMU and JLab type PMT gain profiles from channel index 130 and 137 respectively (indexing from 0). The profiles are similar across types with small variations and differences between them owing to the number of dynodes present in PMTs.

HV value (HV_{min}, V) and maximum HV value (HV_{max}, V). Deviation from the average over all HV settings greater than 20% mark the boundaries of the plateau region. Figure 65 depicts an example plateau region.

The photoelectron response is a function of LED brightness. As such, plateau regions are mapped for each of the first four LED settings. All extracted plateau regions can be found in Appendix C, table **??**.

4.5.3 Cosmic Analysis and Gain Matching

After extraction of alpha parameters with LEDs, cosmic rays were used to initially set HV and gain parameters. Using HCal's dual sets of cosmic paddles to trigger on vertical cosmic rays, many sets of cosmic data with different HV settings over all HCal PMTs were taken. Figure 66 depicts the ADC response in RAU from a single trigger with cosmic paddles in HCal.

The average cosmic ray deposits approximately $E_\mu \approx 14$ MeV in scintillators for a single PMT, corresponding to an fADC integral of roughly 8 pC[99]. A target raw output for ADCs in RAU

[99]The average energy loss in scintillator due to ionization is 1.8 MeV/cm[126]. The average path length a cosmic muon takes through HCal modules is 15cm and roughly half of that is scintillator (the rest is steel). $E_\mu \approx$1.8 MeV/cm $\cdot$ 7.5 cm $\approx$ 14 MeV.

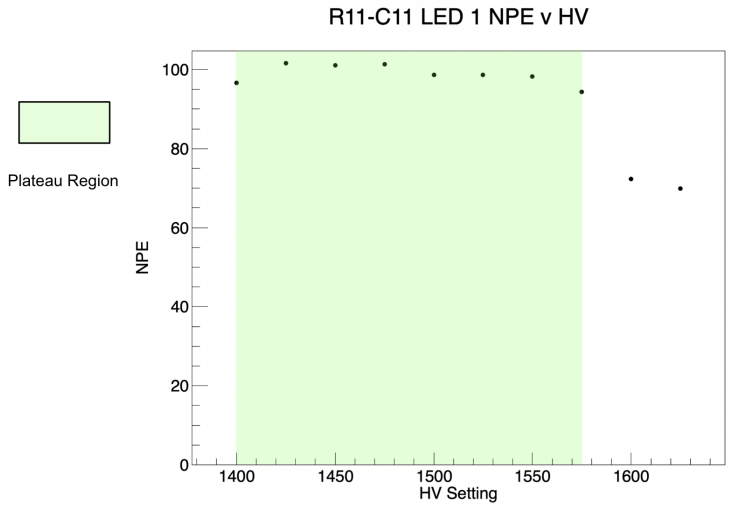

Figure 65: CMU and JLab type PMT gain profiles from channel index 130 and 137 respectively (indexing from 0). The profiles are similar across types with small variations and different between them owing to the number of dynodes present in PMTs.

follows from this energy and the following considerations:

- Latencies were set in the ADC ROCs to center cosmic signals in the first third of the window (beween sample 1 and sample 20 out of 60 samples at 4 ns per sample). This ensured that integrated ADC values accurately included the full signal pulse.
- RAU are assessed per channel with pedestal taken from the from the first four samples in the ADC.
- To ensure full-path cosmic tracks, cuts are placed on all hits over threshold to ensure a hit above and below exists before it is included in the ADC spectrum for each channel and run.
- The Max energy deposited per PMT for the highest Q^2 setting (Q^2=13.6 GeV^2) in **GMn** is 700 MeV.
- Saturation in the ADC is at 4095 RAU.
- The raw signal is affected by attenuation and amplification which results in an overall attenuation factor of 0.75.

Figure 66: HCal single event display depicting a cosmic muon (μ) passing through the third quadrant (from the top) of the detector. Hits which are used to calibrate the HV are boxed in green.

This leads to the target ADC signal[100]:

$$\mathrm{RAU_{target}} = (4095\ \mathrm{RAU} \cdot 0.75) \cdot (14\ \mathrm{MeV}/700\ \mathrm{MeV}) = \mathbf{61\ RAU}, \tag{4.26}$$

and from 4.24, the high voltage setting:

$$\mathrm{HV_{target}} = \frac{\mathrm{HV_{set}}}{\left[\frac{\mathrm{RAU_{measured}}}{\mathrm{RAU_{target}}}\right]^{\frac{1}{\alpha}}} \tag{4.27}$$

High voltage settings are extracted with this process via iteration where if $|\mathrm{HV_{set}}$ - $\mathrm{HV_{target}}| > 50$

[100] Sampling fraction considerations cancel on the energy ratio.

V, the HV setting is constrained to ±50 V from the set value. After setting the HV several times, the response from cosmic muons will converge to the target value (observed for these operations at 61 RAU). Figure 67 depicts convergence of HV values over cosmic gain matching operations[101].

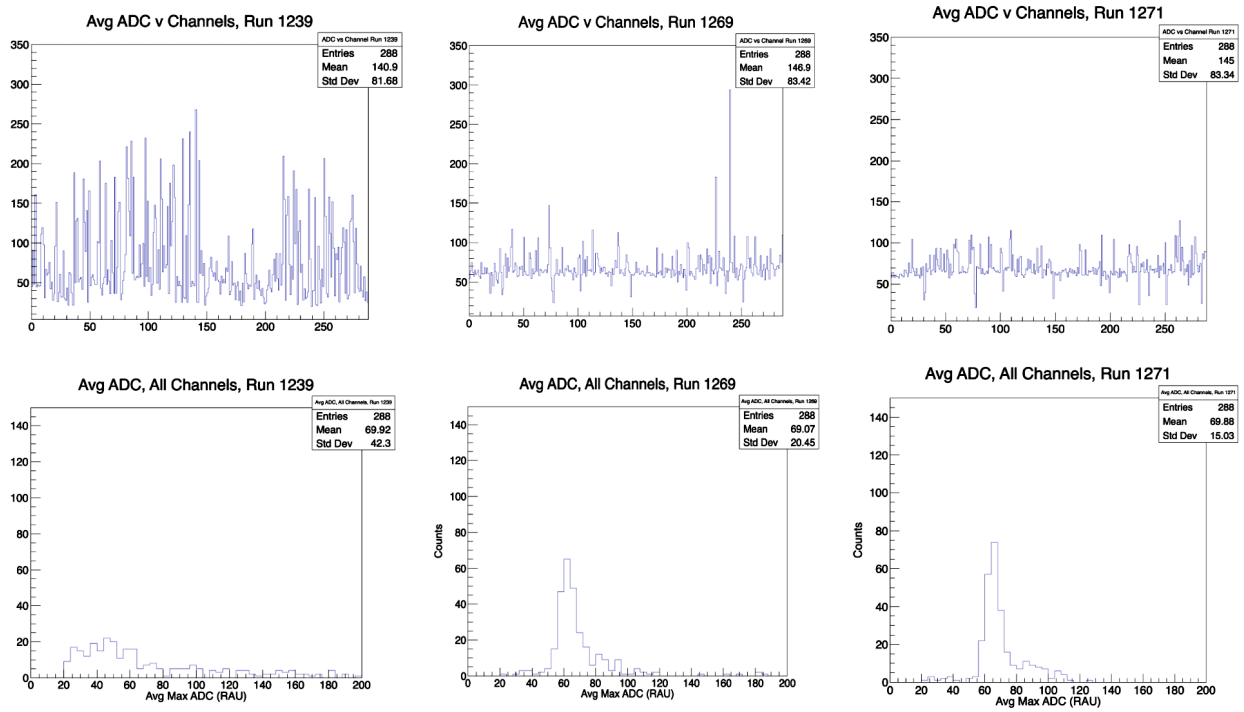

Figure 67: Three (out of many) iterations over cosmic gain matching cycles. The ADC response can be seen to converge over cycles in the bottom set of plots, which are y-axis projections of the top row. Alignment is made more difficult for edge modules and due to the energy resolution limitations of HCal, even for those processes whose primary transduction mechanism is ionization.

It is important to note that the initial HV settings for **GMn** were determined with three considerations:

- A single HV setting capable of efficiently resolving quasielastic nucleon signals across all **GMn** kinematics was desired.
- The HV settings were set somewhat below optimal for low Q^2 kinematics in order to avoid saturation at high Q^2 kinematics.

[101] The threshold conversion factor used throughout **GMn** can be calculated from the energy deposited by cosmic muons. The ADC spectra from cosmic muons in RAU peaks at 18 mV. Tracking back through the signal chain and accounting for attenuation and amplification, 18 mV equates to 4.5 mV out of PMTs. This signal propagated through the trigger signal chain results in a signal with an amplitude of 2.025 mV into the remote controlled discriminator. This gives 2.025 mV/14 MeV or 6.914 MeV/mV as in 3.1.

- The lower gain for many channels were not addressed directly.

The last of these considerations emerged as a concern for HCal analysis very shortly before **GMn**.

4.5.4 Obstructed Modules

It became obvious during HCal signal analysis that many channels were gain matched with abnormally high HV via cosmic analysis and that their energy spectra included uncharacteristically wide FWHM, poor separation from pedestal, and long tails. By examining cosmic signals at the output of the PMT channel by channel, affected channels were identified by setting the HV to the average per PMT type and examining the persist signal amplitudes with an oscilloscope. Figure 68 demonstrates the difference between a normal and an affected channel with integrated ADC spectra from cosmic data.

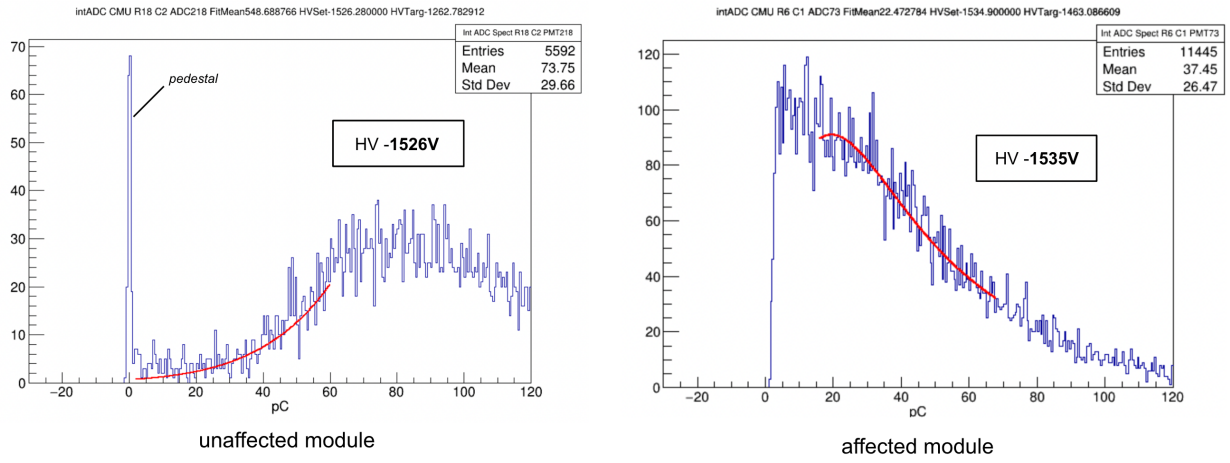

Figure 68: Example of two different modules with attached CMU PMT integrated spectra (in pC) with similar HV settings. Each channel is set much higher than prescribed by the aforementioned gain matching procedure to emphasize the difference in signal profiles. The PMT on left is a normal channel. The PMT on the right is affected by module internal signal loss.

To isolate the source of the abnormality, PMTs were switched between affected and unaffected modules while holding the HV setting fixed for each PMT. In each case, the resulting spectral profile did *not* follow the PMT, indicating that the module itself was the source of the discrepancy in signal strength. It was found that driving the HV very high for these affected channels could

eventually see some separation from pedestal and match the gain for most PMTs, but the wider FWHM of these distributions and relatively poor separation from pedestal were still apparent[102].

Early in **GMn**, a second set of high voltage settings for these affected channels was introduced to drive better separation from pedestal and to improve signal to background. This will be addressed in beam energy calibrations later in the chapter. Appendix C contains a map of all affected channels.

4.5.5 Position Calibrations with Beam Data

Due to unavoidable small separations between modules in the HCal module stack, the face-on position spacing for HCal blocks is not precisely 15 cm from center-to-center in the dispersive and transverse direction. These center-to-center positions are improved with more precise geometry from design CAD files. These effective dimensions are as follows:

- HCal module width (y-distance, center to center): **15.875** cm
- HCal module height (x-distance, center to center): **15.494** cm

The origin point for HCal in its coordinate system is not optimized at the geometric center in both x and y on the face of HCal. Instead, a more appropriate origin point accounts for the vertical offset of HCal. This offset (Δx) positions the vertical geometric center of HCal 75 cm above the beam height to optimize proton acceptance. Thus, the origin point in the vertical direction is offset by 75 cm from the geometric center, while the origin point in the horizontal direction remains at the geometric center of HCal.

4.5.6 Timing Calibrations with Beam Data

HCal is equipped with a dedicated ADC and TDC channel per module, each of which contains valuable timing information per event[103]. Each of these channels is configured in its associated

[102] These effects are consistent with light loss internal to the module, possibly due to a compromise between light guide and WLS panel. No further effort was made to investigate this possibility.

[103] ADC timing is assessed as the threshold crossing time in samples, then converted to ns.

ROC to operate efficiently. Configuration settings set the window width, the precision of the measurement, the latency between trigger signal and data collection, the analog dynamic range, input thresholds, and readout mode, among other parameters[104].

After data is collected, data reconstruction processes the timing and amplitude data from ADC and TDC channels, converting them into particle kinematics and time-of-flight measurements. This involves applying calibration constants such as time offsets and gain coefficients to convert raw data into meaningful physical quantities.

As mentioned earlier in the chapter, the difference between the BBCal ADC signal and the HCal ADC signal is used to build coincidence time distributions and to select on quasielastic events. This selection depends on two important factors:

- Signal resolution is sufficient to efficiently separate signal and background.
- All channel timing is aligned such that the combined signal distribution has a single, distinct peak.

A single, sharp signal peak which emerges from properly aligned channels is important for quasielastic selection, as in 53, but also important for data reconstruction. The tmax selection criteria for clustering (discussed earlier in the chapter) is only effective when the time differences for common detection events between modules are synchronized.

Alignments account for detector and signal chain effects, such as cable length differences, but also partially account for ToF effects. Because alignments do not account for the geometry of HCal and relative position of modules explicitly, nucleon path length differences are effectively absorbed into timing alignments per channel. ToF differences arising from path length between one side of a module and the other side of the same module are not absorbed in this way, but these differences are small and can be safely ignored[105]. Differences to ToF arising from nucleon momentum differences are not absorbed by channel alignments and can be corrected with e' track information per event.

Post-reconstruction per-event timing corrections to improve signal resolution are possible, but

[104]For more information, see [57] and [59]

[105]These differences are on the order of 100 ps.

have not been used for **GMn** analysis due to the effectiveness of timing corrections to ADC time available during data reconstruction in SBS-offline[106]. Alignment of timing signals over all HCal channels is necessary and must be performed at minimum between kinematic settings. In general, timing alignments should be adjusted whenever:

- The spectrometer configuration or beam energy is changed. These changes introduce time of flight (ToF) differences which will affect alignments.
- The DAQ introduces latency differences which shift signal peaks. These "latency jumps" must be accounted for during timing calibrations to ensure alignment of timing data *between runs*.

The latter of these emerged as an issue with data acquisition early during **GMn** running. Extracted offset parameters are entered into the data reconstruction database for processing.

HCal timing in isolation is subject to variation in timing due to the trigger. HCal timing can be evaluated with respect to the timing hodoscope in order to correct for this variation via cancellation of the jitter in the trigger reference time. The timing hodoscope correction improves the resolution of HCal timing for all kinematics significantly (nearly 25% vs raw ADC and TDC times). Alternatively, the time difference between BBCal ADC time and HCal time (both ADC and TDC) improves timing resolution via the same mechanism. Potentially, the timing hodoscope correction can provide the best correction after proper calibration due to the intrinsic timing resolution of the detector as read out by TDCs. All alignment operations consider the timing difference parameter, either HCal time - Hodoscope time or HCal time - BBCal time, for calibrations. Examples that follow in this section consider the HCal time - Hodoscope time difference and refer to reconstruction pass 2[161].

Just as properly aligned timing is important to select elastic events, a sample of quasielastic events is important to provide a source of signals with known time-of-flight. This selection, and the related timing resolution, is most precise with hydrogen targets. However, due to statistical

[106] A linear interpolation methodology is employed in SBS-offline to account for timewalk effects. This method takes the first two consecutive ADC samples whose amplitudes straddle the ADC hit threshold and interpolates a time between them.

limitations and the need to adequately populate each of HCal's 288 channels with sufficient signals, deuterium data is also used. Selection of quasielastic events for this calibration step maximally employs the following cuts:

- PID (BBCal preshower and GRINCH where available, electron arm)
- Track cuts (GEM hits and track vertex, electron arm)
- e' E/p (electron arm)
- Minimum BBCal energy (electron arm)
- W^2 (electron arm)
- Minimum HCal energy (hadron arm)
- Nucleon spot cuts (hadron arm)

These cuts are used in different configurations at different steps in the process.

Due to latency shifts throughout **GMn**, before channel alignment can be performed, calibration sets must be determined. This entails assessment of the timing spectra over all channels as a function of run number per kinematic to determine the presence and location of DAQ-related latency shifts. Each shift requires a different calibration set. Figure 69 demonstrates a kinematic which requires two sets of offset parameters to accommodate the data for both ADC time and TDC time. It is noteworthy that these shifts do not occur at the same time or with the same magnitude between ADC and TDC times.

After calibration sets have been assessed, the channel alignment process may be performed. Adding stricter hadron arm cuts often results in bad fits resulting from low statistics on many cells. To address this and any HCal - Hodoscope time difference vs HCal x position correlations at the same time, the alignment procedure is constructed to get timing info per channel in the following way:

1. Build HCal - Hodoscope time difference vs channel distributions for both electron arm alone (call this histogram h1) and electron arm + hadron arm elastic cuts (h2).
2. Build HCal - Hodoscope time difference vs HCal row distributions similarly with electron arm + hadron arm cuts (h3).

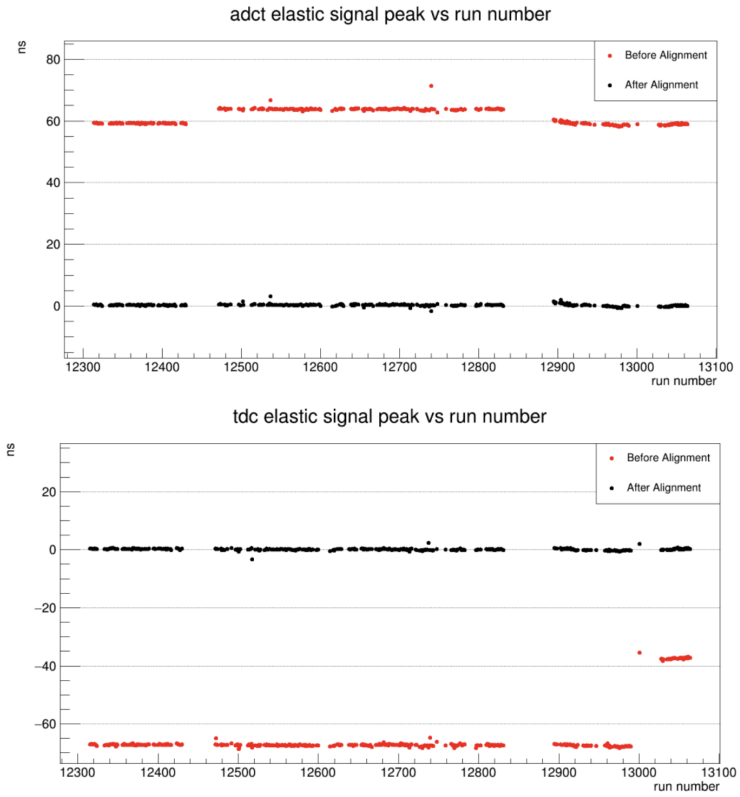

Figure 69: Example of aggregate channel ADC and TDC timing distribution mean values vs run number for Q^2 = 13.6 GeV^2 (SBS-11). The latency shift in ADC time can be seen to occur roughly between runs 12440 and 12480 and then return to normal after roughly run 12840. The TDC latency jump occurs for the same kinematic near run 13000. Adequate assessment of calibration groups allows for alignment over all runs.

3. Build an all-channel aggregate distribution of HCal - Hodoscope time difference over all channels with electron arm + hadron cuts (h4).
4. Check h2 statistics per channel. If sufficient statistics exist, fit the distribution with a skewed Gaussian and extract offset parameter from the fit MPV.
5. If (4) fails, check h3 statistics for the row associated with the channel. If sufficient statistics exist, fit the distribution with a skewed Gaussian and extract offset parameter from the fit MPV.
6. If (5) fails, check h1 statistics for channel. If sufficient statistics exist, fit and extract offset parameter.
7. If (6) fails, fit the h4 distribution with a skewed Gaussian and extract offset parameter from

the fit MPV.

An optimal number of statistics per channel is ideally 1000, but with as little as 300 events a reasonable mean can be extracted, albeit with channel-by-channel checks on fit quality. The difference between the extracted mean per distribution and the alignment target constitutes the extracted offset. For ease of analysis, the peak-location target for all alignment operations to extract offset parameters is 0 ns. Additionally, the old offset parameters used to reconstruct the data under analysis must be accounted for when generating a new set. This process is consistent between ADC and TDC alignments[107]. Figure 70 demonstrates the peak-alignment procedure for ADC and TDC channels.

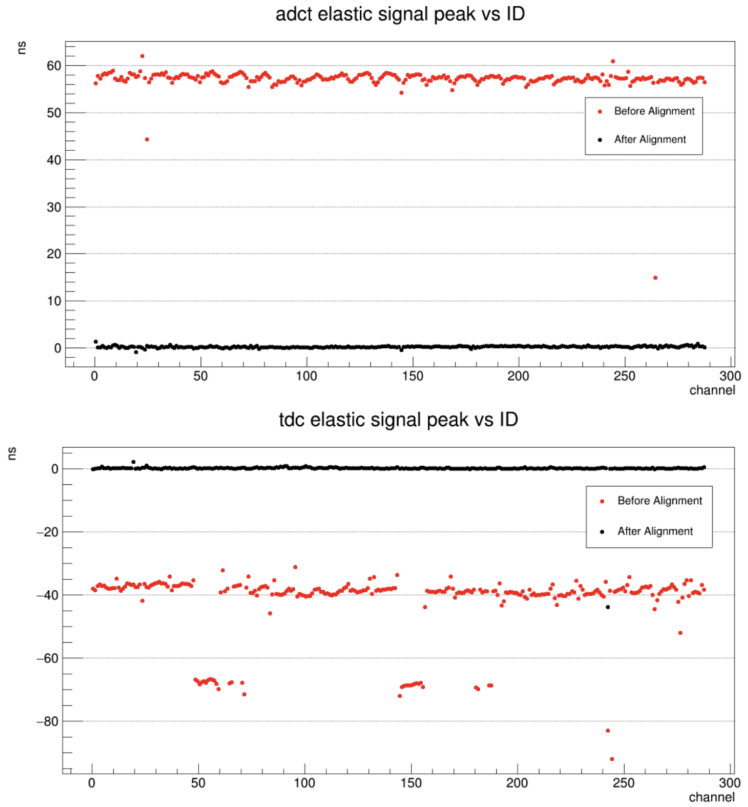

Figure 70: Example of before and after ADC time and TDC alignment calibrations for Q^2 = 7.5 GeV^2 (SBS-14). Each red point is the peak position of a skewed Gaussian fit to timing distributions with cuts before reconstruction pass-2 alignment calibrations. The black points are the same, but after calibrated offset parameters are used to reconstruct the data.

[107] One important caveat exists for TDC alignments - namely that the TDC calibration constant in ns/RTU, or raw TDC units, must be applied between offsets passed to the SBS-offline database and those extracted in ns.

The utility in this approach is that rough alignments can be achieved for many channels which see limited statistics, but those channels which enjoy an abundance of quasielastic events are able to benefit from tight elastic cuts. These more "pure" quasielastic distributions tighten the timing distributions within them and improve the quality of the alignments. Figure 71 zooms in to show the utility in the decision tree approach outlined when adjustments are applied to previously aligned data. All **GMn** kinematics are currently calibrated with this procedure[161].

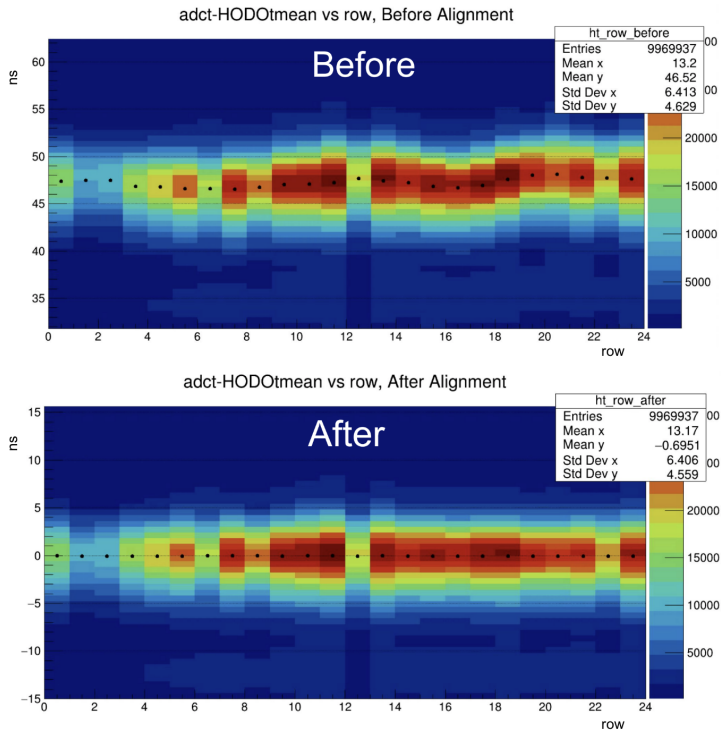

Figure 71: Example of before (left) and after (right) ADC time calibrations for $Q^2 = 7.5$ GeV^2 (SBS-14). The black points indicate the peak positions of skewed Gaussian fits to events with cuts before reconstruction pass-2 alignment calibrations. The fine per-channel improvements lead to a roughly 1-2 ns improvement in all-channel distribution standard deviations over kinematics.

4.5.7 Energy Calibrations with Beam Data

Values for HV and gain coefficients obtained from cosmic analysis provided a starting point for analysis of beam data, but were updated quickly during **GMn** commissioning. Where cosmic

muons provided a benchmark energy which was leveraged to set HV, quasielastic nucleon kinetic energy provided a benchmark which was leveraged to set both software gain coefficients per PMT and refined HV settings[108].

The essential aim of energy calibrations is to convert signal from ADC channels (in pC) to energy (in GeV) as accurately as possible. Making a tight selection on elastic events, elastic kinematics are used to calculate the expected kinetic energy (KE, ν) of elastically scattered hadrons resulting from e' tracks reconstructed in BigBite. Event selection is essentially the same as detailed for timing calibrations, but must be evaluated with tighter W^2 and nucleon spot cuts and include a coincidence time cut (available with calibrated timing offsets). Additionally, an HCal active area cut is essential to prevent the energy leakage evident on peripheral modules to significantly influence the calibrations.

Per event which passes these cuts, the calibration procedure equates the summed energy deposit over all blocks in the primary cluster with the expected nucleon KE. Summing all of these clusters over all events, a system of linear equations is built and chi-squared is minimized to extract the most probable value of the gain coefficient per block which best reproduces the ADC response given expected KE per event.

$$\chi^2 = \sum_{i=1}^{n} \left(E_i - \sum_j c_j A_j^i \right)^2 / \sigma_E^2 \tag{4.28}$$

$$\sigma_E^2 \approx E_i \tag{4.29}$$

$$\frac{\mathrm{d}\chi^2}{\mathrm{d}c_k} = 2 \sum_{i=1}^{n} \frac{1}{E_i} \left(E_i - \sum_j c_j A_j \right) A_k = 0 \tag{4.30}$$

$$\sum_i A_k = \sum_i \sum_j A_j c_j \frac{A_k}{E_i} \tag{4.31}$$

This standard approach is adapted from the BigCal electromagnetic calorimeter calibration code developed by Andrew Puckett for the GEp-III experiment conducted at Jefferson Lab[76, 95][109].

[108] During SBS-4, one additional set of HV settings were obtained from beam data which were used for the remainder of **GMn**.

[109] This script can be found on the HCal_replay git repository with the path *HCal_replay/scripts/archive/puckett*.

For a hadron calorimeter, however, some differences exist with this approach. Foremost, the expected KE per event must be corrected for by the HCal sampling fraction (S_f) estimated by Monte-Carlo simulations[110]. This factor, usually between 5%-10%, reduces the expected energy normalization per event. Second, the above scheme and formula is more accurately applied to electromagnetic calorimeters (EMCals) where the sampling fraction is much higher - nearly 100% - and $\sigma_E^2 \approx E$ is a fair approximation. In reality for HCal, the σ_E^2/E_i ratio is not nearly unity and must be evaluated per kinematic — ideally per channel. To account for the energy dependence of the response, one typically finds of the energy resolution the following quadrature sum[85]:

$$\frac{\sigma}{E} = \frac{a}{\sqrt{E}} \oplus \frac{b}{E} \oplus c \tag{4.32}$$

As in electromagnetic calorimeters, a is the stochastic term that reflects the number of photo-electrons generated over events, b is the noise term that reflects electronics effects including pile-up, and c reflects dimensional variations and non-uniformity from detector geometry. For hadron calorimeters (HCals), the stochastic term dominates because the fluctuations in the energy deposition by hadrons are more significant compared to electronic noise and geometrical non-uniformities. While the stochastic term drops out of the chi-squared minimization after differentiation, the other terms, in principle, do not. However, to ensure that the data spectra match those produced by the Monte Carlo (MC) simulations, a single factor R is introduced to adjust the Sampling Fraction S_f. This factor R accounts for any discrepancies in the energy spectra due to inaccuracies in the MC energy spectra arising from geometry and detector response.

A more accurate way to extract this factor is via empirical fits to the energy spectra per channel, however sufficient data to extract this ratio accurately does not exist on all channels over kinematics. With the expected energy resolution of HCal between 30% and 70%, it is sufficient to estimate the energy spectra over all channels with MC and tune a single R factor per kinematic (all channels)

[110] See Appendix C for additional details.

to match MC. The resulting scheme is as follows:

$$\chi^2 = \sum_{i=1}^{n} \frac{\left(E_i - \sum_j c_j A_j^i\right)^2}{\sigma_E^2} \tag{4.33}$$

$$S_f^* = S_f \cdot R \tag{4.34}$$

$$E_i = \nu_i \cdot S_f^* \tag{4.35}$$

$$\sigma_E^2 \approx \nu_i \cdot S_f^* \tag{4.36}$$

$$\frac{d\chi^2}{dc_k} = 2\sum_{i=1}^{n} \frac{1}{\nu_i \cdot S_f^*} \left(\nu_i \cdot S_f^* - \sum_j c_j A_j^i\right) A_k^i = 0 \tag{4.37}$$

$$\sum_i A_k^i = \sum_i \sum_j \frac{A_j^i c_j A_k^i}{\nu_i \cdot S_f^*} \tag{4.38}$$

Where ν_i (the nucleon kinetic energy) is calculated from the elastic e' track per event, S_f is evaluated from MC, R is allowed to float to match calibration results to MC energy spectra, and A is ADC response summed over all block indices j,k and then over all events i. The last step in the scheme follows from minimizing the difference in the next-to-last step.

With this process in mind, the essential steps of the energy calibration are as follows:

1. Obtain a tight selection on elastic events with enough data to populate each channel in HCal with roughly 1000 events.
2. Loop over all events and calculate W^2 and the coincidence time (coin) for that event. Skip all events which fail global elastic cuts on subsystems and whose W^2 and coin values lie outside of the elastic mean $\pm 3\sigma$. Apply spot cuts to isolate elastic nucleons.
3. On each event, calculate the expected elastic recoil nucleon HCal location (x_{exp} and y_{exp}) and expected energy ν from the e' track. Skip all events whose expected positions do not lie within one block of the periphery on HCal.
4. On each event, calculate the expected event energy normalization (from above, $\nu * S_f/R$).
5. On each event, divide each ADC value from the primary block with its previous gain factor from the database. These values are one-to-one with HCal channels and are available for all

blocks on all events. This returns the raw pC value of the data.

6. On each event, add ADC values to the A_k vector (the left-hand side of 4.38, 288 elements) where they exist in the primary cluster.
7. On each event, add coupled ADC values to the $A_j \cdot A_k$ matrix (right-hand side of 4.38, 288 x 288 elements, $M_{j,k}$) and normalize each value in the matrix by the expected event energy normalization.
8. After the loop over events, check each element of the A_k vector to ensure sufficient events exist to calibrate (ideally, 100) and that the ratio of diagonal matrix elements $M_{k,k}$ to the A_k vector element is reasonable (a good lower limit is 5%). For each element which fails one of these tests:
   - Set $M_{k,k} = 1.0$.
   - Set $A_k = 1.0$.
   - Set $M_{k,j} = 0.0$ for all j≠k.
   - Set $M_{j,k} = 0.0$ for all j≠k.
9. Invert the matrix and calculate the coefficients: $M^{-1}_{j,k} \cdot A_k = c_j$.

After computing the coefficients (in GeV/pC), they are ready for the database.

Because ADC gain coefficients are affected by PMT HV and should not change as a function of nucleon momentum in the linear gain regime, a single set of coefficients for all kinematics is all that is necessary, in principle. However, due to the obstructed modules which led to a second set of HV settings used early in **GMn**, two total sets of ADC gain coefficients are included during data reconstruction[111]. Figure 72 depicts the match between data and Monte Carlo for sampling fraction and energy spectra using the same set of gain coefficients and the same value of R.

4.5.8 Supplemental Timing

Further timing corrections are possible for HCal signals by assessing and implementing adjustments for nucleon momentum dependent ToF and by using integrated ADC data to improve time-

[111]The second set of ADC gain coefficients are implemented with database timestamp for all runs after 2021-10-24 04:30:00. The plots in 72 are from the second set which covers the majority of **GMn** data.

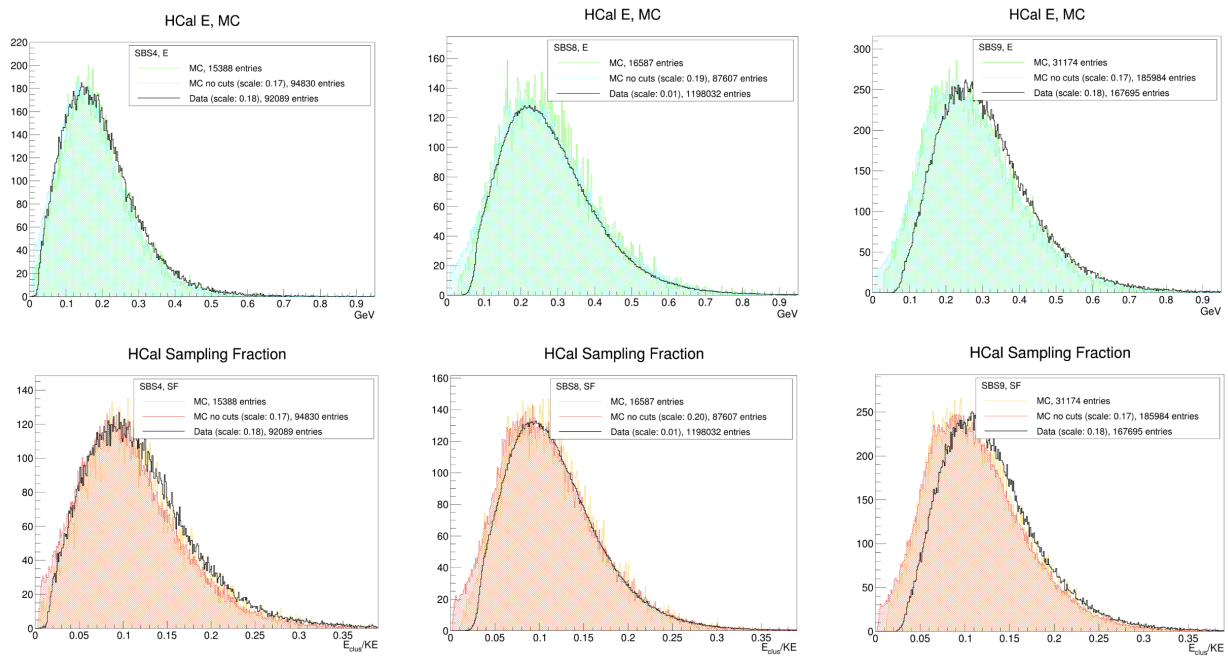

Figure 72: Data/MC comparisons after energy calibrations in HCal. The top row are energy spectra, the bottom row are sampling fraction spectra, the first column is from Q^2 =3.0 GeV^2 (SBS-4), the second column is from Q^2 =4.5 GeV^2 (SBS-8), and the third column is from Q^2 =4.5 GeV^2 (SBS-9). Quasielastic MC data are presented with and without cuts on electron track quality, HCal ADC time, W^2, and the dx vs dy proton spot. Data are presented with the same cuts placed on MC.

walk adjustments[112]. Both of these methods have been shown to modestly improve resolution for both ADC time and TDC time post-reconstruction.

To correct for nucleon momentum, simulations of elastic protons and neutrons from deuterium are first performed, configured per kinematic. A parameterized functional correction extracted from simulation distributions can be passed per event which depends only on the recoil nucleon momentum ($p_{N,\text{expected}}$, calculated per event from the e' track). Figure depicts the MC ToF vs p_N distributions determined from HCal surface crossing times for nucleons using the G4SBS elastic generator. This method depends on the functional form of the fit to ToF vs p_N for a given SBS configuration, but is typically adequate with 4 parameters, including an offset. The offset is ignored and the momentum dependence is isolated when issuing an event-by-event correction[113].

[112]The path-length dependence of ToF is largely absorbed into module-specific timing offset calibrations.

[113]Appendix C includes additional data including fits and fit parameters for all kinematics. Better timing calibrations

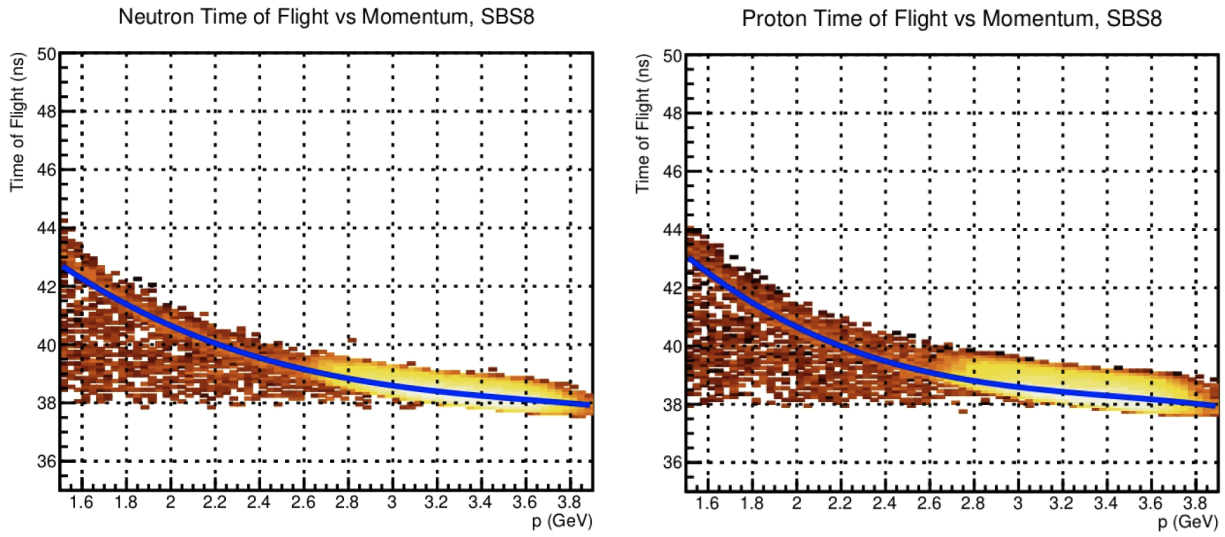

Figure 73: MC ToF vs p_N distributions using the G4SBS elastic generator (neutron on left, proton on right). The HCal sensitive detector boundary crossing time is used for ToF and MC truth information provides nucleon momentum and nucleon identification.

On determination of TDC and ADC time signals, there exists a dependence of the signal on amplitude of the raw analog waveform. This arises from the method used to extract TDC and ADC time, where both depend on an analog threshold crossing and the finite rise time of analog waveforms. This effect on timing measurements is known as *timewalk* and can see supplemental corrections channel-by-channel or with a single set of parameterized corrections.

For a channel-by-channel approach to account for this effect, it is enough to fit time vs energy distributions (after elastic cuts) and extract fit parameters by channel, then apply them event-by-event to correct for timewalk. The process is as follows:

1. Obtain a wide selection on elastic events with enough data to populate each channel in HCal with roughly 1000 events.
2. Populate 2D histograms from the primary cluster of TDC vs primary block energy and ADC time vs primary block energy.
3. Fit these distributions. Several fits are possible, such as polynomial or dying exponential,

may be achieved via a simultaneous fit to all parameters which impact timing offsets and distributions, but this analysis is not presented here.

but the traditional fit is recommended for these data:

$$\Delta t = p_0 + p_1/E^{p_2}, \tag{4.39}$$

where p_0, p_1, and p_2 are fit parameters and E is the energy derived from integrated ADC per event. Typically p_2 is constrained to be 0.5 or very close to 0.5. The p_0 arbitrary offset can be safely ignored when passing corrections with this fit.

4. Obtain fit parameters by block. For the traditional fit, this entails 288 (channels) x 2 (fit) parameters.
5. Loop over all data again and calculate the correction for the primary block in the primary cluster. Apply these corrections to TDC and ADC time values.

Within a 100-200 ps, a single set of fit parameters gathered from data over all channels exacts the same utility. Figure 74 demonstrates the utility of post-reconstruction timewalk corrections to TDC signals where low amplitude variation on the order of 2-3 ns can be seen.

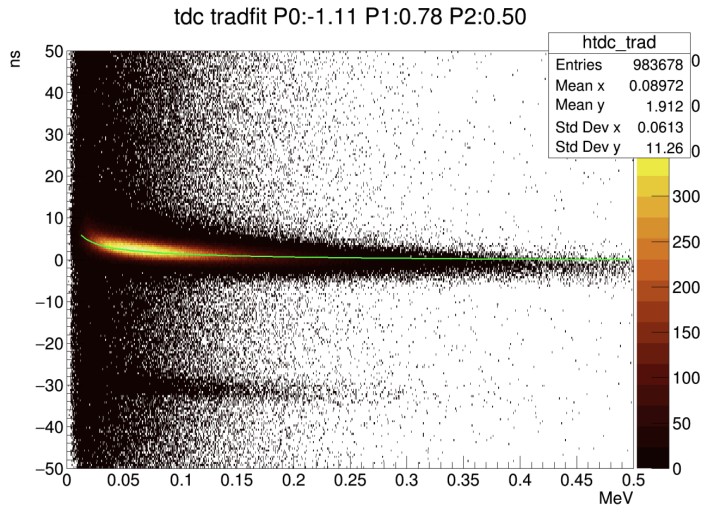

Figure 74: Aggregate TDC (all channels) vs HCal primary block energy depicting timewalk effects. The green fit is of the form in 4.39 and fit parameters are included in the title of the histogram.

Note that the linear interpolate method used to calculate the ADC time which already exists in SBS-offline largely mitigates the emergence of timewalk. As such, post-reconstruction timewalk

corrections are primarily useful for improving TDC times in HCal.

4.5.9 TDC Efficiency and Latency Jumps

Throughout **GMn** analysis, ADC time will be used to provide the means to subtract random coincidences and better select on elastic events, despite the better timing resolution inherent to TDC measurements. Primarily, this is because many TDC signals are not available for channels with good ADC hits and times. In terms of the reconstructed data tree, missing TDC signals are represented by a measurement of 1e38 for the channel - a placeholder indicating that no relevant leading edge TDC signal exists for the event. Due to the adequacy of ADC time for **GMn** analysis and potential loss of important data if TDC signals are required, ADC time is preferred for coincidence time cuts in this analysis.

The frequency of TDC signal loss can be quantified in terms of "TDC efficiency" (TDC_{eff}) defined in the usual manner for efficiency:

1. $TDC_{eff} = \frac{TDC_{det}}{TDC_{exp}}$,

where TDC_{det} is the total TDC signals detected and TDC_{exp} is the total TDC signals expected. To determine TDC_{exp}, the total number of events which pass the following three criteria is assessed:

- Pass wide elastic cuts
- The HCal primary cluster centroid exists and is within active area
- The elastic projection from e' track lands on the active area of HCal

To determine TDC_{det}, three methods are viable:

- Method "Primary block": The primary block in the primary cluster has TDC data.
- Method "Reconstructed": Any block in the primary cluster has TDC data.
- Method "TDiff Reconstructed": Any block which has TDC data and also survives a wide time consistency cut (same-block ADC time - same-block TDC time) ensuring time is not due to unrelated hit in the same channel.

Figure 75 demonstrates the decline in TDC efficiency as a function of nucleon KE for all three TDC_{det} assessment methods.

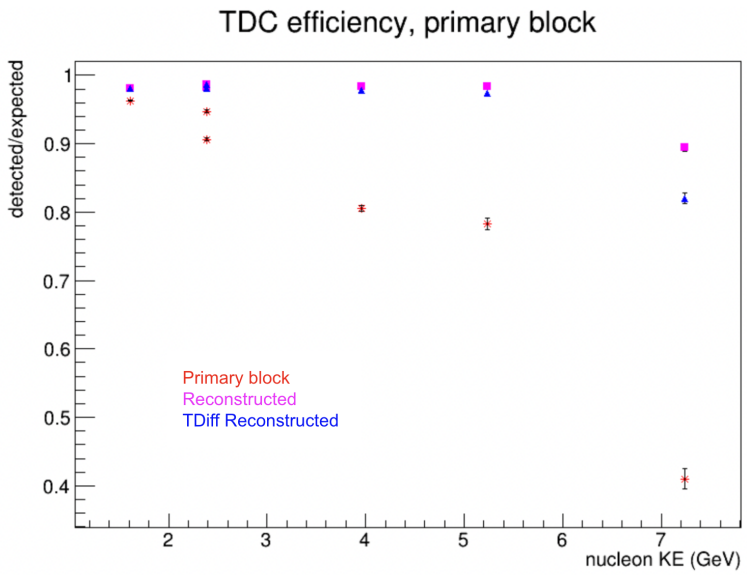

Figure 75: TDC signal efficiency (TDC_{det}/TDC_{exp}) vs quasielastic nucleon central momentum over all **GMn** kinematics. The different methods to assess TDC_{det} are indicated by color and marker type, with "Primary block" red stars, "Reconstructed" magenta squares, and "TDiff Reconstructed" blue triangles. The trend towards lower efficiency at higher nucleon momentum is obvious. Error bars are binomial error.

The fundamental flaw in the TDC data taken during **GMn** is related to the TDC threshold set at the beginning of **GMn**. In order to prevent loss of signals at low amplitude and in recognition of the multi-hit buffer which F1TDCs feature, TDC signal thresholds were set very low ($\approx$ 10 mV). However, whether due to pileup or signal buffer overload, signals with higher central quasielastic nucleon KE result in many hits which overwhelm the ability of the TDC to resolve signals. By raising the TDC threshold, many low amplitude signals are lost, but importantly, the high amplitude signals are preserved[114]. This issue was corrected for later SBS experiments where the high resolution of TDCs in HCal are more important for the analysis.

While the TDC signal loss mechanism was discovered and rectified, the DAQ-related latency jumps which necessitate multiple timing calibration sets has not. While these latency jumps can, in principle, be calibrated via offset parameter and corrected, in extreme cases during **GMn** the

[114]It is an important note that the best timing signature from any cluster in HCal most probably arises from the highest energy block within it.

latency shifts were large enough to shift the ADC signal out of the window. While such extreme latency shifts were rare and swiftly corrected, they resulted in several hours of wasted beam time[115].

4.5.10 GMn Performance

Broadly speaking, HCal performance in GMn matched expectations set by simulation generated before **GMn**, with a few caveats. Simulations describe the position and energy resolution of HCal with confidence, but calibrations for MC timing have room for improvement. As such, early expectations for timing resolution in HCal were often set primarily by the precision of F1TDCs and their prior performance; around 500 ps. These expectations would always be a reach because they fail to explicitly account for added variance in time measurements caused by experimental conditions including radiation propagation and shower formation in HCal.

As a result, timing resolution analysis here is presented as a current status of an ongoing effort. Resolution is taken to be the standard deviation of the elastic HCal time signal peak after various corrections[116]. These corrections include all those introduced during data reconstruction and also the following:

- Trigger corrections using the BBCal shower ADC time
- Best cluster selection using the "in-time" algorithm
- Timewalk corrections using traditional fit parameters and cluster energy
- Nucleon momentum-dependent time of flight corrections using the expected elastic nucleon momentum derived from e' track information

Naturally, the following also apply to this analysis:

- Good electron track cuts, elastic selection, and coincidence time cuts to subtract randoms and improve corrections
- Zero field data to eliminate variation in scattered nucleon path length

[115] Several other issues including rollover timing, double peaking, and 4ns jitter were noted and addressed throughout analysis and experimental running. See [162] for more details.

[116] Loose cuts on elastic events (W^2 and proton spot) are sufficient for this analysis.

- Hydrogen data to isolate protons and constrain target nucleon momentum

Figure 76 demonstrates the effectiveness of these supplemental methods alongside the resolution improvement from the trigger correction after reconstruction. The data presented are over many aggregated channels, so 76 does not represent the baseline resolution of HCal TDC timing.

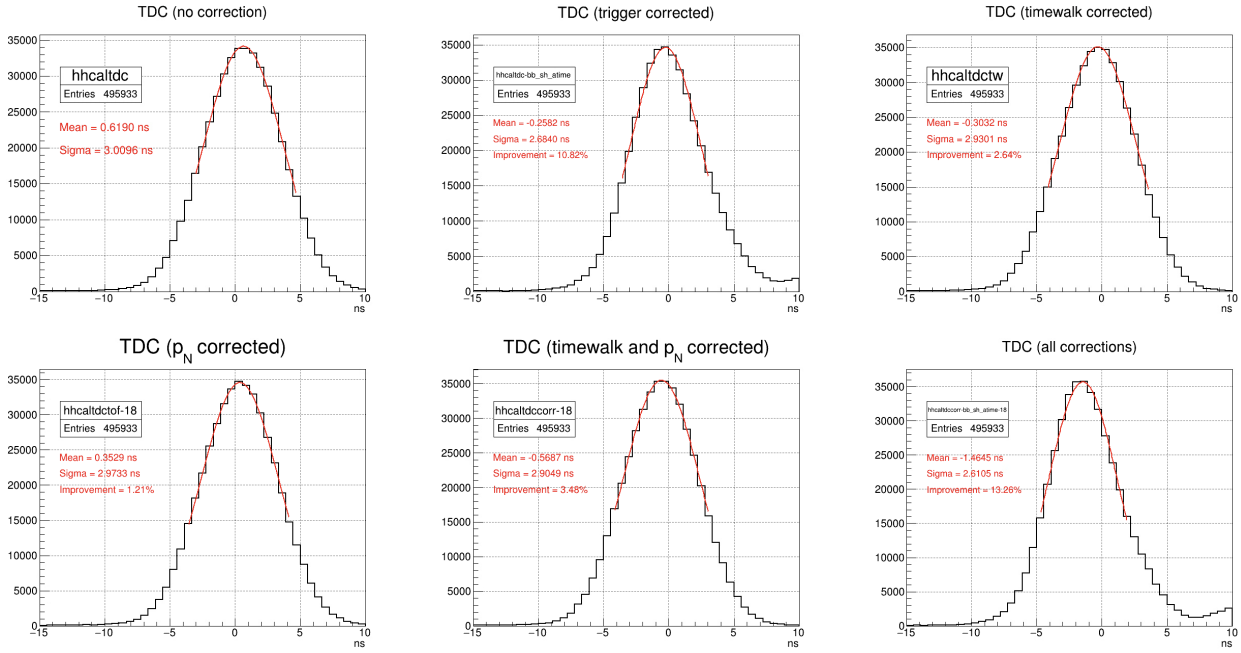

Figure 76: Elastic TDC data from $Q^2 = 4.5$ GeV^2 (SBS-8) over all HCal channels demonstrating the effects of the various supplemental and trigger corrections to TDC time. All fits Gaussian from the first point at half-maximum to the second point at half-maximum. The percent improvement from the uncorrected TDC are included. The smaller peak emerging on the "all corrections" plot is related to ADC "double peaking" introduced with the trigger correction, which has recently been corrected.

A better, but by no means perfect, measure of the baseline HCal TDC timing resolution is possible by taking the difference between the highest energy and second highest energy blocks in the primary cluster per event. To account for possible variation from misalignment between channels, a series of histograms may be built between each block and its immediate neighbor in index sequence. This results in 287 potential distributions on a data set of the difference in TDC time from highest energy block in the primary cluster (index i) and the next-highest energy block in the primary cluster (index $i+1$). Each of these distributions is fitted with a Gaussian and the

standard deviation is assessed. A distribution of these standard deviations gives a measure of the central limit of internal TDC resolution for HCal. This measure is not sensitive to variation from the trigger, time of flight effects, or alignments. Figure 77 shows the distribution of all differences between the highest energy block and the second highest energy block (left) along with the series approach (right) for Q^2 = 3.0 GeV^2 data (SBS-4)[117]. Table 22 aggregates this information.

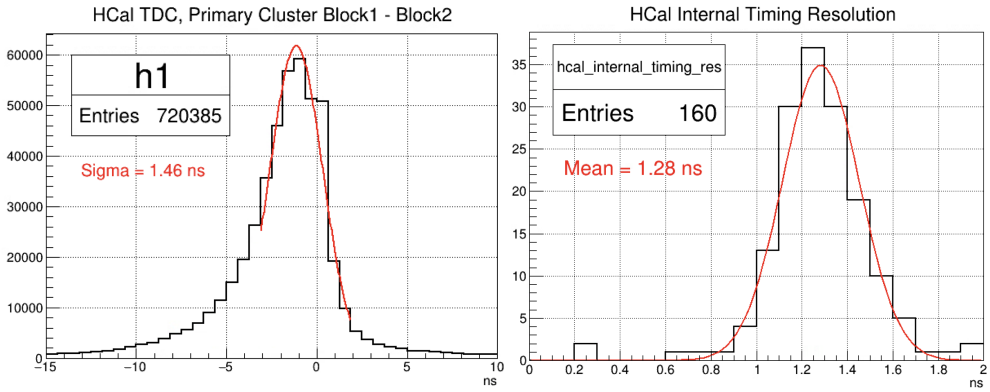

Figure 77: Comparison of internal timing resolution measurements for HCal. On the left is the total distribution of all primary cluster highest energy block (b1) and primary cluster second-highest energy block (b2) differences. On the right is the distribution of all of these differences with the constraint that b2 is positioned adjacent to the right of b1, with peak positions aligned. Timewalk corrections have been applied to the highest energy block only due to the inaccuracy of these corrections for low energy signals.

TDC Correction	Resolution (ns)	Improvement (%)
None	3.01	0
Trigger	2.68	10.82
Timewalk and p_N	2.93	2.64
p_N	2.97	1.21
Timewalk and p_N	2.9	3.48
Trigger, Timewalk, and p_N	2.61	13.26
Internal b1 - b2	1.46	51.50
Internal b1 - b2 (adjacent)	1.28	57.48

Table 22: HCal TDC Timing Resolution by Correction (Q^2 = 3.0 GeV^2, SBS-4)

It should be noted that timing variation introduced by the trigger which are not, as of this writing, adequately corrected for by Hodoscope calibrations greatly impact the baseline timing

[117]The timing resolution of HCal is likely to improve with higher nucleon momentum kinematics, but datasets are limited after cuts and make characterization of block to block differences difficult.

resolution of HCal. Inclusion of improved trigger timing corrections on later reconstruction passes present an opportunity to return to this HCal analysis with better potential to estimate the best possible in-beam resolution from HCal TDCs and ADCs.

In terms of consistency with expected resolutions, position reconstruction is better calibrated. Simulated data reproduces the relevant experimental conditions and geometries well and provides a good baseline for comparison. Position resolutions are the standard deviations of dx and dy plots generated with the proton and neutron gun generators in G4SBS[118]. These raw data, generated over a large range of nucleon momentum and constrained by the position acceptance limits of HCal, are digitized and replayed to more accurately model detector response. Figure 78 depicts the result of these simulations for many values of the proton and neutron momentum.

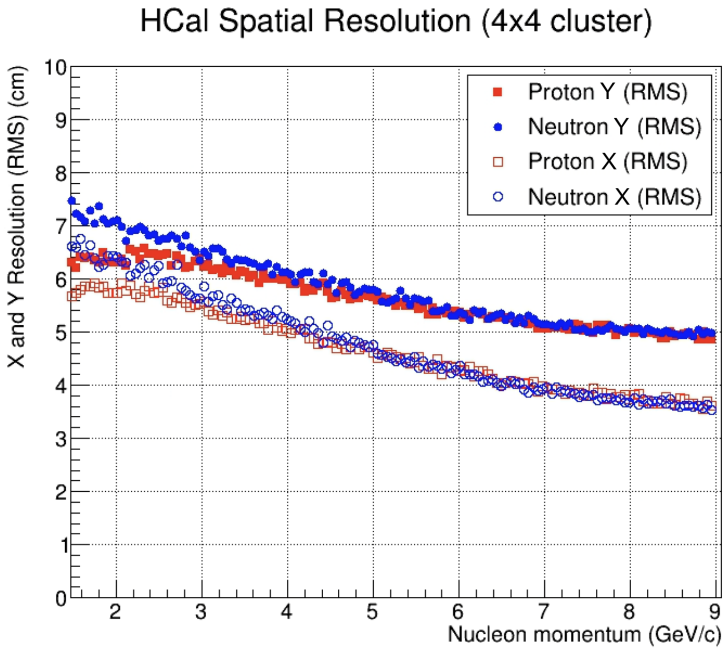

Figure 78: Digitized and reconstructed MC results for dx and dy using the proton and neutron gun event generators in G4SBS. These results are presented as a function of the nucleon momentum.

Obtaining the position resolution from real data is also possible[119]. Simple fits over zero-

[118] dx and dy are calculated with a slight difference - MC truth information informs the expected location of the nucleon.

[119] A better approximation of the baseline HCal position resolution would require unfolding the contributions from particle kinematics and BigBite angle, vertex, and momentum resolutions.

SBS-field hydrogen $dx(dy)$ distributions with good electron track cuts, W^2 cuts, $dy(dx)$ cuts, and coincidence time cuts isolate and characterize the peaks well[120]. Gaussian fits to these distributions and subsequent extraction of the standard deviation from these fits estimate real data resolutions[121]. Fits to these data are presented in figures 79 and 80. Table 23 contains resolutions extracted for each kinematic setting containing data taken with hydrogen and SBS field at zero percent.

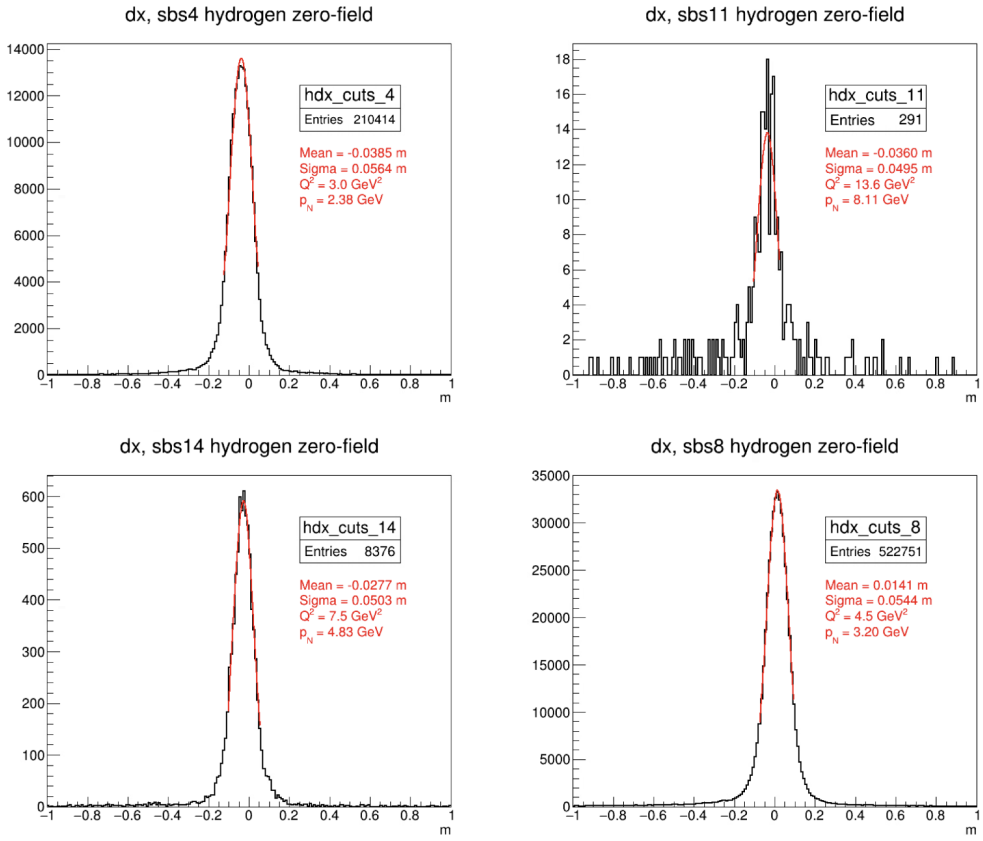

Figure 79: Position resolution extractions from all kinematics with available zero-field hydrogen data. All plots are over the dispersive x direction.

During normal ADC gain calibration operations, energies and sampling fractions for HCal are checked against MC results as an essential part of the process[161]. These comparisons show that MC reproduces the real data energy and sampling fraction spectra well. Table 24 describes the

[120]For instance, for dx a good independent kinematic correlation cut would be $|dy| < 0.3$ m.

[121]dx and dy are not strictly speaking normal distributions due to their long radiative tails. Gaussian fits to the peaks, however, represent the data well. A fit scheme is used which fits the one-third-max amplitude on either side of the mean to extract a standard deviation.

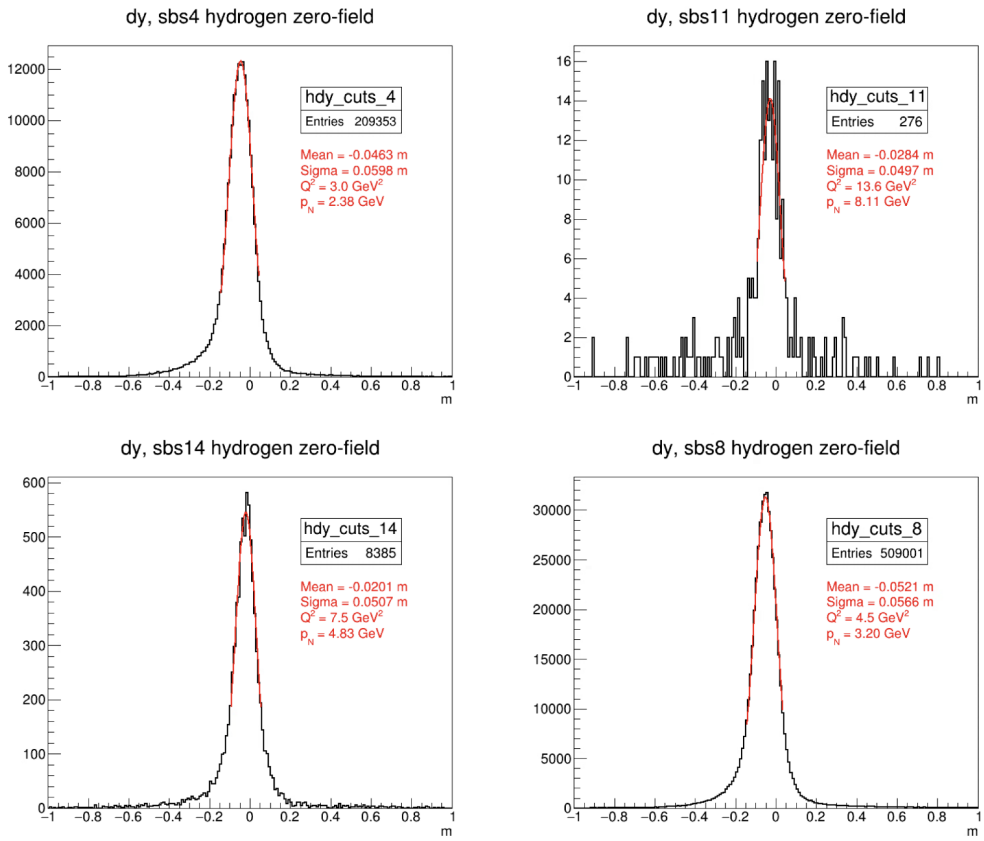

Figure 80: Position resolution extractions from all kinematics with available zero-field hydrogen data. All plots are over the transverse y direction.

overall energy resolution per kinematic, where the resolution E_{res} is as usual for calorimeters:

$$E_{\text{res}} = \frac{\sigma_E}{E} \tag{4.40}$$

4.6 HCal Detection Efficiency

Clean detection of quasielastic events in BigBite does not guarantee that a quasielastic nucleon will be detected in HCal. The detection efficiency of HCal ($\varepsilon_{\text{HCal}}$) can be defined thus:

$$\varepsilon_{\text{HCal}} = \frac{N_{\text{detected}}}{N_{\text{expected}}} \tag{4.41}$$

Kinematic	p_N (GeV)	x-resolution (cm)	y-resolution (cm)
4	2.38	5.64	5.98
11	8.11	4.95	4.97
14	4.83	5.03	5.07
8	3.2	5.44	5.66

Table 23: HCal position resolution by kinematic. All data with SBS magnetic field at 0% where available, otherwise the largest dataset is analyzed.

Kinematic	Q^2	KE_N (GeV)	HCal σ/E
4	3.0	1.62	67 %
7	10.0	5.26	42 %
11	13.6	7.22	41 %
14	7.5	3.98	41 %
8	4.5	2.40	55 %
9	4.5	2.40	45 %

Table 24: HCal Energy Resolution

This efficiency is expected to vary depending on the detected nucleon, owing to the differences in principal forces experienced by charged quasielastic protons and neutral quasielastic neutrons as they traverse HCal. Further, precise determination of this efficiency is crucial for absolute cross section measurements to normalize quasielastic yields.

For **GMn**, nucleon detection efficiency cannot, in principle, be ignored in the ratio method. Fortunately, HCal's design leads to high and similar detection efficiencies for both protons and neutrons, reducing the impact on the extraction of the cross-section ratio. However, this does not eliminate the need to verify nucleon detection efficiency in HCal. Deviations from unity in the HCal nucleon detection efficiency ratio are a significant source of systematic error that must be estimated. Efforts will be presented here to determine the HCal nucleon detection efficiency from MC and from real data. Comparisons will inform estimates of systematic error.

4.6.1 Monte Carlo

As in the extraction of HCal position resolution, extraction of HCal nucleon detection efficiency in MC is performed with the isolated proton and neutron generators. These generators build separate energy spectra per nucleon across a configurable phase space where the position acceptance is limited by HCal geometry and the momentum range is configured to cover the kinematics of **GMn**.

Roughly 500k events are sufficient to populate each channel in HCal with 1000 events, where the simulation throws flat in position and p_N. Figure 81 depicts the mean and standard deviations from Gaussian fits to many energy spectra slices in p_N. The HCal detection efficiency (HDE) is computed from these slices:

$$\text{HDE} = \frac{N_{\text{pass}}}{N_{\text{total}}}, \tag{4.42}$$

where N_{pass} is the total number of events passing a $\overline{E}/4$ threshold per slice and N_{total} is the total number of events per slice. This method is designed to estimate the efficiency of HCal based on the energy losses dependent only on the geometries and materials in HCal.

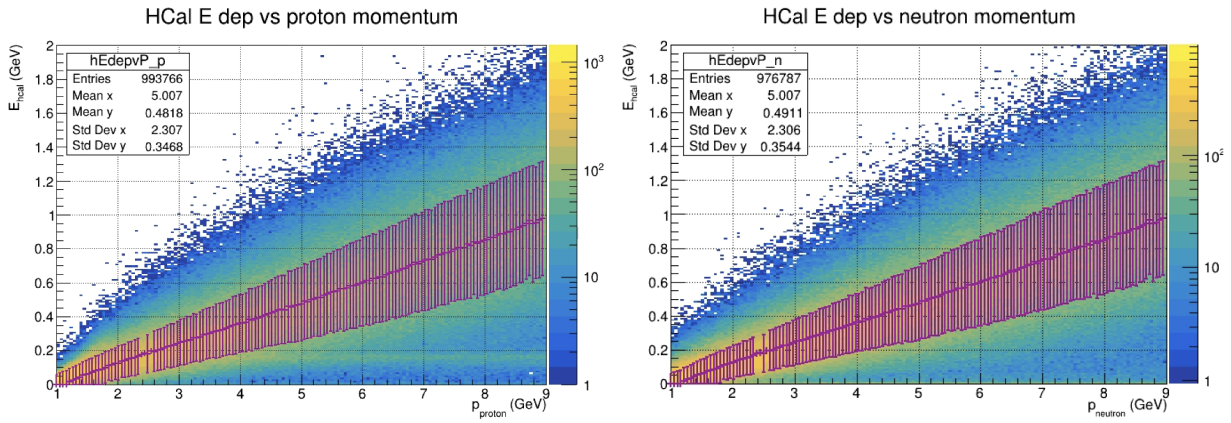

Figure 81: Simulated HCal energy vs proton(neutron) momentum on the left(right). Simulated data are from G4SBS proton and neutron generators then digitized and replayed. Gaussian fit means ($\overline{E}$) and standard deviations are indicated in red.

There is no *a priori* reason to set the threshold to $\overline{E}/4$, and adjustment of this threshold between $\overline{E}/4$ and $\overline{E}/2$ uniformly shifts HDE roughly 3%. Relative HDE between neutrons and protons is roughly uniform, however, and HDE remains high even when the threshold is adjusted to nearly half of the mean energy.

4.6.2 Real Data Methods

Comparing the HDE modeled in MC to real data provides assurance that simulated results for HCal variables are reliable. Many methods have been explored to extract the proton HDE from

data. Perhaps the most straightforward method can be called the "delta spot check method." Of the methods explored, this method has the advantage that it provides extracted efficiency as a function of HCal position.

To extract the expected number of protons, the method is as follows:

- Use hydrogen data to select on proton events.
- Make tight optics validity cuts on the data[122].
- Make tight track validity cuts on the data. These cuts include track vertex position, track maximum χ^2, and minimum GEM plane hits on primary track cuts.
- Make tight electron arm elastic and PID cuts to select on elastic electrons. These include cuts on W^2 and BBCal preshower energy. The W^2 cut should be very tight to eliminate significant inelastic contamination.
- Make fiducial cuts on the expected nucleon positions which eliminate events which project protons off of the active area of HCal.

Events which pass these cuts are the expected elastic protons, as determined from electron arm variables and sensitive to the acceptance limits of HCal. To extract the detected number of protons, the method is the same - save one difference:

- Make a spot cut on kinematic correlations dx vs dy.

This added cut checks to see if an event with an expected proton on HCal has a corresponding detection close to the expected position. The proton HDE is the ratio of detected to expected, as usual. For each of the detected and expected sets, one can plot x_{exp} and y_{exp}. Division of these two histograms yields the proton HDE as a function of x_{exp} and y_{exp}. Figure 82 depicts the result of this method for the $Q^2 = 3.0$ GeV^2 hydrogen data set.

The size of the spot cut strongly influences the proton HDE. Due to the non-Gaussian tails evident in dx and dy, an empirical method is used to determine the spot cut parameters for efficiencies extracted with this method. The mean is first assessed via Gaussian fit to each of the dx and dy peaks. Then the number of standard deviations necessary to include 97% of the data in each is

[122] See Appendix B for more details.

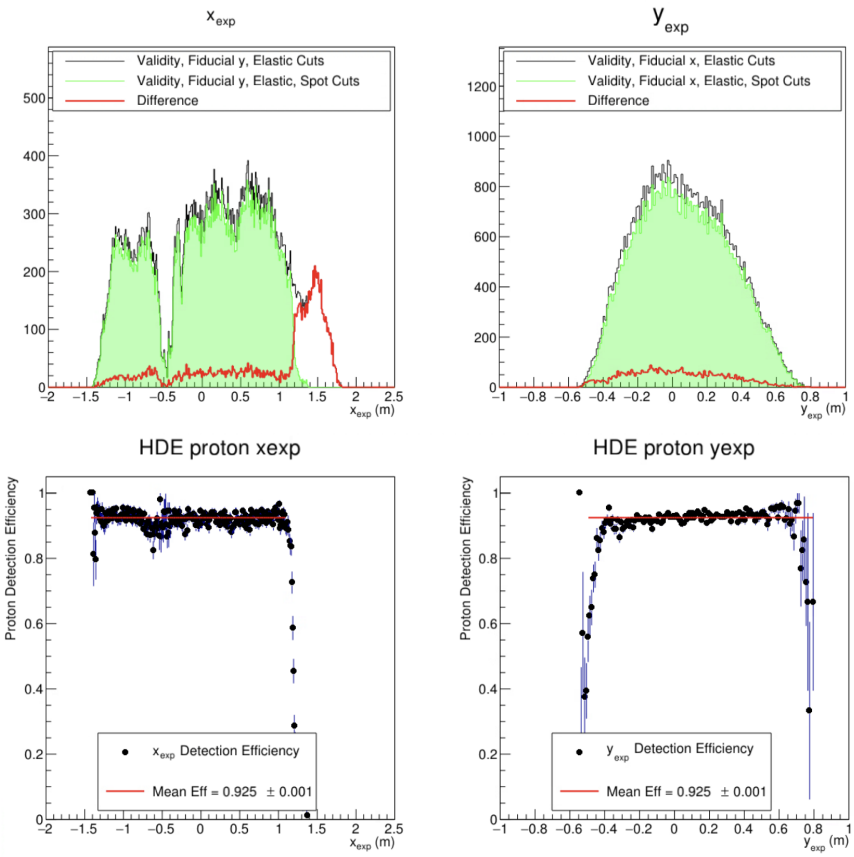

Figure 82: (**top row**) Clean elastic proton events with projections on HCal (black) are plotted with detected elastic events (green) and the difference (red). (**bottom row**) Proton HDE as a function of expected location of elastic protons from e' tracks. The relatively empty areas are due to dead GEM sectors.

determined for Q^2 = 3.0 GeV^2 data (SBS-4)[123]. SBS-4 provides a good baseline because signal to background is very high after tight elastic selection[124].

After establishing spot cut limits in terms of nucleon dx and dy nucleon peak standard deviations from high signal to background in real data, the same set is applied to other Q^2 data sets to extract proton HDE from those data sets, accounting for the value of σ_{dx} and σ_{dy} per data set. Without further analysis, data and MC agree within a few percent without adjustment of the MC energy threshold cut. While the overall scales of the MC and data can be adjusted—by setting a larger spot cut region in the case of data or by adjusting the detected threshold energy for MC—the

[123]While the delta distributions are not Gaussian and exhibit radiative tails, their peaks evaluated from half-max are modeled well by a Gaussian fit. These standard deviations are referenced here.

[124]These empirical spot cut limits are $\sigma_{dx} = 5$ and σ_{dy}=6.

relative positions of data within each set should remain consistent[125]. Following this reasoning, better comparisons between data and MC can be made by setting the MC energy threshold cut to achieve a match between data and MC HDE. With this adjustment to proton HDE, figure 83 depicts a comparison between predicted MC and data at p_N = 3.2 GeV. The red markers indicate points without a "dip correction" which will be addressed in the next section.

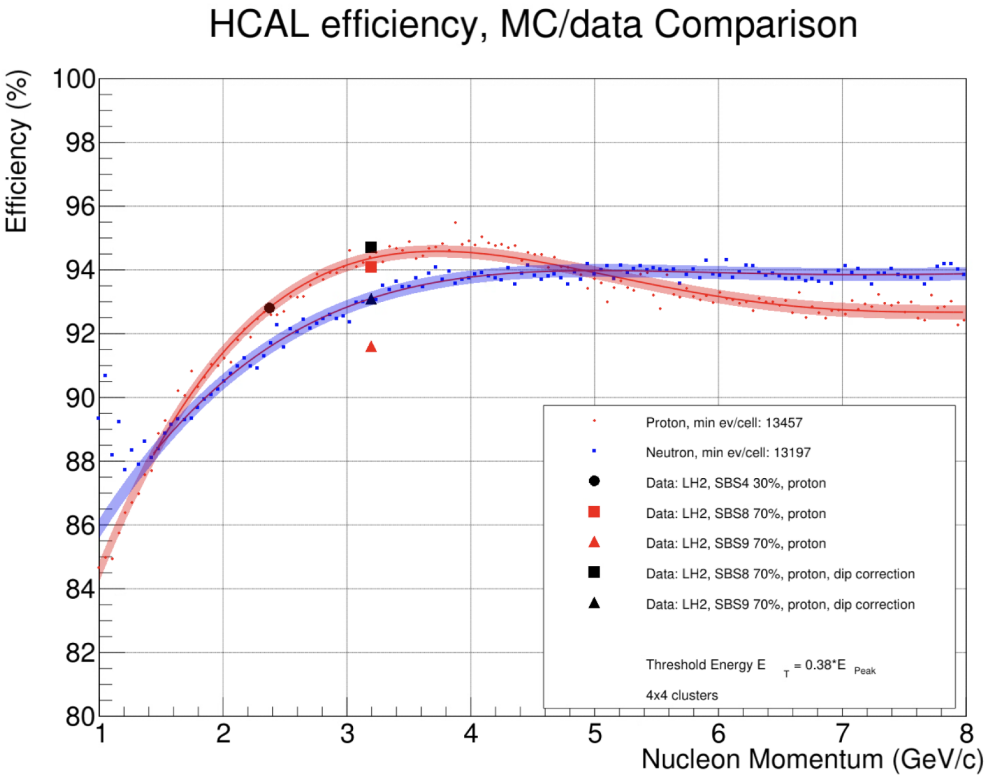

Figure 83: Comparison of HCal HDE for proton between data and MC. The match at p_N = 2.4 GeV (SBS-4) is arbitrary while the comparisons at p_N = 3.2 GeV (SBS-8 and SBS-9) are not arbitrary and represent the ability of the MC to reproduce the measured proton HDE. MC error band is binomial error. The MC energy threshold is indicated in the legend. Real data includes error bars which are too small to see on the scale of the figure.

This method can also be used on deuterium data, but the efficiencies suffer from precision losses due to cross-nucleon contamination in dx and poorer position resolution due to fermi smearing, added inelastic contamination, and acceptance losses. Additional HDE extraction methods are included in Appendix B.

[125]The principal assumption, which may be verified by MC, is that the shape of the dx and dy radiative tails relative to their respective peaks does not change significantly as a function of SBS field strength.

4.6.3 Efficiency Uniformity

HCal is designed to have uniform detection efficiency across its acceptance. However, as has been previously described, several channels in HCal exhibit poor performance consistent with obstructed light within the associated module. Figure 84 depicts the dispersive direction proton HDE extracted from $Q^2 = 4.5$ GeV^2 (SBS-9). The large "dip" at around 0.3 m is consistent with modules with poor efficiency. This inefficiency is notably pronounced in SBS-9 due to the relative concentration of quasielastic nucleons on the face of HCal for this kinematic configuration. Measurement of the proton detection efficiency can be made to exclude this "dip" region, as in 83, to provide a better comparison to raw MC which does not account for inefficient HCal modules.

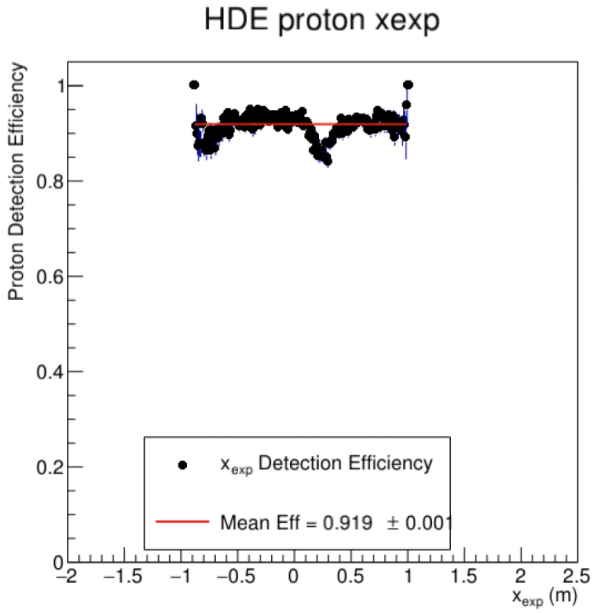

Figure 84: HCal proton detection efficiency for $Q^2 = 4.5$ GeV^2 (SBS-9). The significant non-uniformity is clear around 0.3 m and affects the proton HDE significantly for this kinematic.

Efforts have been made to account for this efficiency loss in MC via the modification of channel-specific gain factors during reconstruction of MC events. By reducing the gain factors for all channels observed to be affected by light obstruction (as in 117 and 118) significantly, a qualitative agreement between real data and MC proton HDE is recovered[63][126]. Figure 85 de-

[126]The reduction factor decreases the baseline gain from 10^6 to 10^3, effectively reducing all but the strongest signals

picts this comparison.

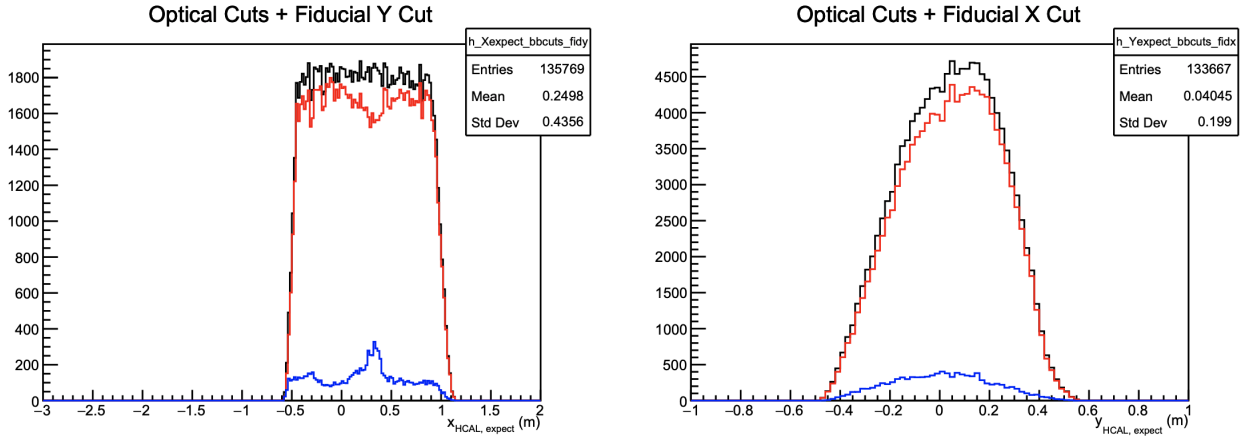

Figure 85: Proton HDE determined from gain-adjusted MC. All HCal channel affected by light obstruction have gains reduced by a factor of 10^3[63]. "Optical cuts" are optics validity cuts described earlier in the chapter.

For real data collected at Q^2 = 4.5 GeV^2 (SBS-8 and SBS-9), empirical efficiency maps can be created from SBS magnet setting hydrogen data at 0%(70%) to account for the efficiency loss of neutrons(protons). A combined efficiency map which is the product of the factors from both field settings is included in Appendix C[127]. This method suffers from only partial coverage over kinematics and, due to the ad-hoc nature of the correction, fails to address the issue at the root — namely the PMT gain. Reproduction of the empirical proton HDE distributions with gain adjustments during MC data reconstruction is a more robust and consistent method to address this non-uniformity, but may not meet the precision possible with an efficiency map. Further analysis of HDE will clarify this.

4.6.4 Remarks on Neutron Detection Efficiency

While proton HDE is more easily measured with a hydrogen target, extracting neutron HDE is very challenging. This difficulty arises from the lack of a clean and unambiguous denominator for an NDE calculation. In quasielastic scattering from deuterium, it is impossible to know *a priori*

from these channels to zero. Additional tuning of these gain factors will be necessary to better represent the gain reduction observed in the real data energy spectra for each affected channel.

[127] Validity of this efficiency map assumes similar detection efficiency between protons and neutrons.

whether the scattering occurred on a proton or a neutron. Although a clean sample of neutrons can be obtained from $\gamma p \to \pi^+ n$ events using downbending track analysis, the acceptance for this event topology is very small, populating only a limited region at the bottom of HCal. Additionally, BigBite's resolution is insufficient to suppress backgrounds from non-exclusive final states, such as multi-pion production, which are necessary to establish a denominator for the NDE calculation, especially with an untagged photon beam with a wide energy spectrum.

The compared proton HDE between real data and MC demonstrate reasonable agreement, along with HCal energy and sampling fraction spectra over a large range of Q^2, so it is assumed for this analysis that neutron HDE agrees within a similar margin of error[128].

4.7 Additional Corrections

Due to the emergence of HDE position-dependent losses likely related to obstructed blocks, corrections to the MC may be passed per event with HCal efficiency maps to weight the event based upon the projected x position, accounting for both protons and neutrons. To apply these corrections and to calculate physics quantities per event, this analysis makes use of a second data reconstruction step[129]. A single HDE weight per event is produced which can be applied to kinematic correlation plots to correct quasielastic yields and the scale factor ratio R_{sf}.

A second correction is applied to all real data events to account for the correlation between dx and the HCal dispersive position x evident in each data set. This correlation arises due to the incident-angle, which is related to the longitudinal profile of hadronic shower development. The correlation can be corrected by assuming an "effective z" displacement that is larger than the nominal value from the survey. This involves projecting to a plane inside HCal or even beyond

[128] Much work was done to make the case for a tagged neutron kinematic point using the $\gamma p \to \pi^+ n$ channel during the SBS experiment **GEn-RP** using Hall A's HRS spectrometer. Unfortunately, such a kinematic point was not added. See [55] for details.

[129] Many additional calculated quantities like kinematic correlations and timing corrections are added to the output tree during the second reconstruction step. The output of this step is a flat tree structure which enables simple draws of all variables, removing the need to loop explicitly over all events to perform analyses. In addition to being much faster, analysis tools like uproot and python libraries are much more capable after the data has been "cooked" in this fashion. This step is performed for simulated results as well to ensure parallel analyses of both data sets.

its back surface, rather than to the front surface. Figure 86 demonstrates the effectiveness of this offset in reducing the correlation for $Q^2 = 4.5\,\mathrm{GeV}^2$ data (SBS-8)[140]. Table 25 summarizes the offset-corrected distances used in this analysis to correct real data distributions.

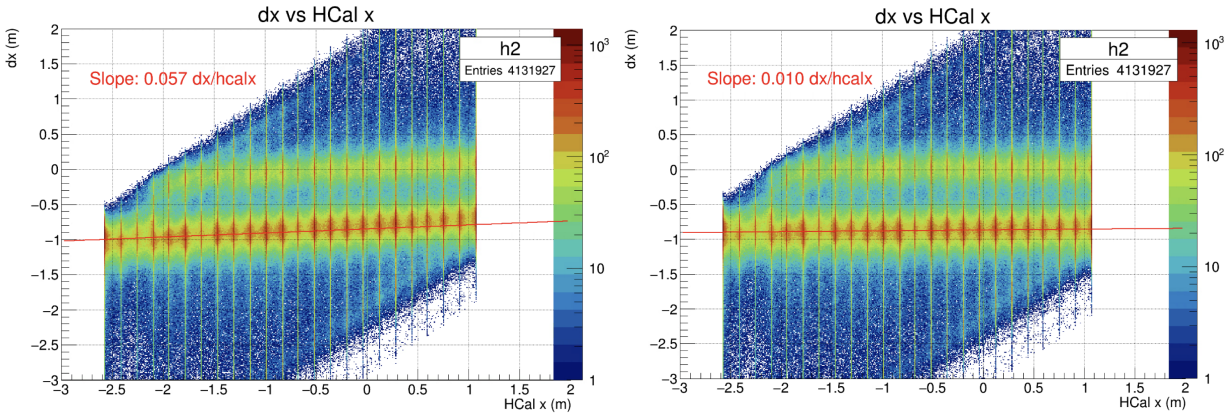

Figure 86: dx vs HCal vertical position x. The left(right) plot shows the correlation between the two apriori uncorrelated variables before(after) "effective-z" corrections. The new HCal-target distance with effective-z correction reduces the correlation between dx and HCal x by 82.5%.

Kinematic	Q^2 (GeV^2)	HCal-Target Distance (nominal, m)	HCal-Target Distance (effective, m)
4	3.0	11.0	11.65
7	10.0	14.0	14.925
11	13.6	14.5	15.77
14	7.5	14.0	15.13
8	4.5	11.0	11.77
9	4.5	11.0	11.7

Table 25: HCal-Target Distances

4.8 GMn

Extraction of **GMn** can be performed with implicit nuclear and radiative corrections with a scaled match between simulated and real data. The simulated data include all significant corrections with weights and several branches exist on the tree which include MC truth information. Nucleon type is part of this set. What remains is to extract the quasielastic cross section ratio with this information.

4.8.1 Ratio Method and Fiducial Cuts

Via separation and simultaneous detection of scattered protons and neutrons from $d(e,e'n)p$ and $d(e,e'p)n$ reactions, the SBS spectrometer measured the ratio of proton to neutron yields N_n/N_p. In the absence of a sufficiently dense free neutron target, deuterium is ideal and was used due to the loose binding between the proton and neutron in the deuteron and high density when kept liquid (22° K).

The yield ratio is the experimental observable R'':

$$R'' = \frac{N_n}{N_p} = \frac{\frac{d\sigma}{d\Omega}\Big|_{\text{d(e,e'n)}}}{\frac{d\sigma}{d\Omega}\Big|_{\text{d(e,e'p)}}}, \tag{4.43}$$

which expresses the raw uncorrected quasielastic cross sections and does not account for nuclear effects and radiative corrections. After corrections are applied where $R' = R''/(1+\varepsilon_{\text{nuc}})$, R' can be obtained which is related to G_M^n with the Born approximation (equation 1.74):

$$R' = \frac{\frac{d\sigma}{d\Omega}\Big|_{\text{n(e,e')}}}{\frac{d\sigma}{d\Omega}\Big|_{\text{p(e,e')}}} \equiv \frac{\frac{\sigma_{\text{Mott}}}{\varepsilon_n(1+\tau_n)}\left(\varepsilon_n G_E^{n^2} + \tau_n G_M^{n^2}\right)}{\frac{d\sigma}{d\Omega}\Big|_{\text{p(e,e')}}} \tag{4.44}$$

Here, R' is the corrected quasielastic cross section ratio. The σ_{Mott} term cancels on the right hand side of the equation[130]. Solving for G_M^n:

$$G_M^n = \sqrt{R' \cdot \frac{\varepsilon_n(1+\tau_n)}{\tau_n \varepsilon_p(1+\tau_p)} \cdot \sigma_r^p - \frac{\varepsilon_n G_E^{n^2}}{\tau_n}}, \tag{4.45}$$

where σ_r^p is the reduced cross section of the proton and all other parameters defined as usual.

Because many of the systematic uncertainties are shared between simultaneous measurements and cancel on the cross section ratio, R'' sees a substantial reduction of systematic error. Among these systematics, R'' is insensitive to target thickness, target density, beam intensity, data acquisition (DAQ) dead time, trigger efficiency, electron acceptance losses, track reconstruction efficiency,

[130] $\frac{d\sigma}{d\Omega}\Big|_{\text{p(e,e')}} = \frac{\sigma_{\text{Mott}}}{\varepsilon_p(1+\tau_p)}\left(\varepsilon_p G_E^{p^2} + \tau_p G_M^{p^2}\right)$, consistent with 1.74, and the reduced cross section $\sigma_r^p = \varepsilon_p G_E^{p^2} + \tau_p G_M^{p^2}$.

and most nuclear corrections. R' handles the remaining nuclear corrections, but is still (to varying degrees) exposed to systematic uncertainties related to inelastic contamination and nucleon HDE.

To ensure the clean cancellation of uncertainties, protons and neutrons must not suffer significantly from unequal losses due to efficiency — or from acceptance. Fiducial cuts are placed on the electron kinematics to ensure that both a quasi-elastically scattered proton and neutron would lie within the HCal active area, with an appropriate "safety margin" which accounts for the spread of the quasielastic signal in real data. These cuts are placed on the q-vector projections (expected HCal x and y) and ensure that for each proton(neutron) detected in HCal, a neutron(proton) *would have been* detected. This accounts for the vertical deflection applied to all protons passing through the SBS magnetic field. An accurate fiducial cut matches the acceptance losses for protons and neutrons.

These fiducial cuts include a safety margin which accounts for the Fermi smearing which affects dx and dy distributions. This safety margin is measured in widths of the dx and dy real data distributions and is tuned to ensure stability in the final physics result — set to between 2-3 σ for all kinematic settings. Stability analysis will be described later in the chapter. Figure 87 demonstrates the need for a fiducial cut by showing the impact on the q-vector projections after proton and neutron spot cuts on Q^2 = 4.5 GeV^2 (SBS-8, 100% field) data.

The final fiducial cut by kinematic configuration is validated by assessing neutron to proton ratio vs expected quasielastic nucleon location with deuterium data. Fiducial cuts are determined as the boundaries of the stable n:p ratio over both expected nucleon location directions, $x_{expected}$ and $y_{expected}$. Figure 88 depicts the neutron to proton ratio for Q^2 = 4.5 GeV^2 (SBS-8, 100% field) in both dispersive $x_{expected}$ and transverse $y_{expected}$, fitted only in the stable fiducial region.

4.8.2 Scale Factor Ratio

A match between real data and MC is performed with a total fit function which includes the following factors:

- The MC quasielastic neutron distribution with an overall scale factor P1 and horizontal shift

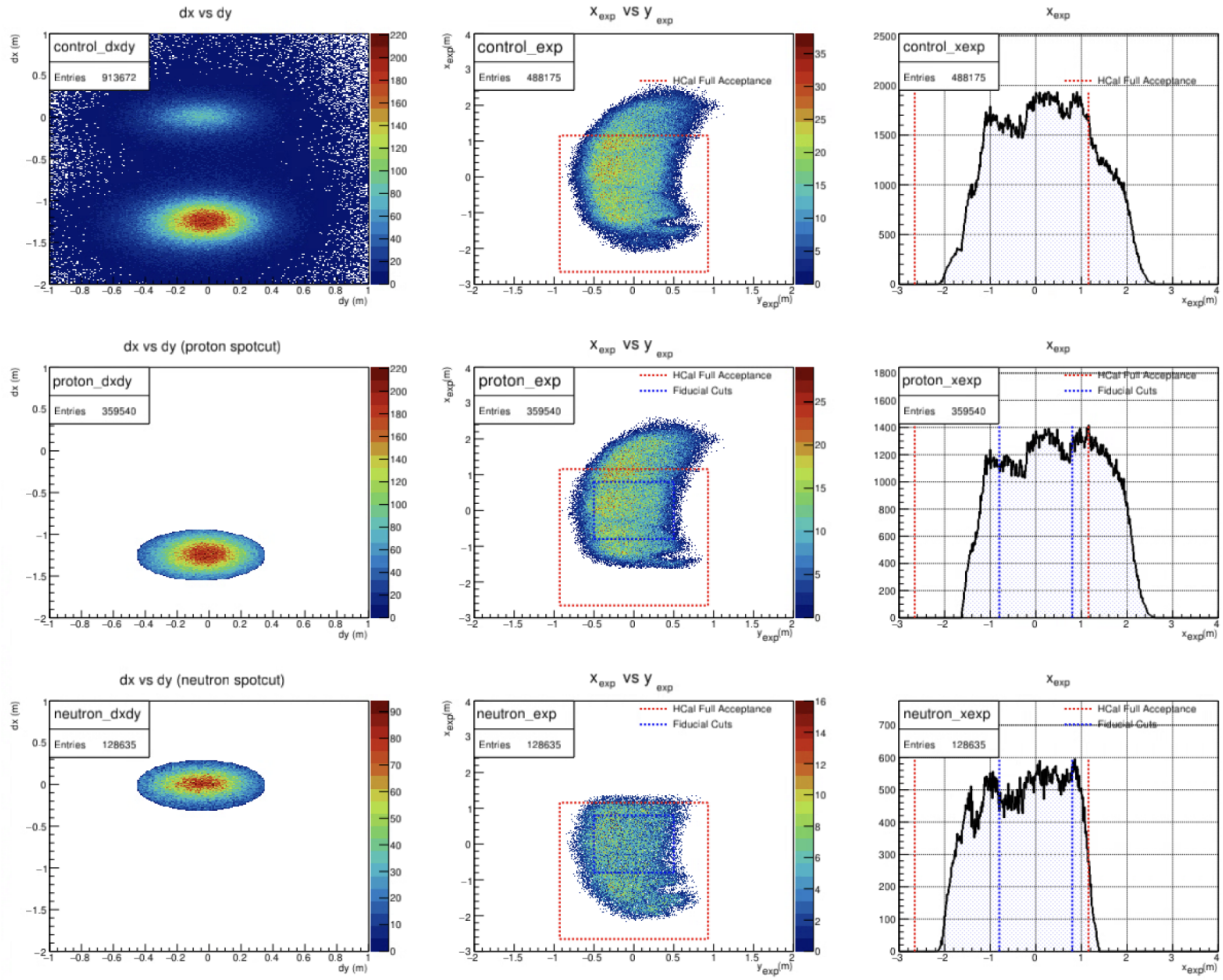

Figure 87: Plots of dx, dy, and expected HCal quasielastic nucleon position using the "neutron hypothesis" demonstrating losses due to acceptance at $Q^2 = 4.5\,\mathrm{GeV}^2$ (SBS-8, 100% field). The first column shows kinematic correlations, the second column shows q-vector projected positions, and the third column shows dispersive projections of column 2. The top-left plot shows the entire dx vs dy distribution, while the remaining plots in the first row include both spot cuts (proton and neutron), the second row includes proton spot cuts only, and the third row includes neutron spot cuts only. The red dotted line indicates the natural edge of the HCal acceptance, and the blue dotted line indicates aggressive fiducial cuts. The significant reduction in q-vector projected location data after applying spot cuts highlights the necessary constraints on the HCal fiducial region. These losses are evident at the bottom of the HCal acceptance in the center-middle plot, where the expected neutron positions project below the bottom of HCal, and at the top of the HCal acceptance in the bottom-middle plot, where expected proton positions project above the top of HCal (note the offset for protons of about 1.5 m evident in the top-left plot).

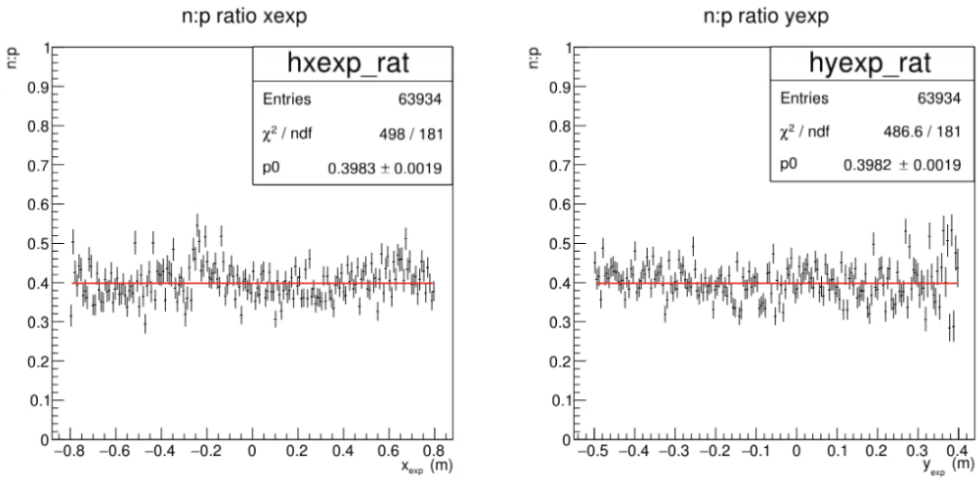

Figure 88: The neutron to proton ratio at Q^2 = 4.5 GeV^2 (SBS-8, 100% field). The red line indicates a zeroth-order polynomial fit to the data with extent bounded by the fiducial cut.

parameter P3. This will model the protons in the data set and correct for small variations in the position of the proton peak which do not match data.

- The MC quasielastic proton distribution with an overall scale factor P2 and horizontal shift parameter P4. This will model the neutrons in the data set and correct for small variations in the position of the neutron peak with do not match data.
- A background function to model remaining inelastic background. The number of parameters will vary based on the chosen background fit.

The overall fit is the sum of the proton, neutron, and background with free parameters optimized to minimize χ^2 over the real data set. An example of this fit and extraction method can be found in figure 89. The scale factor ratio R_{sf} = P1/P2 is important for later analysis.

While the proton deflection angle can be calculated with the SBS magnetic field, the optimal SBS field setting in MC is more accurately determined empirically from the data peak locations in dx and dy. Any significant mismatch between the MC and real data peak locations leading to a shift factor (P3 or P4) greater than the position resolution of HCal (roughly 5 cm) demands generation of new MC data to better match peak locations. Significant discrepancies can lead to proton distributions with inaccurate widths (from field smearing). To avoid wasted effort, an

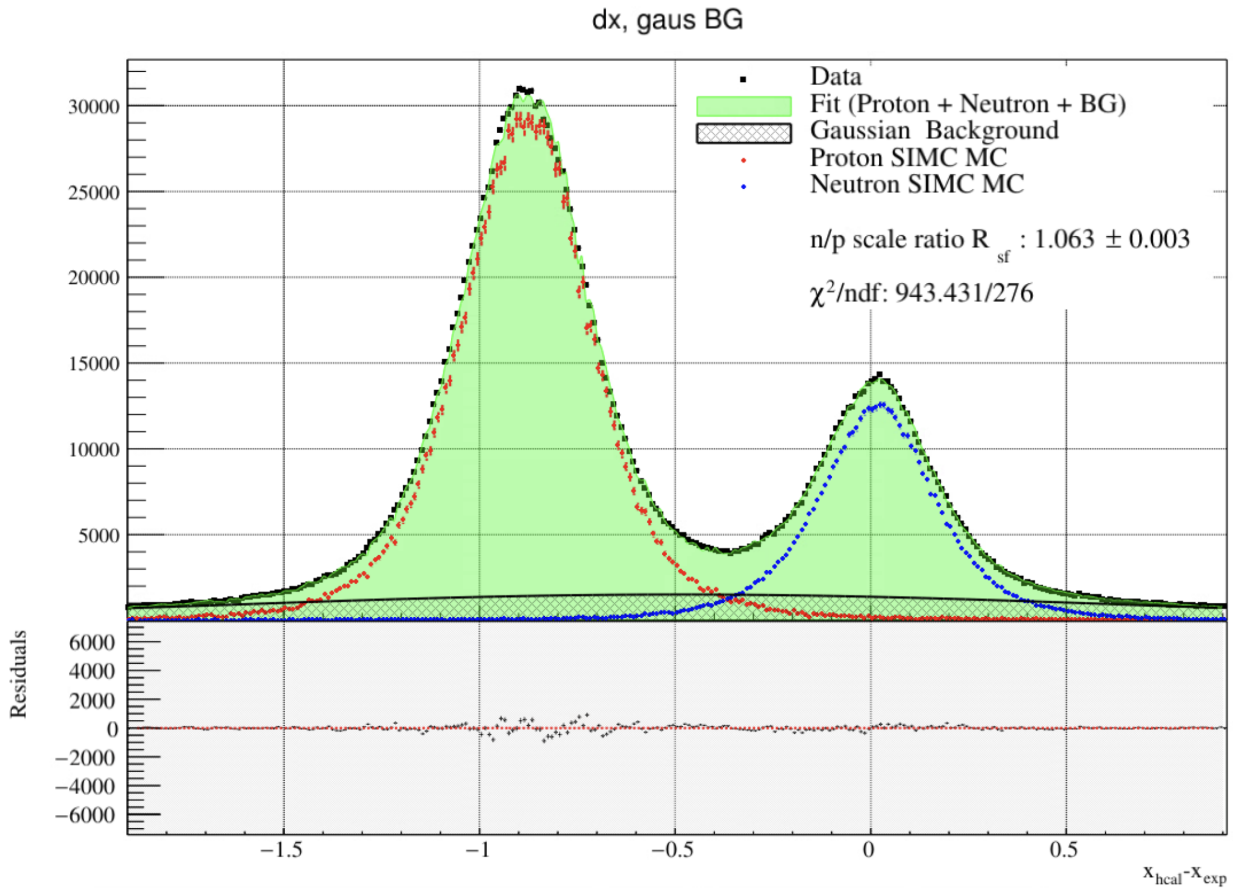

Figure 89: Example of real data and MC comparisons with best fit results. The total fit in shaded green is the sum of MC proton, MC neutron, and a Gaussian model background. The scale factor ratio R_{sf} is displayed. The residuals are the difference between the data (black squares) and the total fit in green. This data from Q^2 = 4.5 GeV^2 (SBS-8, 70% field).

iterative study with smaller MC data sets was performed for all SBS kinematics to determine optimized field scale parameters in simulation[66]. An ad-hoc smearing parameter may also be used to best match the data to MC, but due to the impressive match between unmodified MC and real data peaks, such a parameter has not been introduced for this analysis.

The extraction of the corrected quasielastic cross section ratio R' follows from R_{sf} and the built-in MC quasielastic cross section ratio R_{MC}. R_{sf} is the experimental correction to the MC assumed neutron to proton cross section ratio and the product of the two is the model-independent

experimental cross section ratio:

$$R_{sf} \cdot \frac{\frac{d\sigma}{d\Omega}\Big|_{\text{n(e,e')},\text{MC}}}{\frac{d\sigma}{d\Omega}\Big|_{\text{p(e,e')},\text{MC}}} = R' \tag{4.46}$$

The total experimental systematic and statistical uncertainty of the extracted G_M^n is propagated forward through 4.45[131].

4.8.3 Extraction Method

In Chapter 1, several methods for extracting G_E^p, G_M^p, and G_E^n were introduced, which involve the evaluation of fit models to world data at a given Q^2. The extraction of G_M^n requires the evaluation of the other form factors at the same Q^2 from selected fits of this sort. A single-valued Q^2 is often cited for similar experiments at Jefferson Lab in reference to the value of the Q^2 distribution corresponding to the central spectrometer angle, sensitive to cuts. Table 26 includes the values of Q^2 for all kinematics in **GMn** evaluated with the SIMC event generator over all angles and used to calculate form factors from fit parametrizations. Due to the asymmetric nature of these distributions, the median is taken as the representative value. Table 27 describes ε values evaluated in the same way. τ is calculated from the average nucleon mass and Q^2 values in Table 26.

Kinematic	SBS Field	Mean	Median	Mode
4	30	3.01	2.99	2.92
4	50	3.00	2.98	2.92
7	85	9.87	9.86	9.78
11	100	13.54	13.53	13.36
14	70	7.46	7.46	7.42
8	50	4.44	4.40	4.23
8	70	4.44	4.41	4.24
8	100	4.44	4.40	4.22
9	70	4.48	4.47	4.47

Table 26: Q^2 distribution statistics for different kinematic configurations evaluated from MC using the SIMC event generator. See 6 for more information.

Because the ratio method is sensitive to TPE effects and many of the available proton fits are heavily influenced by PT data (insensitive to TPE effects), this analysis opts to use the Arrington07

[131] See Appendix B for error propagation and budget.

Kinematic	SBS Field	Mean	Median	Mode
4	30	0.72	0.723	0.739
4	50	0.72	0.725	0.743
7	85	0.50	0.501	0.505
11	100	0.41	0.415	0.423
14	70	0.47	0.467	0.477
8	50	0.80	0.807	0.825
8	70	0.80	0.807	0.827
8	100	0.80	0.807	0.827
9	70	0.51	0.517	0.531

Table 27: ε distribution statistics for different kinematic configurations evaluated from MC using the SIMC event generator. See 6 for more information.

"TPE corrected" parameterization for both G_E^p and G_M^p to obtain the proton reduced cross section σ_r^p at each Q^2. The error is interpolated from the table provided in the publication and supplemental materials and treats both sources of error (from G_E^p and G_M^p) as independent at each value of Q^2[10][132]. The Ye et al. parameterized fit to G_E^n world data is used to obtain this form factor at each central Q^2 with the error from the dedicated parameterization[184].

Precision G_E^n extractions in the Q^2 range covered by **GMn** are scarce and world data is relatively imprecise. For this reason, G_M^n and σ_r^n extracted with this analysis will be reported here. With successful extractions of G_E^n from **GEn-II** (experiment E12-09-016, see 7), full extraction of G_M^n will be more precise.

4.8.4 Cut Stability

Initial cut values are determined from experimental distributions and from known physics detailed earlier in this chapter. For example, on the electron arm the pion peak is distinct from the electron peak in both BBCal preshower energy and GRINCH time over threshold and a single cut is placed to remove pion contamination. Other distributions, like E/p and W^2, are distributed around a mean expected value and cuts are placed on either side of that mean to optimize the statistics in the signal distribution and remove backgrounds. On the hadron arm, HCal energy initial cuts are

[132]This method likely over-estimates the propagated error, which leaves room for improvement in subsequent analysis.

placed where the shape of MC energy spectra significantly deviates from data after calibrations (see figure 72).

On a first pass over the data to assess the stability of each cut, a purely data-driven approach is possible. Applying the "delta spot check method" outlined earlier to deuterium data, neutron to proton ratios can be extracted by placing the spot cuts appropriately to identify nucleons. Figure 90 depicts this neutron to proton ratio as a function of several potential cut variables where the red fit line is bounded by the stable region for each. The efficacy of this method is constrained greatly by the available statistics for each dataset.

To further refine these cuts, small variations around initial cut parameters are used to determine the most stable and optimal placement of the cut. A plot of dx versus the examined cut is produced with elastic cuts added but any correlated cuts removed[133]. From this plot, many dx projections with variations of the examined cut parameter can be subsequently produced. On each variation, an extraction of R_{sf} is performed and stability is assessed over several extractions. All cuts must be matched between data and MC used per extraction. Generally speaking, if R_{sf} varies in a way that is inconsistent with the simulation in a given region of any cut variable, this indicates a poor match to MC quasielastic signal and that the region should be excluded. Of course, this is only true for variables that are represented accurately in MC[134]. Variations are centered on the cut limits determined by previous methods.

For example, the BBCal - HCal coincidence ADC time can be plotted against dx for cut stability analysis. Figure 91 depicts this plot with many lines which indicate cut regions where same-color lines bound a single variation region. Figure 92 demonstrates this method with many fits to each bounded region in 91. Each of the R_{sf} values extracted in 92 are plotted against the cut range variable in Figure 93. The total amount of events cut on each variation is included in the plot. All figures which describe this stability for cuts per data set can be found in Appendix D.

It is noteworthy that the time offset between protons and neutrons is obvious in figure 91 and

[133] Among common elastic cut variables, dy and W^2 are the only combination that are strongly correlated. See Appendix D for correlated cut analysis.

[134] Examples of variables that are not represented well in MC include BBCal - HCal coincidence time, e' E/p, and BBCal preshower energy.

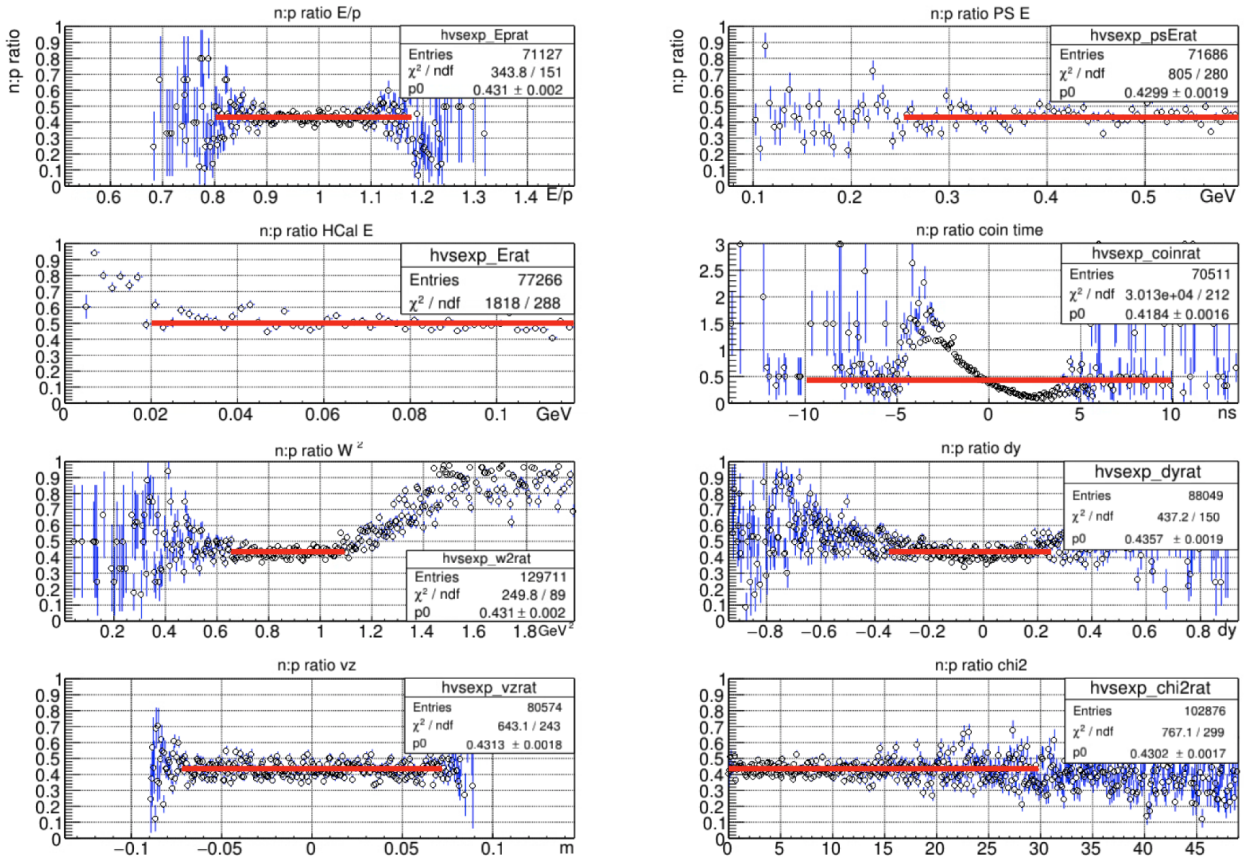

Figure 90: Neutron to proton ratios vs cut variables with tight elastic cuts and spot cuts to select each nucleon for the ratio. Red lines are zeroth-order polynomial fits to the data constrained by stability region in each cut variable. Cut variables from the top left to bottom right: e' E/p, BBCal preshower energy, HCal energy, BBCal - HCal coincidence ADC time, W^2, dy, track vertex z, track χ^2. This data from Q^2 = 3.0 GeV^2 (SBS-4, 30% field). Because protons and neutrons are offset in time, the coincidence time cut includes significant variation over its range. HCal and BBCal preshower energy ranges are zoomed on the cut opening because no closing cut is placed for these variables.

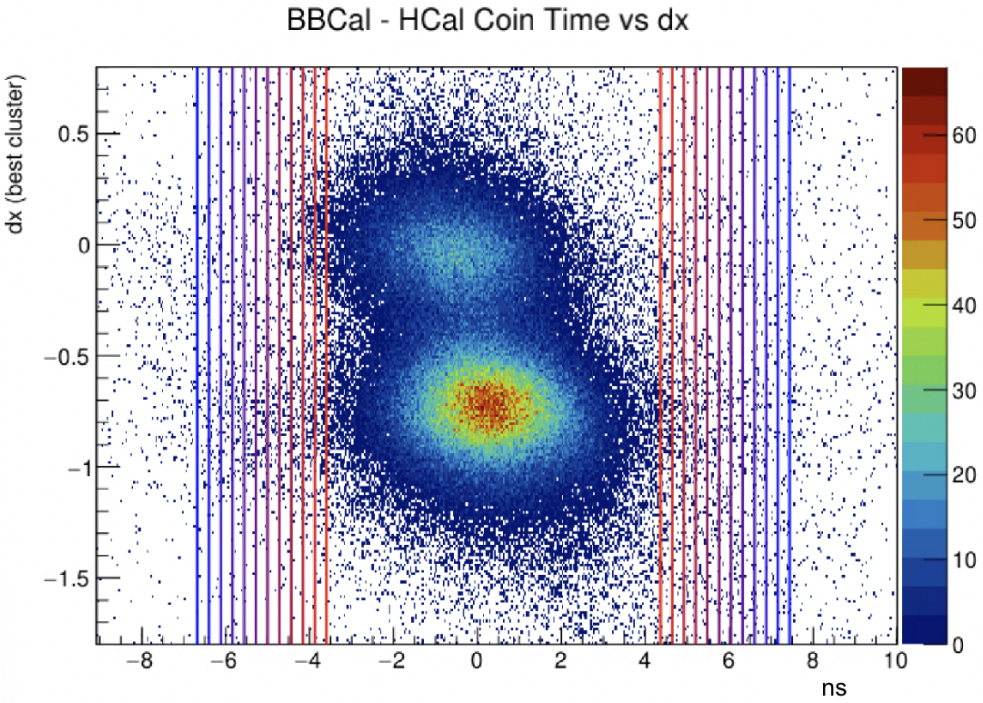

Figure 91: BBCal - HCal ADC coincidence time vs dx from Q^2 = 3.0 GeV^2 (SBS-4, 30% field) data. Each pair of shared-colored lines bounds an individual variation on the coincidence time cut.

that this offset is not explainable by time-of-flight variations alone. For some cuts, like this one, the optimized variation region includes all distinct nucleon signal and stabilizes after this signal is fully included.

4.8.5 Fit Stability

Because the extraction method relies on accurate fits to data using MC distributions, it is important to validate the fitting procedure and choose both the binning and range of the fit properly.

To determine the optimal number of bins in a histogram, several rules of thumb can be employed. Sturges' rule, suitable for moderate-sized datasets, suggests that the number of bins k should be calculated using the formula $k = \lceil \log_2(n) + 1 \rceil$, where n is the number of data points [169]. For larger datasets, Scott's rule minimizes the integrated mean square error and is defined as Bin Width $= 3.5\sigma/n^{1/3}$, where σ is the standard deviation of the data [159]. The Freedman-Diaconis rule, which is robust to outliers and skewed data, determines the bin width using the

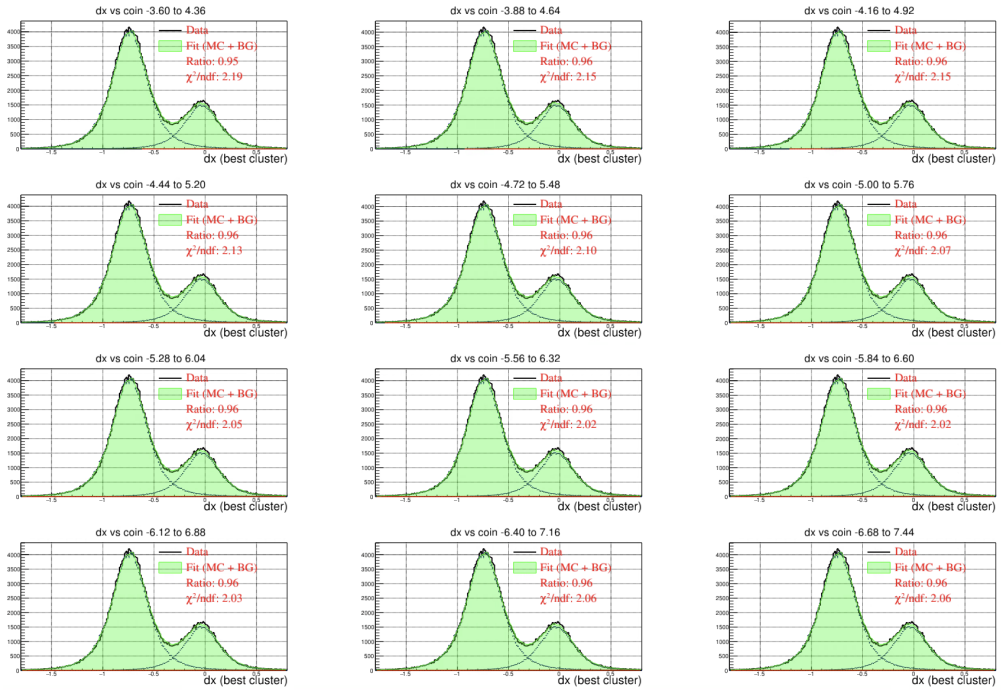

Figure 92: Data/MC fits to dx over several cut variations in BBCal - HCal ADC coincidence time. R_{sf} is extracted from each and plotted by variation (in coin peak sigma) in 93. Data from Q^2 = 3.0 GeV^2 (SBS-4, 30% field).

interquartile range (IQR) as follows [61]: Bin Width $= 2 \cdot IQR/n^{1/3}$. The last of these methods provides a good starting point for this data set where it resolves important features well via qualitative assessment. Figure 94 depicts assessment of initial binning.

With this binning fixed, stability analysis can be performed in the same manner as is done with cuts, where R_{sf} and χ^2/ndf is assessed for a range of binned values. In order to keep the binning similar between MC and data over different kinematics, a single bin quantity is fixed for all datasets. 400 bins per dx histogram maintains stable R_{sf} over all examined ranges and kinematic settings. Figure 95 depicts this analysis for Q^2 = 3.0 GeV^2 data.

In addition to binning, the optimal fit range for background stability is also assessed. R_{sf} should be stable over small variations of the fit range and the essential features of dx should be included in the fit window. These features include quasielastic signal with non-Gaussian radiative tails and any remaining inelastic background after elastic cuts. A stability study is performed for plot ranges where R_{sf} is extracted from histograms over several range parameters and different

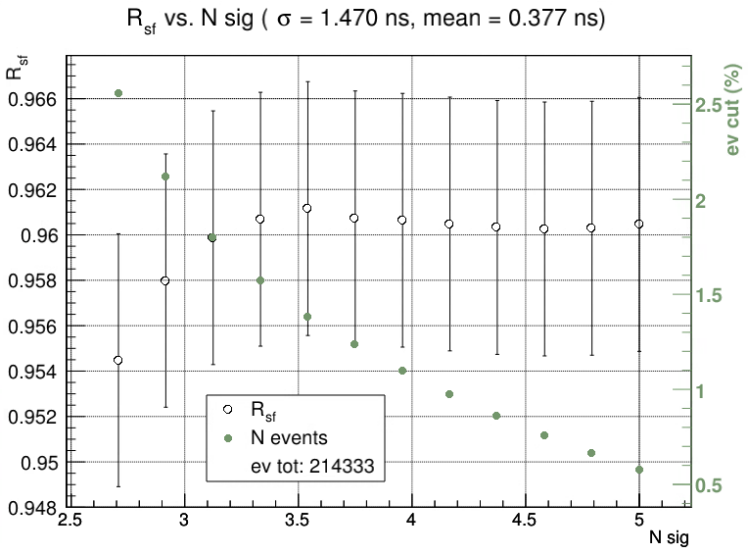

Figure 93: R_{sf} extractions over several cut variations in BBCal - HCal ADC coincidence time. The percentage of total events removed at each cut interval is included on the right-hand side of the plot in green. "Sig" refers to the width of the proton peak in ns. "ev tot" is the total number of events before any coincidence time cuts are applied. Data is from Q^2 = 3.0 GeV^2 (SBS-4, 30% field).

background functions. Figure 96 depicts this assessment with MC quasielastic signal and a second-order polynomial background fits to Q^2 = 3.0 GeV^2 data. Figure 97 aggregates the findings. For this dataset, a fit range width of 2.6 m optimizes stable R_{sf} with low χ^2/NDF.

4.8.6 Systematic Uncertainty

Estimation of the systematic uncertainty on R_{sf} is evaluated primarily for the inelastic contamination in the dx distribution, from which R_{sf} is evaluated. A preliminary estimation of this uncertainty may be determined by matching several background models during the extraction of R_{sf}. The standard deviation of the R_{sf} distribution characterizes the spread of the data dependent upon the inelastic contamination in the signal, modeled with MC. An example of several backgrounds used to extract R_{sf} from Q^2 = 3.0 GeV^2 data (SBS-4, 30% field) is given in figure 98.

To bound the systematic uncertainty from variation of HDE across the HCal acceptance, relative measurements of the proton HDE from different field settings may be compared to a central value determined by MC. Because all current methods to extract proton HDE from data include

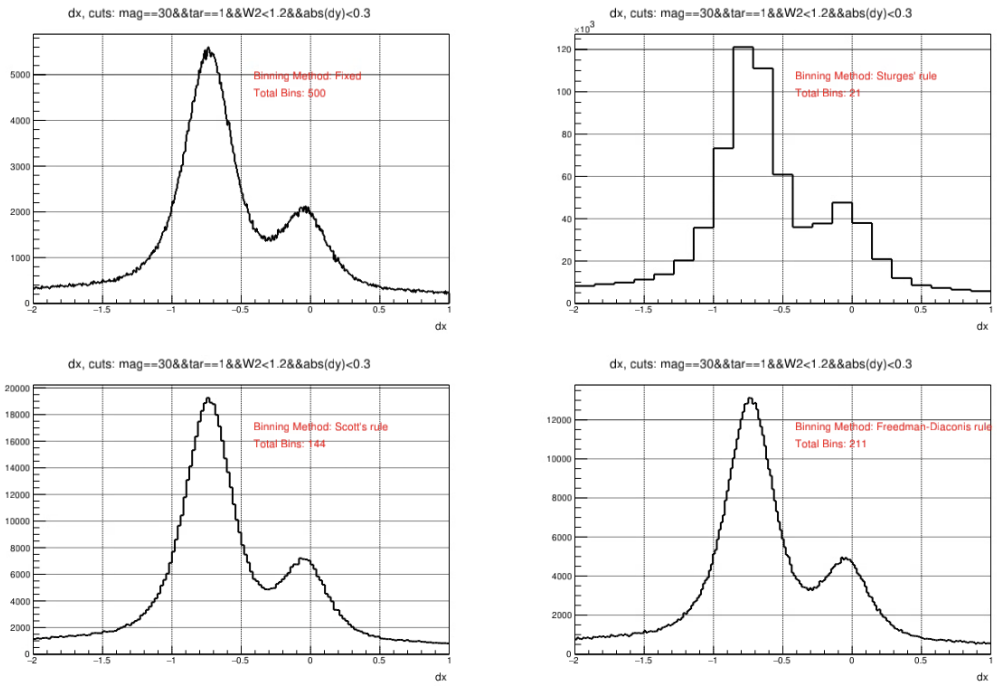

Figure 94: Data dx from $Q^2 = 3.0$ GeV^2 depicting results of each binning method. The Freedman-Diaconis method resolves the proton and neutron peaks expected from these data and is used to determine a starting point for further binning analysis. The titles indicate the branches used to generate the plots with tree structure defined with parsing scripts.

significant scale variation based on spot cuts, proton HDE estimation is compared to the MC central value after a match is achieved at $p_{proton} = 2.3$ GeV (as in figure 83)[135]. Figure 99 depicts a comparison between proton HDE from all available field settings at $p_N = 3.2$ GeV ($Q^2 = 4.5$ GeV^2, SBS-8) and the expected value from MC. An estimation of the systematic error from the spread of these data around the central value can be obtained with the central value (MC) $\varepsilon_{\text{central}} = 0.9434$ and the proton HDE values $\varepsilon_1 = 0.9366$, $\varepsilon_2 = 0.9458$, and $\varepsilon_3 = 0.9443$, the calculated deviations are -0.0068, 0.0024, and 0.0009 respectively, leading to a systematic error $\sigma_{\text{sys}} \approx 0.0024$[136].

Systematic uncertainty may also be evaluated with more precision by extracting R_{sf} for equal-statistics, independent slices of dx in each cut parameter. The variation across the inclusive cut region gives a measure of the systematic uncertainty by cut[137]. Applying this methodology to

[135] Further analysis is possible with digitized and reconstructed MC data which may provide a better real-data vs MC comparison for HDE.

[136] More details about this error extraction and propagation through R_{sf} can be found in Appendix B.

[137] While this machinery is in place to conduct this analysis, it is incomplete and not presented here.

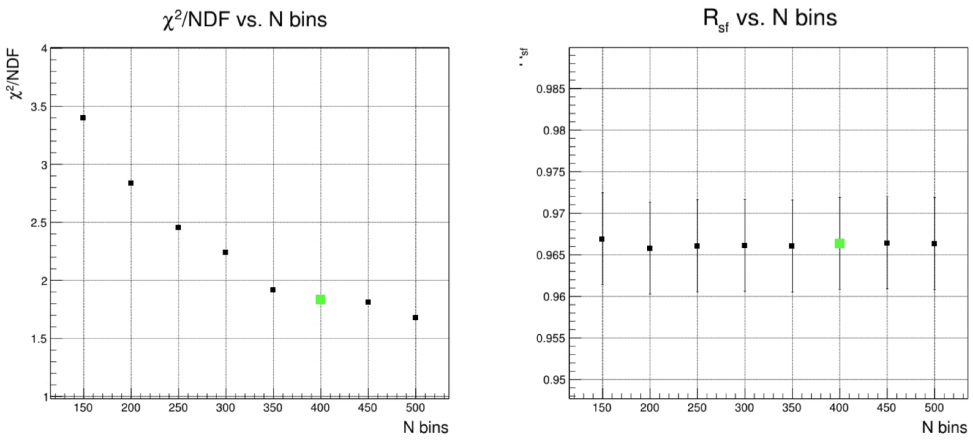

Figure 95: R_{sf} extractions employing second-order polynomial background and MC signal from dx from Q^2 = 3.0 GeV^2 data. The fit quality and extractions are plotted against various total bins in dx to assess stability. The green point is stable in R_{sf}. Error in R_{sf} is statistical.

cut stability analysis is made more difficult due to the minimum statistics requirements needed to extract R_{sf} per slice with slice widths sufficient to inform precise cuts. Figure 100 illustrates this difficulty for $Q^2 = 3.0\,\mathrm{GeV}^2$ data (SBS-4, 30% field), where the cut region in the preshower energy between 100 MeV and 200 MeV is divided into four regions with equal statistics. Fits to these data are poor, even with a tenfold increase in MC statistics available to fit the data.

4.8.7 Statistical Uncertainty

Statistical uncertainty is determined by the statistical error on the fit, after cuts. MC statistics are considered during extraction of these errors, but will be effectively infinite over the fit range on final extractions as more MC data is generated. Residuals are included on all R_{sf} extractions as confirmation that systematic trends are minimized and fluctuations about the sum MC and background fit are dominated by statistical contributions.

The statistical error on the fit parameters is obtained using the built-in Root function `GetParError()` available for custom fits. This function provides the standard errors of the parameters resulting from the fit, calculated from the covariance matrix of the parameters. Specifically, `GetParError()` returns the square root of the diagonal elements of the covariance matrix, which represent the vari-

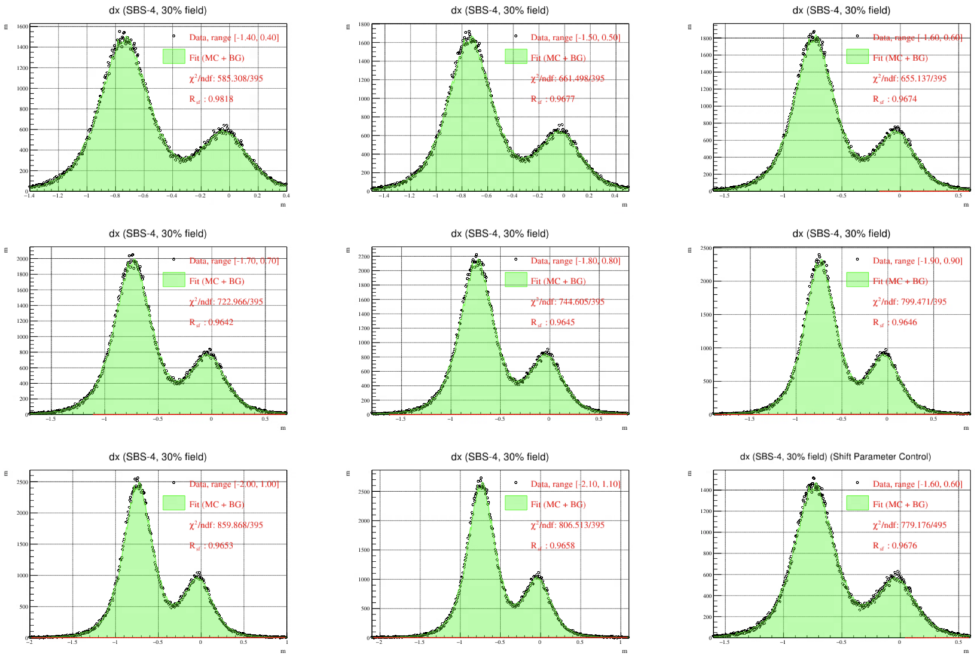

Figure 96: Data dx from Q^2 = 3.0 GeV^2 (SBS-4, 30% field) depicting overall fits with MC and second-order polynomial background on different fit ranges. The final histogram represents the fit range used to fix all MC signal shift parameters used in all other plots.

ances of the fit parameters. These errors are propagated through any further calculations involving the fit parameters, including the scale factor ratio R_{sf}.

4.9 nTPE

The analysis of nTPE data will continue beyond the scope of this thesis. Notably, the inefficiencies in HCal modules must be accounted for in MC before a proper extraction is possible. What is presented here is a current status and should not be considered finished work or a complete analysis of the data.

4.9.1 Extraction

The Rosenbluth Slope (RS) can be extracted by measuring the reduced neutron cross section at two values of ε to evaluate the TPE contribution to the elastic electron-neutron cross section. The technique starts with the ratio method to obtain the cross section ratio R', measured in the same

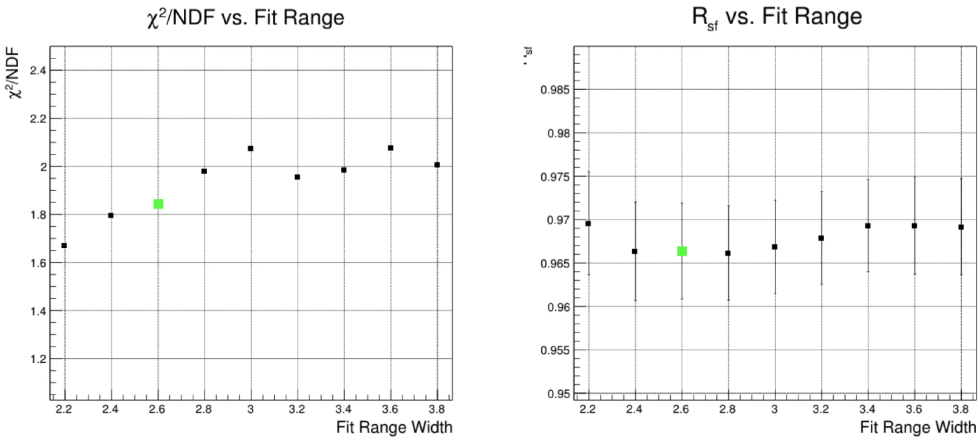

Figure 97: R_{sf} extractions employing second-order polynomial background and MC signal from dx from Q^2 = 3.0 GeV^2 data. The fit quality and extractions are plotted against various ranges in dx to assess stability. The green point is stable in R_{sf} with fit quality improved within the region of stability. Error in R_{sf} is statistical.

manner as is done for G_M^n extraction. From equations 4.44 and 1.74, the quasielastic cross section ratio can rewritten:

$$R' = \left[\frac{\sigma^n_{\text{Mott}}(1+\tau_p)}{\sigma^p_{\text{Mott}}(1+\tau_n)}\right] \cdot \frac{\sigma^n_r}{\sigma^p_r}, \tag{4.47}$$

where ε is absorbed into the Mott cross section and denoted by p(n) for proton(neutron). In order to extract the RS, **nTPE** obtains R' from two values of ε at R'_{ε_1} and R'_{ε_2} by holding Q^2 fixed and varying θ_e. From these two R' observables, the aggregate observable $\mathscr{A}$ is formed:

$$\mathscr{A} = \frac{R'_{\varepsilon_1}}{R'_{\varepsilon_2}} \tag{4.48}$$

This "super-ratio" is expected to cancel shared systematic error between each ε point in the same manner as in the Durand technique. R' can be related to the transverse and longitudinal cross sections (σ_L^N and σ_T^N respectively):

$$R' = \frac{\sigma^n_{\text{Mott}}(1+\tau_p)}{\sigma^p_{\text{Mott}}(1+\tau_n)} \cdot \frac{\sigma^n_T + \varepsilon_n \sigma^n_L}{\sigma^p_T + \varepsilon_p \sigma^p_L} \tag{4.49}$$

$$= \frac{\sigma^n_{\text{Mott}}(1+\tau_p)}{\sigma^p_{\text{Mott}}(1+\tau_n)} \cdot \frac{\sigma^n_T}{\sigma^p_T} \cdot \frac{1+\varepsilon_n R S^n}{1+\varepsilon_p R S^p}, \tag{4.50}$$

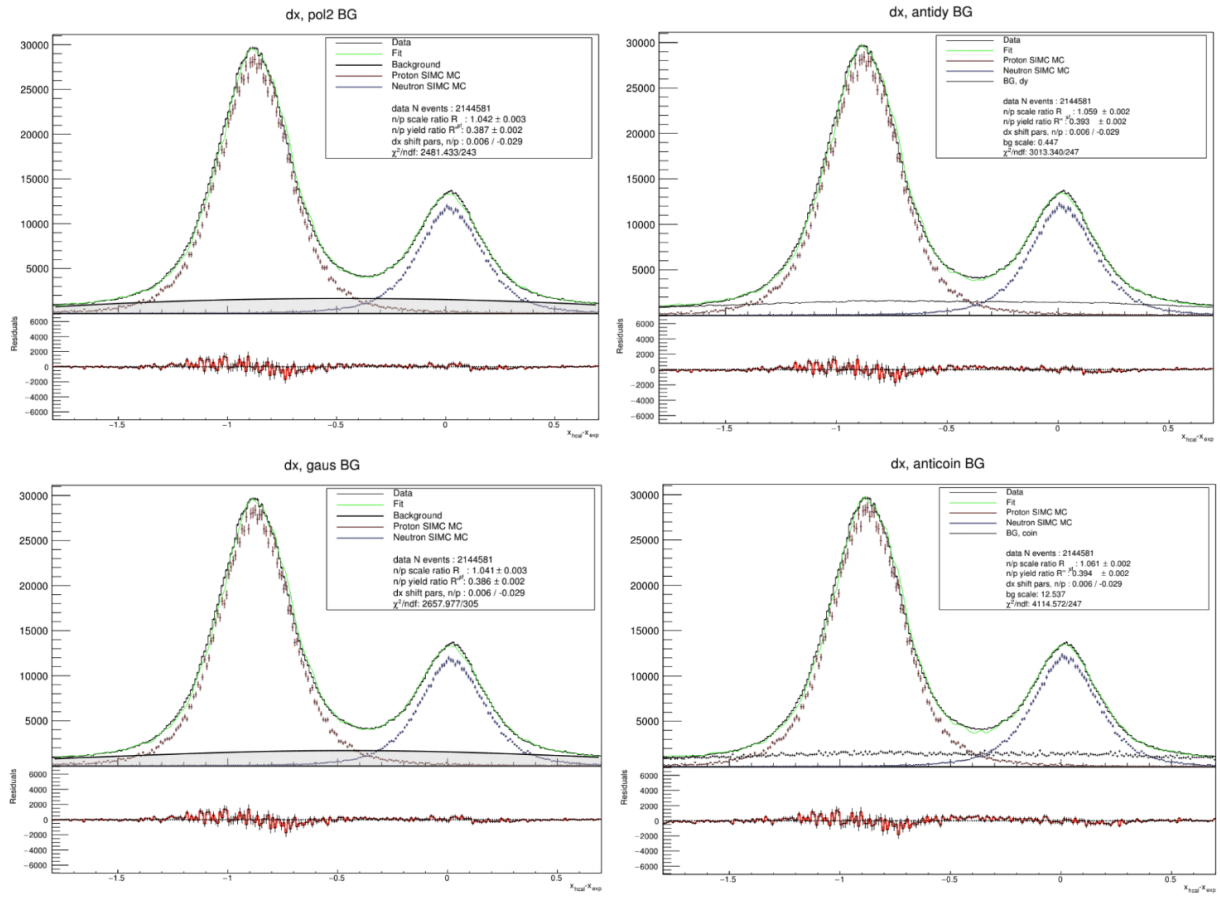

Figure 98: Example MC signal fits to Q^2 = 3.0 GeV^2 data (SBS-4, 30%= field) data which employ multiple backgrounds. From top left to bottom right these backgrounds are second-order polynomial, *dy* anticut, Gaussian background, and BBCal - HCal anticut background. Anticut backgrounds share all other cuts with the data plotted.

where $RS = \sigma_L/\sigma_T = G_E^2/(\tau \cdot G_M^2)$[138]. For succinctness, the Mott ratio R_{Mott} can be defined as:

$$R_{\text{Mott}} = \frac{\sigma^n_{\text{Mott}}(1+\tau_p)}{\sigma^p_{\text{Mott}}(1+\tau_n)} \approx 1, \tag{4.51}$$

where variations from unity are related to the small mass differences between the proton and the neutron and any significant differences in kinematic distributions between neutron and pro-

[138]This definition differs from the one presented in chapter 1 which standard in the literature, where $RS^N = (\mu_N G_E^N/G_M^N)^2$. As usual, capital N stands for nucleon.

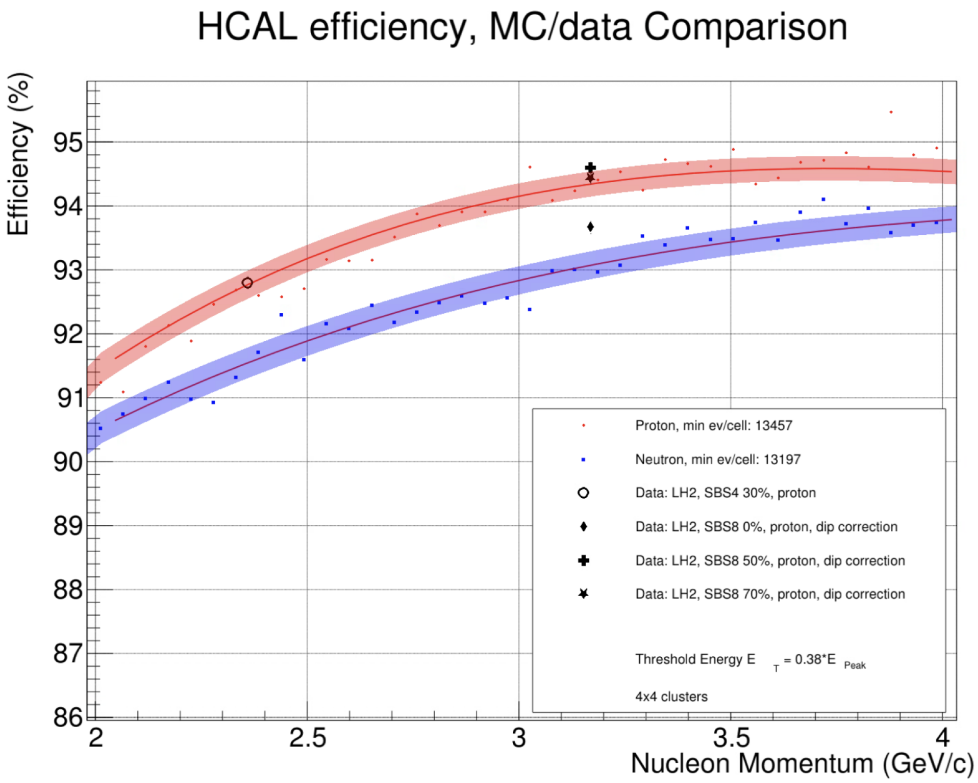

Figure 99: Data proton HDE from p_N = 3.17 GeV (SBS-8) with results for all field settings (0%, 50%, and 100%). The scale for MC and data are fixed at p_N = 2.36 GeV, providing an accurate comparison between data and MC for the various field settings of SBS-8.

ton events after cuts. Additionally,

$$\frac{\sigma_T^n}{\sigma_T^p} \approx 1, \tag{4.52}$$

which can be assumed as long as kinematic variables expected to be the same at each ε do not vary considerably[139]. With this, the aggregate observable $\mathscr{A}$ becomes:

$$\mathscr{A} = \frac{R_{\text{Mott},\varepsilon_1}}{R_{\text{Mott},\varepsilon_2}} \cdot \frac{1+\varepsilon_1 RS^n}{1+\varepsilon_2 RS^n} \cdot \frac{1+\varepsilon_2 RS^p}{1+\varepsilon_1 RS^p} \tag{4.53}$$

Now the term $\mathscr{B}$ is introduced which does not depend on the neutron RS:

$$\mathscr{B} = \frac{R_{\text{Mott},\varepsilon_1}}{R_{\text{Mott},\varepsilon_2}} \cdot \frac{1+\varepsilon_2 RS^p}{1+\varepsilon_1 RS^p} \tag{4.54}$$

[139]These variables include Q^2, which must be held fixed between both ε points.

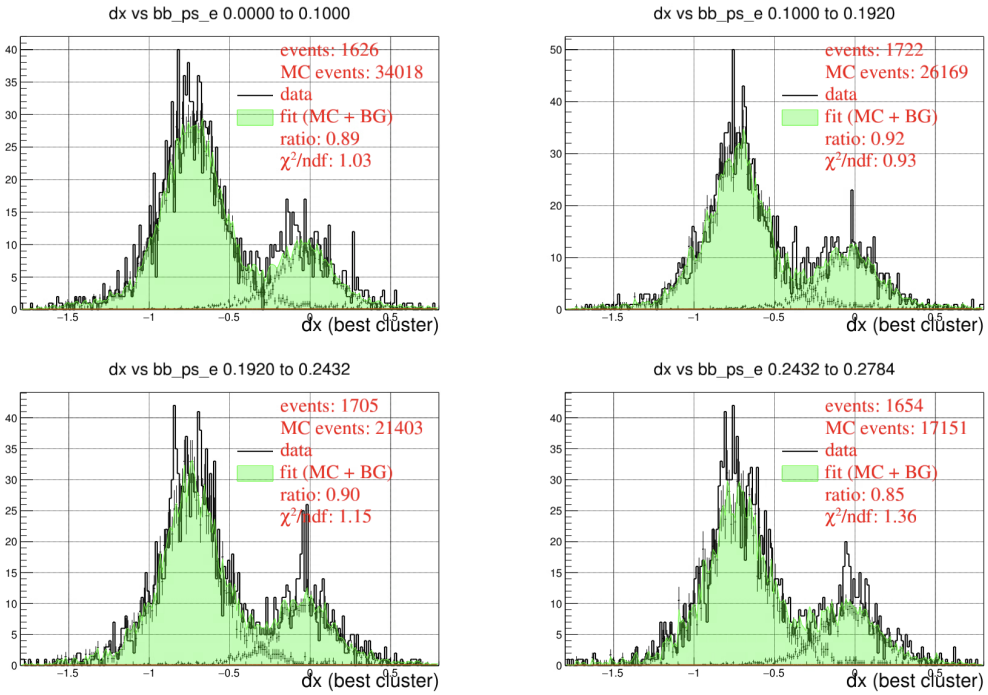

Figure 100: Equal-statistics slices of dx over BBCal preshower energy Q^2 = 3.0 GeV^2 data (SBS-4, 30% field). Because the the number of slices and range is set to be precise enough to inform cut location, the lack of data (here the preshower energy) makes this an ineffective method to assess cut stability.

Notably R_{Mott} can be determined to very high accuracy at our kinematics and RS^p is known from world data ($RS^p = 0.107 \pm 0.010$)[5]. Taking advantage of this $\mathscr{A}$ can be written in terms of $\mathscr{B}$ [5]:

$$\mathscr{A} = \mathscr{B} \cdot \frac{1 + \varepsilon_1 RS^n}{1 + \varepsilon_2 RS^n} \tag{4.55}$$

$$\approx \mathscr{B}(1 + RS^n \Delta\varepsilon) \tag{4.56}$$

Solving for RS^n, where $\Delta\varepsilon = \varepsilon_1 - \varepsilon_2$, gives the form of the Rosenbluth slope for the neutron in terms of experimental observables $\mathscr{A}$ and $\mathscr{B}$:

$$RS^n = \frac{\mathscr{A} - \mathscr{B}}{\mathscr{B}\Delta\varepsilon}, \tag{4.57}$$

or exactly by keeping ε_1 and ε_2 separate:

$$RS^n = \frac{\mathscr{A} - \mathscr{B}}{\mathscr{B}\varepsilon_1 - \mathscr{A}\varepsilon_2} \tag{4.58}$$

For **nTPE**, $\mathscr{B}$ will be determined from our data. From equation 1.74, the $\mu_n G_E^n / G_M^n$ FFR can be compared to the world data employing PT methods to evaluate the difference between measurements of the FFR. With sufficient precision, this difference can serve to distinguish between theoretical TPE models.

Due to the sensitivity of the extracted RS^n on each R' value in the super-ratio and the sensitivity of R' to non-uniformity in HCal detection efficiency, rigorous determination of systematic error and verification of the cancellation of systematic errors is ongoing. At minimum, the position-dependent inefficiencies apparent in the nucleon HDE manifest in HCal must be modeled accurately in MC. However, without the ultimately necessary corrections for nuclear and radiative effects provided by MC, the neutron to proton ratio can be examined for a ballpark estimate of the RS^n. These ratios are extracted from data without comparison to MC using the "delta spot cut method." Each of the two datasets with different ε are matched to the most constrained fiducial cuts and only the data between both ε configurations which share the same SBS field strength are used to extract RS^n (70% field). R' is taken as the n:p ratio for each ε on this estimation. On this comparison, position dependent HDE is expected to cancel on the super-ratio. The results are presented in the next section.

5 Results

Preliminary $G_M^n/(\mu_n G_D)$ extractions are presented here with the expectation that systematic uncertainty estimation will be improved before final extractions are complete. Each figure represents the best fit to data using one of several backgrounds which participate in the quoted $G_M^n/(\mu_n G_D)$ value and uncertainty. The selection of the background in each figure is arbitrary. $G_M^n/(\mu_n G_D)$ is determined from world data and a weighted mean from these background functions:

- Second-order polynomial.
- Third-order polynomial.
- Gaussian.
- BBCal - HCal coincidence time anticut (all other cuts shared with data).
- *dy* anticut (all other cuts shared with data).

Systematic uncertainty derived from inelastic contamination is determined from variance over all background fits. Total systematic error includes the component derived from HDE propagated through R_{sf} and added in quadrature. All extractions and uncertainties are included in table 28.

Kine	**Field**	**GMn (prelim)**	**Err (stat)**	**Err (syst, inel)**	**Err (syst, hde)**	**Err ($\sigma_{r,proton}$)**	**Err (G_E^n)**	**Err (total)**
4	30	0.959	0.003	0.002	0.004	0.022	0.005	0.023
4	50	0.988	0.007	0.005	0.005	0.021	0.005	0.024
8	50	0.949	0.005	0.001	0.004	0.030	0.009	0.032
8	70	0.943	0.002	0.002	0.004	0.030	0.009	0.032
8	100	0.938	0.004	0.002	0.004	0.031	0.009	0.032
9	70	0.951	0.001	0.002	0.004	0.029	0.006	0.029

Table 28: Preliminary $G_M^n/(\mu_n G_D)$ Extraction Results with uncertainties. The column labeled **GMn** (prelim) contains preliminary extractions of $G_M^n/(\mu_n G_D)$. Statistical uncertainty (stat) is taken from fits to MC quasielastic distributions and backgrounds. Systematic uncertainty is divided into two parts. The first is from inelastic contamination (syst, inel) an is evaluated from the standard deviation of all R_{sf} extractions with five different backgrounds and propagated to $G_M^n/(\mu_n G_D)$. The second is from HDE (syst, hde) and is determined from the standard deviation of HDE estimations at $Q^2 = 4.5$ GeV^2 (SBS-8) and propagated to $G_M^n/(\mu_n G_D)$ for each kinematic setting separately. The errors from parameterized fits to proton form factors (denoted $\sigma_{r,proton}$) and G_E^n (denoted G_E^n) are calculated using prescriptions in the relevant literature and described in chapter 1. For more information on kinematics, see table 6. For more information on error, see Appendix B.

5.1 SBS-4, 30% Field

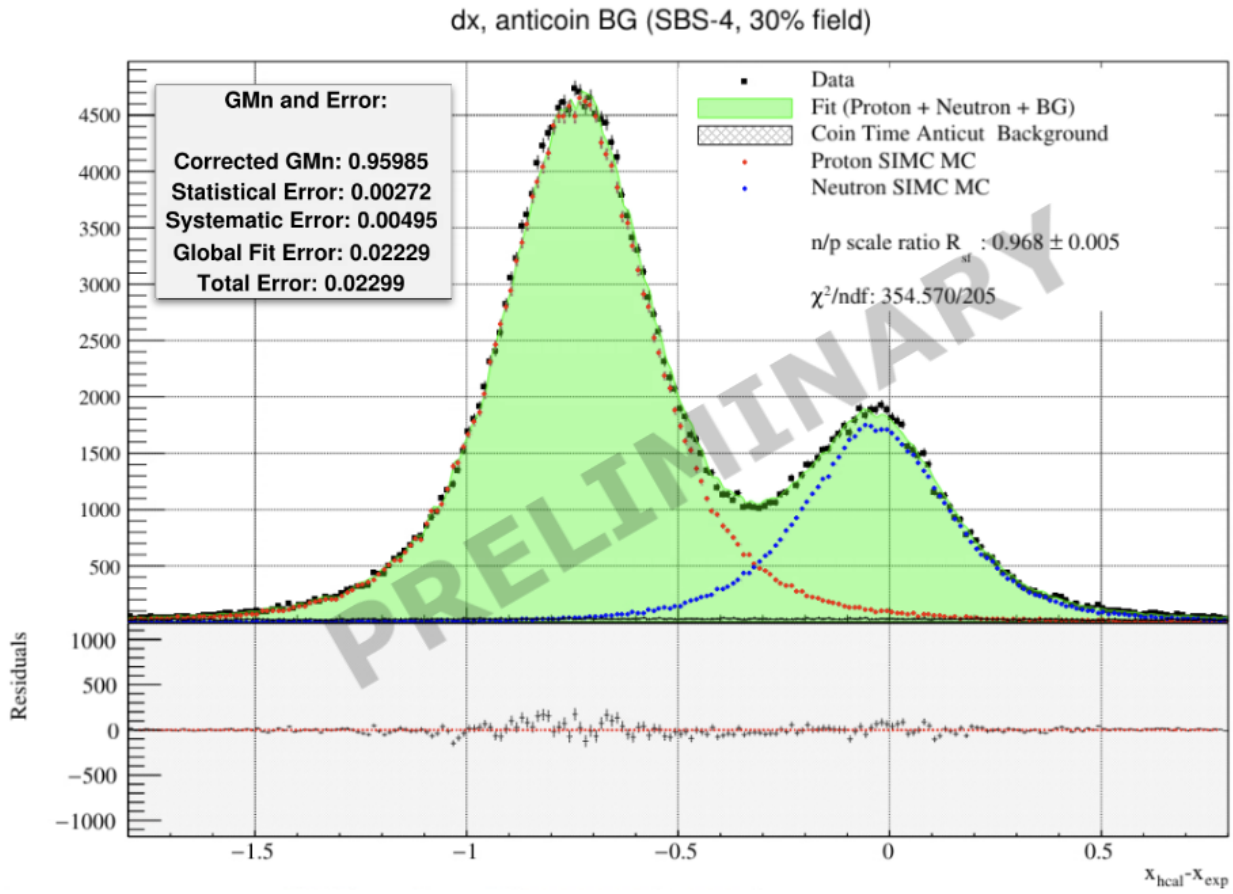

Figure 101: Preliminary $G_M^n/(\mu_n G_D)$ extraction at Q^2 = 3.0 GeV^2 (SBS-4, 30% field). The label **Corrected GMn** refers to $G_M^n/(\mu_n G_D)$. Quoted $G_M^n/(\mu_n G_D)$ and error uses mean R_{sf} from fits with MC quasielastic signal and various backgrounds. **GMn and Error** precision is left without proper truncation to indicate differences between kinematic settings.

5.2 SBS-4, 50% Field

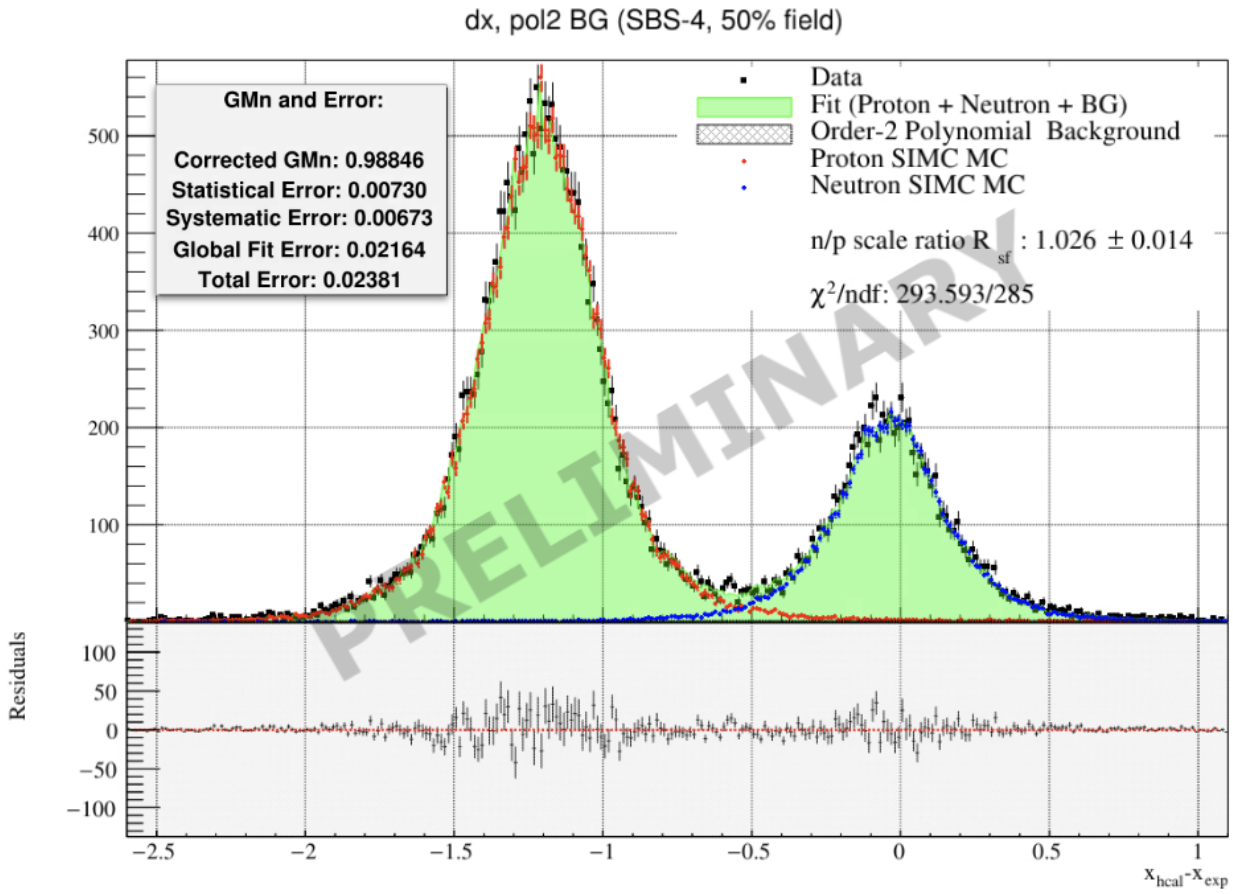

Figure 102: Preliminary $G_M^n/(\mu_n G_D)$ extraction at $Q^2 = 3.0$ GeV^2 (SBS-4, 50% field). The label **Corrected GMn** refers to $G_M^n/(\mu_n G_D)$. Quoted $G_M^n/(\mu_n G_D)$ and error uses mean R_{sf} from fits with MC quasielastic signal and various backgrounds. **GMn and Error** precision is left without proper truncation to indicate differences between kinematic settings.

5.3 SBS-8, 50% Field

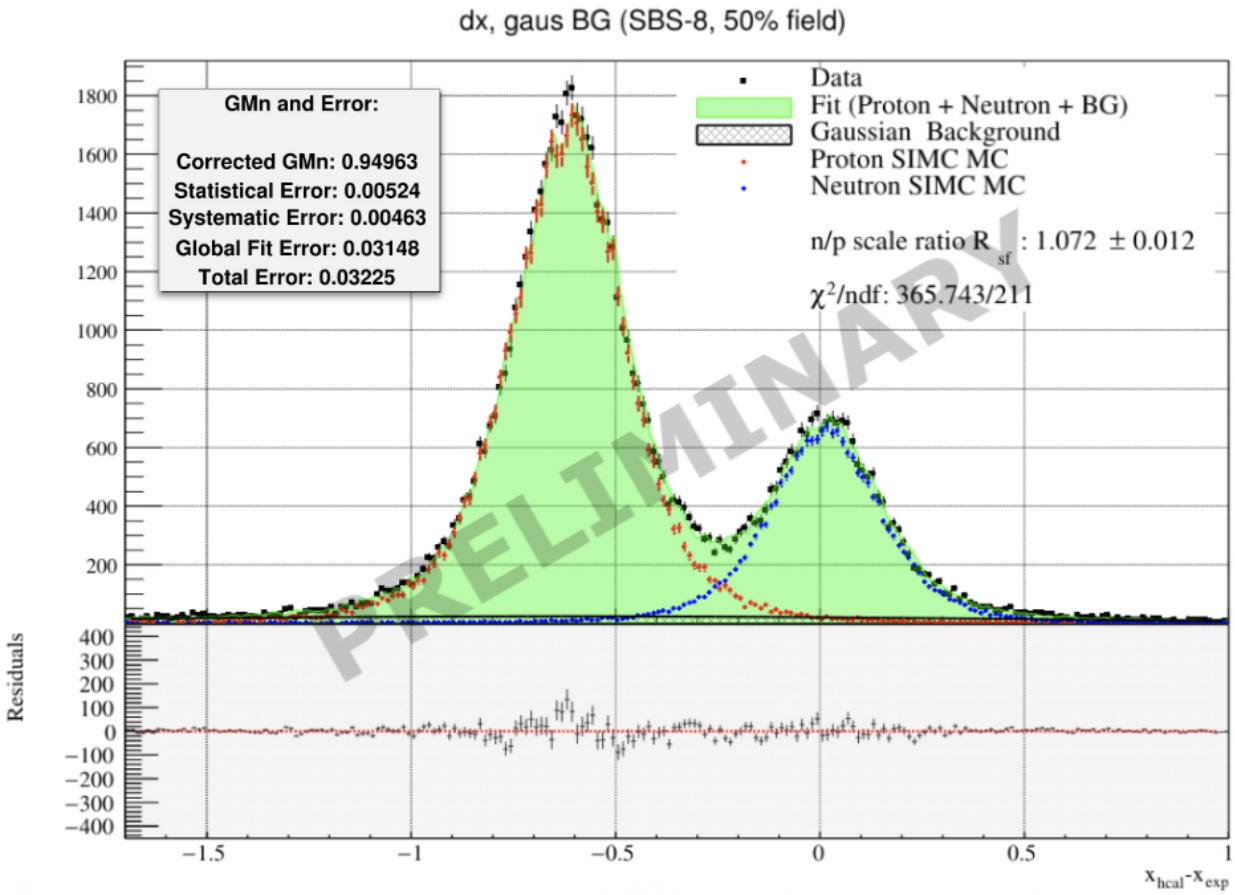

Figure 103: Preliminary $G_M^n/(\mu_n G_D)$ extraction at $Q^2 = 4.5$ GeV^2 (SBS-8, 50% field). The label **Corrected GMn** refers to $G_M^n/(\mu_n G_D)$. Quoted $G_M^n/(\mu_n G_D)$ and error uses mean R_{sf} from fits with MC quasielastic signal and various backgrounds. **GMn and Error** precision is left without proper truncation to indicate differences between kinematic settings.

5.4 SBS-8, 70% Field

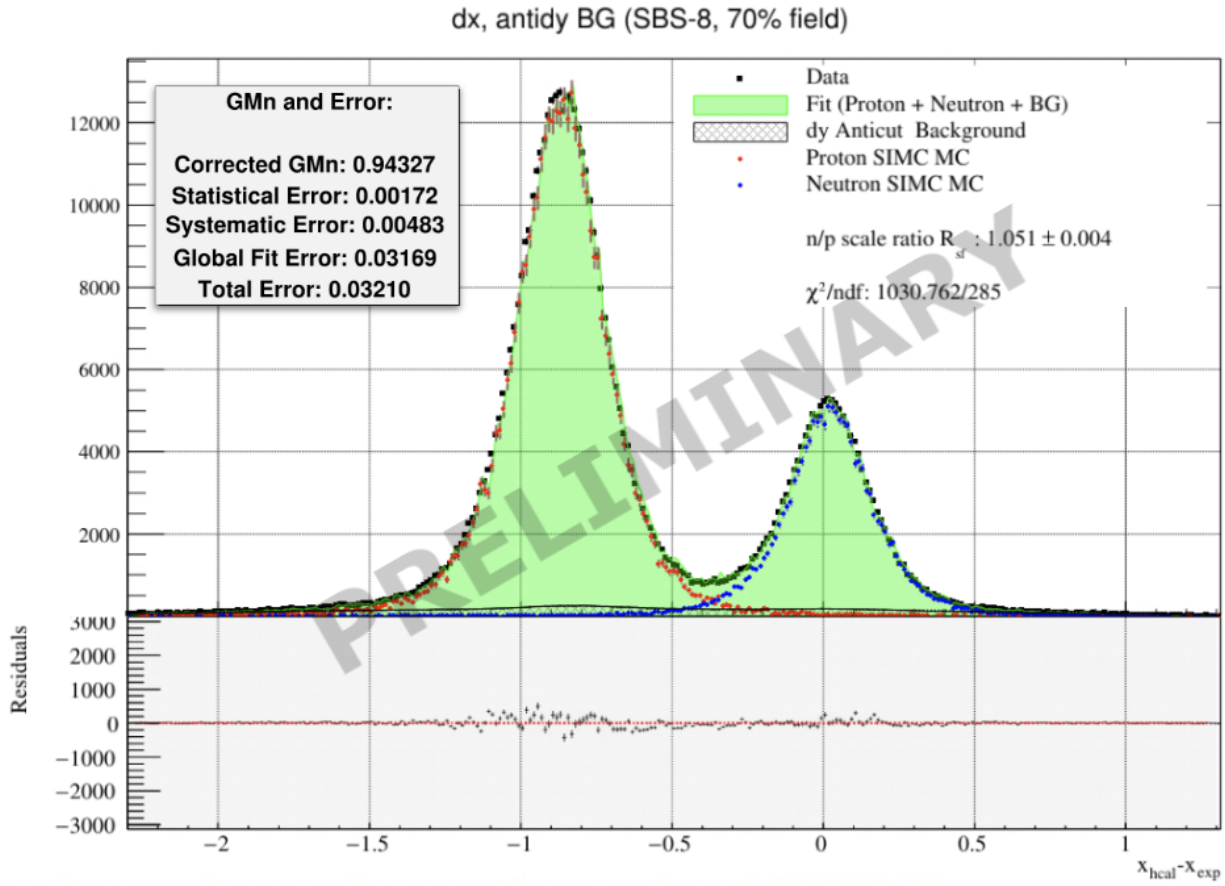

Figure 104: Preliminary $G_M^n/(\mu_n G_D)$ extraction at $Q^2 = 4.5$ GeV^2 (SBS-8, 70% field). The label **Corrected GMn** refers to $G_M^n/(\mu_n G_D)$. Quoted $G_M^n/(\mu_n G_D)$ and error uses mean R_{sf} from fits with MC quasielastic signal and various backgrounds. **GMn and Error** precision is left without proper truncation to indicate differences between kinematic settings.

5.5 SBS-8, 100% Field

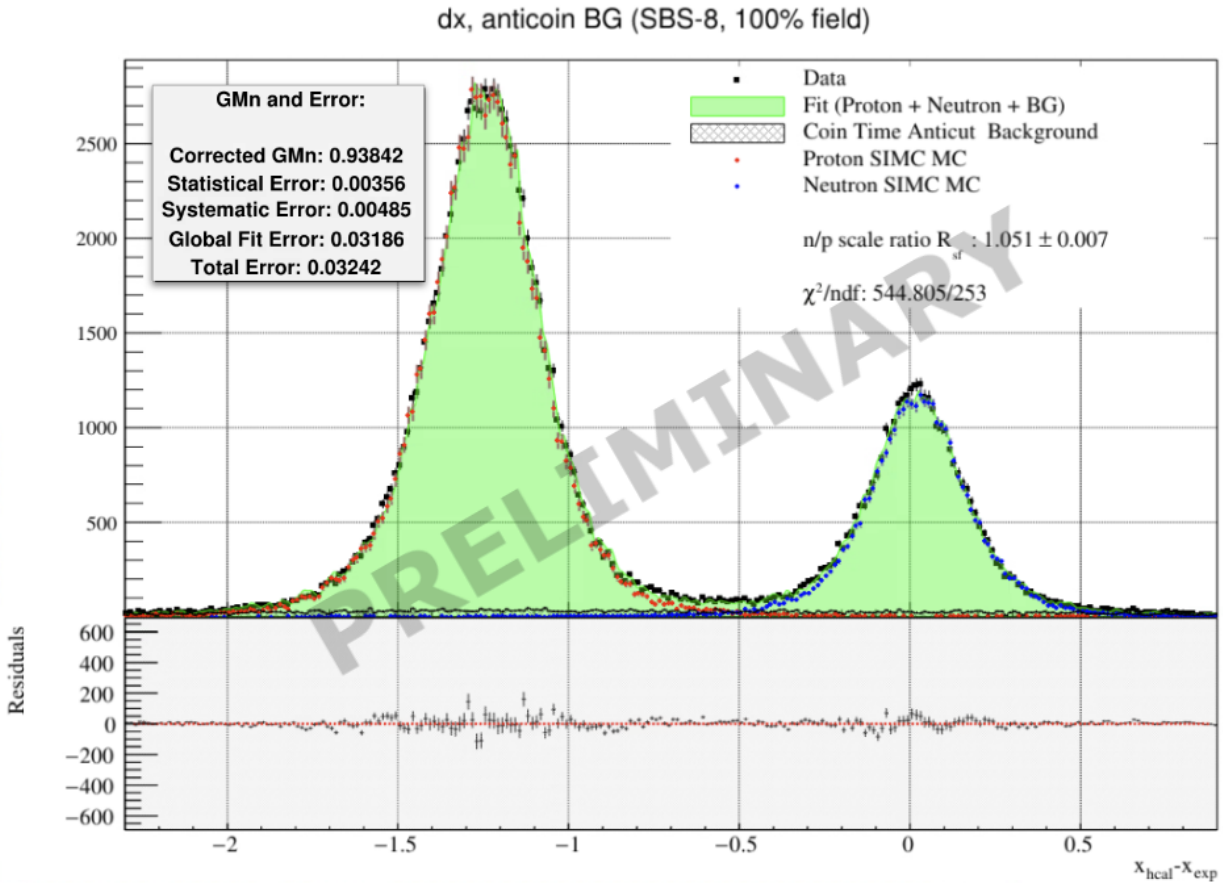

Figure 105: Preliminary $G_M^n/(\mu_n G_D)$ extraction at $Q^2 = 4.5$ GeV^2 (SBS-8, 100% field). The label **Corrected GMn** refers to $G_M^n/(\mu_n G_D)$. Quoted $G_M^n/(\mu_n G_D)$ and error uses mean R_{sf} from fits with MC quasielastic signal and various backgrounds. **GMn and Error** precision is left without proper truncation to indicate differences between kinematic settings.

5.6 SBS-9, 70% Field

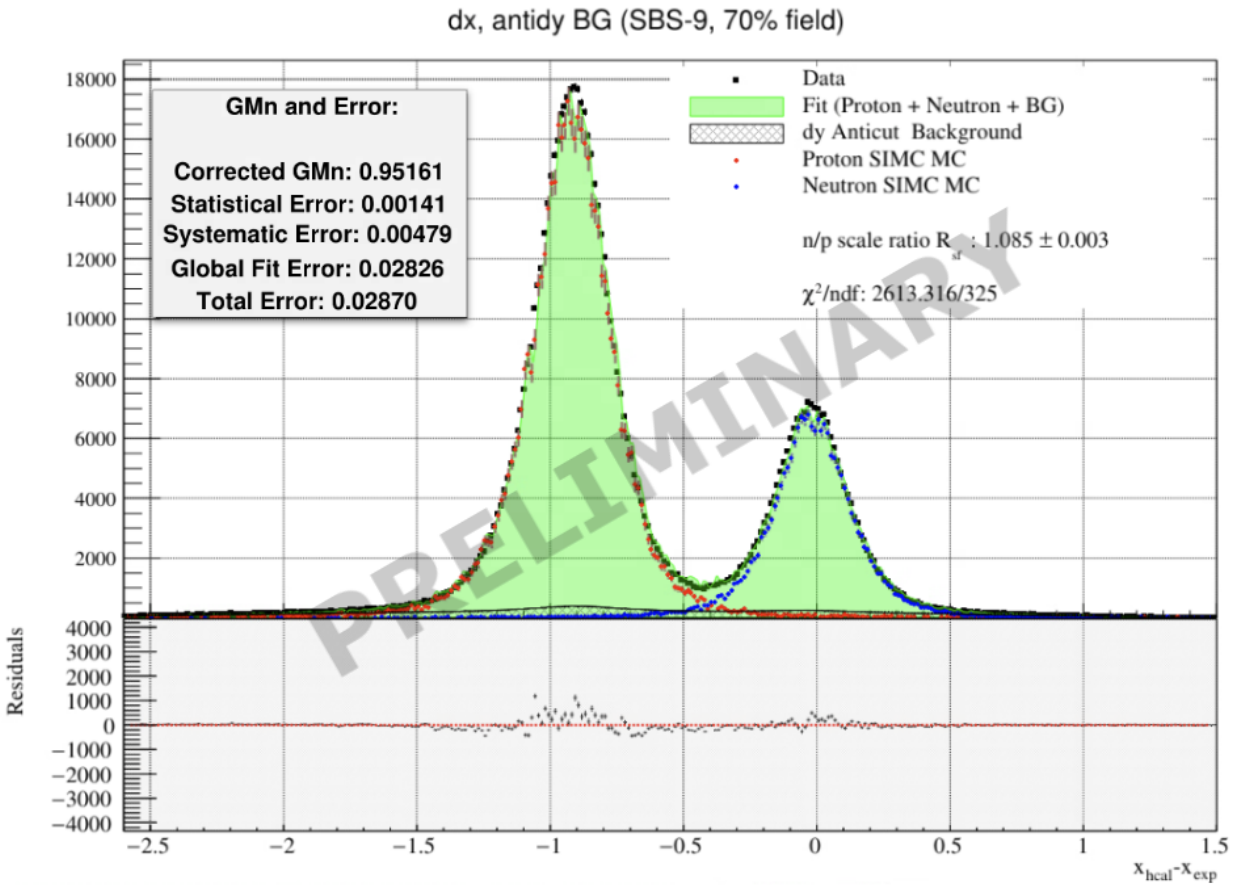

Figure 106: Preliminary $G_M^n/(\mu_n G_D)$ extraction at $Q^2 = 4.5$ GeV^2 (SBS-9, 70% field). The label **Corrected GMn** refers to $G_M^n/(\mu_n G_D)$. Quoted $G_M^n/(\mu_n G_D)$ and error uses mean R_{sf} from fits with MC quasielastic signal and various backgrounds. **GMn and Error** precision is left without proper truncation to indicate differences between kinematic settings.

Results from SBS-9 are systematically higher than those from SBS-8. This shift might be expected without sufficient corrections applied to MC to account for HCal detection efficiency losses. This is evident when examining the correlation in the ”dip” region between the nucleon detection ratio and the neutron to proton ratio in SBS-9 (see figure 108). The nucleon detection ratio indicated in figure 108 is the ratio of events with:

- good electron track cuts,
- fiducial cuts on the expected nucleon y position,

- W^2 cuts,
- a global "OR" on 2σ proton and neutron spot cuts,

and the same events without nucleon spot cuts[140]. The reduction in nucleon detections in expected x (from e' tracks) corresponds to an overall increase in the neutron to proton ratio, consistent with the systematic increase seen in SBS-9 results.

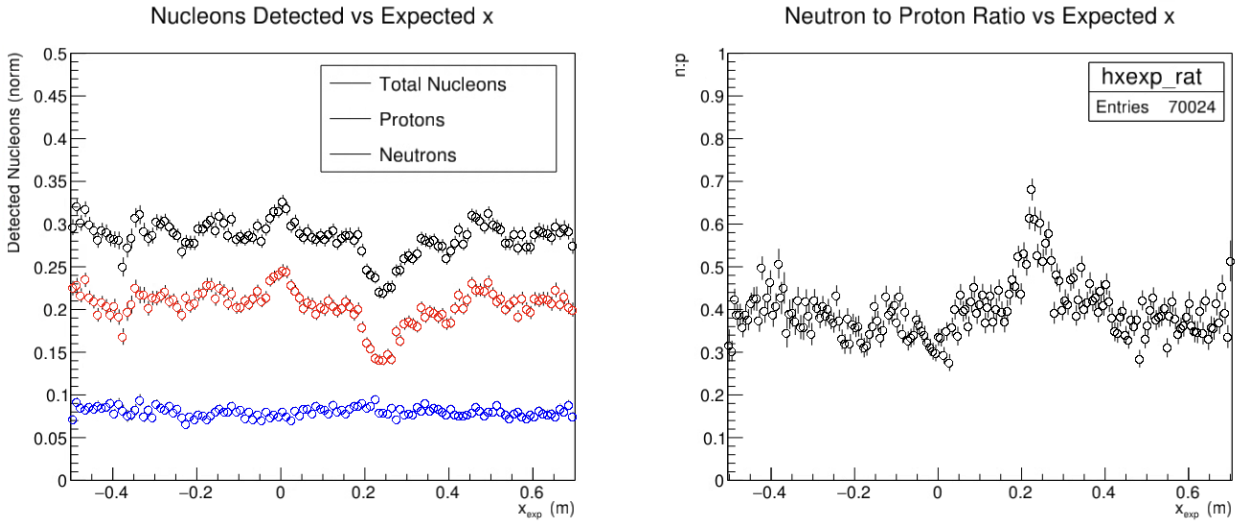

Figure 107: Nucleon detections and n:p ratio vs expected nucleon x position (SBS-9, 70% field). Both plots are bounded by the fiducial cut on this kinematic setting. The y-axis on the left plot includes an arbitrary normalization. The significant variation in detected protons is strongly pronounced for this kinematic setting at $x_{exp} = 0.25$ and results in a systematic upward shift in the n:p ratio at the same expected x position.

A more accurate extraction of $G_M^n/(\mu_n G_D)$ for SBS-9 is expected following nucleon HDE corrections applied to HCal gain coefficients in MC or with the use of HCal detection efficiency maps.

5.7 Super-ratio Systematics

The neutron to proton ratio at each ε kinematic setting can be estimated (as before) by selecting good electron tracks in BigBite, applying a coincidence time cut, and selecting neutrons(protons)

[140]The nucleon detection ratio presented here does not properly account for expected nucleons from e' tracks, over-constrains spot cuts, and should be considered arbitrarily normalized.

with a neutron(proton) spot cut. The variation of the ratio of selected neutrons to protons as a function of the projected x and y variables provides an estimate of the HCal position-dependent systematics. By constraining the fiducial cut in SBS-8 ($\varepsilon_1 = 0.807$) to match SBS-9 ($\varepsilon_2 = 0.517$), these systematic effects can be compared between the two kinematics. Figure 108 depicts these comparisons and the SBS-8 to SBS-9 ratio of neutron to proton ratios from each kinematic (the uncorrected $R_{\varepsilon_1}/R_{\varepsilon_2}$ super-ratio). The cancellation of these HCal position-dependent systematics is evident and provides assurance that, with proper fiducial cuts, systematic errors between the two kinematic settings will cancel in the super-ratio.

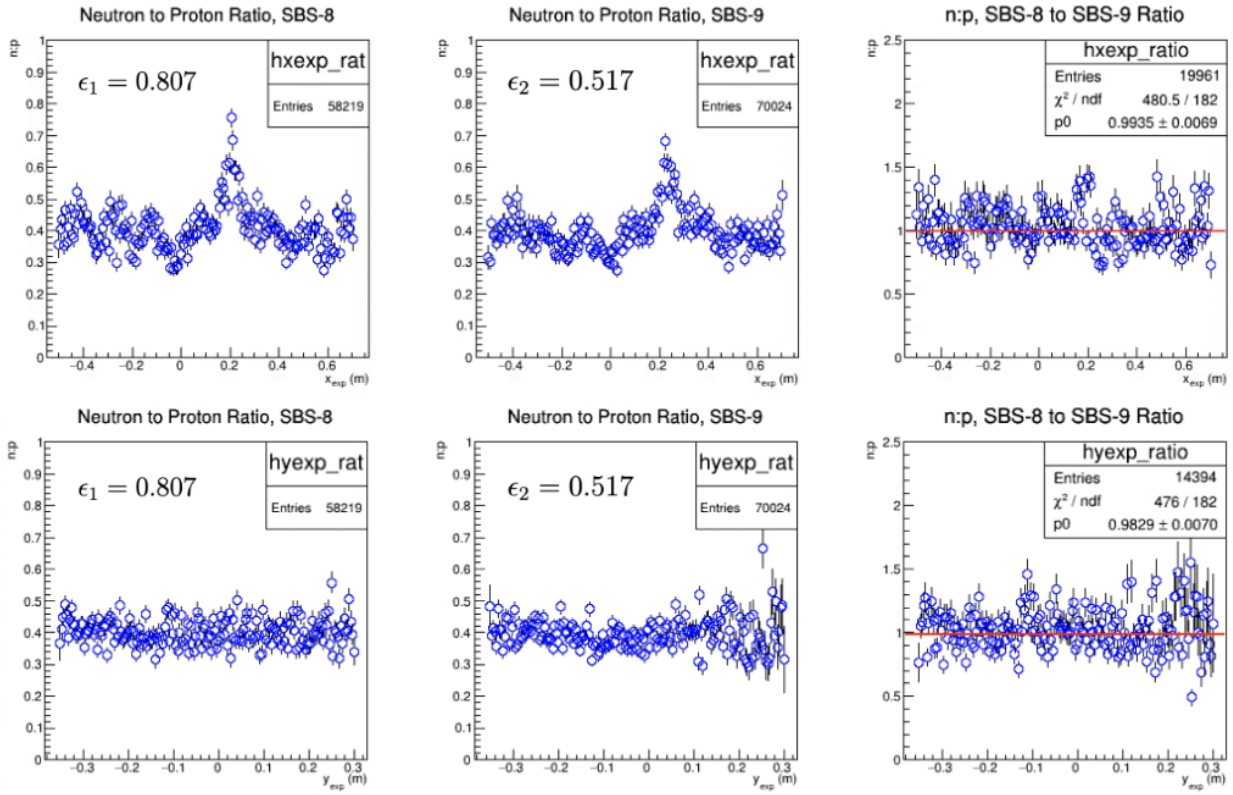

Figure 108: The top row plots are neutron to proton ratio vs expected x from e' projections. The bottom row plots are the same, except vs expected y from e' projections. The first column plots are from SBS-8 ($\varepsilon_1 = 0.807$). The second column plots are from SBS-9 ($\varepsilon_2 = 0.517$). The third column plots are ε_1 n:p ratio (SBS-8, 70% field) divided by ε_2 n:p ratio (SBS-9, 70% field). The pronounced systematic effects, consistent with losses in detection efficiency, are shared across kinematics and largely cancel in the super-ratio.

6 Prospective

G_M^n extractions from $Q^2 = 4.5$ GeV^2 exhibit systematic deviations from central values over different kinematic settings (SBS-8 and SBS-9) and field strengths, depending on the relative concentration of nucleons projected to HCal. The most pronounced effects are observed in SBS-9 data. More accurate extractions are expected from data matched to MC with updated HCal gains that account for "bad block" maps identifying modules with apparent light leaks[141]. Targeted HCal energy calibrations on the data side may also improve this discrepancy. However, for the kinematics presented here, the signal response from the affected modules appears negligible, making the MC solution more robust.

Timing differences between protons and neutrons currently show inconsistencies with simple time-of-flight differences. Improved elastic selection can be achieved by determining the root cause of this discrepancy and applying possible corrections. Therefore, at least one additional data reconstruction pass is likely necessary before publishable G_M^n and RS^n extractions can be obtained.

No RS^n results are presented in this thesis due to the necessary corrections, particularly for SBS-9 data, that account for variations in nucleon detection efficiency across HCal. RS^n measurements are highly sensitive to systematic uncertainties because they involve comparing data across different kinematic settings. Even small changes in efficiency, detector response, or background subtraction can significantly impact the extracted values. However, the apparent cancellation of HCal position-dependent systematics in the uncorrected neutron to proton ratio provides confidence that the final error budget will meet the expectations set by the proposal.

Work will continue to refine the results presented here, although significant deviations from those that are presented are not expected. The overall agreement between extracted G_M^n values and the parameterized Ye et al. fits is encouraging and is presented for all Q^2 points in this analysis in Figures 109 and 110.

[141] See Appendix C for HCal "bad block" maps.

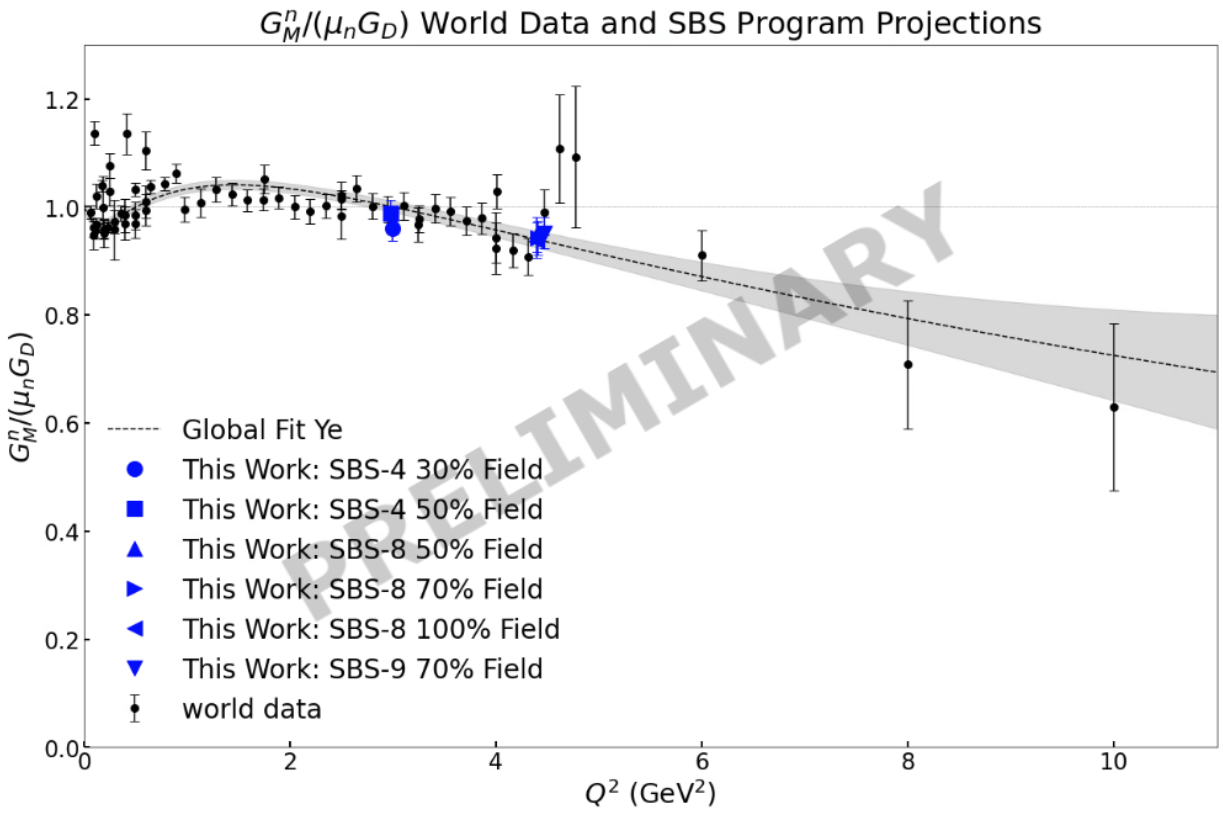

Figure 109: $G_M^n/(\mu_n G_D)$ extractions from this work plotted along with world data taken from [87] and Ye et al. fit[184].

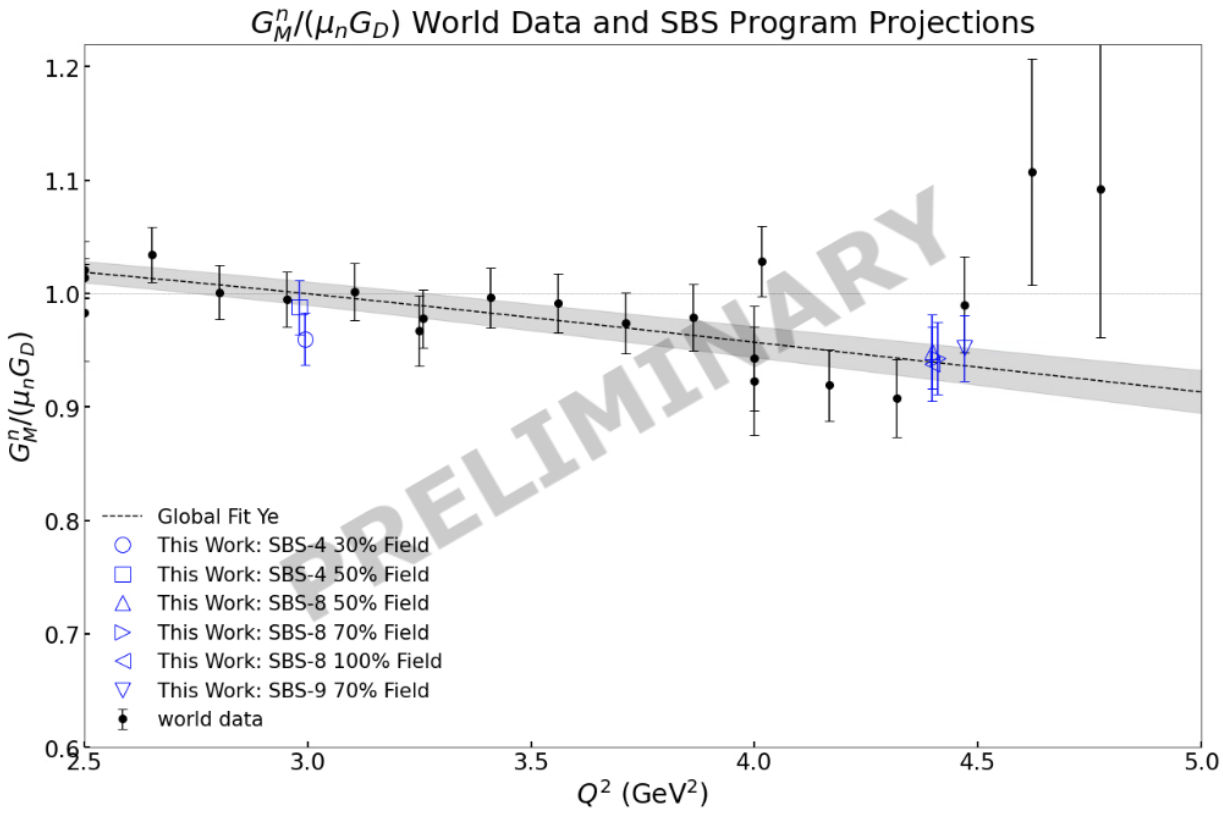

Figure 110: $G_M^n/(\mu_n G_D)$ extractions from this work plotted along with world data taken from [87] and Ye et al. fit[184]. Window is zoomed to resolve individual extractions.

7 Appendix A, Formulae and Parameters

7.1 Basic Definitions

- c: Speed of light (≈ 2.998 m/s in vacuum)
- E: Electron beam energy or incident electron energy
- E': Scattered electron energy
- q: Virtual photon four-momentum
- Q: Four-momentum transfer
- ν: Energy transferred from electron to nucleon
- k: Momentum four-vector for incoming electron
- k': Momentum four-vector for outgoing electron
- p: Momentum four-vector for stationary nucleon
- p': Momentum four-vector for outgoing nucleon
- κ: Anomalous magnetic moment
- θ_e: Electron scattering angle with respect to beamline
- θ_N: Nucleon scattering angle with respect to beamline
- τ: Q^2 scaling variable
- ε: Polarization of virtual photon
- σ_r: Reduced cross section
- σ_r^0: Reduced cross section arising from one-photon exchange only
- σ_{Mott}: Mott cross section
- σ_L: Longitudinal cross section
- σ_T: Transverse cross section
- F_1: Pauli electromagnetic form factor
- F_2: Dirac electromagnetic form factor
- G_E: Sachs electric form factor
- G_M: Sachs magnetic form factor

7.2 Lab-frame Scattering Formulae

$$Q^2 = -q^2 \tag{7.1}$$

$$Q^2 = 4EE' \sin^2\left(\frac{\theta}{2}\right) \tag{7.2}$$

$$\tau = \frac{Q^2}{4M^2} \tag{7.3}$$

$$\varepsilon = \frac{1}{1 + (2(1+\tau)\tan^2(\frac{\theta}{2}))} \tag{7.4}$$

$$k = (E_e, \mathbf{k}) \tag{7.5}$$

$$k' = (E_{e'}, \mathbf{k'}) \tag{7.6}$$

$$p = (M_N, \mathbf{p}) \tag{7.7}$$

$$p' = (E_{N'}, \mathbf{p'}) \tag{7.8}$$

$$q = (\nu, \mathbf{q}) \tag{7.9}$$

7.3 Formulae for Radiation Transport

7.3.1 Bethe-Bloch

Mean rate of energy loss (Stopping power) for a charged particle is given by the Bethe-Bloch formula:

$$-\frac{dE}{dx} = Kz^2 \frac{Z}{A} \frac{1}{\beta^2} \left[\frac{1}{2} \ln \frac{2m_e c^2 \beta^2 \gamma^2 T_{\max}}{I^2} - \beta^2 - \frac{\delta(\beta\gamma)}{2} \right] \tag{7.10}$$

Where,

- A: atomic mass of the absorber
- $\frac{K}{A} = 4\pi N_A r_e^2 m_e c^2 / A = 0.307075$ MeV g^{-1}cm^2, for $A = 1$g mol^{-1}
- z: atomic number of incident particle
- Z: atomic number of absorber

- $T_{\max}$: max. transferable energy

$$T_{\max} = \frac{2m_e c^2 \beta^2 \gamma^2}{1 + 2\gamma \frac{m_e}{m_o} + \left(\frac{m_e}{m_o}\right)^2} \tag{7.11}$$

- N_A: Avogadro's Number ($\approx 6.022e23$)
- m_e: Mass of the electron ($\approx 511keV$)
- β: Particle velocity relative to c (v/c)
- γ: Lorentz factor ($1/\sqrt{1-\beta^2}$)
- I: characteristic ionization constant material dependent
- $\delta(\beta\gamma)$: density effect correction
- $x = \rho s$, mass thickness, where, s is the length

7.3.2 Radiation Length

The radiation length X_0 is given by the following equation:

$$\frac{1}{X_0} = 4\alpha r_e^2 N_A \left[\frac{Z}{A}\left(L_{\text{rad}} - f(Z)\right) + ZL'_{\text{rad}}\right] \tag{7.12}$$

Where the variables are defined as:

- X_0: Radiation length
- α: Fine-structure constant
- r_e: Classical electron radius
- N_A: Avogadro's number
- Z: Atomic number of the material
- A: Atomic mass of the material
- L_{rad}: Material-specific radiation length constant
- $f(Z)$: Fitting function for the radiation length, represented to 4-place accuracy by

$$f(Z) = a^2 \left[(1+a^2)^{-1} + 0.20206 - 0.0369a^2 + 0.0083a^4 - 0.002a^6\right],$$

where $a = \alpha Z$.

- L'_{rad}: Correction factor for the radiation length

The following table lists the values of L_{rad} and L'_{rad} for use in calculating the radiation length in an element using the above equation and is generally good up to Uranium:

Element	L_{rad}	L'_{rad}
H	5.31	6.144
He	4.79	5.621
Li	4.74	5.805
Be	4.71	5.924
Others	$\ln\left(184.15 \cdot Z^{-1/3}\right)$	$\ln\left(1194 \cdot Z^{-2/3}\right)$

Table 29: Tsai's L_{rad} and L'_{rad} for calculating the radiation length

7.4 Form Factor Parametrization Coefficients

This section provides coefficients used to extract G_M^n from R' (the corrected quasielastic $d(e,e'N)$ cross section ratio) from parametrized fits to world data. It also contains coefficients for the parametrizations used in SIMC to generate corrected quasielastic events in simulation[165].

Name	Form Factor Qty	a_1	a_2	a_3	b_1	b_2	b_3	b_4	b_5
Riordan	G_E^n	1.52	2.629	3.055	5.222	0.04	11.438	0	0
JJ Kelly	G_E^p	1.0	-0.24	0	10.98	12.82	21.97	0	0
JJ Kelly	G_M^p/μ_p	2.793	0.12	0	10.97	18.86	6.55	0	0
JJ Kelly	G_M^n/μ_n	-1.913	2.33	0	14.72	24.2	84.1	0	0
Arrington07	G_E^p	3.439	-1.602	0.068	15.055	48.061	99.304	0.012	8.65
Arrington07	G_M^p/μ_p	-1.465	1.26	0.262	9.627	0	0	11.179	13.245

Table 30: Coefficients for Various Form Factor Parametrizations. Coefficients from [165, 10].

Coefficient	Parameters a_i	Error Parameters a_i
a_1	0.048919981	-2.07194073
a_2	-0.064525054	1.13809127
a_3	-0.240825897	1.01431277
a_4	0.392108745	-0.31330138
a_5	0.300445259	-0.273293676
a_6	-0.661888687	0.257350595
a_7	-0.17563977	-0.206042113
a_8	0.624691724	-0.168497322
a_9	-0.077684299	0.137784515
a_{10}	-0.236003975	0.075759196
a_{11}	0.090401973	-0.02675113
a_{12}	0	-0.017525731
a_{13}	0	0.000703582
a_{14}	0	0.001479621
a_{15}	0	0.000197375

Table 31: Coefficients for Ye et al Parametrization of G_E^n. All values from [184].

8 Appendix B, Analysis Methods

8.1 Error Propagation for GMn Extraction

Assuming significant errors only on G_E^n, σ_r^p, and R', the equation used to extract G_M^n is:

$$G_M^n = \sqrt{R' \cdot \frac{\varepsilon_n(1+\tau_n)}{\tau_n \varepsilon_p(1+\tau_p)} \cdot \sigma_r^p - \frac{\varepsilon_n G_E^{n^2}}{\tau_n}}$$

Where no significant error exists in τ and ε, denote:

$$A = \frac{\varepsilon_n(1+\tau_n)}{\tau_n \varepsilon_p(1+\tau_p)}$$

$$B = \frac{\varepsilon_n}{\tau_n}$$

So the equation becomes:

$$G_M^n = \sqrt{R' \cdot A \cdot \sigma_r^p - B \cdot G_E^{n^2}}$$

The errors for G_E^n, σ_r^p, and R' need to be propagated. First, consider the function $f(R', \sigma_r^p, G_E^n)$:

$$f(R', \sigma_r^p, G_E^n) = R' \cdot A \cdot \sigma_r^p - B \cdot G_E^{n^2}$$

The error propagation formula for a function $f(x,y,z)$ is given by:

$$\sigma_f = \sqrt{\left(\frac{\partial f}{\partial x}\sigma_x\right)^2 + \left(\frac{\partial f}{\partial y}\sigma_y\right)^2 + \left(\frac{\partial f}{\partial z}\sigma_z\right)^2}$$

In the current case:

$$\sigma_{G_M^n} = \frac{1}{2}\left(R' \cdot A \cdot \sigma_r^p - B \cdot G_E^{n^2}\right)^{-\frac{1}{2}} \cdot \sqrt{\left(\frac{\partial f}{\partial R'}\sigma_{R'}\right)^2 + \left(\frac{\partial f}{\partial \sigma_r^p}\sigma_{\sigma_r^p}\right)^2 + \left(\frac{\partial f}{\partial G_E^n}\sigma_{G_E^n}\right)^2}$$

Calculating each partial derivative:

$$\frac{\partial f}{\partial R'} = A \cdot \sigma_r^p$$

$$\frac{\partial f}{\partial \sigma_r^p} = R' \cdot A$$

$$\frac{\partial f}{\partial G_E^n} = -2 \cdot B \cdot G_E^n$$

Thus, the total error $\sigma_{G_M^n}$ is:

$$\sigma_{G_M^n} = \frac{1}{2}\left(R' \cdot A \cdot \sigma_r^p - B \cdot G_E^{n^2}\right)^{-\frac{1}{2}} \cdot \sqrt{\left(A \cdot \sigma_r^p \cdot \sigma_{R'}\right)^2 + \left(R' \cdot A \cdot \sigma_{\sigma_r^p}\right)^2 + \left(-2 \cdot B \cdot G_E^n \cdot \sigma_{G_E^n}\right)^2}$$

This formula gives the propagated error for G_M^n considering significant errors only on G_E^n evaluated from a fit to world data, σ_r^p evaluated from fits to world data for G_E^p and G_M^p, and R' evaluated from the MC scale factor ratio systematic and statistical errors.

8.1.1 Error Budget

To account for separate systematic and statistical errors in R', as well as model errors in G_E^n and σ_r^p, introduce the following terms:

- $\sigma_{R',\text{stat}}$: Statistical error in R'
- $\sigma_{R',\text{sys}}$: Systematic error in R'
- $\sigma_{\sigma_r^p,\text{model}}$: Model error in σ_r^p
- $\sigma_{G_E^n,\text{model}}$: Model error in G_E^n

Here, each component of the error is calculated separately:

- The statistical error component:

$$\sigma_{G_M^n,\text{stat}} = \frac{1}{2}\left(R' \cdot A \cdot \sigma_r^p - B \cdot G_E^{n^2}\right)^{-\frac{1}{2}} \cdot \left(A \cdot \sigma_r^p \cdot \sigma_{R',\text{stat}}\right)$$

- The systematic error component:

$$\sigma_{G_M^n,\text{sys}} = \frac{1}{2}\left(R' \cdot A \cdot \sigma_r^p - B \cdot G_E^{n^2}\right)^{-\frac{1}{2}} \cdot \left(A \cdot \sigma_r^p \cdot \sigma_{R',\text{sys}}\right)$$

- The model error components:

$$\sigma_{G_M^n,\text{model},1} = \frac{1}{2}\left(R' \cdot A \cdot \sigma_r^p - B \cdot G_E^{n^2}\right)^{-\frac{1}{2}} \cdot \left(R' \cdot A \cdot \sigma_{\sigma_r^p,\text{model}}\right)$$

$$\sigma_{G_M^n,\text{model},2} = \frac{1}{2}\left(R' \cdot A \cdot \sigma_r^p - B \cdot G_E^{n^2}\right)^{-\frac{1}{2}} \cdot \left(-2 \cdot B \cdot G_E^n \cdot \sigma_{G_E^n,\text{model}}\right),$$

where $\sigma_{G_M^n,\text{model},1}$ is the uncertainty introduced by the model reduced proton cross section $\sigma_{\sigma_r^p}$ and $\sigma_{G_M^n,\text{model},2}$ is the uncertainty introduced by the model G_E^n. Each of the model errors are determined by the parameterized error from the fit model used to extract values for comparison [165, 10, 184, 104].

9 Systematic Error from HDE

The following describes the method for propagating the error in HCal detection efficiency (HDE) through the ratio R_{sf}. The errors considered include both statistical and systematic components.

The following definitions are used:

- ε: Detection efficiency
- $\delta\varepsilon$: Systematic error in detection efficiency (equivalent to σ_{sys})
- R_{sf}: Neutron-to-proton ratio
- δR_{sf}: Error in R_{sf}
- N_{neutrons}: Number of detected neutrons
- N_{protons}: Number of detected protons

- σ_{weighted}: Statistical error of the weighted mean detection efficiency
- σ_{sys}: Systematic error of the detection efficiency (equivalent to $\delta\varepsilon$)
- σ_{combined}: Combined error of the detection efficiency

To estimate the systematic error using three samples and a central tendency value from MC, one can follow the following steps:

- **Calculate the Deviations**: For each sample, calculate the deviation from the central value:

$$d_i = \varepsilon_i - \varepsilon_{\text{central}}, \quad \text{for } i = 1,2,3$$

- **Compute the Variance**: Compute the variance of these deviations:

$$\sigma_{\text{sys}}^2 = \frac{1}{3}\sum_{i=1}^{3}(d_i)^2$$

- **Estimate the Systematic Error**: Take the square root of the variance to get the standard deviation, which represents the systematic error:

$$\sigma_{\text{sys}} = \sqrt{\frac{1}{3}\sum_{i=1}^{3}(d_i)^2}$$

This approach provides a robust estimate of the systematic error by quantifying the spread of the sample values around the central tendency value.

9.0.1 Error Propagation with Different Efficiencies for Protons and Neutrons

To include different detection efficiencies for protons (ε_p) and neutrons (ε_n) while keeping the error in the efficiency is the same ($\delta\varepsilon = \sigma_{\text{sys}}$), the propagation of error through R_{sf} is modified as follows:

The error in the ratio R_{sf} due to systematic errors in detection efficiency can be approximated using the propagation of uncertainty formula for division:

$$\left(\frac{\delta R_{\text{sf}}}{R_{\text{sf}}}\right)^2 = \left(\frac{\delta N_{\text{neutrons}}}{N_{\text{neutrons}}}\right)^2 + \left(\frac{\delta N_{\text{protons}}}{N_{\text{protons}}}\right)^2$$

Since $\delta N_{\text{neutrons}}$ and $\delta N_{\text{protons}}$ are proportional to $\delta\varepsilon$:

$$\delta N_{\text{neutrons}} = N_{\text{neutrons}} \cdot \frac{\delta\varepsilon}{\varepsilon_n}$$

$$\delta N_{\text{protons}} = N_{\text{protons}} \cdot \frac{\delta\varepsilon}{\varepsilon_p}$$

Thus:

$$\left(\frac{\delta R_{\text{sf}}}{R_{\text{sf}}}\right)^2 = \left(\frac{\delta\varepsilon}{\varepsilon_n}\right)^2 + \left(\frac{\delta\varepsilon}{\varepsilon_p}\right)^2$$

$$\frac{\delta R_{\text{sf}}}{R_{\text{sf}}} = \sqrt{\left(\frac{\delta\varepsilon}{\varepsilon_n}\right)^2 + \left(\frac{\delta\varepsilon}{\varepsilon_p}\right)^2}$$

The error in R_{sf} due to detection efficiency when the efficiencies are different but the error is the same is:

$$\delta R_{\text{sf}} = R_{\text{sf}} \cdot \sqrt{\left(\frac{\delta\varepsilon}{\varepsilon_n}\right)^2 + \left(\frac{\delta\varepsilon}{\varepsilon_p}\right)^2}$$

The Final Error Form

The final form of the error in R_{sf} combines both nucleon sources of error to provide an estimate of the error from HDE. The systematic error from the detection efficiency ($\delta R_{\text{sf, syst hde}}$) is derived from the systematic error in the detection efficiency (σ_{sys}). This simplifies the error propagation, as the relative impact on R_{sf} is proportional to the efficiency error. For all calculations, the systematic error in detection efficiency is assumed to be the same for protons and neutrons. This entails that the proton to neutron detection efficiency ratio stays the same as a function of HCal position.

9.1 Cluster Selection Algorithms

For most analysis, the primary cluster in HCal is used to evaluate the position, timing, and energy of the nucleon detected there. However, each event has possibly many clusters in HCal which are formed from ADC signals over thresholds in many blocks. HCal cluster selection after cluster reconstruction in SBS-offline must be sensitive to the timing difference between the cluster ADC time and the BBCal trigger time (the coincidence ADC time) and the energy of the cluster. At least two algorithms are used to perform this selection. Both of these algorithms require the mean of the normally distributed coincidence ADC time peak. The "E-t scoring" algorithm requires also the standard deviation of that peak.

9.1.1 In-time Algorithm

The "in-time" algorithm loops over all available clusters in an event and proceeds in two steps:

1. Make a wide cut on the absolute mean difference between the ADC time for the highest energy block in the cluster (the cluster ADC time) and the BBCal ADC time (Δt). For all kinematics in this thesis, $\Delta t = 10$ ns.

2. Select the cluster with the highest energy sum from among blocks in the cluster.

The cluster which is selected is promoted to primary. Due to the simplicity and negligible benefit of the "E-t scoring" algorithm for the kinematics considered in this thesis, the "in-time" algorithm is used throughout the analysis presented here.

9.1.2 E-t Scoring

The "E-t scoring" algorithm loops over all available clusters in an event and evaluates the following two quantities per cluster:

- The probability density deriving from Δt on the event and the unity-normalized Gaussian profile of the observed coincidence time distribution (*PDF* value). This returns a value between zero and unity which is the value of the Gaussian profile at Δt.

- The cluster sum energy normalized by the highest sum energy among clusters for the event.

The product of these two values gives a value between zero and unity, where the highest score among clusters is promoted to primary.

9.1.3 Comparisons

Figure 111 depicts a comparison of these methods for SBS-4 with liquid hydrogen and SBS magnetic field off. The number of events collected in the elastic proton peak indicates the relative efficiency of the algorithm. It is worthy to note here that one can use position information to select the cluster closest to the expected location of an elastic nucleon in HCal (as projected from the e' track), but this method has been demonstrated to promote background into signal and is not used during the analysis.

9.2 Optics Validity Cuts

Strict tracking cuts can be made with focal plane variables on the tree. These cuts ensure that track projections to the BigBite midplane are within the acceptance. These cuts are taken in two directions[139]:

- Vertical, focal plane (fp) x, $x_{mid} = x_{\rm fp} - 0.9 \cdot \theta_{\rm fp}$, typically $x_{mid} < 0.3$ m
- Horizontal, focal plane (fp) y, $y_{mid} = y_{\rm fp} - 0.9 \cdot \phi_{\rm fp}$, typically $y_{mid} < 0.1$ m

These cuts can vary slightly based on kinematic setting and are primarily used to normalize detection efficiency extractions. Figures 112 and 113 depict x_{mid} and y_{mid} and describe cut placement.

9.3 Physics Blinding Procedure

No organized blinding procedure was devised or supported before and throughout the analysis among the collaboration. It was accepted that blinding was not a necessary step for an analysis like this, considering the relatively small size of the analysis effort and the expected SNR for all kinematics. Nevertheless, a blinding procedure was devised for this purpose and is presented here.

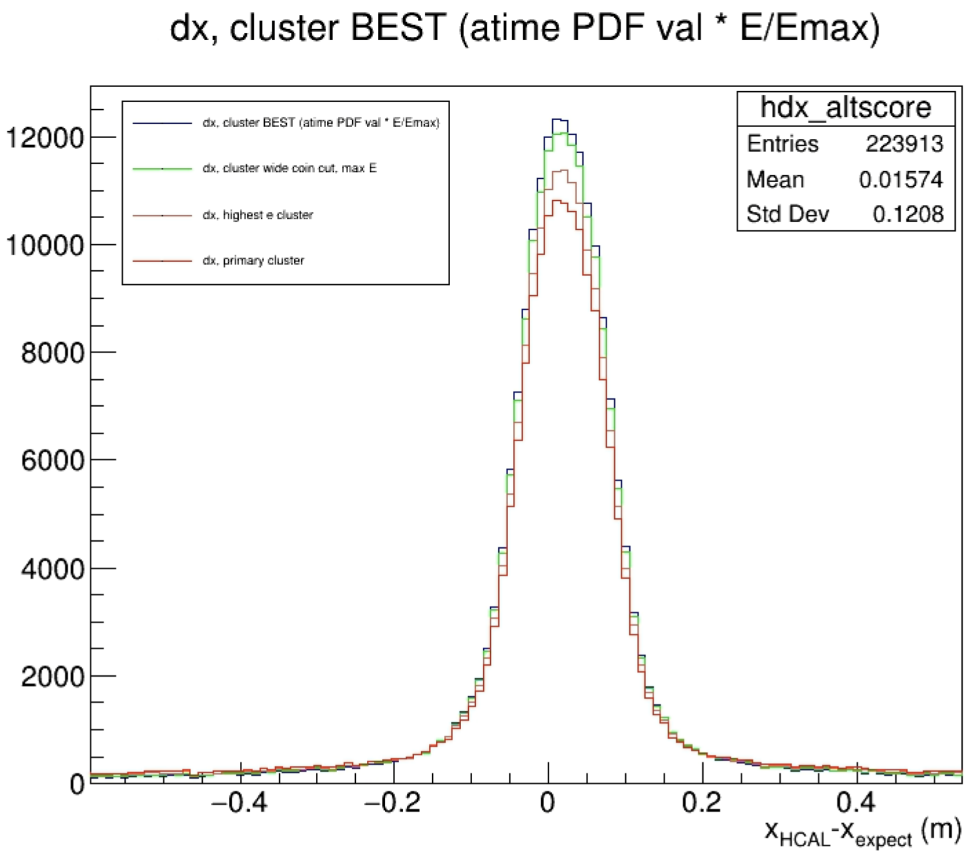

Figure 111: Proton signal peak in *dx* with various HCal primary cluster selections for SBS-4, LH2 target, and zero field. The "E-t score" (in black) algorithm performs best, the "in-time" algorithm (green) a close second, a simple selection of highest cluster sum energy (orange) a significantly distanced third, and the default primary block after reconstruction (red) coming in last.

9.3.1 Parsing and MC Blinded Weight

To blind the $n : p$ ratios in the analysis, a function (called blinder) is implemented during data parsing to assign a random scaling factor to the weights of MC proton events. The blinder function generates a random number using a four-letter passkey, ensuring a consistent seed for the random number generator. The generated number scales the proton event weights within the range [0.95, 1.05], while neutron event weights remain unchanged. The key for the random number is stored but not used until the analysis parameters, including cuts and methods, are finalized. This ensures unbiased analysis until the final extraction steps.

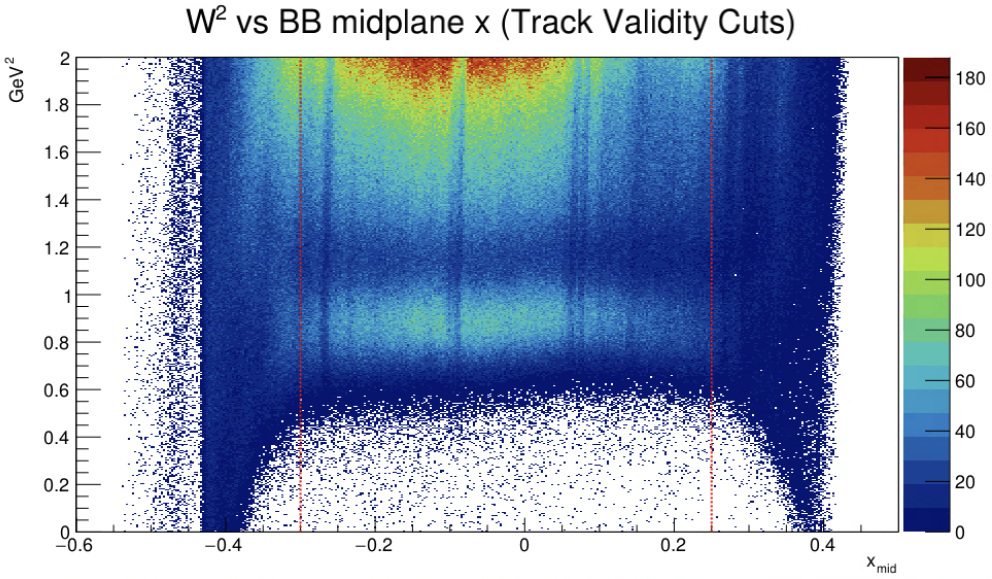

Figure 112: W^2 vs track BigBite midplane vertical projection. Cuts (red dotted lines) are placed before significant non-uniform low W tracks impact the W^2 distribution.

Data parsing is conducted to reduce the raw output of data reconstruction to a smaller data footprint and to add calculated physics parameters important for later analysis. This technique allows for the loop over data to be performed only once, with all other analysis performed on a flat tree structure with variables which can be drawn directly. No further loops over each event are necessary during extractions and other analysis.

9.4 Supplemental HCal Detection Efficiency Methods

There are several methods explored to extract the proton HDE for comparison to MC. The methods that follow suffer from high sensitivity to cuts and fit ranges. Additionally, they give only one overall HDE without an explicit check on uniformity. Nevertheless, they are explained here where they may yet have some utility where confirmation of other methods is useful.

9.4.1 Inclusive W^2 Anticut Method

This method focuses on protons from liquid hydrogen (LH2) with high signal to noise (SBS 4, high elastic yield / C, relatively low Q^2). Data with SBS magnetic field at 0% is also preferred to

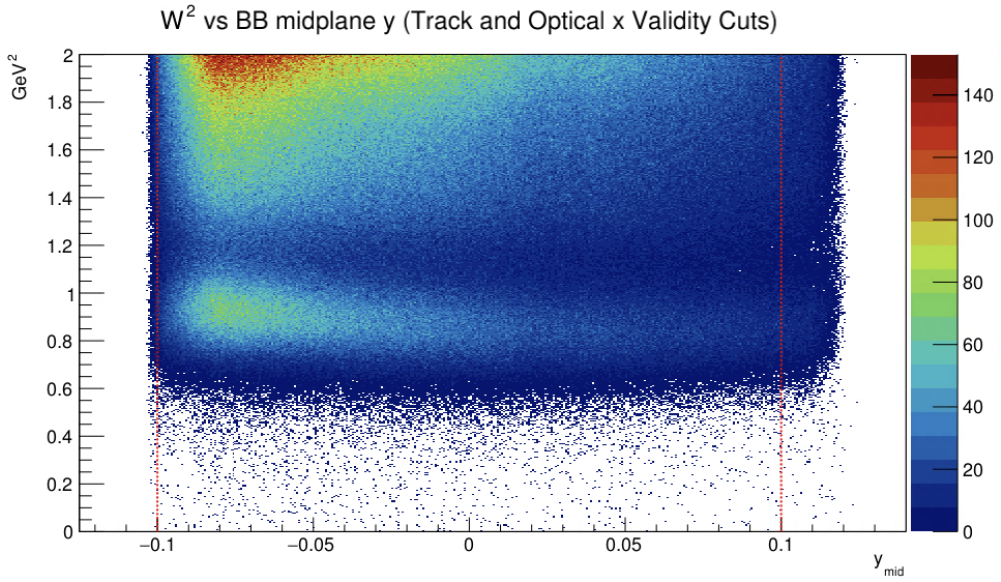

Figure 113: W^2 vs track BigBite midplane horizontal projection. Cuts (red dotted lines) are placed before the W^2 distribution suffers uniformity losses.

reduce proton spot smearing on HCal and acceptance matching cuts on elastic projections. The overall efficiency, HDE, is defined as HDE = N_{det}/N_{exp} as usual.

The expected number of elastics N_{exp} is derived from the W^2 distribution. The "full" histogram ($h1$) is populated with an acceptance matching cut only. This acceptance matching cut removes all events whose projections would not land on the active area of HCal[142]. A "pure" elastic sample is obtained from very tight elastic cuts on both arms. These cuts include tight W^2 and proton spot cuts on dx and dy. The "full" histogram $h1$ is fit to the scaled elastic sample shape and a polynomial for the background. Background is subtracted from the "full" histogram to obtain the expected elastics from the integral of what remains in $h1$.

Detected elastics N_{det} are derived from W^2 with a HCal anticut. The "anticut" histogram ($h2$) is populated with an acceptance matching cut and HCal spot *anticuts*. The $h2$ histogram is fitted again with the "pure" elastic shape and polynomial background. The background is subtracted from $h2$ and the integral extracts the elastic events that HCal *missed*, N_{miss}. N_{det} is the difference between N_{exp} and N_{miss}. Proton HDE is then given by the ratio of detected elastics to expected

[142]For kinematics where no zero-field data is available, an average separation gathered from the dx difference between proton and neutron spots will suffice.

elastics.

9.4.2 Sideband dx Signal Method

This method follows a similar procedure to the Inclusive W^2 Anticut Method for determining N_{exp}. However, it focuses on extracting N_{det} from the dx distribution. The dx histogram uses all the same cuts as the "full" W^2 histogram. The total number of detected elastics is obtained by performing a sideband polynomial fit to the background in dx avoiding the elastic signal peak, subtracting this background, and integrating the remaining signal in the dx histogram.

9.4.3 Elastic Selection Cuts and Fit Details

For the following cuts, `kine` refers to the kinematic configuration, `mag` refers to the SBS magnetic field strength in percent, `lh2` refers to hydrogen cryotarget, and `ld2` refers to deuterium cryotarget. The following represent cuts applied to data when extracting G_M^n, RS^n, and various HCal detection efficiencies. Tighter cuts, where mentioned, override the following.

kine	mag	target	bb_etot_over_p
4	0	lh2	bb_etot_over_p>0.8&&bb_etot_over_p<1.18
4	30	lh2	bb_etot_over_p>0.8&&bb_etot_over_p<1.18
4	50	lh2	bb_etot_over_p>0.8&&bb_etot_over_p<1.18
4	30	ld2	bb_etot_over_p>0.81&&bb_etot_over_p<1.17
4	50	ld2	bb_etot_over_p>0.81&&bb_etot_over_p<1.17
8	0	lh2	bb_etot_over_p>0.8&&bb_etot_over_p<1.18
8	50	lh2	bb_etot_over_p>0.8&&bb_etot_over_p<1.18
8	70	lh2	bb_etot_over_p>0.8&&bb_etot_over_p<1.18
8	100	lh2	bb_etot_over_p>0.8&&bb_etot_over_p<1.18
8	50	ld2	bb_etot_over_p>0.84&&bb_etot_over_p<1.16
8	70	ld2	bb_etot_over_p>0.84&&bb_etot_over_p<1.16
8	100	ld2	bb_etot_over_p>0.84&&bb_etot_over_p<1.16
9	70	lh2	bb_etot_over_p>0.8&&bb_etot_over_p<1.18
9	70	ld2	bb_etot_over_p>0.8&&bb_etot_over_p<1.18

Table 32: Elastic selection cuts: e' E/p

kine	mag	target	hcale
4	0	lh2	hcale>0.02
4	30	lh2	hcale>0.02
4	50	lh2	hcale>0.027
4	30	ld2	hcale>0.0224
4	50	ld2	hcale>0.0224
8	0	lh2	hcale>0.02
8	50	lh2	hcale>0.055
8	70	lh2	hcale>0.055
8	100	lh2	hcale>0.055
8	50	ld2	hcale>0.08
8	70	ld2	hcale>0.08
8	100	ld2	hcale>0.08
9	70	lh2	hcale>0.055
9	70	ld2	hcale>0.08

Table 33: Elastic selection cuts: HCal energy

kine	mag	target	coin
4	0	lh2	coin>-10.0&&coin<10.0
4	30	lh2	coin>-10.0&&coin<10.0
4	50	lh2	coin>-10.0&&coin<10.0
4	30	ld2	coin>-10.0&&coin<10.0
4	50	ld2	coin>-10.0&&coin<10.0
8	0	lh2	coin>-10.0&&coin<10.0
8	50	lh2	coin>-10.0&&coin<10.0
8	70	lh2	coin>-10.0&&coin<10.0
8	100	lh2	coin>-10.0&&coin<10.0
8	50	ld2	coin>-10.0&&coin<10.0
8	70	ld2	coin>-10.0&&coin<10.0
8	100	ld2	coin>-10.0&&coin<10.0
9	70	lh2	coin>-10.0&&coin<10.0
9	70	ld2	coin>-10.0&&coin<10.0

Table 34: Elastic selection cuts: BBCal - HCal coincidence time

kine	mag	target	W2
4	0	lh2	W2>0.65&&W2<0.95
4	30	lh2	W2>0.65&&W2<0.95
4	50	lh2	W2>0.22&&W2<1.24
4	30	ld2	W2>0.595&&W2<1.16
4	50	ld2	W2>0.595&&W2<1.16
8	0	lh2	W2>0.65&&W2<0.95
8	50	lh2	W2>0.65&&W2<0.95
8	70	lh2	W2>0.65&&W2<0.95
8	100	lh2	W2>0.65&&W2<0.95
8	50	ld2	W2>0.49&&W2<1.09
8	70	ld2	W2>0.49&&W2<1.09
8	100	ld2	W2>0.49&&W2<1.09
9	70	lh2	W2>0.5&&W2<1.1
9	70	ld2	W2>0.49&&W2<1.09

Table 35: Elastic selection cuts: W^2

kine	mag	target	bb_ps_e
4	0	lh2	bb_ps_e>0.25
4	30	lh2	bb_ps_e>0.25
4	50	lh2	bb_ps_e>0.25
4	30	ld2	bb_ps_e>0.234
4	50	ld2	bb_ps_e>0.234
8	0	lh2	bb_ps_e>0.2
8	50	lh2	bb_ps_e>0.2
8	70	lh2	bb_ps_e>0.2
8	100	lh2	bb_ps_e>0.2
8	50	ld2	bb_ps_e>0.3
8	70	ld2	bb_ps_e>0.288
8	100	ld2	bb_ps_e>0.3
9	70	lh2	bb_ps_e>0.3
9	70	ld2	bb_ps_e>0.3

Table 36: Elastic selection cuts: BBCal preshower energy

kine	mag	target	bb_tr_vz
4	0	lh2	abs(bb_tr_vz)<0.073
4	30	lh2	abs(bb_tr_vz)<0.073
4	50	lh2	abs(bb_tr_vz)<0.073
4	30	ld2	abs(bb_tr_vz)<0.073
4	50	ld2	abs(bb_tr_vz)<0.073
8	0	lh2	abs(bb_tr_vz)<0.073
8	50	lh2	abs(bb_tr_vz)<0.073
8	70	lh2	abs(bb_tr_vz)<0.073
8	100	lh2	abs(bb_tr_vz)<0.073
8	50	ld2	abs(bb_tr_vz)<0.073
8	70	ld2	abs(bb_tr_vz)<0.073
8	100	ld2	abs(bb_tr_vz)<0.073
9	70	lh2	abs(bb_tr_vz)<0.073
9	70	ld2	abs(bb_tr_vz)<0.073

Table 37: Elastic selection cuts: e' track vertex z

kine	mag	target	bb_gem_track_nhits
4	0	lh2	bb_gem_track_nhits>2
4	30	lh2	bb_gem_track_nhits>2
4	50	lh2	bb_gem_track_nhits>2
4	30	ld2	bb_gem_track_nhits>2
4	50	ld2	bb_gem_track_nhits>2
8	0	lh2	bb_gem_track_nhits>2
8	50	lh2	bb_gem_track_nhits>2
8	70	lh2	bb_gem_track_nhits>2
8	100	lh2	bb_gem_track_nhits>2
8	50	ld2	bb_gem_track_nhits>2
8	70	ld2	bb_gem_track_nhits>2
8	100	ld2	bb_gem_track_nhits>2
9	70	lh2	bb_gem_track_nhits>2
9	70	ld2	bb_gem_track_nhits>2

Table 38: Elastic selection cuts: BigBite GEM N hits

kine	mag	target	hcalon
4	0	lh2	hcalon==1
4	30	lh2	hcalon==1
4	50	lh2	hcalon==1
4	30	ld2	hcalon==1
4	50	ld2	hcalon==1
8	0	lh2	hcalon==1
8	50	lh2	hcalon==1
8	70	lh2	hcalon==1
8	100	lh2	hcalon==1
8	50	ld2	hcalon==1
8	70	ld2	hcalon==1
8	100	ld2	hcalon==1
9	70	lh2	hcalon==1
9	70	ld2	hcalon==1

Table 39: Elastic selection cuts: HCal Active Area

kine	mag	target	xexp
4	0	lh2	xexp<0.8&&xexp>-1.3
4	30	lh2	xexp<0.8&&xexp>-1.3
4	50	lh2	xexp<0.7&&xexp>-1.1
4	30	ld2	xexp<0.8&&xexp>-1.3
4	50	ld2	xexp<0.7&&xexp>-1.1
8	0	lh2	xexp<1.0&&xexp>-1.9
8	50	lh2	xexp<1.5&&xexp>-1.9
8	70	lh2	xexp<1.5&&xexp>-1.9
8	100	lh2	xexp<1.0&&xexp>-1.9
8	50	ld2	xexp<0.8&&xexp>-0.9
8	70	ld2	xexp<0.8&&xexp>-0.8
8	100	ld2	xexp<0.8&&xexp>-0.8
9	70	lh2	xexp<0.7&&xexp>-0.7
9	70	ld2	xexp<0.8&&xexp>-0.8

Table 40: Elastic selection cuts: expected dispersive position from e' track

kine	mag	target	yexp
4	0	lh2	yexp<0.45&&yexp>-0.25
4	30	lh2	yexp<0.45&&yexp>-0.25
4	50	lh2	yexp<0.45&&yexp>-0.25
4	30	ld2	yexp<0.45&&yexp>-0.25
4	50	ld2	yexp<0.73&&yexp>-0.73
8	0	lh2	yexp<0.65&&yexp>-0.5
8	50	lh2	yexp<0.5&&yexp>-0.5
8	70	lh2	yexp<0.5&&yexp>-0.5
8	100	lh2	yexp<0.5&&yexp>-0.5
8	50	ld2	yexp<0.4&&yexp>-0.4
8	70	ld2	yexp<0.4&&yexp>-0.4
8	100	ld2	yexp<0.4&&yexp>-0.4
9	70	lh2	yexp<0.3&&yexp>-0.4
9	70	ld2	yexp<0.2&&yexp>-0.4

Table 41: Elastic selection cuts: expected transverse y position from e' track

kine	mag	target	dy
4	0	lh2	dy>-0.35&&dy<0.25
4	30	lh2	dy>-0.35&&dy<0.25
4	50	lh2	dy>-0.35&&dy<0.25
4	30	ld2	dy>-0.36&&dy<0.264
4	50	ld2	dy>-0.36&&dy<0.264
8	0	lh2	dy>-0.35&&dy<0.25
8	50	lh2	dy>-0.35&&dy<0.25
8	70	lh2	dy>-0.35&&dy<0.25
8	100	lh2	dy>-0.35&&dy<0.25
8	50	ld2	dy>-0.3&&dy<0.2
8	70	ld2	dy>-0.3&&dy<0.2
8	100	ld2	dy>-0.3&&dy<0.2
9	70	lh2	dy>-0.3&&dy<0.2
9	70	ld2	dy>-0.3&&dy<0.2

Table 42: Elastic selection cuts: *dy*

kine	mag	target	bb_grinch_tdc_clus_size
4	0	lh2	
4	30	lh2	
4	50	lh2	
4	30	ld2	
4	50	ld2	
8	0	lh2	bb_grinch_tdc_clus_size>1
8	50	lh2	bb_grinch_tdc_clus_size>1
8	70	lh2	bb_grinch_tdc_clus_size>1
8	100	lh2	bb_grinch_tdc_clus_size>1
8	50	ld2	bb_grinch_tdc_clus_size>1
8	70	ld2	bb_grinch_tdc_clus_size>1
8	100	ld2	bb_grinch_tdc_clus_size>1
9	70	lh2	bb_grinch_tdc_clus_size>1
9	70	ld2	bb_grinch_tdc_clus_size>1

Table 43: Elastic selection cuts: GRINCH cluster size

kine	mag	target	bb_grinch_tdc_clus_trackindex
4	0	lh2	
4	30	lh2	
4	50	lh2	
4	30	ld2	
4	50	ld2	
8	0	lh2	bb_grinch_tdc_clus_trackindex==0
8	50	lh2	bb_grinch_tdc_clus_trackindex==0
8	70	lh2	bb_grinch_tdc_clus_trackindex==0
8	100	lh2	bb_grinch_tdc_clus_trackindex==0
8	50	ld2	bb_grinch_tdc_clus_trackindex==0
8	70	ld2	bb_grinch_tdc_clus_trackindex==0
8	100	ld2	bb_grinch_tdc_clus_trackindex==0
9	70	lh2	bb_grinch_tdc_clus_trackindex==0
9	70	ld2	bb_grinch_tdc_clus_trackindex==0

Table 44: Elastic selection cuts: GRINCH cluster track matched

kine	mag	target	pspot
4	0	lh2	(pow(dx_bc+0.0381,2)/ pow(0.263,2))+(pow(dy_bc+0.0509,2)/pow(0.33,2))<=1
4	30	lh2	(pow(dx_bc+0.7358,2)/pow(0.3581,2))+(pow(dy_bc+0.0481,2)/pow(0.3660,2))<=1
4	50	lh2	(pow(dx_bc+1.2125,2)/pow(0.3725,2))+(pow(dy_bc+0.0505,2)/pow(0.3378,2))<=1
4	30	ld2	(pow(dx_bc+0.71,2)/pow(0.32,2))+(pow(dy_bc+0.05,2)/pow(0.40,2))<=1
4	50	ld2	(pow(dx_bc+1.20,2)/pow(0.25,2))+(pow(dy_bc+0.05,2)/pow(0.3,2))<=1
8	0	lh2	(pow(dx_bc-0.0167,2)/pow(0.3375,2))+(pow(dy_bc+0.0567,2)/pow(0.33,2))<=1
8	50	lh2	(pow(dx_bc+0.6197,2)/pow(0.3375,2))+(pow(dy_bc+0.0535,2)/pow(0.33,2))<=1
8	70	lh2	(pow(dx_bc+0.8482,2)/pow(0.4426,2))+(pow(dy_bc+0.0466,2)/pow(0.3636,2))<=1
8	100	lh2	(pow(dx_bc+0.9,2)/pow(0.3,2))+(pow(dy_bc+0.07,2)/pow(0.3,2))<=1
8	50	ld2	(pow(dx_bc+0.62,2)/pow(0.26,2))+(pow(dy_bc+0.07,2)/pow(0.36,2))<=1
8	70	ld2	(pow(dx_bc+0.88,2)/pow(0.12,2))+(pow(dy_bc+0.07,2)/pow(0.18,2))<=1
8	100	ld2	(pow(dx_bc+1.25,2)/pow(0.3,2))+(pow(dy_bc+0.05,2)/pow(0.36,2))<=1
9	70	lh2	(pow(dx_bc+0.9049,2)/pow(0.3423,2))+(pow(dy_bc+0.0294,2)/pow(0.3323,2))<=1
9	70	ld2	(pow(dx_bc+0.91,2)/pow(0.12,2))+(pow(dy_bc+0.03,2)/pow(0.18,2))<=1

Table 45: Elastic selection cuts: *dx* vs *dy* proton spot selection

kine	mag	target	nspot
4	0	lh2	
4	30	lh2	
4	50	lh2	
4	30	ld2	(pow(dx_bc+0.05,2)/pow(0.32,2))+(pow(dy_bc+0.05,2)/pow(0.40,2))<=1
4	50	ld2	(pow(dx_bc+0.0,2)/pow(0.25,2))+(pow(dy_bc+0.05,2)/pow(0.3,2))<=1
8	0	lh2	
8	50	lh2	
8	70	lh2	
8	100	lh2	
8	50	ld2	(pow(dx_bc+0.0,2)/pow(0.26,2))+(pow(dy_bc+0.07,2)/pow(0.36,2))<=1
8	70	ld2	(pow(dx_bc+0.0,2)/pow(0.12,2))+(pow(dy_bc+0.07,2)/pow(0.18,2))<=1
8	100	ld2	(pow(dx_bc+0.01,2)/pow(0.3,2))+(pow(dy_bc+0.05,2)/pow(0.36,2))<=1
9	70	lh2	
9	70	ld2	(pow(dx_bc+0.0,2)/pow(0.12,2))+(pow(dy_bc+0.03,2)/pow(0.18,2))<=1

Table 46: Elastic selection cuts: *dx* vs *dy* neutron spot selection

kine	mag	dx bins	dx fit range low	dx fit range high
4	30	400	-1.8	0.8
4	50	400	-2.6	1.1
8	50	400	-1.7	1
8	70	400	-2.3	1.3
8	100	400	-2.3	0.9
9	70	400	-2.6	1.5

Table 47: Elastic selection: bin number and fit range *dx*

10 Appendix C, Experimental Methods

10.1 PMT Coupling Procedure

No notable differences exist between XP2262 or XP2282 (JLab or CMU) PMTs for this process. This first process details the removal of PMTs from the the HCal frame, application of optical grease, and return of the PMT to the frame.

1. Wear gloves, thoroughly clean surface (ideally clean room environment).
2. Safely power down the HV.
3. Label all cables (signal and HV) and detach from PMTs installed onto frame via mounting jig.
4. Remove PMT housing from the mounting jig. This entails unscrewing it from the mounting jig (ccw to unscrew). Base may also be removed.
5. Remove the PMT from the housing. Two plastic rivets must be removed from either side of the housing to free the PMT and base. These rivets can be worked loose using a flat-head screwdriver. WARNING: once the rivets are loose, the PMT is free to slide out of the housing. Stage PMT on clean work surface.
6. Use solid plastic to apply grease and kim wipes for cleanup.
7. Apply grease to center of PMT active area (for XP2262 or XP2282, approximately 5 mL).
8. Using plastic utensil, spread the grease outward from the center allowing for a small gradient where more grease is in the center of the active area than the edges. Ensure that the entire surface is covered.
9. Check for bubbles in the grease. Smooth them out as well as is possible.
10. Reconnect base if necessary.

11. Return the PMT to housing and affix using rivets. Note that pins may only reattach in a single orientation of the PMT in the housing.

12. Return the PMT housing to the mounting jig (cw to tighten). The PMT will make contact with the cylindrical part of the waveguide and need additional tightening to compress the face of the PMT to the waveguide. The jig is constructed to provide counter-pressure with springs. As such excessive over-tightening is necessary to damage PMTs and waveguides. That said, do not over-tighten.

The second part of the process details the testing and optimization of light collection as a function of housing position.

1. Ensure the mounting jig has a clear mark at 12 o'clock above the PMT housing (silver magic marker works well here against the black plastic).

2. Return HV settings and power HCal ON. HV settings should be configured for cosmic running. Do not adjust HV at any time during this process.

3. Attach a scope to the signal output and use horizontal cursors to mark signal amplitude.

4. Rotate PMT slowly and watch signal amplitude adjusting the cursor to follow the maximum. Where possible, ensure a full 360 degree rotation is explored. NOTE: this may entail cw and ccw rotation from nominal.

5. Return PMT rotation to position which maximizes signal amplitude.

6. Mark PMT housing at 12 o'clock such that the housing and mounting jig alignment marks match (again, silver magic marker works well here).

Repeat as necessary for all PMTs.

10.2 HCal Sampling Fraction, MC Results.

Raw G4SBS results for total energy deposited in scintillator at different kinematic settings informs energy calibration targets. The sampling fraction is defined this way:

$$S_f = \frac{E_{\text{det}}}{E_{\text{beam}} - p_{e'}} = E_{\text{HCal}}/\nu = E_{\text{HCal}}/KE_N \tag{10.1}$$

where E_{det} is the sum of energy deposited in HCal scintillator, E_{beam} is the beam energy per kinematic, and $p_{e'}$ is the scattered electron momentum. For these simulations, the elastic generator was used along with standard kinematic parameters and the total energy deposited in BBCal PS, BBCal SH, and HCal is required to be non-zero. Figure 114 depicts the fits and distributions that sampling fractions are extracted from. Table 48 gives each sampling fraction by **GMn** kinematic.

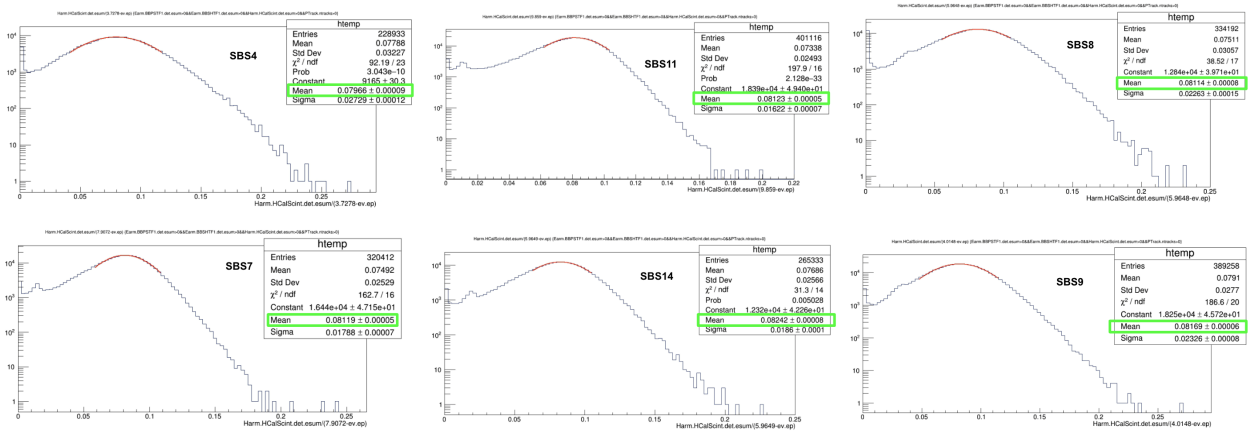

Figure 114: Monte Carlo results for HCal sampling fraction by **GMn** kinematic. Each plot is labeled by kinematic, and the sampling fraction is determined with the fitted mean of the distribution.

Kinematic	Beam Energy (GeV)	Sampling Fraction
SBS4	3.7278	0.07966
SBS8	5.9648	0.08114
SBS11	9.859	0.08123
SBS7	7.9072	0.08119
SBS14	5.9649	0.08242
SBS9	4.0148	0.08169

Table 48: Kinematic settings, beam energy, and sampling fraction extracted from the provided plots.

10.3 Parameterized p_N Dependent ToF Corrections

The following sets of parameters (tables 49 and 50) represent a third order polynomial fit (figures 115 and 116) to ToF vs p_N (nucleon momentum) distributions generated with G4SBS elastic generator. ToF is determined by sensitive detector boundary crossing time as proton or neutron crosses into the volume of HCal. These parameters can be used to correct timing measurements event-by-event with p_N assessed with elastic projections from e' tracking information.

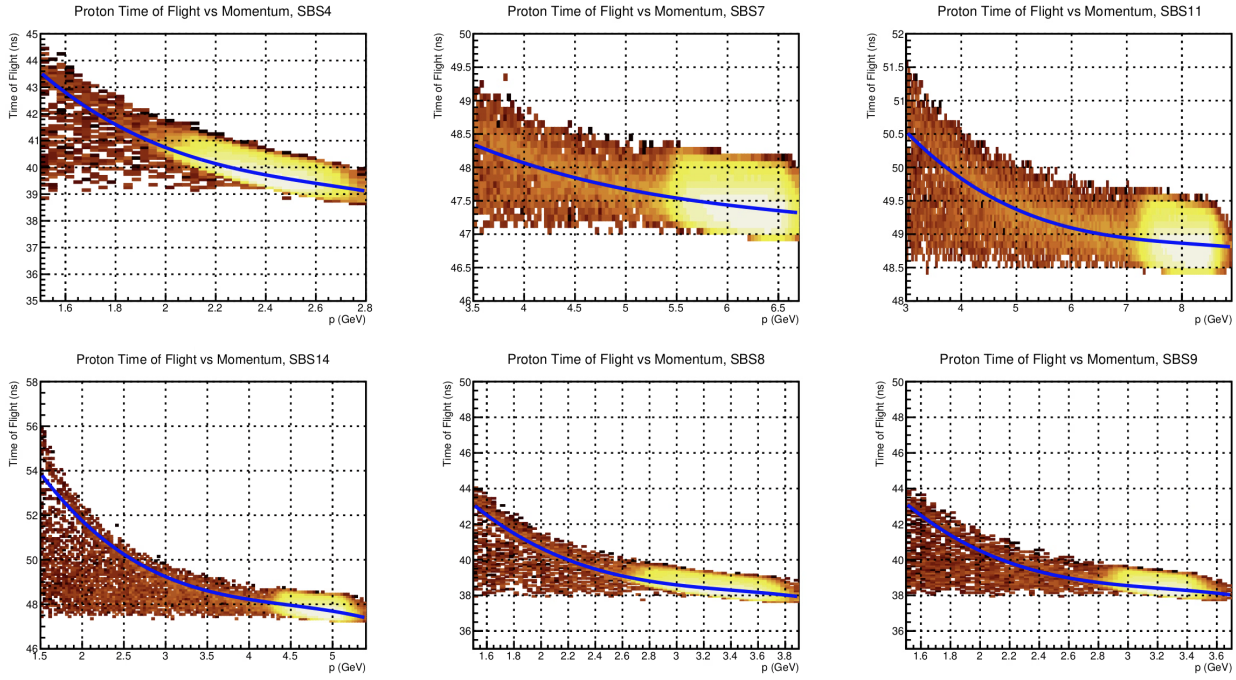

Figure 115: MC results for HCal ToF vs proton momentum. Each plot is labeled with its associated kinematic and a third-order polynomial fit to the data is in blue.

Kinematic	SBS Field Setting	p0	p1	p2	p3
4	30	73.7816	-35.8806	12.90060	-1.60996
7	85	52.7549	-2.05791	0.273797	-0.01309
11	100	54.6380	-1.97939	0.231943	-0.00934
14	70	65.2843	-10.6005	2.252520	-0.16723
8	70	60.6177	-18.2422	5.123620	-0.49684
9	70	63.9328	-22.3211	6.673740	-0.68472

Table 49: Polynomial fit parameters for proton Time-of-Flight (ToF) data.

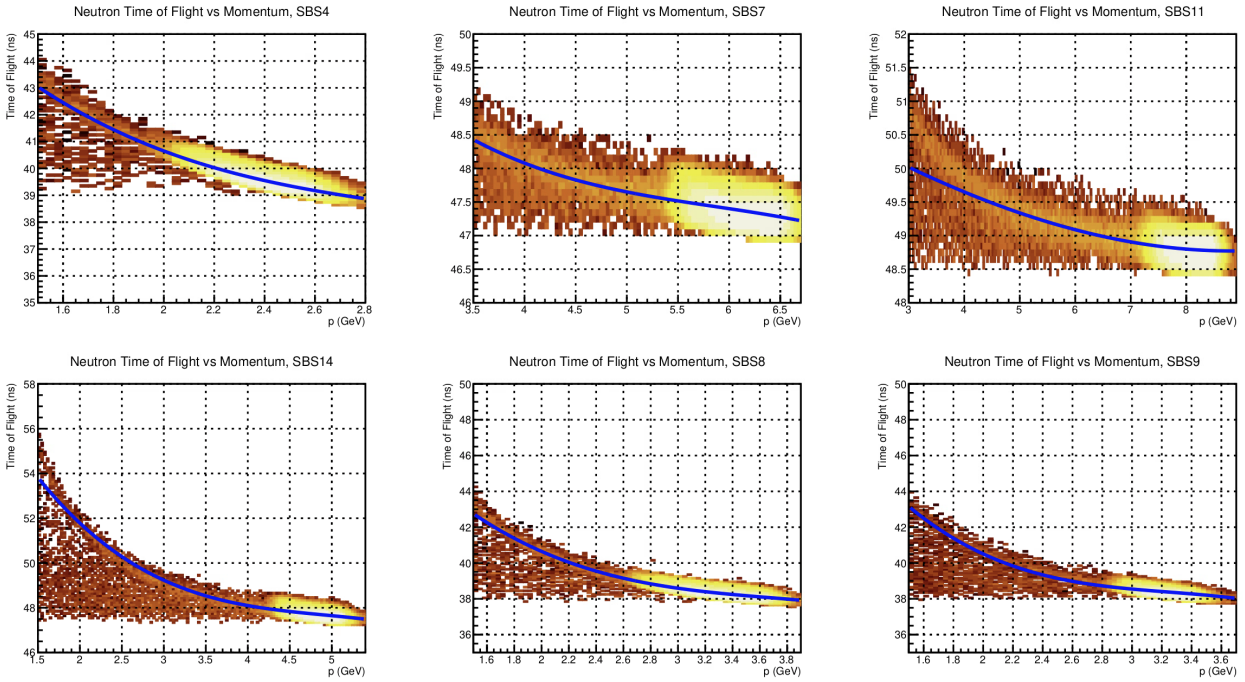

Figure 116: MC results for HCal ToF vs neutron momentum. Each plot is labeled with its associated kinematic and a third-order polynomial fit to the data is in blue.

Kinematic	SBS Field Setting	p0	p1	p2	p3
4	30	62.1158	-20.8086	6.464510	-0.71342
7	85	55.8218	-3.84358	0.617647	-0.03516
11	100	51.4030	-0.51868	0.016076	0.001009
14	70	64.1014	-9.30317	1.818670	-0.12324
8	70	56.1597	-13.4154	3.449660	-0.30995
9	70	63.9328	-22.3211	6.673740	-0.68472

Table 50: Polynomial fit parameters for neutron Time-of-Flight (ToF) data.

10.4 TDC Timewalk Fit Parameters

With functional fits to all-channel aggregate HCal TDC time vs primary block energy distributions of the form in 4.39, per-event corrections are possible post-reconstruction. Fit parameters (p_0, p_1, and p_2) for all kinematics follow in table 51.

kine	p0	p1	p2
4	-1.11	0.78	0.5
7	-0.28	0.63	0.5
11	0.54	0.5	0.5
14	0	0.48	0.5
8	0.75	0.46	0.5
9	-0.21	0.55	0.5

Table 51: HCal TDC timewalk third order polynomial coefficients for various kinematic settings. These fits are over TDC time vs primary block energy.

10.5 Compromised Modules

Many HCal modules display ADC spectra which must be driven with higher than average HV to resolve signals consistently. Figures 117 and 118 provide a map for all identified modules by channel index that are affected.

Impacted

Top Half

~23 Mods affected

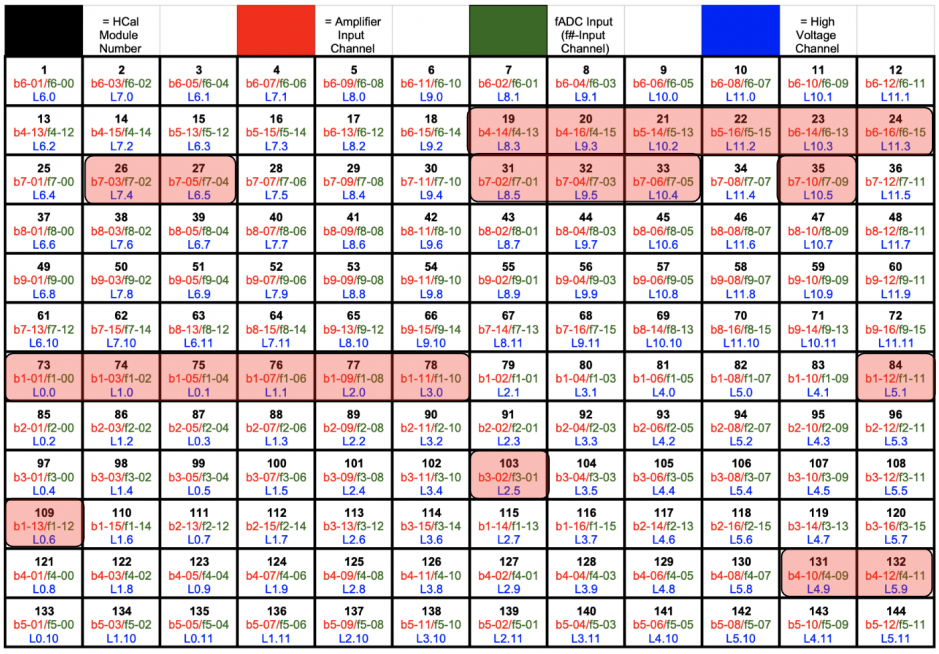

1 b6-01/f6-00 L6.0	2 b6-03/f6-02 L7.0	3 b6-05/f6-04 L6.1	4 b6-07/f6-06 L7.1	5 b6-09/f6-08 L8.0	6 b6-11/f6-10 L9.0	7 b6-02/f6-01 L8.1	8 b6-04/f6-03 L9.1	9 b6-06/f6-05 L10.0	10 b6-08/f6-07 L11.0	11 b6-10/f6-09 L10.1	12 b6-12/f6-11 L11.1
13 b4-13/f4-12 L6.2	14 b4-15/f4-14 L7.2	15 b5-13/f5-12 L6.3	16 b5-15/f5-14 L7.3	17 b6-13/f6-12 L8.2	18 b6-15/f6-14 L9.2	19 b4-14/f4-13 L8.3	20 b4-16/f4-15 L9.3	21 b5-14/f5-13 L10.2	22 b5-16/f5-15 L11.2	23 b6-14/f6-13 L10.3	24 b6-16/f6-15 L11.3
25 b7-01/f7-00 L6.4	26 b7-03/f7-02 L7.4	27 b7-05/f7-04 L6.5	28 b7-07/f7-06 L7.5	29 b7-09/f7-08 L8.4	30 b7-11/f7-10 L9.4	31 b7-02/f7-01 L8.5	32 b7-04/f7-03 L9.5	33 b7-06/f7-05 L10.4	34 b7-08/f7-07 L11.4	35 b7-10/f7-09 L10.5	36 b7-12/f7-11 L11.5
37 b8-01/f8-00 L6.6	38 b8-03/f8-02 L7.6	39 b8-05/f8-04 L6.7	40 b8-07/f8-06 L7.7	41 b8-09/f8-08 L8.6	42 b8-11/f8-10 L9.6	43 b8-02/f8-01 L8.7	44 b8-04/f8-03 L9.7	45 b8-06/f8-05 L10.6	46 b8-08/f8-07 L11.6	47 b8-10/f8-09 L10.7	48 b8-12/f8-11 L11.7
49 b9-01/f9-00 L6.8	50 b9-03/f9-02 L7.8	51 b9-05/f9-04 L6.9	52 b9-07/f9-06 L7.9	53 b9-09/f9-08 L8.8	54 b9-11/f9-10 L9.8	55 b9-02/f9-01 L8.9	56 b9-04/f9-03 L9.9	57 b9-06/f9-05 L10.8	58 b9-08/f9-07 L11.8	59 b9-10/f9-09 L10.9	60 b9-12/f9-11 L11.9
61 b7-13/f7-12 L6.10	62 b7-15/f7-14 L7.10	63 b8-13/f8-12 L6.11	64 b8-15/f8-14 L7.11	65 b9-13/f9-12 L8.10	66 b9-15/f9-14 L9.10	67 b7-14/f7-13 L8.11	68 b7-16/f7-15 L9.11	69 b8-14/f8-13 L10.10	70 b8-16/f8-15 L11.10	71 b9-14/f9-13 L10.11	72 b9-16/f9-15 L11.11
73 b1-01/f1-00 L0.0	74 b1-03/f1-02 L1.0	75 b1-05/f1-04 L0.1	76 b1-07/f1-06 L1.1	77 b1-09/f1-08 L2.0	78 b1-11/f1-10 L3.0	79 b1-02/f1-01 L2.1	80 b1-04/f1-03 L3.1	81 b1-06/f1-05 L4.0	82 b1-08/f1-07 L5.0	83 b1-10/f1-09 L4.1	84 b1-12/f1-11 L5.1
85 b2-01/f2-00 L0.2	86 b2-03/f2-02 L1.2	87 b2-05/f2-04 L0.3	88 b2-07/f2-06 L1.3	89 b2-09/f2-08 L2.2	90 b2-11/f2-10 L3.2	91 b2-02/f2-01 L2.3	92 b2-04/f2-03 L3.3	93 b2-06/f2-05 L4.2	94 b2-08/f2-07 L5.2	95 b2-10/f2-09 L4.3	96 b2-12/f2-11 L5.3
97 b3-01/f3-00 L0.4	98 b3-03/f3-02 L1.4	99 b3-05/f3-04 L0.5	100 b3-07/f3-06 L1.5	101 b3-09/f3-08 L2.4	102 b3-11/f3-10 L3.4	103 b3-02/f3-01 L2.5	104 b3-04/f3-03 L3.5	105 b3-06/f3-05 L4.4	106 b3-08/f3-07 L5.4	107 b3-10/f3-09 L4.5	108 b3-12/f3-11 L5.5
109 b1-13/f1-12 L0.6	110 b1-15/f1-14 L1.6	111 b2-13/f2-12 L0.7	112 b2-15/f2-14 L1.7	113 b3-13/f3-12 L2.6	114 b3-15/f3-14 L3.6	115 b1-14/f1-13 L2.7	116 b1-16/f1-15 L3.7	117 b2-14/f2-13 L4.6	118 b2-16/f2-15 L5.6	119 b3-14/f3-13 L4.7	120 b3-16/f3-15 L5.7
121 b4-01/f4-00 L0.8	122 b4-03/f4-02 L1.8	123 b4-05/f4-04 L0.9	124 b4-07/f4-06 L1.9	125 b4-09/f4-08 L2.8	126 b4-11/f4-10 L3.8	127 b4-02/f4-01 L2.9	128 b4-04/f4-03 L3.9	129 b4-06/f4-05 L4.8	130 b4-08/f4-07 L5.8	131 b4-10/f4-09 L4.9	132 b4-12/f4-11 L5.9
133 b5-01/f5-00 L0.10	134 b5-03/f5-02 L1.10	135 b5-05/f5-04 L0.11	136 b5-07/f5-06 L1.11	137 b5-09/f5-08 L2.10	138 b5-11/f5-10 L3.10	139 b5-02/f5-01 L2.11	140 b5-04/f5-03 L3.11	141 b5-06/f5-05 L4.10	142 b5-08/f5-07 L5.10	143 b5-10/f5-09 L4.11	144 b5-12/f5-11 L5.11

Figure 117: Set of channels (modules) whose associated ADC spectra that are affected by abnormal distributions are shaded in red. All channels from the top half of HCal (channels 1-144, from 1).

Impacted

Bottom Half

~12 Mods affected

	= Module Number			= Amplifier Input Channel			fADC Input (ff-Input Channel)			= High Voltage Channel	
145 a1-01/f10-00 L0.0	146 a1-03/f10-02 L1.0	147 a1-05/f10-04 L0.1	148 a1-07/f10-06 L1.1	149 a1-09/f10-08 L3.0	150 a1-11/f10-10 L4.0	151 a1-02/f10-01 L3.1	152 a1-04/f10-03 L4.1	153 a1-06/f10-05 L5.0	154 a1-08/f10-07 L6.0	155 a1-10/f10-09 L5.1	156 a1-12/f10-11 L6.1
157 a2-01/f11-00 L0.2	158 a2-03/f11-02 L1.2	159 a2-05/f11-04 L0.3	160 a2-07/f11-06 L1.3	161 a2-09/f11-08 L3.2	162 a2-11/f11-10 L4.2	163 a2-02/f11-01 L3.3	164 a2-04/f11-03 L4.3	165 a2-06/f11-05 L5.2	166 a2-08/f11-07 L6.2	167 a2-10/f11-09 L5.3	168 a2-12/f11-11 L6.3
169 a3-01/f12-00 L0.4	170 a3-03/f12-02 L1.4	171 a3-05/f12-04 L0.5	172 a3-07/f12-06 L1.5	173 a3-09/f12-08 L3.4	174 a3-11/f12-10 L4.4	175 a3-02/f12-01 L3.5	176 a3-04/f12-03 L4.5	177 a3-06/f12-05 L5.4	178 a3-08/f12-07 L6.4	179 a3-10/f12-09 L5.5	180 a3-12/f12-11 L6.5
181 a1-13/f10-12 L0.6	182 a1-15/f10-14 L1.6	183 a2-13/f11-12 L0.7	184 a2-15/f11-14 L1.7	185 a3-13/f12-12 L3.6	186 a3-15/f12-14 L4.6	187 a1-14/f10-13 L3.7	188 a1-16/f10-15 L4.7	189 a2-14/f11-13 L5.6	190 a2-16/f11-15 L6.6	191 a3-14/f12-13 L5.7	192 a3-16/f12-15 L6.7
193 a4-01/f13-00 L0.8	194 a4-03/f13-02 L1.8	195 a4-05/f13-04 L0.9	196 a4-07/f13-06 L1.9	197 a4-09/f13-08 L3.8	198 a4-11/f13-10 L4.8	199 a4-02/f13-01 L3.9	200 a4-04/f13-03 L4.9	201 a4-06/f13-05 L5.8	202 a4-08/f13-07 L6.8	203 a4-10/f13-09 L5.9	204 a4-12/f13-11 L6.9
205 a5-01/f14-00 L0.10	206 a5-03/f14-02 L1.10	207 a5-05/f14-04 L0.11	208 a5-07/f14-06 L1.11	209 a5-09/f14-08 L3.10	210 a5-11/f14-10 L4.10	211 a5-02/f14-01 L3.11	212 a5-04/f14-03 L4.11	213 a5-06/f14-05 L5.10	214 a5-08/f14-07 L6.10	215 a5-10/f14-09 L5.11	216 a5-12/f14-11 L6.11
217 a6-01/f15-00 L7.0	218 a6-03/f15-02 L8.0	219 a6-05/f15-04 L7.1	220 a6-07/f15-06 L8.1	221 a6-09/f15-08 L9.0	222 a6-11/f15-10 L10.0	223 a6-02/f15-01 L9.1	224 a6-04/f15-03 L10.1	225 a6-06/f15-05 L11.0	226 a6-08/f15-07 L12.0	227 a6-10/f15-09 L11.1	228 a6-12/f15-11 L12.1
229 a4-13/f13-12 L7.2	230 a4-15/f13-14 L8.2	231 a5-13/f14-12 L7.3	232 a5-15/f14-14 L8.3	233 a6-13/f15-12 L9.2	234 a6-15/f15-14 L10.2	235 a4-14/f13-13 L9.3	236 a4-16/f13-15 L10.3	237 a5-14/f14-13 L11.2	238 a5-16/f14-15 L12.2	239 a6-14/f15-13 L11.3	240 a6-16/f15-15 L12.3
241 a7-01/f16-00 L7.4	242 a7-03/f16-02 L8.4	243 a7-05/f16-04 L7.5	244 a7-07/f16-06 L8.5	245 a7-09/f16-08 L9.4	246 a7-11/f16-10 L10.4	247 a7-02/f16-01 L9.5	248 a7-04/f16-03 L10.5	249 a7-06/f16-05 L11.4	250 a7-08/f16-07 L12.4	251 a7-10/f16-09 L11.5	252 a7-12/f16-11 L12.5
253 a8-01/f17-00 L7.6	254 a8-03/f17-02 L8.6	255 a8-05/f17-04 L7.7	256 a8-07/f17-06 L8.7	257 a8-09/f17-08 L9.6	258 a8-11/f17-10 L10.6	259 a8-02/f17-01 L9.7	260 a8-04/f17-03 L10.7	261 a8-06/f17-05 L11.6	262 a8-08/f17-07 L12.6	263 a8-10/f17-09 L11.7	264 a8-12/f17-11 L12.7
265 a9-01/f18-00 L7.8	266 a9-03/f18-02 L8.8	267 a9-05/f18-04 L7.9	268 a9-07/f18-06 L8.9	269 a9-09/f18-08 L9.8	270 a9-11/f18-10 L10.8	271 a9-02/f18-01 L9.9	272 a9-04/f18-03 L10.9	273 a9-06/f18-05 L11.8	274 a9-08/f18-07 L12.8	275 a9-10/f18-09 L11.9	276 a9-12/f18-11 L12.9
277 a7-13/f16-12 L7.10	278 a7-15/f16-14 L8.10	279 a8-13/f17-12 L7.11	280 a8-15/f17-14 L8.11	281 a9-13/18-12 L9.10	282 a9-15/18-14 L10.10	283 a7-14/f16-13 L9.11	284 a7-16/f16-15 L10.11	285 a8-14/f17-13 L11.10	286 a8-16/f17-15 L12.10	287 a9-14/f18-13 L11.11	288 a9-16/f18-15 L12.11

Figure 118: Set of channels (modules) whose associated ADC spectra that are affected by abnormal distributions are shaded in red. All channels from the bottom half of HCal (channels 145-288, from 1).

10.6 HCal Dispersive Efficiency Maps

The values in 53 are extracted from proton HDE as measured from SBS-8. These values can be applied to **GMn** data at Q^2 = 4.5 GeV^2 to account for dispersive direction efficiency losses in HCal.

10.7 HCal Cable Attenuation Factors

All attenuation factors were measured with a signal generator at the FE and oscilloscope at the DAQ and are included in table 54. Cable lengths were measured with TDR.

11 Appendix D, Supplemental Plots

11.1 Delta Spot Check HDE

Supplemental proton detection efficiency plots follow (119, 120, and 121).

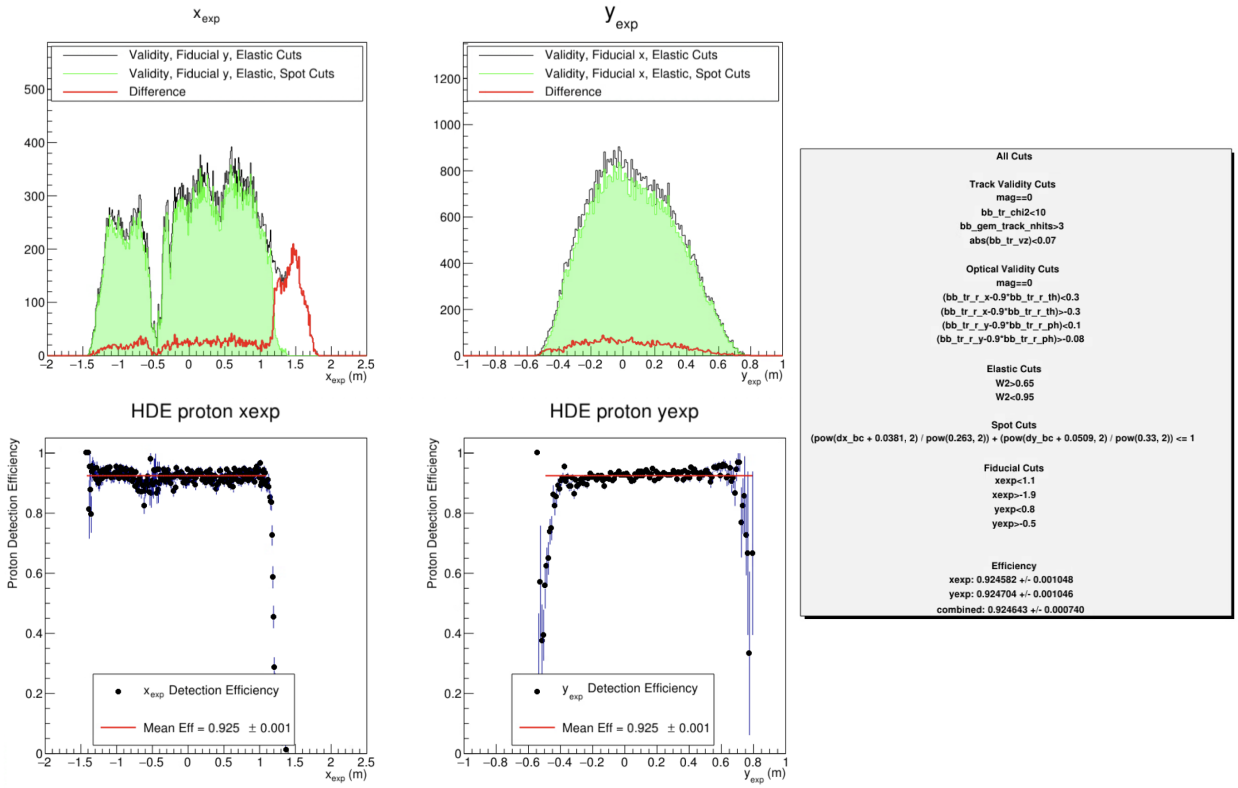

Figure 119: HCal proton detection efficiency using delta spot check method for SBS-4 ($Q^2 = 3.0$ GeV^2) at zero SBS magnet field. All cuts are indicated where the $_bc$ qualifiers indicate that best cluster selection was used with the "in-time" algorithm.

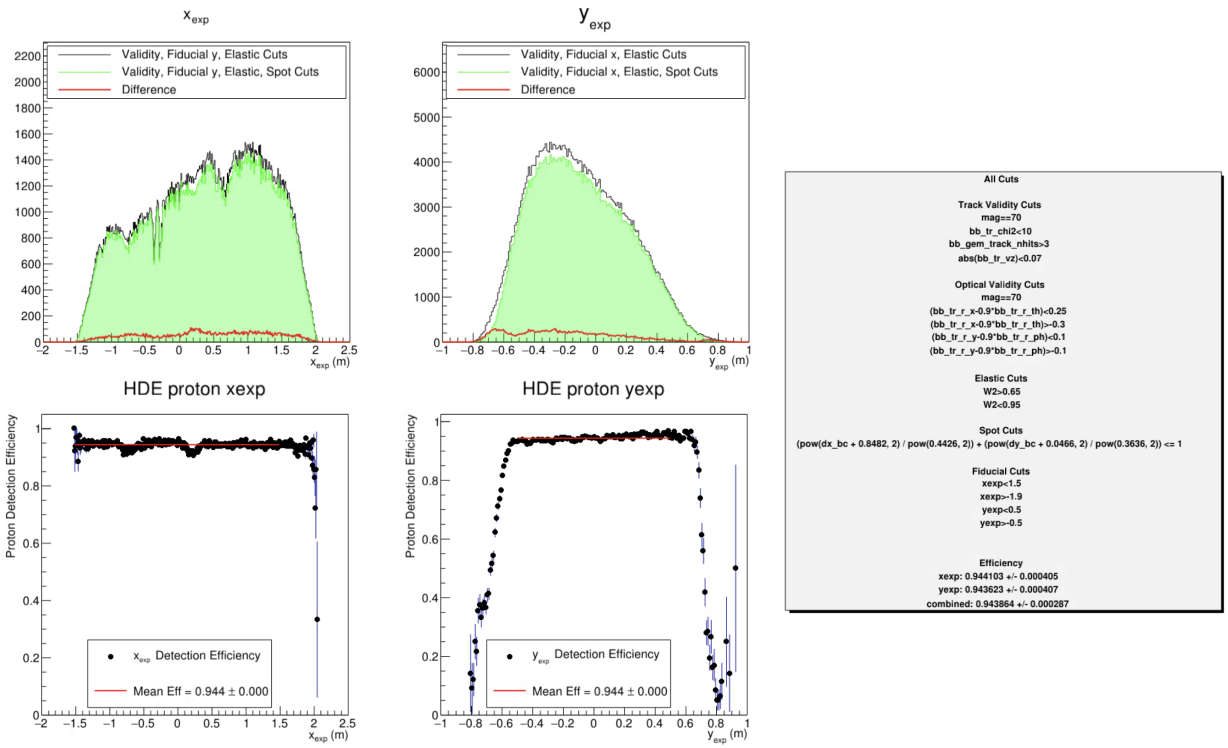

Figure 120: HCal proton detection efficiency using delta spot check method for SBS-8 ($Q^2 = 4.5$ GeV^2) at 70% SBS magnet field.

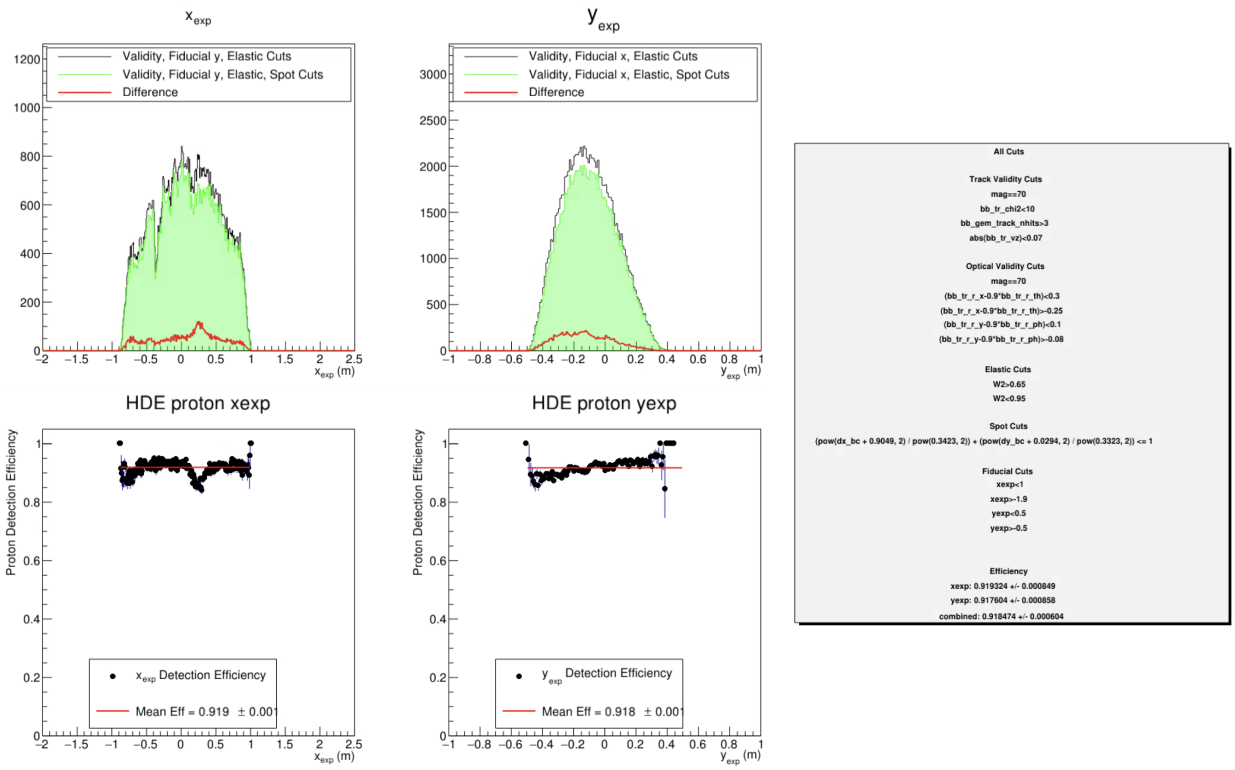

Figure 121: HCal proton detection efficiency using delta spot check method for SBS-9 ($Q^2 = 4.5$ GeV^2) at 70% SBS magnet field.

11.2 TDC Internal Resolution

Figure 122 includes sample fits whose sigma extractions fill 77 (right histogram). These fits are to position-adjacent blocks whose signals per event are primary cluster first and second highest energy blocks as well.

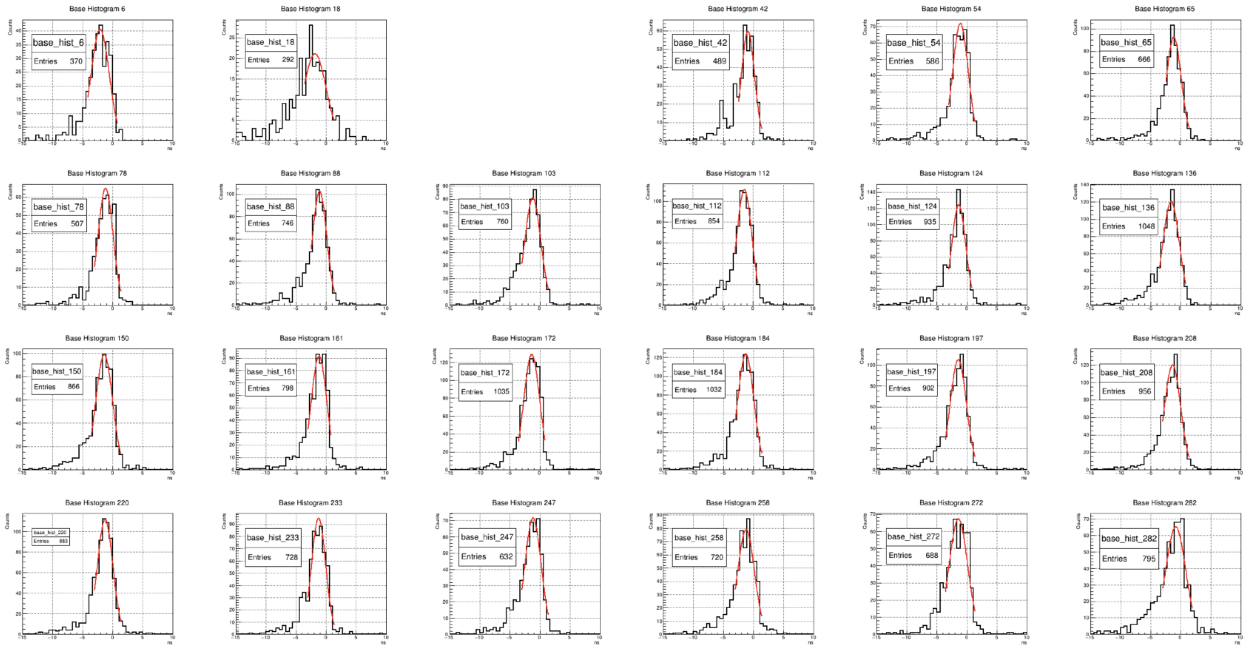

Figure 122: Distributions of HCal TDC_i - TDC_{i+1}, where i is the block index. These plots require that block i is the highest energy block in the primary cluster and that block $i+1$ is the second highest energy block in the primary cluster.

11.3 Q^2 Statistics

Figure 123 includes all MC distributions after elastic and fiducial cuts placed on data used to extract the central values in 26.

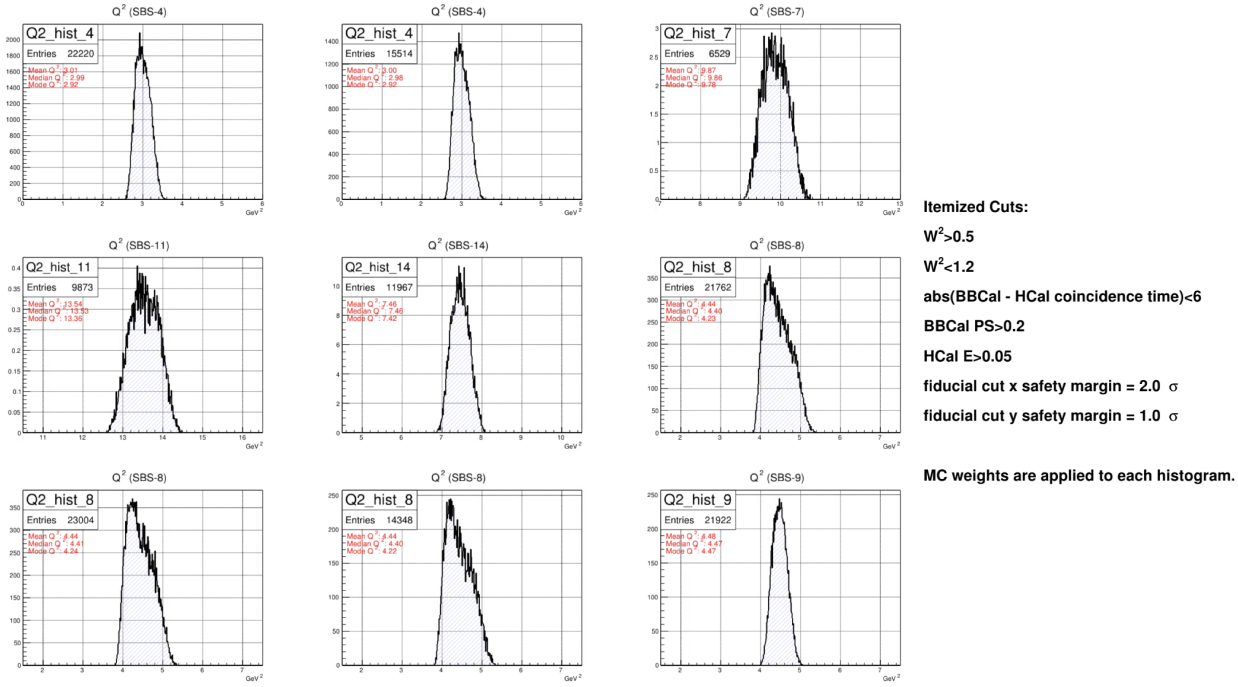

Figure 123: MC Q^2 distributions by kinematic and field setting. The median is used as the central value for extractions. Cuts used are included in the figure.

11.4 ε Statistics

Figure 124 includes all MC distributions after elastic and fiducial cuts placed on data used to extract the central values in 26.

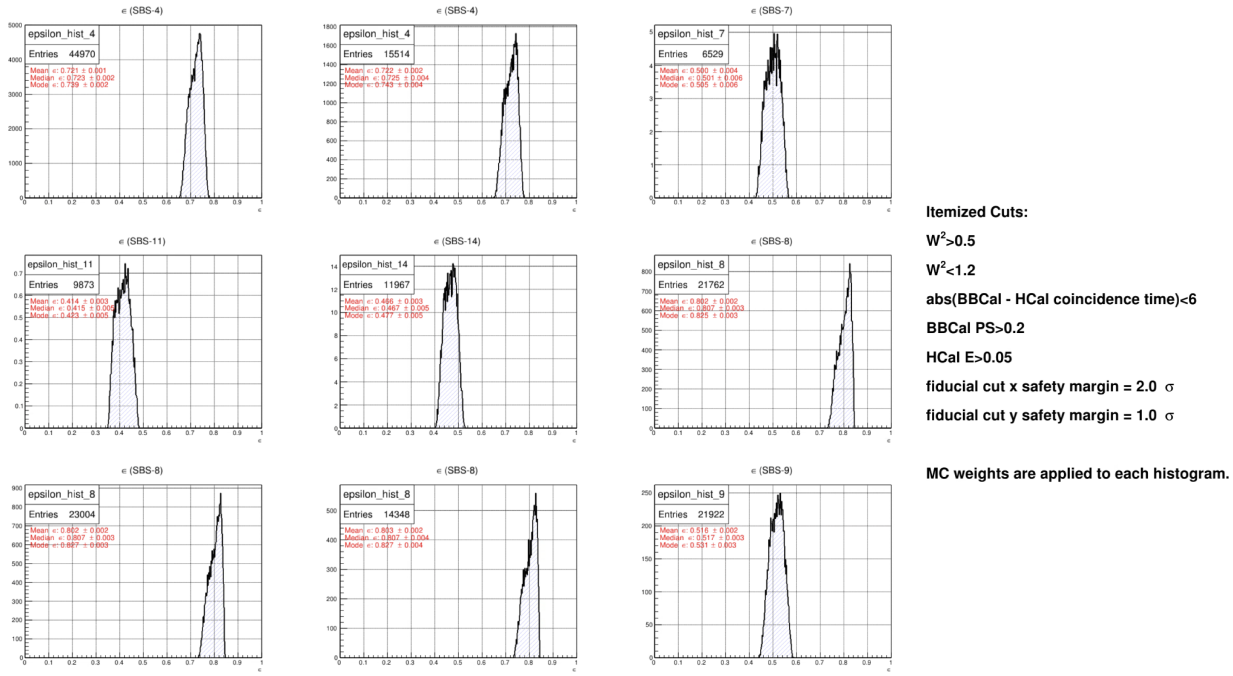

Figure 124: MC ε distributions by kinematic and field setting. The median is used as the central value for extractions. Error is estimated with a MC bootstrapping method. Cuts used are included in the figure.

11.5 p_N Statistics

Figure 125 includes all MC distributions after elastic and fiducial cuts placed on data used extract the central values in 52. The median is emphasized due to the asymmetric nature of these distributions.

Kinematic	SBS Field	Mean	Median	Mode	Central (Median)
4	30	2.36389	2.356	2.3	**2.356**
4	50	2.36049	2.356	2.292	**2.356**
7	85	6.12043	6.1085	6.1465	**6.1085**
11	100	8.08978	8.082	8.07	**8.082**
14	70	4.82094	4.818	4.758	**4.818**
8	50	3.17315	3.156	3.02	**3.156**
8	70	3.17336	3.1545	2.9925	**3.1545**
8	100	3.16936	3.1455	3.0015	**3.1455**
9	70	3.19752	3.1995	3.1635	**3.1995**

Table 52: p_N distribution statistics for different kinematics

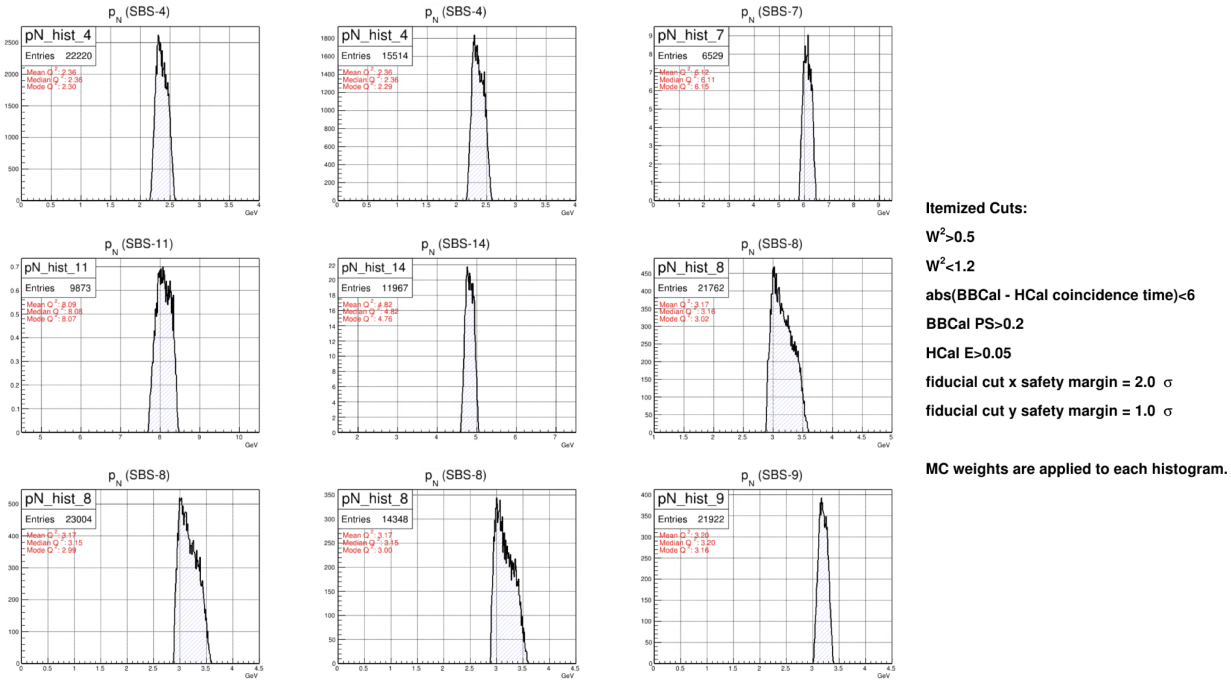

Figure 125: MC p_N distributions by kinematic. The median is used as the central value for extractions. Cuts used are included in the figure.

11.6 Cut Region Supplemental

The following figures inform the course selection choice for elastic cuts by kinematic after apriori assumptions are applied. SBS-4, 30% field is omitted as it is included in the general text.

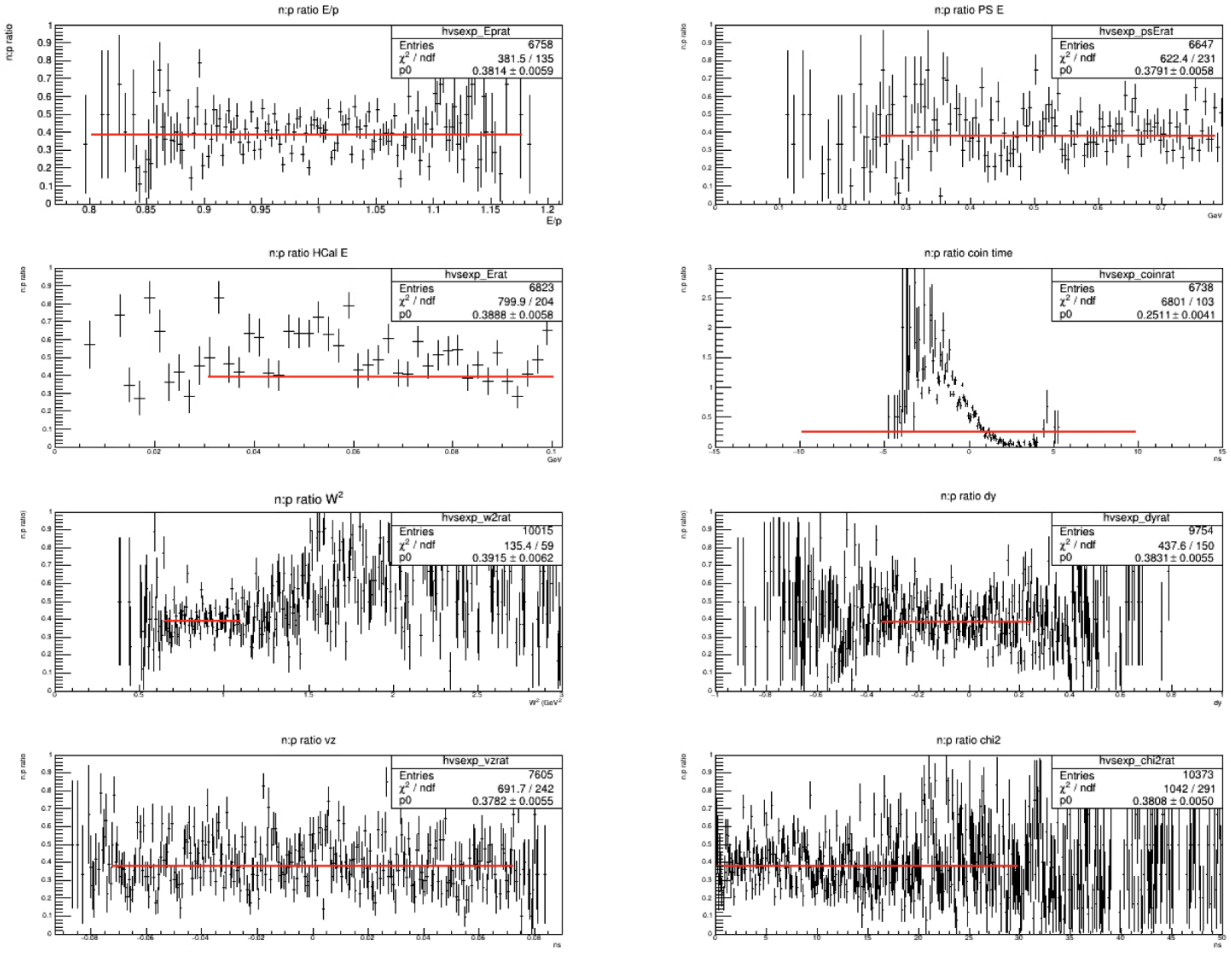

Figure 126: Data from Q^2 = 3.0 GeV^2 (SBS-4, 30% field) dx vs cut variables (from left to right W^2, e' E/p, and BBCal preshower energy). R_{sf} extracted per cut variation is plotted against the variation region. Same color lines indicate a bounded cut region.

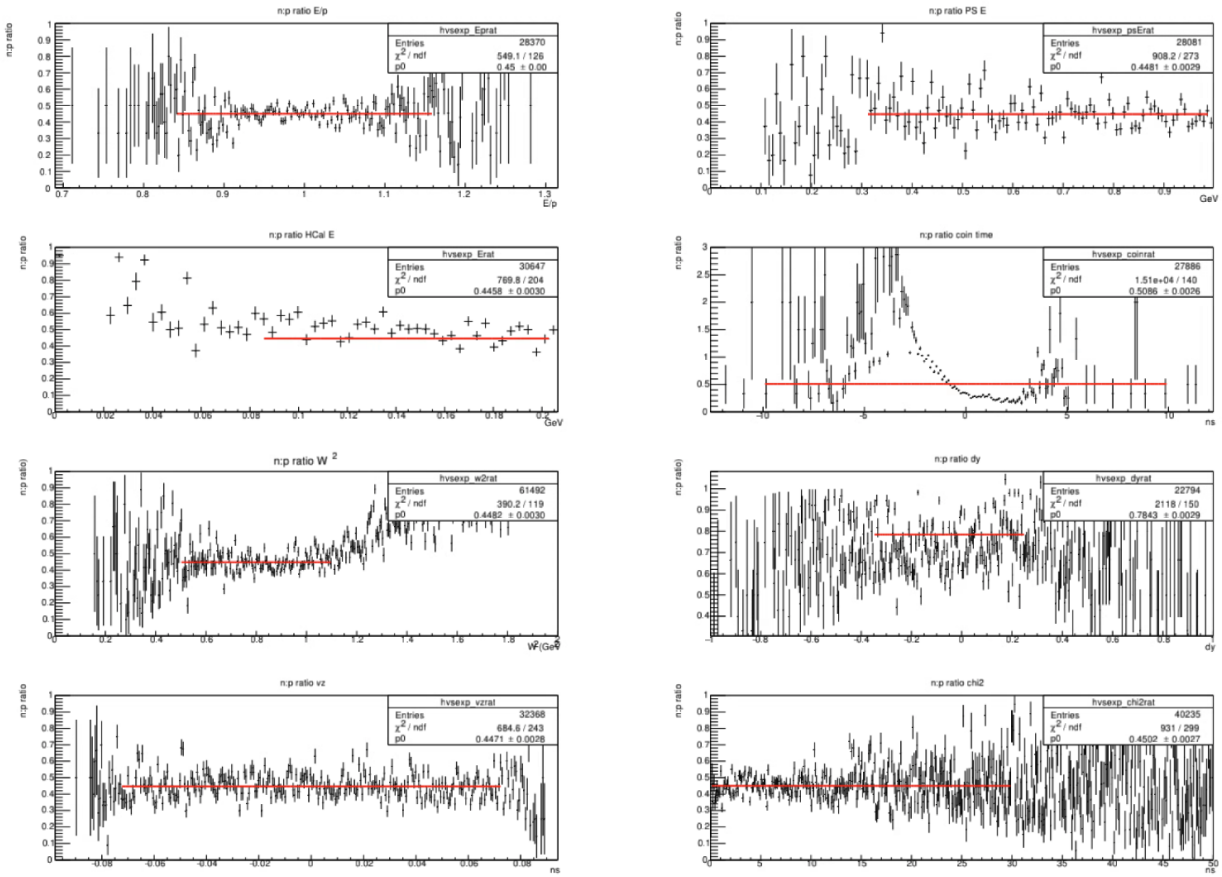

Figure 127: Data from Q^2 = 3.0 GeV^2 (SBS-8, 50% field) dx vs cut variables (from left to right W^2, e' E/p, and BBCal preshower energy). R_{sf} extracted per cut variation is plotted against the variation region. Same color lines indicate a bounded cut region.

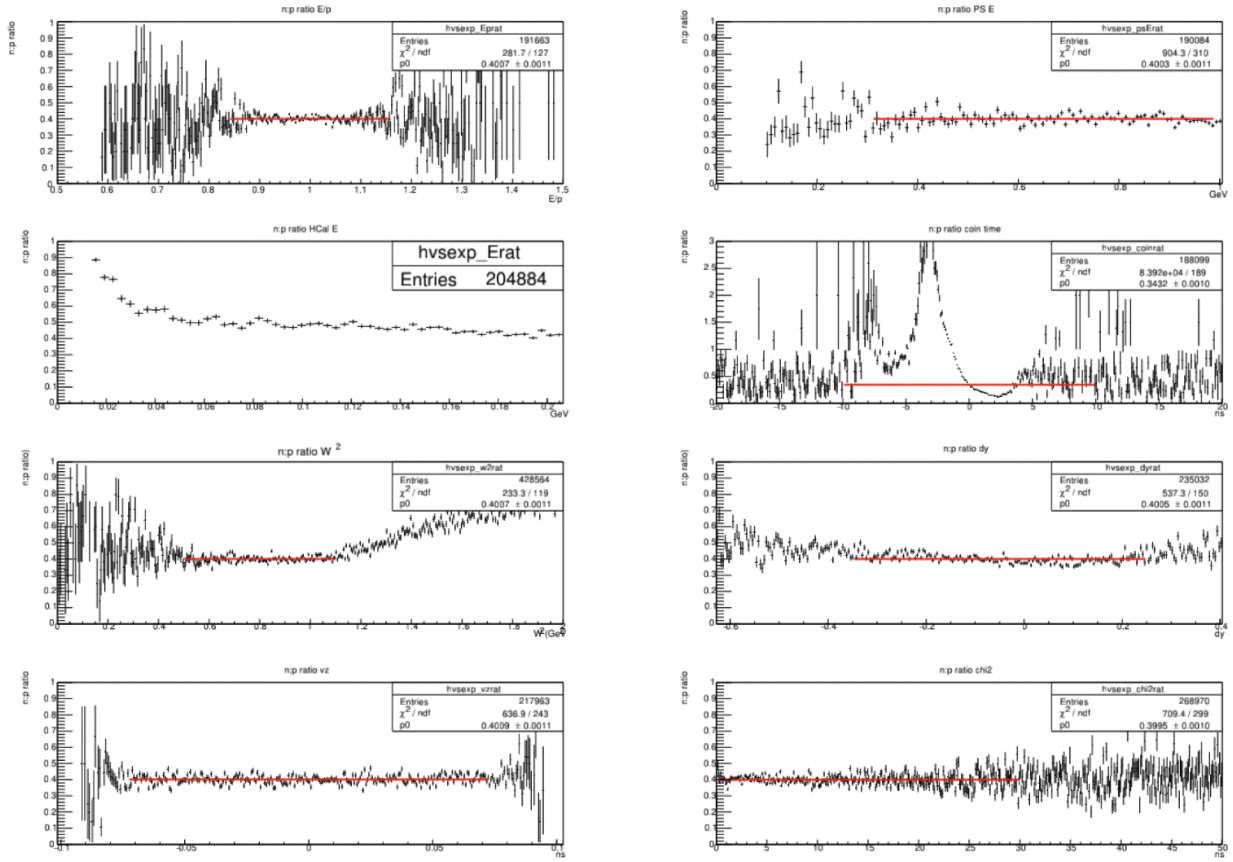

Figure 128: Data from $Q^2 = 4.5$ GeV^2 (SBS-8, 70% field) dx vs cut variables (from left to right W^2, e' E/p, and BBCal preshower energy). R_{sf} extracted per cut variation is plotted against the variation region. Same color lines indicate a bounded cut region.

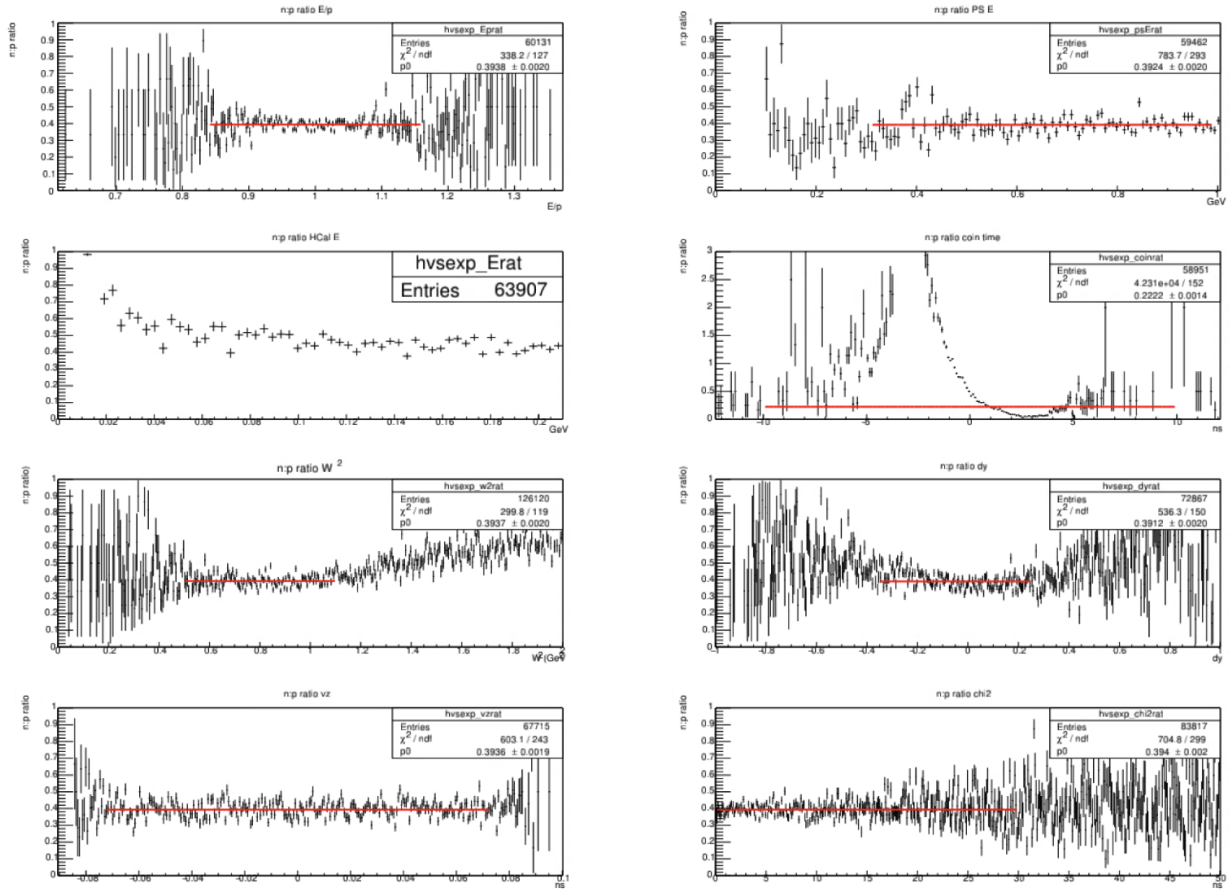

Figure 129: Data from Q^2 = 4.5 GeV^2 (SBS-8, 100% field) dx vs cut variables (from left to right W^2, e' E/p, and BBCal preshower energy). R_{sf} extracted per cut variation is plotted against the variation region. Same color lines indicate a bounded cut region.

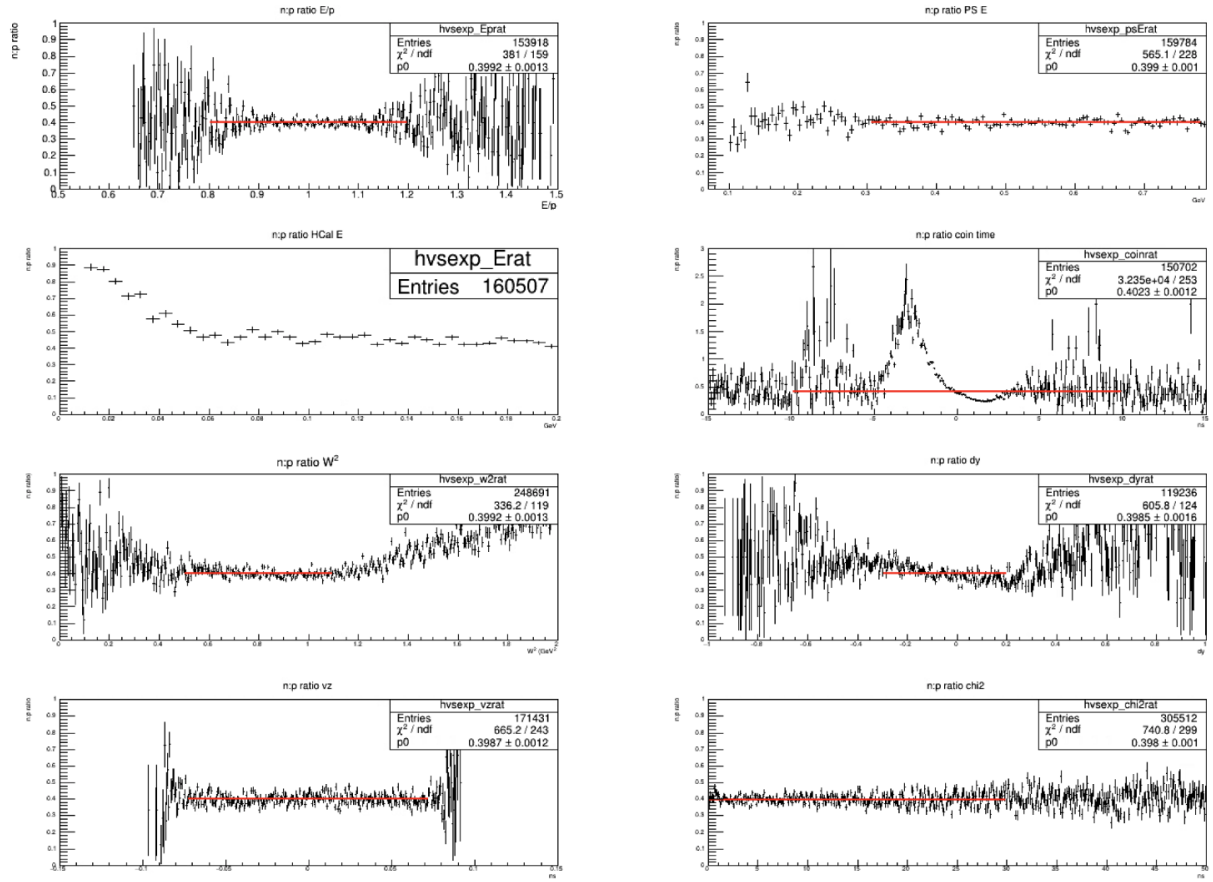

Figure 130: Data from Q^2 = 4.5 GeV^2 (SBS-9, 70% field) dx vs cut variables (from left to right W^2, e' E/p, and BBCal preshower energy). R_{sf} extracted per cut variation is plotted against the variation region. Same color lines indicate a bounded cut region.

11.7 Cut Stability Supplemental

The following figures inform fine selection choice for elastic cuts by kinematic and spectrometer arm. For datasets which share all kinematic settings other than SBS magnetic field settings, electron arm cuts are constrained to be within 5% of one another unless otherwise noted. Several notes:

- BBCal preshower energy stability below 200 MeV is an indication that tracking and timing cuts very effectively remove pion contamination — nevertheless, a pion cut is placed around 200 MeV due to negligible loss of statistics.

- The W^2 mean is the squared nucleon mass.
- R_{sf} vs HCal energy displays a consistent downward trend over the cut region. Consistency between similar kinematic settings is prioritized to avoid low energy fluctuations.
- Corrections are applied to account for correlations between dy and W^2 on stability analysis over each of these variables.

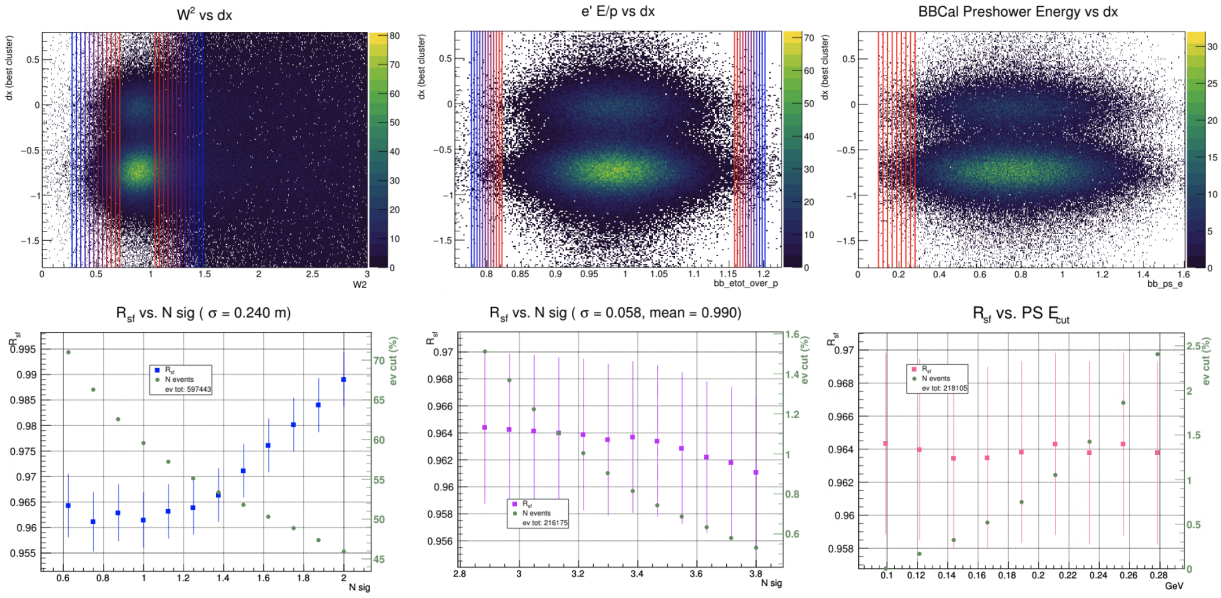

Figure 131: Data from Q^2 = 3.0 GeV^2 (SBS-4, 30% field) dx vs cut variables (from left to right W^2, e' E/p, and BBCal preshower energy). R_{sf} extracted per cut variation is plotted against the variation region. Same color lines indicate a bounded cut region.

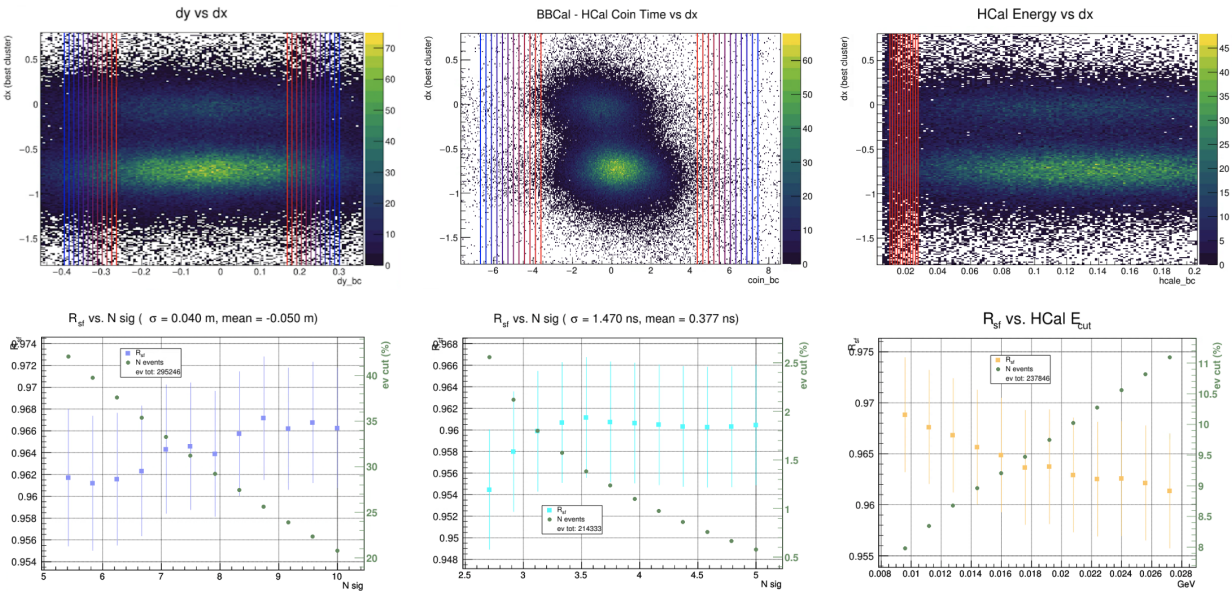

Figure 132: Data from $Q^2 = 3.0$ GeV^2 (SBS-4, 30% field) dx vs cut variables (from left to right dy, BBCal - HCal coincidence time, and HCal energy). R_{sf} extracted per cut variation is plotted against the variation region. Same color lines indicate a bounded cut region.

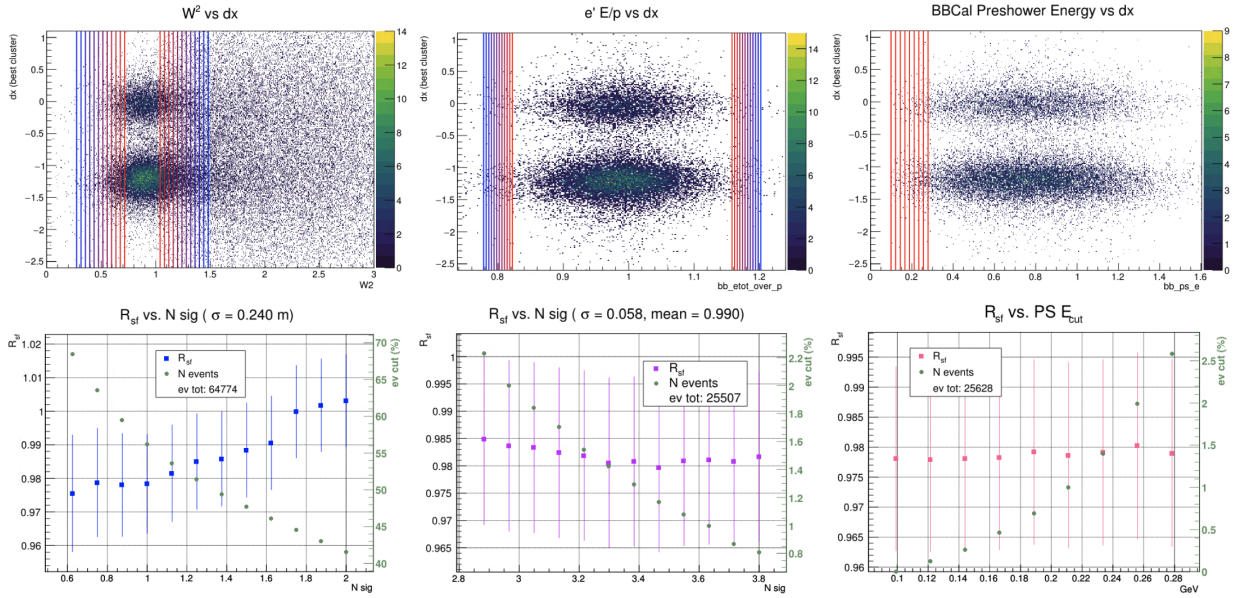

Figure 133: Data from $Q^2 = 4.5$ GeV^2 (SBS-4, 30% field) dx vs cut variables (from left to right W^2, e' E/p, and BBCal preshower energy). R_{sf} extracted per cut variation is plotted against the variation region. Same color lines indicate a bounded cut region.

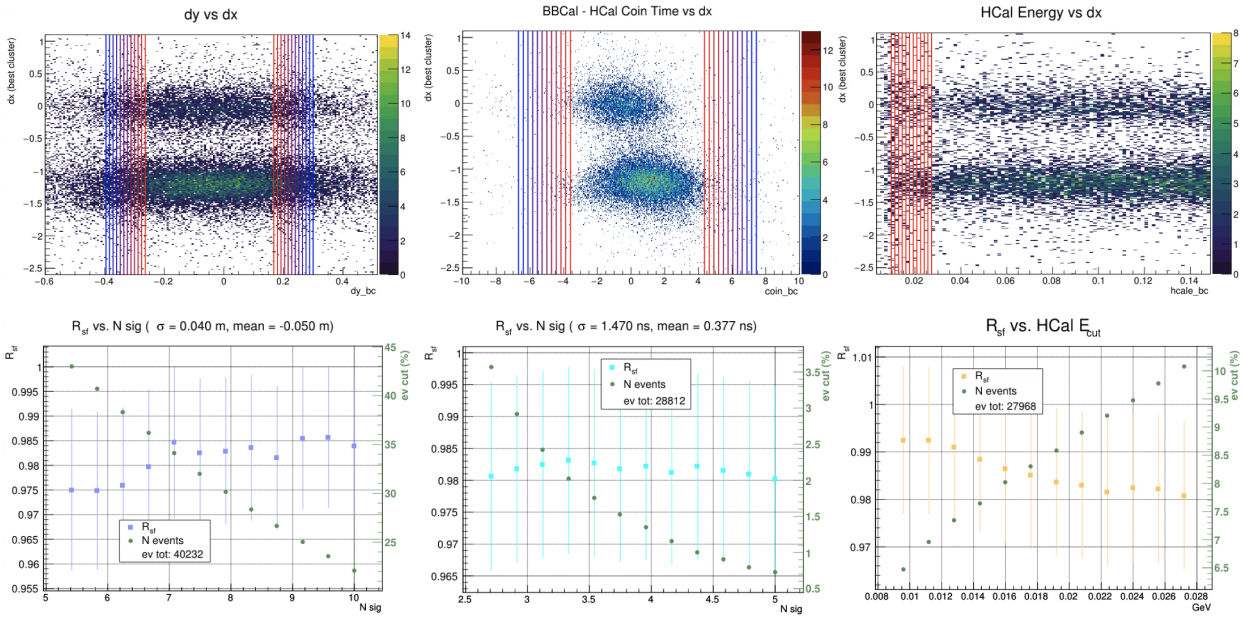

Figure 134: Data from $Q^2 = 4.5$ GeV^2 (SBS-4, 30% field) dx vs cut variables (from left to right dy, BBCal - HCal coincidence time, and HCal energy). R_{sf} extracted per cut variation is plotted against the variation region. Same color lines indicate a bounded cut region.

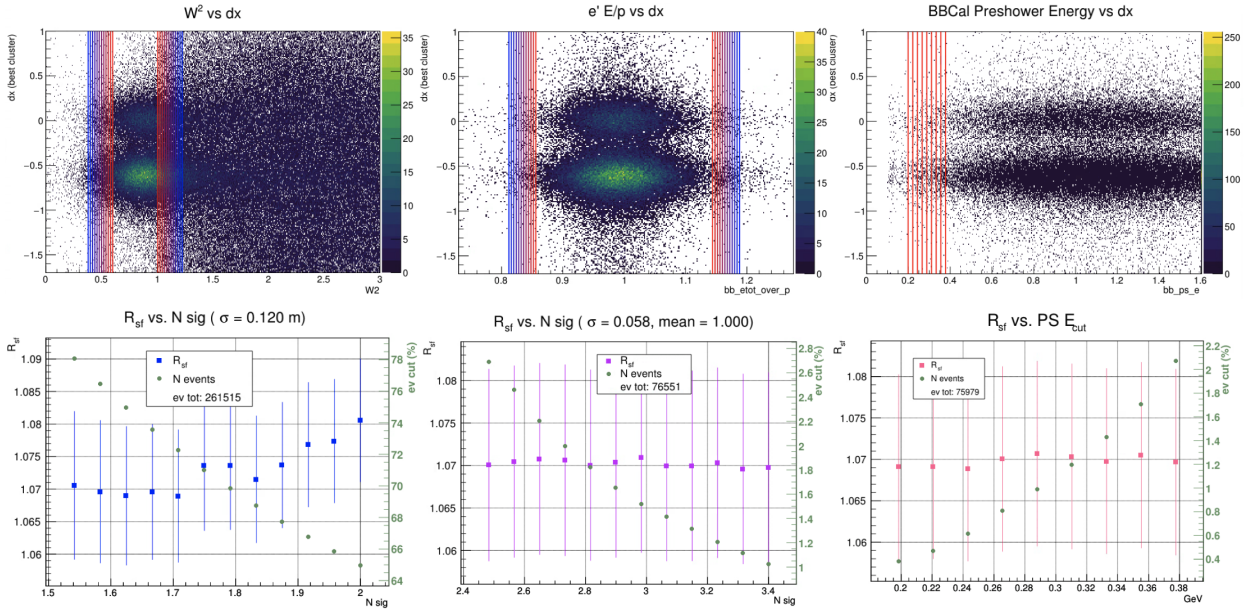

Figure 135: Data from $Q^2 = 4.5$ GeV^2 (SBS-8, 50% field) dx vs cut variables (from left to right W^2, e' E/p, and BBCal preshower energy). R_{sf} extracted per cut variation is plotted against the variation region. Same color lines indicate a bounded cut region.

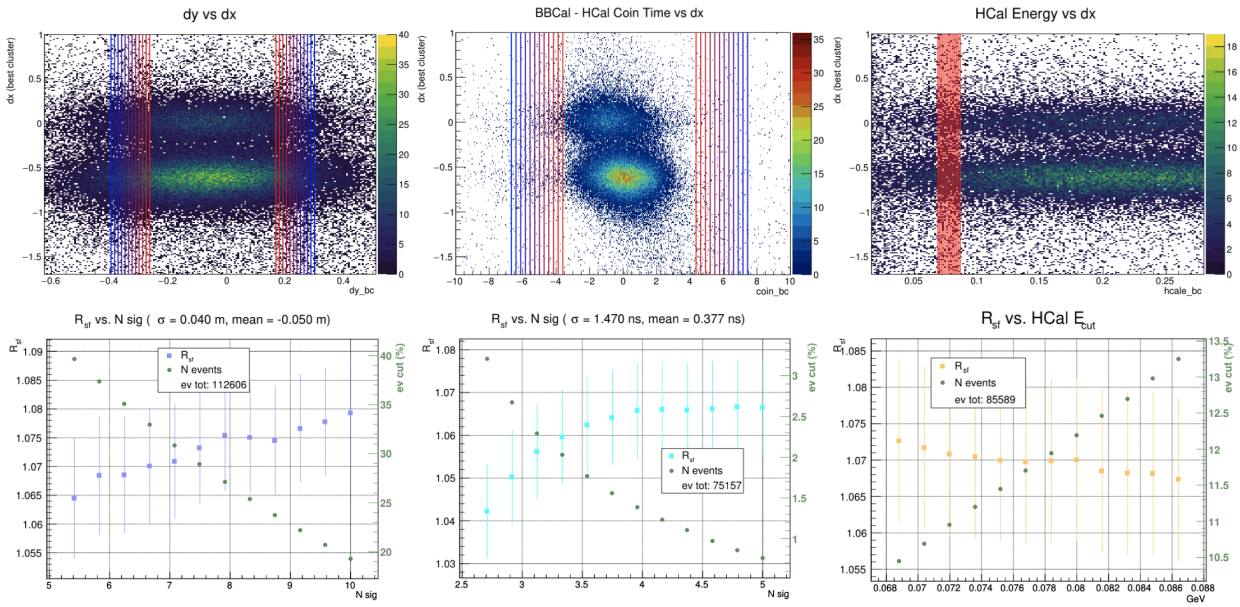

Figure 136: Data from $Q^2 = 4.5$ GeV^2 (SBS-8, 50% field) dx vs cut variables (from left to right dy, BBCal - HCal coincidence time, and HCal energy). R_{sf} extracted per cut variation is plotted against the variation region. Same color lines indicate a bounded cut region.

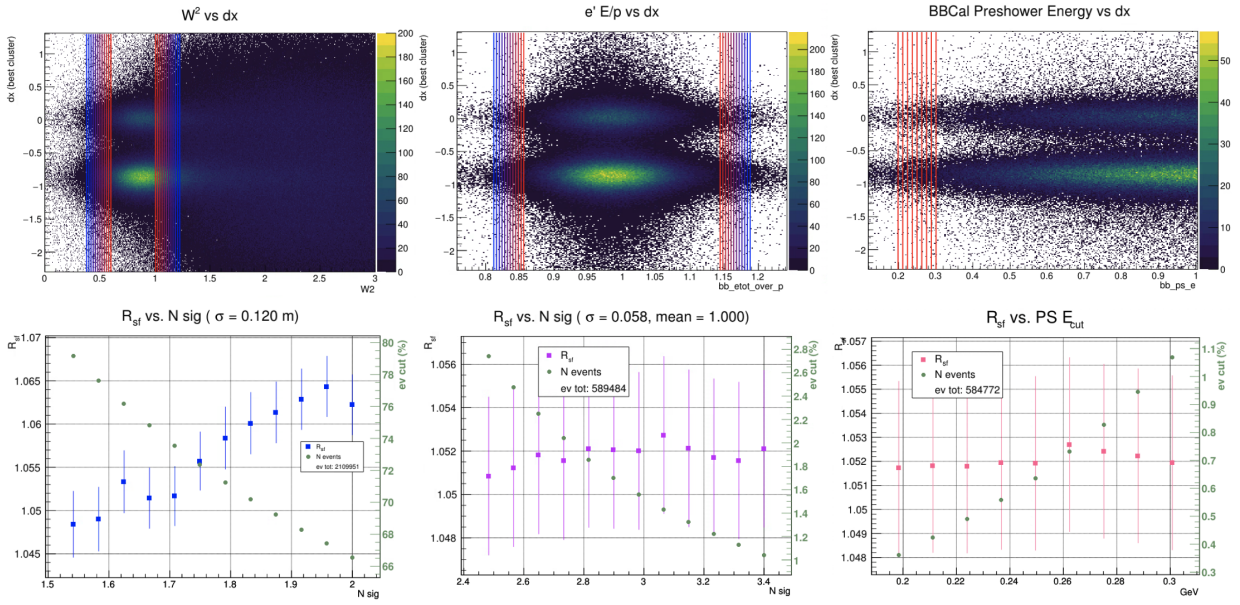

Figure 137: Data from $Q^2 = 4.5$ GeV^2 (SBS-8, 70% field) dx vs cut variables (from left to right W^2, e' E/p, and BBCal preshower energy). R_{sf} extracted per cut variation is plotted against the variation region. Same color lines indicate a bounded cut region.

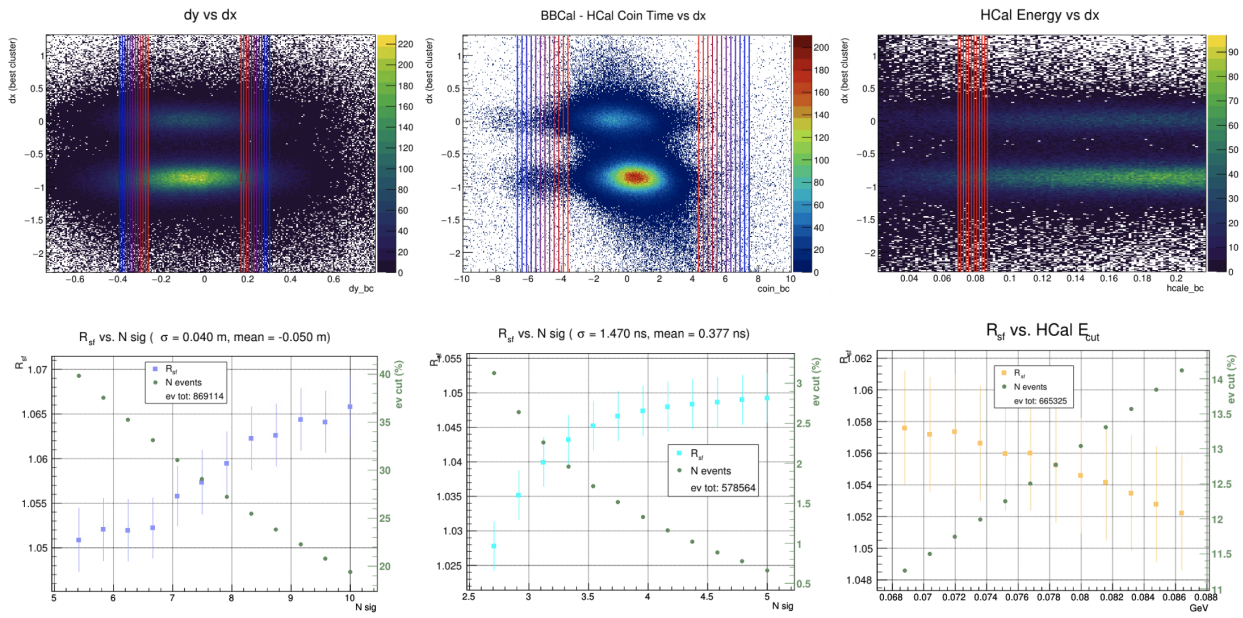

Figure 138: Data from Q^2 = 4.5 GeV^2 (SBS-8, 70% field) dx vs cut variables (from left to right dy, BBCal - HCal coincidence time, and HCal energy). R_{sf} extracted per cut variation is plotted against the variation region. Same color lines indicate a bounded cut region.

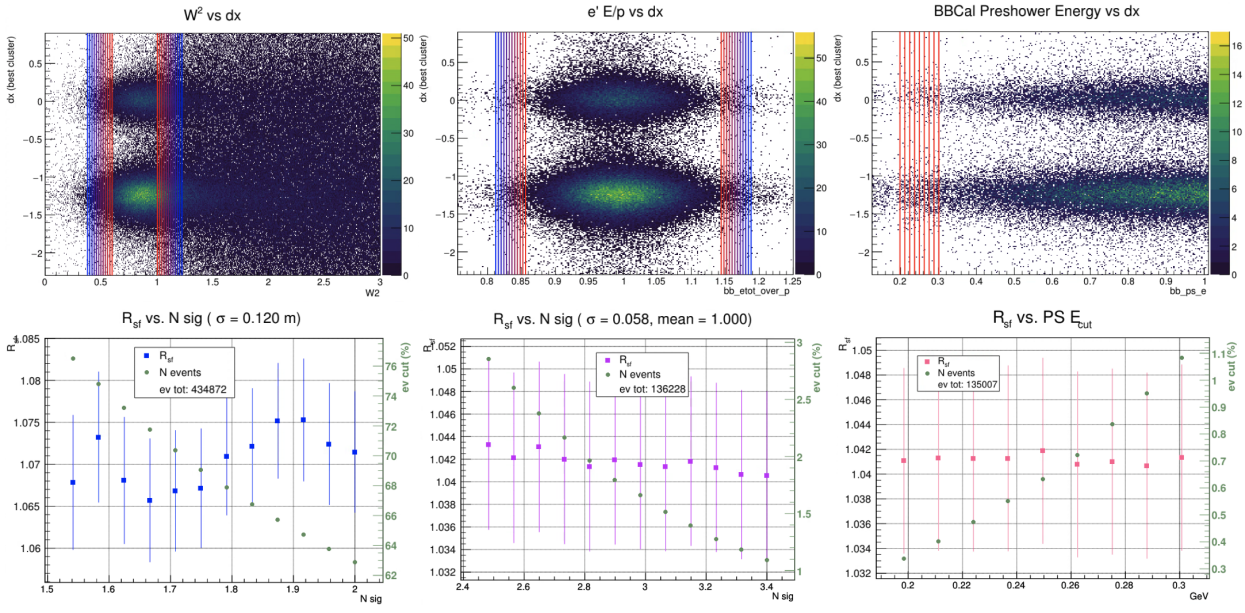

Figure 139: Data from Q^2 = 4.5 GeV^2 (SBS-8, 100% field) dx vs cut variables (from left to right W^2, e' E/p, and BBCal preshower energy). R_{sf} extracted per cut variation is plotted against the variation region. Same color lines indicate a bounded cut region.

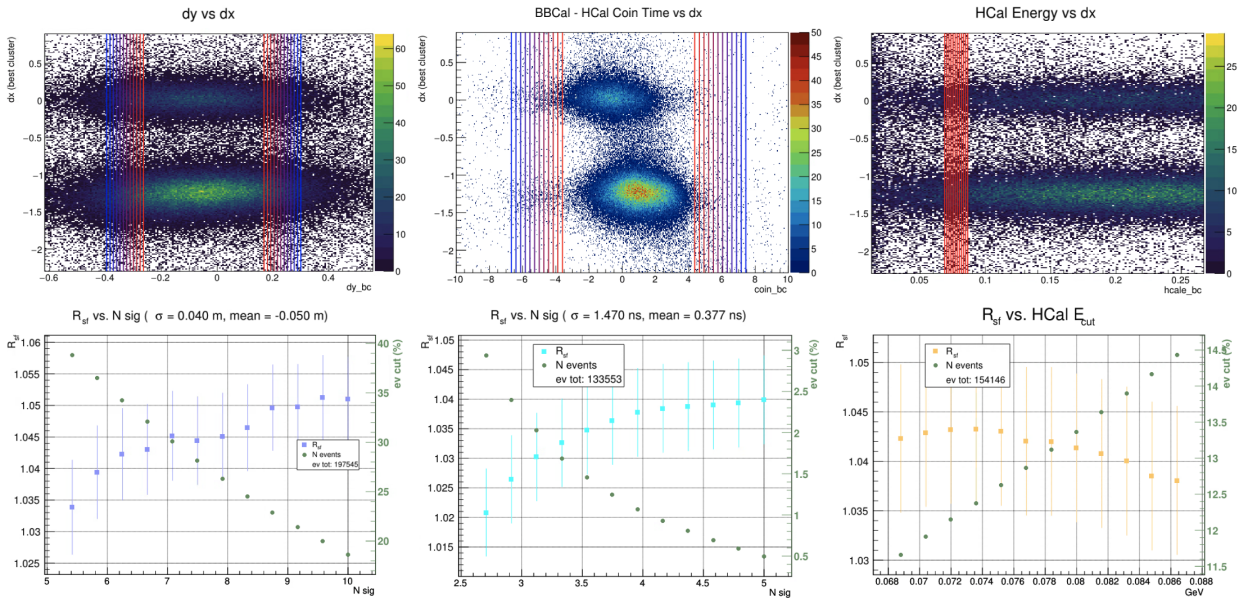

Figure 140: Data from Q^2 = 4.5 GeV^2 (SBS-8, 100% field) dx vs cut variables (from left to right dy, BBCal - HCal coincidence time, and HCal energy). R_{sf} extracted per cut variation is plotted against the variation region. Same color lines indicate a bounded cut region.

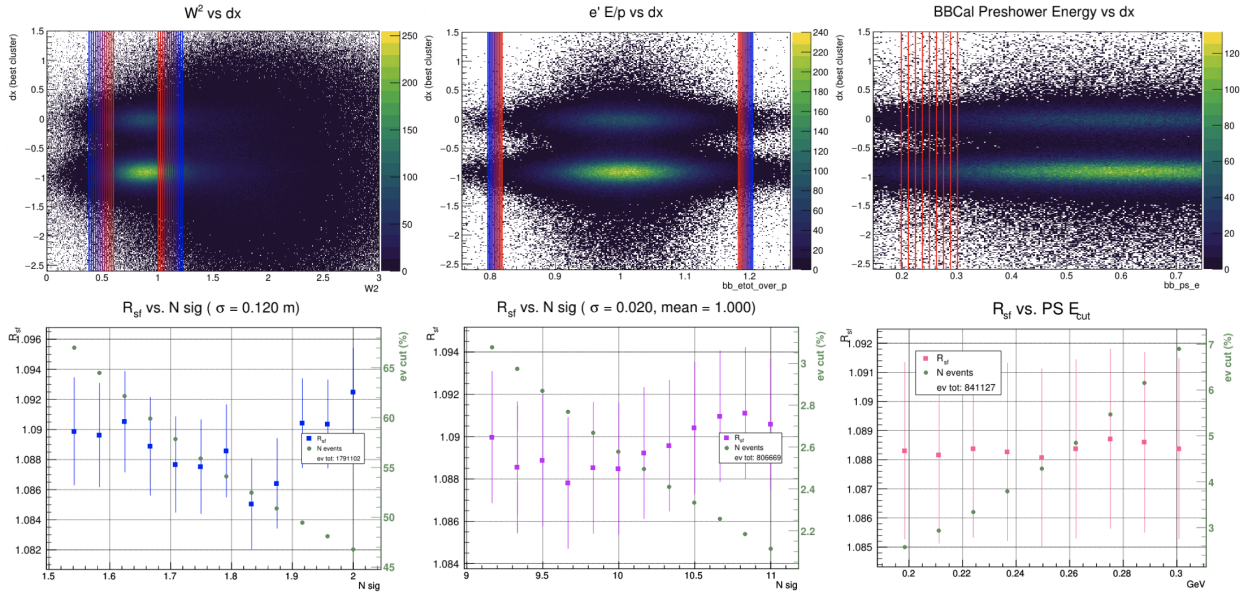

Figure 141: Data from Q^2 = 4.5 GeV^2 (SBS-9, 70% field) dx vs cut variables (from left to right W^2, e' E/p, and BBCal preshower energy). R_{sf} extracted per cut variation is plotted against the variation region. Same color lines indicate a bounded cut region.

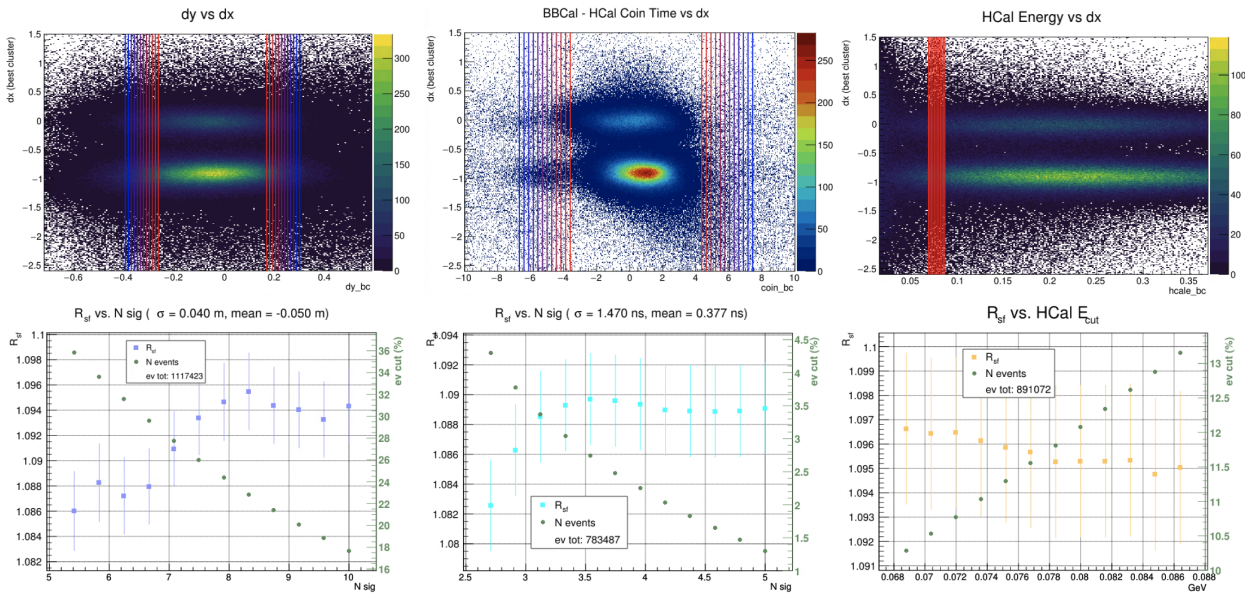

Figure 142: Data from Q^2 = 4.5 GeV^2 (SBS-9, 70% field) dx vs cut variables (from left to right dy, BBCal - HCal coincidence time, and HCal energy). R_{sf} extracted per cut variation is plotted against the variation region. Same color lines indicate a bounded cut region.

11.8 Binning and Ranges Supplemental

Figure 143 provides an example supplement to 94 depicting the adequacy of the Freedman-Diaconis method to resolve important features in W^2 data from Q^2 = 3.0 GeV^2.

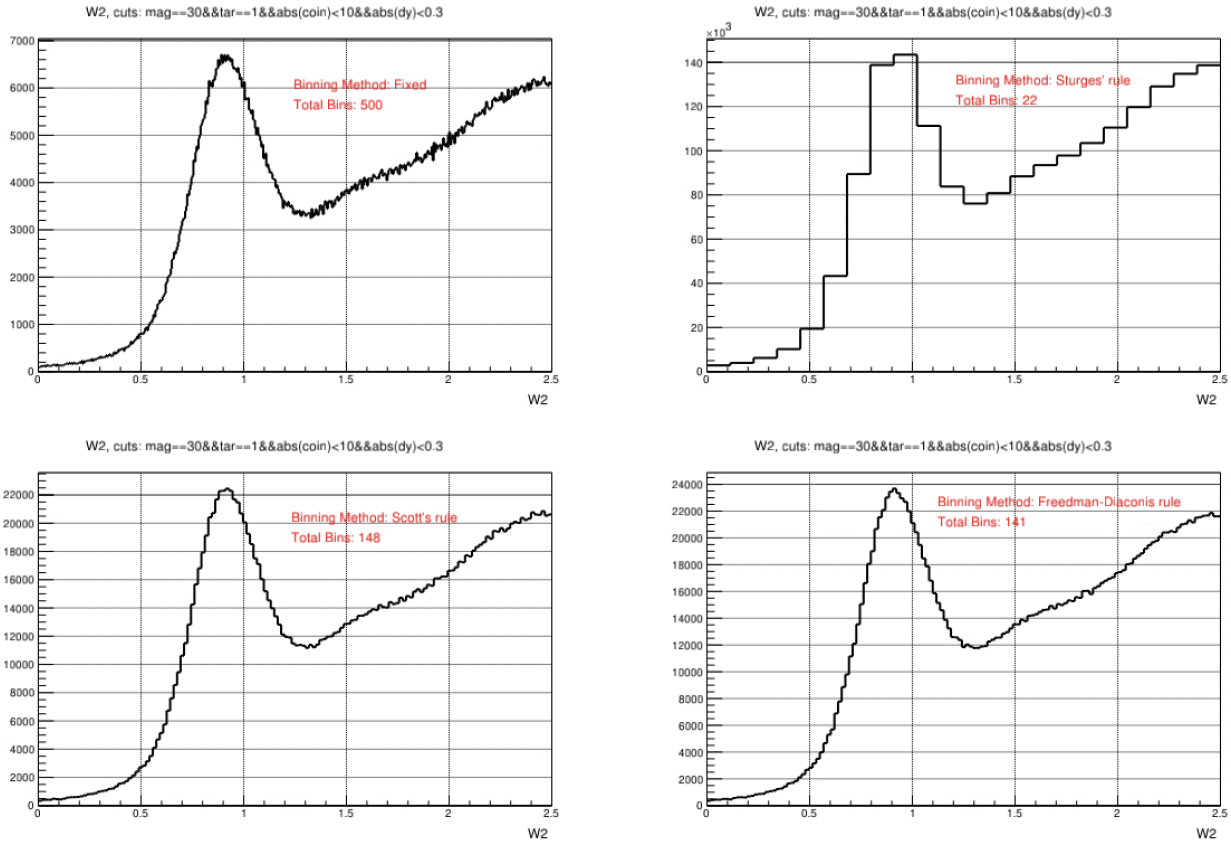

Figure 143: Data W^2 from Q^2 = 3.0 GeV^2 (SBS-4) depicting different binning starting points. Wide elastic cuts are indicated in the title of each histogram.

The plots in figure 144 qualify the selection of fit ranges from Q^2 = 3.0 GeV^2 and Q^2 = 4.5 GeV^2 data.

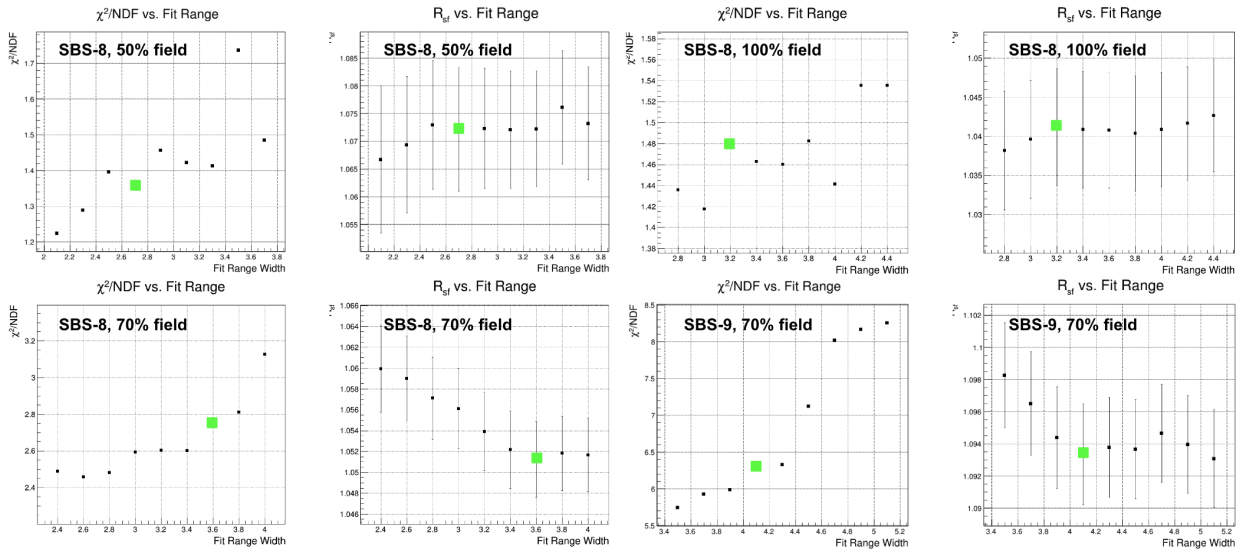

Figure 144: R_{sf} extractions from Q^2 = 4.5 GeV^2 (SBS-8/9) depicting different ranges. Each point is extracted from MC signal + second-order polynomial background fit to data over the given range magnitude.

11.9 Correlated Cuts

To determine the correlation factor (r) defined thus:

$$r = \frac{\sum(x_i - \bar{x})(y_i - \bar{y})}{\sqrt{\sum(x_i - \bar{x})^2}\sqrt{\sum(y_i - \bar{y})^2}}, \tag{11.1}$$

for cut variables, many combinations of cut variables plotted against each other (cut x vs cut y) were produced. Correlation factors which deviate strongly from zero indicate that the examined cut variables are correlated. Two sets of these correlation plots were made. The first set admits the full range of each cut, including other elastic cuts, but imposing no constraints on x or y. The second set is the same, but restricts the range of both x and y based on the elastic cut range for these cut variables. Figure 145 depicts the correlation factors for both sets.

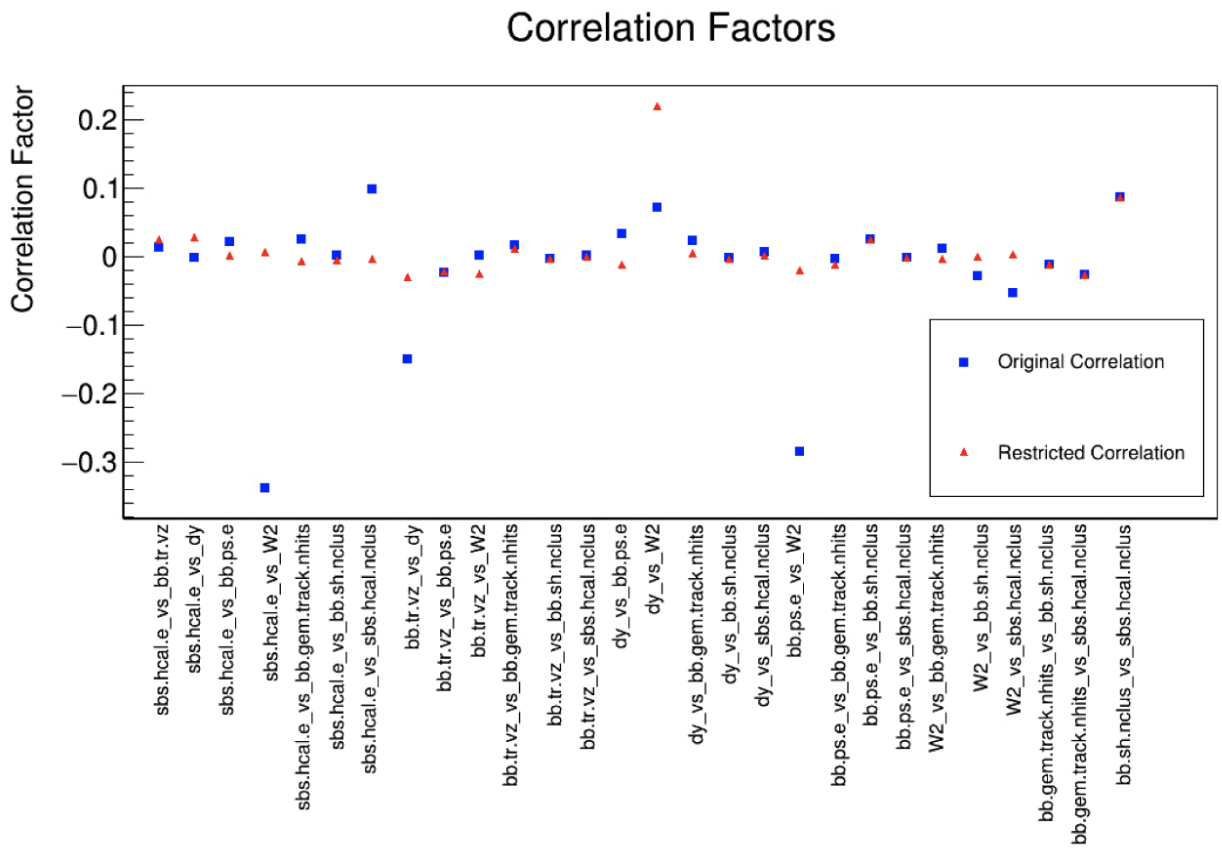

Figure 145: Correlation factors from Q^2 = 3.0 GeV^2 (SBS-4, 30% field) for many cut variables. All factors from cut variables plotted with elastic cuts. Blue points omit elastic cut constraints on the cut variables plotted against each other, where red points do not.

11.10 Rosenbluth Slope Supplemental

The following plots qualify additional cuts placed on data to select quasielastic protons and neutrons necessary for the super ratio $R'_{\varepsilon_1}/R'_{\varepsilon_2}$. R' is taken as the neutron to proton ratio over both the expected x (*xexp*) and y (*yexp*) position from e' tracks in HCal coordinates. No inefficiency corrections are applied and are assumed to cancel on the super ratio $R'_{\varepsilon_1}/R'_{\varepsilon_2}$. A weighted average of constant fits to these ratios over both dimensions (*xexp* and *yexp*) yield the neutron to proton ratio for each ε point.

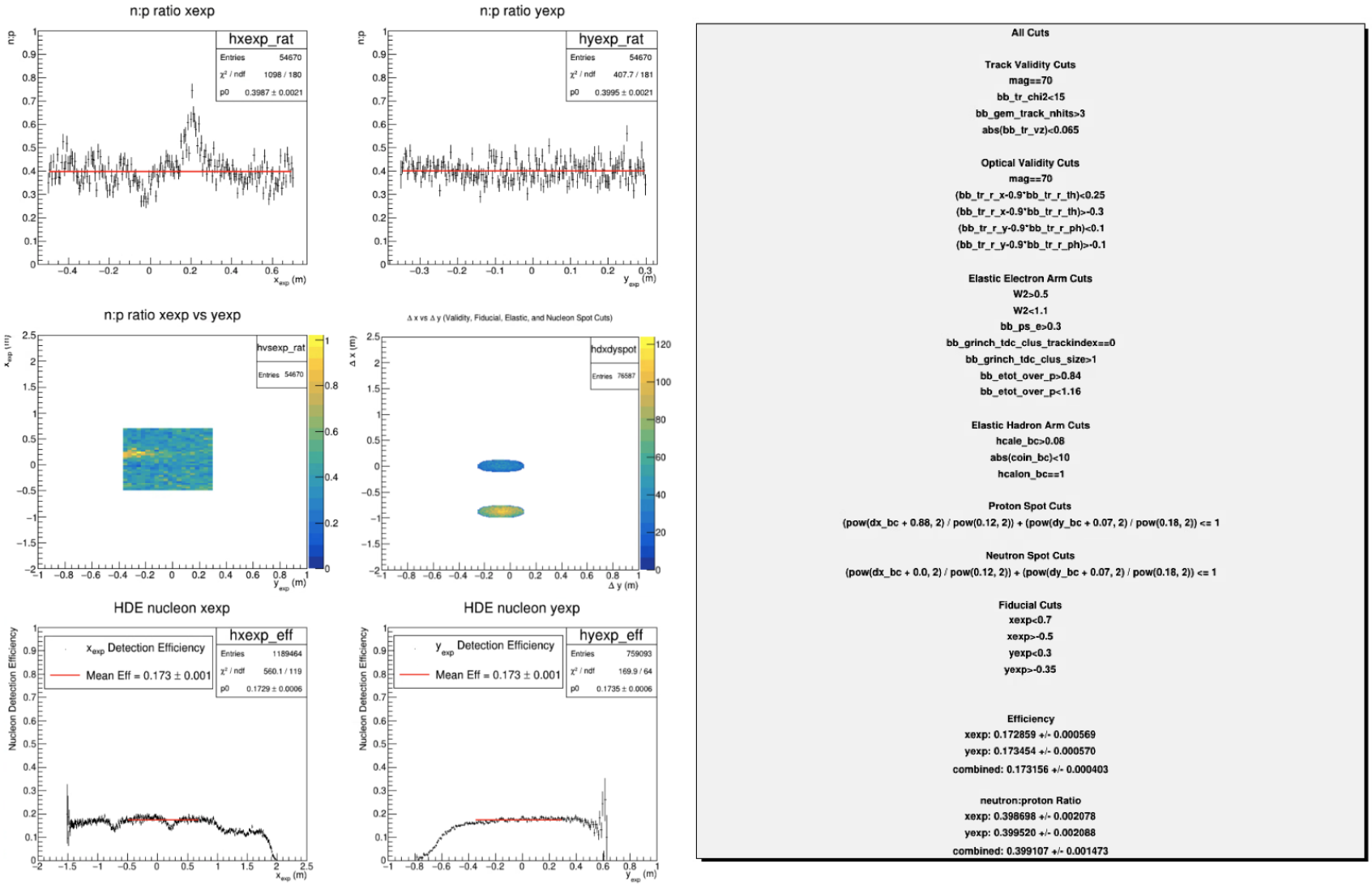

All Cuts

Track Validity Cuts
mag==70
bb_tr_chi2<15
bb_gem_track_nhits>3
abs(bb_tr_vz)<0.065

Optical Validity Cuts
mag==70
(bb_tr_r_x-0.9*bb_tr_r_th)<0.25
(bb_tr_r_x-0.9*bb_tr_r_th)>-0.3
(bb_tr_r_y-0.9*bb_tr_r_ph)<0.1
(bb_tr_r_y-0.9*bb_tr_r_ph)>-0.1

Elastic Electron Arm Cuts
W2>0.5
W2<1.1
bb_ps_e>0.3
bb_grinch_tdc_clus_trackindex==0
bb_grinch_tdc_clus_size>1
bb_etot_over_p>0.84
bb_etot_over_p<1.16

Elastic Hadron Arm Cuts
hcale_bc>0.08
abs(coin_bc)<10
hcalon_bc==1

Proton Spot Cuts
(pow(dx_bc + 0.88, 2) / pow(0.12, 2)) + (pow(dy_bc + 0.07, 2) / pow(0.18, 2)) <= 1

Neutron Spot Cuts
(pow(dx_bc + 0.0, 2) / pow(0.12, 2)) + (pow(dy_bc + 0.07, 2) / pow(0.18, 2)) <= 1

Fiducial Cuts
xexp<0.7
xexp>-0.5
yexp<0.3
yexp>-0.35

Efficiency
xexp: 0.172859 +/- 0.000569
yexp: 0.173454 +/- 0.000570
combined: 0.173156 +/- 0.000403

neutron:proton Ratio
xexp: 0.398698 +/- 0.002078
yexp: 0.399520 +/- 0.002088
combined: 0.399107 +/- 0.001473

Figure 146: Supplemental cuts and plots for R'_{ε_1} (SBS-8, 70% field).

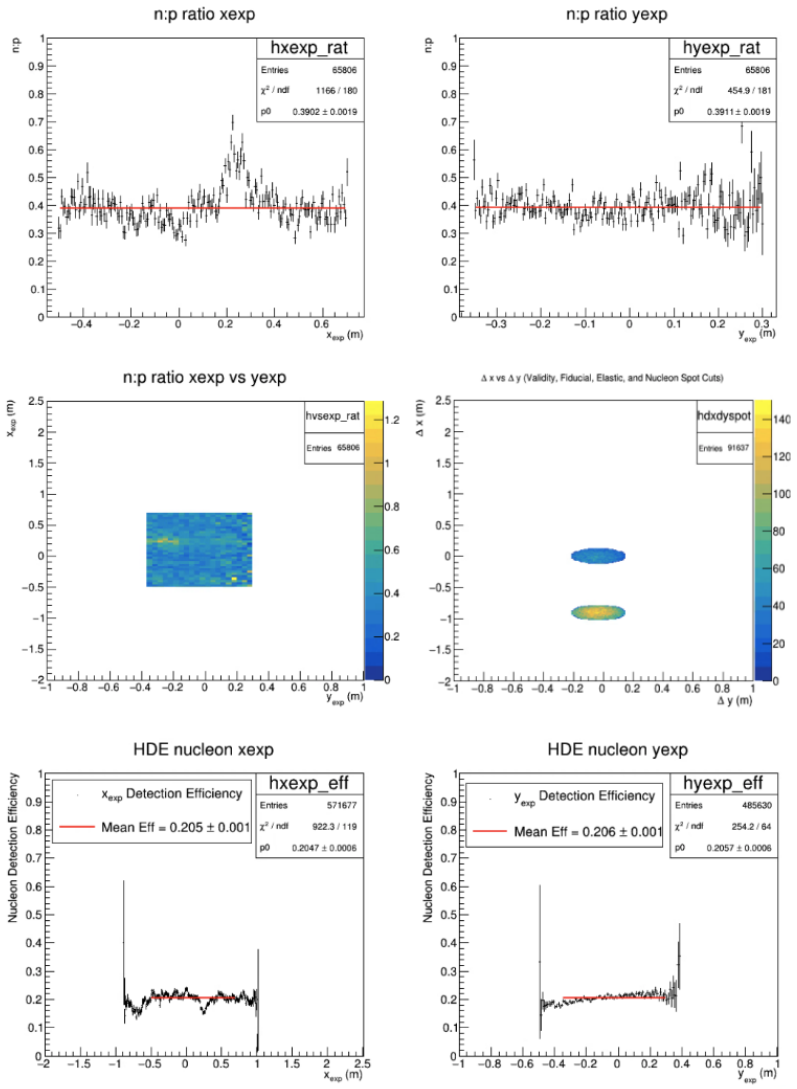

All Cuts

Track Validity Cuts
mag==70
bb_tr_chi2<15
bb_gem_track_nhits>3
abs(bb_tr_vz)<0.065

Optical Validity Cuts
mag==70
(bb_tr_r_x-0.9*bb_tr_r_th)<0.3
(bb_tr_r_x-0.9*bb_tr_r_th)>-0.25
(bb_tr_r_y-0.9*bb_tr_r_ph)<0.1
(bb_tr_r_y-0.9*bb_tr_r_ph)>-0.08

Elastic Electron Arm Cuts
W2>0.5
W2<1.1
bb_ps_e>0.3
bb_grinch_tdc_clus_trackindex==0
bb_grinch_tdc_clus_size>1
bb_etot_over_p>0.8
bb_etot_over_p<1.2

Elastic Hadron Arm Cuts
hcale_bc>0.08
abs(coin_bc)<12
hcalon_bc==1

Proton Spot Cuts
(pow(dx_bc + 0.91, 2) / pow(0.12, 2)) + (pow(dy_bc + 0.03, 2) / pow(0.18, 2)) <= 1

Neutron Spot Cuts
(pow(dx_bc + 0.0, 2) / pow(0.12, 2)) + (pow(dy_bc + 0.03, 2) / pow(0.18, 2)) <= 1

Fiducial Cuts
xexp<0.7
xexp>-0.5
yexp<0.3
yexp>-0.35

Efficiency
xexp: 0.204734 +/- 0.000604
yexp: 0.205663 +/- 0.000606
combined: 0.205197 +/- 0.000428

neutron:proton Ratio
xexp: 0.390216 +/- 0.001888
yexp: 0.391116 +/- 0.001896
combined: 0.390664 +/- 0.001338

Figure 147: Supplemental cuts and plots for R'_{ε_2} (SBS-9, 70% field).

References

[1] H. Abramowicz et al., "Measurement of shower development and its Molière radius with a four-plane LumiCal test set-up," 2017. Available at: https://cds.cern.ch/record/2265765/files/arXiv:1705.03885.pdf.

[2] P. Adderley, J. Clark, J. Grames, J. Hansknecht, M. Poelker, M. Stutzman, R. Suleiman, K. Surles-Law, J. McCarter, M. BastaniNejad, "CEBAF 200KV Inverted Electron Gun," Proceedings of the 2011 Particle Accelerator Conference, New York, NY, USA, 2011. Available at: https://accelconf.web.cern.ch/PAC2011/papers/weods3.pdf, accessed on May 18, 2024.

[3] A. Afanasev, P.G. Blunden, D. Hasell, and B.A. Raue, "Two-photon exchange in elastic electron–proton scattering," Progress in Particle and Nuclear Physics, vol. 95, pp. 245-278, 2017. Available at: https://www.sciencedirect.com/science/article/pii/S0146641017300352, accessed on May 21, 2024.

[4] W. M. Alberico, S. M. Bilenky, C. Giunti, and K. M. Graczyk, "Electromagnetic form factors of the nucleon: New fit and analysis of uncertainties," Physical Review C, vol. 79, no. 6, 065204, Jun. 2009. DOI: 10.1103/PhysRevC.79.065204. Available at: http://dx.doi.org/10.1103/PhysRevC.79.065204.

[5] S. Alsalmi et al. *Measurement of the Two-Photon Exchange Contribution to the Electron-Neutron Elastic Scattering Cross Section* From Jefferson Lab PAC 48; Program Advisory Committee

[6] L.W. Alvarez and F. Bloch, "A Quantitative Determination of the Neutron Moment in Absolute Nuclear Magnetons," *Physical Review*, vol. 57, 1940, pp. 111.

[7] A.B. Arbuzov, "Quantum Field Theory and the Electroweak Standard Model," arXiv:1801.05670, 2018. Available at: https://cds.cern.ch/record/2315477/plots.

[8] R. G. Arnold et al., "Measurements of Transverse Quasielastic Electron Scattering from the Deuteron at High Momentum Transfers," in Proceedings, 1988.

[9] J. Arrington, *How Well Do We Know the Electromagnetic Form Factors of the Proton?*, Phys. Rev. C, 69:022201, 2004. DOI: 10.1103/PhysRevC.69.022201

[10] J. Arrington, "Global Analysis of Proton Elastic Form Factor Data with TPE Corrections," Phys. Rev. C, vol. 76, 035205, 2007. DOI: 10.1103/PhysRevC.76.035205. Available at: https://journals.aps.org/prc/pdf/10.1103/PhysRevC.76.035205 and https://arxiv.org/abs/0707.1861.

[11] J. Arrington, P.G. Blunden, and W. Melnitchouk, "Review of two-photon exchange in electron scattering," Progress in Particle and Nuclear Physics, vol. 66, no. 4, pp. 782–833, Oct. 2011. Available at: http://dx.doi.org/10.1016/j.ppnp.2011.07.003, DOI: 10.1016/j.ppnp.2011.07.003.

[12] T. Averett, H. Yao, and B. Wojtsekhowski, "GRINCH Detector Technical Document v.11," 2012.

[13] X. Bai, J. Boyd, T. Gautam, K. Gnanvo, S. Jeffas, N. Liyanage, A. Puckett, A. Rathnayake, H. Szumila-Vance, and E. Wertz, "Hall A GEM Information and Operations for SBS Experiments." Available at: https://sbs.jlab.org/DocDB/0003/000303/029/GEM_operations.pdf.

[14] S. Barcus, "GMn HCal Energy Deposition Study," Dec. 18, 2020. Available at: https://sbs.jlab.org/DocDB/0000/000068/001/HCal_Energy_Deposition.pdf.

[15] S. Barcus, "HCAL-J: A Segmented Hadron Calorimeter with High Time Resolution," Available at: https://hallaweb.jlab.org/wiki/images/3/3b/HCal_Presentation.pdf, accessed on May 18, 2024.

[16] W. Bartel et al. *Electromagnetic form factors of the neutron at squared four-momentum transfers of 1.0 and 1.5 (GeV/c)*^{2}. Physics Letters B, 39(3), 407-410 (1972). DOI: https://doi.org/10.1016/0370-2693(72)90151-7

[17] "BBCAL Documents," Jefferson Lab Hall A Wiki. Available at: https://hallaweb.jlab.org/wiki/index.php/BBCAL_Documents.

[18] F. Benmokhtar et al. *Precision Measurement of the Neutron Magnetic Form Factor up to* $Q^2 = 18.0\,(\mathrm{GeV/c})^2$ From Jefferson Lab PAC 34; Program Advisory Committee

[19] J. Beringer et al. (Particle Data Group), "Review of Particle Physics," Phys. Rev. D, vol. 86, no. 1, 010001, Jul. 2012. DOI: 10.1103/PhysRevD.86.010001. Available at: https://link.aps.org/doi/10.1103/PhysRevD.86.010001.

[20] P. G. Blunden, W. Melnitchouk, and J. A. Tjon, "Two-photon exchange and elastic electron-proton scattering," Physical Review C, vol. 72, pp. 034612, 2005, doi: 10.1103/PhysRevC.72.034612.

[21] P. G. Blunden *Overview of recent theoretical work on two-photon exchange*. AIP Conference Proceedings 1970, 020003 (2018); link

[22] V. Brio, "HCAL-J Cosmic Ray Test at JLAB," April 2020. Available at: https://hallaweb.jlab.org/wiki/images/d/d1/Report_HCAL-J_April_2020.pdf.

[23] D. Borisyuk and A. Kobushkin, "Two-Photon Exchange in Elastic Electron Scattering on Hadronic Systems," Ukrainian Journal of Physics, vol. 66, no. 1, pp. 3, Jan. 2021. Available at: http://dx.doi.org/10.15407/ujpe66.1.3, DOI: 10.15407/ujpe66.1.3.

[24] Boyd, John, "Measurements of the Neutron Magnetic Form Factor and the Two-Photon Exchange Contribution to the Electron-Neutron Elastic Scattering Cross Section," PhD Dissertation, University of Virginia, 2024, https://libraetd.lib.virginia.edu/public_view/tb09j7238.

[25] J. Boyd, "Crosstalk Analysis," Mar. 10, 2023. Available at: https://sbs.jlab.org/cgi-bin/DocDB/private/ShowDocument?docid=527.

[26] S. J. Brodsky and G. R. Farrar, "Scaling Laws for Large-Momentum-Transfer Processes," Physical Review D, vol. 11, no. 5, pp. 1309–1313, Mar. 1975. DOI: 10.1103/PhysRevD.11.1309.

[27] A. Camsonne et al. *Measurement of the Neutron Electromagnetic Form Factor Ratio GEn/GMn at High* Q^2 From Jefferson Lab PAC 34

[28] C. E. Carlson and M. Vanderhaeghen, "Two-photon physics in hadronic processes," Annual Review of Nuclear and Particle Science, vol. 57, pp. 171-204, 2007, doi: 10.1146/annurev.nucl.57.090506.123116.

[29] J. Chadwick, "Possible Existence of a Neutron," *Nature*, vol. 129, 1932, pp. 312.

[30] M.E. Christy et al. *Form Factors and Two-Photon Exchange in High-Energy Elastic Electron-Proton Scattering*. Physical Review Letters, 128(10), American Physical Society (APS), 2022. DOI: 10.1103/PhysRevLett.128.102002

[31] Tiefenback, Michael *JLab Accelerator Overview* From CLAS Collaboration Meeting, Jefferson Lab, 2016. link

[32] J. Dalton, *A New System of Chemical Philosophy*, (1808).

[33] SBS Collaboration, *Thesis Supplementary Materials*, Aggregated for thesis from Jefferson Lab private document database, 2024.

[34] Thomas Jefferson National Accelerator Laboratory, "CODA CEBAF On-line Data Acquisition User's Manual," March 1993. Available at: https://coda.jlab.org/drupal/content/coda-documentation, accessed on May 18, 2024.

[35] S. Coleman, *Aspects of Symmetry: Selected Erice Lectures*, Cambridge University Press, 1985.

[36] D.H. Coward et al., "Electron-Proton Elastic Scattering at High Momentum Transfers," *Physical Review Letters*, vol. 20, no. 6, 1968, pp. 292-295. DOI: 10.1103/PhysRevLett.20.292.

[37] Arun Tadepalli, "Cryotarget Pictures During Installation in Hall A for SBS GMn Running," Jefferson Lab, https://sbs.jlab.org/cgi-bin/DocDB/private/ShowDocument?docid=573. Accessed on May 18, 2024.

[38] G. Smith, "Cryotarget Training," Jefferson Lab, Available at: https://userweb.jlab.org/~smithg/target/Qweak/HallACTgt_Training.pdf.

[39] P. Datta, "BBCAL Energy Calibration Results for GMn/nTPE Pass2 Readiness." Available at: https://sbs.jlab.org/cgi-bin/DocDB/private/ShowDocument?docid=367.

[40] P. Datta, "Implementation of D(ee'n) process in simc_gfortran," Redmine, Available at: https://redmine.jlab.org/issues/758, accessed on May 18, 2024.

[41] P. Datta, "Procedure And How-to for BBCAL." Available at: https://sbs.jlab.org/cgi-bin/DocDB/private/ShowDocument?docid=313.

[42] P. Datta, A. Tadepalli, and M. Jones, "Study of the Linear Region of Operation for all the Electronic Modules involved in BigBite Calorimeter Circuit," University of Connecticut, Storrs, CT, USA, and Thomas Jefferson National Accelerator Facility, Newport News, VA, USA. Available at: https://sbs.jlab.org/DocDB/0001/000118/001/BBCal_sig_circuit_saturation.pdf.

[43] P. Datta, personal communication, May 18, 2024.

[44] P. Datta, "Implemented rejection sampling (RS) for more efficient event generation," GitHub, 2024. [Online]. Available: https://github.com/MarkKJones/simc_gfortran/pull/6.

[45] P. Datta, S. Jeffas, S. Seeds, "JLab HPC," GitHub, 2024. [Online]. Available: https://github.com/provakar1994/jlab-HPC.

[46] O. S. Deiev, "GEANT 4 Simulation of Neutron Transport and Scattering in Media," National Science Center "Kharkov Institute of Physics and Technology," Kharkov, Ukraine. VANT, vol. 2013, no. 3, pp. 236-240, 2013. Available at: https://vant.kipt.kharkov.ua/ARTICLE/VANT_2013_3/article_2013_3_236.pdf, accessed on May 18, 2024.

[47] Kees de Jager, *Nucleon Structure Studies Through Elastic Electron Scattering: Electromagnetic Form Factors*, Presentation at NPPD, Glasgow, April 4 - 7, 2011. Available at: https://indico.cern.ch/event/131080/contributions/1354372/attachments/94632/135138/dejager_NPPD.pdf.

[48] C.W. de Jager, et al. "The Super-Bigbite Spectrometer for Jefferson Lab Hall A," 2014. Available: https://userweb.jlab.org/~mahbub/HallA/SBS/SBS-CDR_New.pdf

[49] D. Di, "GEM High Rate Management," presented at the 2017 SBS Summer Collaboration Meeting, University of Virginia, July 13, 2017. [Online]. Available: https://hallaweb.jlab.org/12GeV/SuperBigBite/meetings/col_13jul17/talks/Danning_GEMHighRates_SBS_collMeeting_13Jul2017.pdf.

[50] M. Diehl, *Generalized parton distributions*. Physics Reports, 388(2–4), Elsevier BV, 2003. DOI: 10.1016/j.physrep.2003.08.002

[51] P.A.M. Dirac, "The Quantum Theory of the Electron," *Proceedings of the Royal Society A*, vol. 117, 1928, pp. 610-624.

[52] L. Durand, *Inelastic Electron-Deuteron Scattering Cross Sections at High Energies*. Phys. Rev., 115(4), 1020–1038 (1959). DOI: 10.1103/PhysRev.115.1020

[53] F.J. Dyson, "The Radiation Theories of Tomonaga, Schwinger, and Feynman," *Physical Review*, vol. 75, 1949, pp. 486-502.

[54] T. Eden et al., "Electric form factor of the neutron from the ^{2}H(e$\rightarrow$,e'n$\rightarrow$)^{1}H reaction at Q^2=0.255 (GeV/c)^2," Physical Review C, vol. 50, pp. R1749, 1994.

[55] Anuruddha Rathnayake, Andrew Puckett, Nilanga Liyanage, Bogdan Wojtsekhowski, and Sebastian Seeds, "HCal Neutron Detection Efficiency via 'End-Point' Method," August 2023. https://sbs.jlab.org/cgi-bin/DocDB/private/ShowDocument?docid=432

[56] C. Timmer, "EVIO 6.0 User's Guide," Jefferson Lab Experimental Physics Software and Computing Infrastructure group, Jefferson Lab, Newport News, VA, May 3, 2021. [Online]. Available: https://coda.jlab.org/drupal/system/files/coda/evio/evio-6.0/docs/users_guide/evio_Users_Guide.pdf. Accessed: July 22, 2024.

[57] Jefferson Lab, "F1TDC: A High-Resolution, Multi-Hit, VME64x Time-to-Digital Converter User's Manual V1.1," 23 April 2004. Available at: https://halldweb.jlab.org/DocDB/0010/001021/001/F1TDC%20-%20User%20Manual%20V1.1.pdf, accessed on May 18, 2024.

[58] C. W. Fabjan and F. Gianotti, "Calorimetry for Particle Physics," CERN-EP/2003-075, CERN, Geneva, Switzerland, Oct. 31, 2003. Available at: https://cds.cern.ch/record/692252/files/ep-2003-075.pdf.

[59] JLab, "FADC250 User's Manual," https://www.jlab.org/Hall-B/ftof/manuals/FADC250UsersManual.pdf. Accessed on 2/25/24.

[60] R.P. Feynman, "Space-Time Approach to Quantum Electrodynamics," *Physical Review*, vol. 76, 1949, pp. 769-789.

[61] D. Freedman and P. Diaconis, "On the histogram as a density estimator: L2 theory," *Zeitschrift für Wahrscheinlichkeitstheorie und Verwandte Gebiete*, vol. 57, no. 4, pp. 453–476, 1981.

[62] H. Fritzsch, M. Gell-Mann, and H. Leutwyler, "Advantages of the Color Octet Gluon Picture," *Physics Letters B*, vol. 47, no. 4, 1973, pp. 365-368.

[63] E. Fuchey, "SBS9 LH2 efficiency (MC) with adjustments," Jefferson Lab Document Database, https://sbs.jlab.org/DocDB/0005/000570/001/sbs9_mc_hcalvariablegain_step1_effplots.pdf. Accessed on 5/28/24.

[64] E. Fuchey, "Introduction for BigBite Trigger Logic for SBS Form Factors Experiments," Feb. 8, 2021. Available at: https://hallaweb.jlab.org/wiki/images/5/57/BBtrig_introductory.pdf.

[65] SBS Collaboration, "g4sbs: GEANT4 simulation for the Super BigBite Spectrometer (SBS)," GitHub repository, https://github.com/JeffersonLab/g4sbs. Accessed on 2/25/24.

[66] Anuruddha Rathnayake, Ezekiel Wertz, Maria Satnik, Provakar Datta, Sebastian Seeds, John Boyd, "G4SBS SBS magnet fieldscale settings for GMn LD2 data," Jefferson Lab DocDB, https://sbs.jlab.org/cgi-bin/DocDB/private/ShowDocument?docid=578. Accessed on 05/28/2024.

[67] S. Agostinelli et al., "Geant4—a simulation toolkit," *Nuclear Instruments and Methods in Physics Research Section A: Accelerators, Spectrometers, Detectors and Associated Equipment*, vol. 506, no. 3, pp. 250-303, 2003. doi:10.1016/S0168-9002(03)01368-8

[68] J. Allison et al., "Geant4 developments and applications," *IEEE Transactions on Nuclear Science*, vol. 53, no. 1, pp. 270-278, 2006. doi:10.1109/TNS.2006.869826

[69] J. Allison et al., "Recent developments in Geant4," *Nuclear Instruments and Methods in Physics Research Section A: Accelerators, Spectrometers, Detectors and Associated Equipment*, vol. 835, pp. 186-225, 2016. doi:10.1016/j.nima.2016.06.125

[70] Jefferson Lab Hall A Collaboration, "GEM online data reduction summary for GMn" Jefferson Lab Hall A wiki, https://hallaweb.jlab.org/wiki/images/7/77/GEM-data-reduction-11Aug19.pdf. Accessed on 2/25/24.

[71] Jefferson Lab Hall A Collaboration, "Documentation of g4sbs: Overview," Jefferson Lab Hall A wiki, https://hallaweb.jlab.org/wiki/index.php/Documentation_of_g4sbs#Documentation_of_g4sbs:_Overview. Accessed on 2/25/24.

[72] O. Gayou et al., *Measurements of the Elastic Electromagnetic Form Factor Ratio $\mu_p G_{Ep}/G_{Mp}$ via Polarization Transfer*. Phys. Rev. C, 64(3):038202, 2002.

[73] Geant4 Collaboration, "Geant4—a simulation toolkit," *Nuclear Instruments and Methods in Physics Research Section A: Accelerators, Spectrometers, Detectors and Associated Equipment*, vol. 506, no. 3, pp. 250-303, 2003.

[74] Geant4 Collaboration, "Geant4 a Simulation Toolkit: Introduction to Geant4," December 2023. Available at: https://geant4-userdoc.web.cern.ch/UsersGuides/IntroductionToGeant4/fo/IntroductionToGeant4.pdf, accessed on May 18, 2024.

[75] Liyanage, Nilanga *GEM Detectors for SuperBigbite* From SBS DOE Review, 2018. link

[76] Jefferson Lab Hall C, "GEp-III Experiment," *Jefferson Lab Hall C Wiki*, https://hallcweb.jlab.org/experiments/GEp-III/wiki//index.php/Main_Page.

[77] M. Gell-Mann, "Isotopic Spin and New Unstable Particles," *Physical Review*, vol. 92, 1953, pp. 833-834.

[78] M. Gell-Mann, "The Eightfold Way: A Theory of Strong Interaction Symmetry," *California Institute of Technology Synchrotron Laboratory Report CTSL-20*, 1961.

[79] M. Gell-Mann, "A Schematic Model of Baryons and Mesons," *Physics Letters*, vol. 8, 1964, pp. 214-215.

[80] G.P. Gilfoyle et al, *QUEEG: A Monte Carlo Event Generator for Quasielastic Scattering on Nucleons and Nuclei*. Richmond University, 2020. Available at: https://facultystaff.richmond.edu/QUEEG.

[81] S.L. Glashow, "Partial-symmetries of weak interactions," *Nuclear Physics*, vol. 22, 1961, pp. 579-588.

[82] K. Gnanvo, N. Liyanage, V. Nelyubin, K. Saenboonruang, S. Sacher, and B. Wojtsekhowski, "Large Size GEM for Super Bigbite Spectrometer (SBS) Polarimeter for Hall A 12 GeV program at JLab," accepted for publication in Nuclear Inst. and Methods in Physics Research, A. Available at: https://arxiv.org/pdf/1409.5393.

[83] K. Gnanvo, "GEMs Chambers for SBS," August 2019. Available at: https://hallaweb.jlab.org/12GeV/SuperBigBite/meetings/col_2019aug5/talks/KG_SBSCollMeeting20190806.pdf.

[84] K. Gnanvo, "Commissioning of GEM Trackers for SBS at JLAB," RD51 Collaboration Meeting @ CERN, Oct. 22, 2019. Available at: https://indico.cern.ch/event/843711/contributions/3575921/attachments/1930473/3197209/20191922_KG_RD51_CollMeeting.pdf.

[85] D. Green, *The Physics of Particle Detectors*, Cambridge University Press, 1997.

[86] D. Griffiths, "An Introduction to Elementary Particles," Wiley, 1987.

[87] F. Gross et al. *50 Years of quantum chromodynamics: Introduction and Review*. The European Physical Journal C, 83(12), Springer Science and Business Media LLC, 2023. *DOI: 10.1140/epjc/s10052-023-11949-2*

[88] D.J. Gross and F. Wilczek, "Asymptotically Free Gauge Theories. I," *Physical Review D*, vol. 8, no. 10, 1973, pp. 3633-3652.

[89] "General Description of the Hall A Cryogenic Target," Hall A Wiki, Jefferson Lab. [Online]. Available: https://hallaweb.jlab.org/equipment/targets/cryotargets/general.html. Accessed: July 22, 2024.

[90] Hall C DAQ, *Hall C Data Acquisition Wiki*, Jefferson Lab. Accessed: July 22, 2024. [Online]. Available: https://hallcweb.jlab.org/wiki/index.php/Hall_C_DAQ.

[91] G. Smith, "Jefferson Lab HallC (and Hall A) Cryogenic Target System," Available at: https://userweb.jlab.org/~smithg/target/Qweak/#_12_GeV_Era, accessed on May 18, 2024.

[92] F. Halzen and A.D. Martin, *Quarks and Leptons: An Introductory Course in Modern Particle Physics*, Wiley, 1984.

[93] D. Hamilton, "BigBite Timing Hodoscope Performance Update," SBS DAQ Meeting, 5th June 2023, https://sbs.jlab.org/DocDB/0003/000399/001/BB-TH-PerformanceUpdate-v1.pdf, accessed on May 18, 2024.

[94] L. Harwood, "The JLab 12 GeV Energy Upgrade of CEBAF," Proceedings of the PAC2013, Pasadena, CA, USA, MOZAA1, 2013.

[95] S. Seeds, *HCal replay repository*, https://github.com/sebastianseeds/HCal_replay. Code archive for the HCal_replay repository maintained by Sebastian Seeds for use with JLab HCal data analysis and calibrations.

[96] Jefferson Lab, "HCAL Reports/Updates," Available at: https://hallaweb.jlab.org/wiki/index.php/HCAL_Reports/Updates, accessed on May 18, 2024.

[97] W. Heisenberg, "Über den Bau der Atomkerne. I," *Zeitschrift für Physik*, vol. 77, 1932, pp. 1-11.

[98] D. W. Higinbotham and T. Keppel, "Jefferson Lab Hall A Standard Equipment Manual," 2017 Version. Available at: https://hallaweb.jlab.org/github/halla-osp/version/Standard-Equipment-Manual.pdf, accessed on May 18, 2024.

[99] A. Hofler, R. Kazimi, Y. Wang, and K. Surles-Law, "Modeling for the Phased Injector Upgrade for 12 GeV CEBAF," Thomas Jefferson National Accelerator Facil-

ity, Newport News, VA, USA, 2013. Available: https://inspirehep.net/files/3049167518885bfddd03773ce0f66a40

[100] R. Hofstadter, "Electron Scattering and Nuclear Structure," *Reviews of Modern Physics*, vol. 28, 1956, pp. 214-254.

[101] E. B. Hughes, T. A. Griffy, M. R. Yearian, and R. Hofstadter, "Neutron Form Factors from Inelastic Electron-Deuteron Scattering," Physical Review, July 1965.

[102] S. Jeffas and A. Puckett, "SBS GEM Algorithms," Feb. 24, 2023. Available at: https://sbs.jlab.org/DocDB/0003/000368/001/SBS_GEM_Algorithms.pdf.

[103] M. K. Jones et al., *G_{Ep}/G_{Mp} Ratio by Polarization Transfer in $\vec{e}p \to e\vec{p}$*. Phys. Rev. Lett., 84(7):1398–1402, 2000.

[104] J. J. Kelly, "Simple parametrization of nucleon form factors," Phys. Rev. C, vol. 70, 068202, 2004. DOI: 10.1103/PhysRevC.70.068202. Available at: https://journals.aps.org/prc/abstract/10.1103/PhysRevC.70.068202.

[105] G. F. Knoll, *Radiation Detection and Measurement*, 3rd ed., Wiley, 2000.

[106] J. Lachniet, "A High Precision Measurement of the Neutron Magnetic Form Factor Using the CLAS Detector," PhD thesis, Carnegie Mellon University, June 2005.

[107] J. Lachniet, A. Afanasev, H. Arenhövel, W. K. Brooks, G. P. Gilfoyle, D. Higinbotham, S. Jeschonnek, B. Quinn, M. F. Vineyard, et al., *Precise Measurement of the Neutron Magnetic Form Factor G_M^n in the Few-GeV^2 Region*. Phys. Rev. Lett., 102(19):192001, 2009.

[108] W. R. Leo, *Techniques for Nuclear and Particle Physics Experiments: A How-to Approach*, Springer-Verlag, 1994.

[109] R. Madey et al. (The Jefferson Laboratory E93-038 Collaboration), "Measurements of G_E^n/G_M^n from the ^{2}H$(\vec{e},e'\,\vec{n})^1$H Reaction to $Q^2 = 1.45$ (GeV/c)^2," Physical Review Let-

ters, vol. 91, no. 12, pp. 122002, Sep. 2003. DOI: 10.1103/PhysRevLett.91.122002. Available at: https://link.aps.org/doi/10.1103/PhysRevLett.91.122002.

[110] L. C. Maximon and J. A. Tjon, "Radiative Corrections to Electron-Proton Scattering," Physical Review C, vol. 62, no. 5, 054320, 2000.

[111] R. D. McKeown, *The Jefferson Lab 12 GeV Upgrade*. Journal of Physics: Conference Series, 312(3), IOP Publishing, 2011. DOI: 10.1088/1742-6596/312/3/032014

[112] R. D. McKeown, "The Jefferson Lab 12 GeV Upgrade," Journal of Physics: Conference Series, vol. 032014, 2011.

[113] Dave Meekins, "Hall A Target Configuration October 2021 to February 2022," https://logbooks.jlab.org/files/2022/03/3987411/TGT-RPT-22-002.pdf.

[114] M. Mihovilovič, S. Širca, et al., "Methods for optical calibration of the BigBite hadron spectrometer," Nuclear Instruments and Methods in Physics Research Section A: Accelerators, Spectrometers, Detectors and Associated Equipment, Volume 686, 2012, Pages 20-30, https://doi.org/10.1016/j.nima.2012.04.085.

[115] L. W. Mo and Y. S. Tsai, *Radiative Corrections to Elastic and Inelastic ep and μp Scattering*, Rev. Mod. Phys. 41, 205, 1954.

[116] L. W. Mo and Y. S. Tsai, "Radiative Corrections to Elastic and Inelastic ep and μp Scattering," Reviews of Modern Physics, vol. 41, no. 1, pp. 205-235, 1969.

[117] Y. Ne'eman, "Derivation of Strong Interactions from a Gauge Invariance," *Nuclear Physics*, vol. 26, 1961, pp. 222-229.

[118] M.J. Berger, J.S. Coursey, M.A. Zucker, and J. Chang, "ESTAR, Stopping-Power and Range Tables for Electrons," National Institute of Standards and Technology, https://physics.nist.gov/PhysRefData/Star/Text/ESTAR.html.

[119] Nobel Prize Organization, "The Nobel Prize in Chemistry 1908," *NobelPrize.org*, accessed May 21, 2024. Available at: https://www.nobelprize.org/prizes/chemistry/1908/rutherford/biographical/.

[120] Nobel Prize Organization, "The Nobel Prize in Physics 1961," *NobelPrize.org*, accessed May 22, 2024. Available at: https://www.nobelprize.org/prizes/physics/1961/summary/.

[121] Nobel Prize Organization, "The Nobel Prize in Physics 1965," *NobelPrize.org*, accessed May 21, 2024. Available at: https://www.nobelprize.org/prizes/physics/1965/summary/.

[122] Nobel Prize Organization, "The Nobel Prize in Physics 1969," *NobelPrize.org*, accessed May 22, 2024. Available at: https://www.nobelprize.org/prizes/physics/1969/summary/.

[123] Nobel Prize Organization, "The Nobel Prize in Physics 1990," *NobelPrize.org*, accessed May 22, 2024. Available at: https://www.nobelprize.org/prizes/physics/1990/summary/.

[124] M. Tanabashi et al. (Particle Data Group), "Particle Detectors at Accelerators," Phys. Rev. D, vol. 98, 030001, 2018 and 2019 update. Available at: https://pdg.lbl.gov/2019/reviews/rpp2019-rev-particle-detectors-accel.pdf.

[125] Particle Data Group, "Review of Particle Physics," Progress of Theoretical and Experimental Physics, 2022, 083C01.

[126] Particle Data Group, "Passage of Particles Through Matter," in *Review of Particle Physics*, Progress of Theoretical and Experimental Physics, 2021, 083C01. Available at: https://pdg.lbl.gov/2021/reviews/rpp2020-rev-passage-particles-matter.pdf.

[127] R.L. Workman et al. (Particle Data Group), "Review of Particle Physics: Quarks," Prog. Theor. Exp. Phys. 2022, 083C01 (2022). Available at: https://pdg.lbl.gov/2022/tables/rpp2022-sum-quarks.pdf.

[128] C.F. Perdrisat, V. Punjabi, M. Vanderhaeghen, *Nucleon electromagnetic form factors*. Progress in Particle and Nuclear Physics 59, 694-764 (2007). DOI: 10.1016/j.ppnp.2007.05.001

[129] M. E. Peskin and D. V. Schroeder, "An Introduction to Quantum Field Theory," Addison-Wesley, 1995.

[130] Photonis, "Photomultiplier Tube Basics." Available at: https://psec.uchicago.edu/library/photomultipliers/Photonis_PMT_basics.pdf.

[131] C. Pinkenburg, "EIC Simulations: What you need and what to watch out for," Available at: https://indico.phy.ornl.gov/event/38/contributions/185/attachments/218/752/calorimeter_talk.pdf, accessed on May 18, 2024.

[132] H.D. Politzer, "Reliable Perturbative Results for Strong Interactions?," *Physical Review Letters*, vol. 30, no. 26, 1973, pp. 1346-1349.

[133] C. Powell, P.H. Fowler, and D.H. Perkins, "The Study of Elementary Particles by the Photographic Method," *Nature*, vol. 159, 1947, pp. 694-697.

[134] E. Rutherford, "Collision of α Particles with Light Atoms. IV. An Anomalous Effect in Nitrogen," *Philosophical Magazine*, vol. 37, 1919, pp. 581-587.

[135] A. Puckett, "Recoil Polarization Measurements of the Proton Electromagnetic Form Factor Ratio to High Momentum Transfer," arXiv:1508.01456 [nucl-ex], 2015. Available at: https://arxiv.org/abs/1508.01456.

[136] A. Puckett, "Documentation of g4sbs," Feb. 2019. Available at: https://hallaweb.jlab.org/wiki/index.php/Documentation_of_g4sbs.

[137] A. Puckett, "SBS Software and Analysis," University of Connecticut, Hall A Winter Meeting, February 11, 2022, https://indico.jlab.org/event/503/contributions/9279/attachments/7518/10463/Puckett_SBS_software.pdf.

[138] A. Puckett, "SBS-GMN Analysis Overview and Status (NOT "results")," SBS Collaboration Meeting, University of Connecticut, July 17, 2023. Available at: https://indico.jlab.org/event/721/contributions/13211/attachments/10053/14936/PuckettGMN_talk.pdf.

[139] Andrew Puckett, *Assessing uniformity of HCAL proton detection efficiency, SBS-4,8,9*, December 28, 2023. Available: https://sbs.jlab.org/DocDB/0004/000482/002/HCALprotonEfficiencyUniformity.pdf

[140] A. Puckett, private communication with Provakar Datta, April 2024.

[141] A. Puckett, private communication, June 2024.

[142] A. Puckett, "BB/SBS GEM Tracking Software—A Brief Overview," private communication, University of Connecticut, Hall A Winter Meeting, Jan. 17, 2024.

[143] V. Punjabi et al., *Proton Electromagnetic Form Factor Ratios to* $Q^2 = 3.5\,GeV^2$ *by Polarization Transfer*, Phys. Rev. C, 71:055202, 2005. DOI: 10.1103/PhysRevC.71.055202

[144] V. Punjabi, C. F. Perdrisat, M. K. Jones, E. J. Brash, C. E. Carlson, *The Structure of the Nucleon: Elastic Electromagnetic Form Factors*, arXiv:1503.01452 [nucl-ex], 2015.

[145] I. A. Qattan, J. Arrington et al. *Precision Rosenbluth Measurement of the Proton Elastic Form Factors*. Physical Review Letters, 94(14), American Physical Society (APS), 2005. DOI: 10.1103/PhysRevLett.94.142301

[146] B. Quinn, "HCal LED Pulser System." Available at: https://sbs.jlab.org/DocDB/0001/000146/001/Pulser_documentation.pdf.

[147] A. Rathnayake, "Jlab SBS Neutron Magnetic Form Factor (GMn) Experiment and the Use of Time-Deconvolution Techniques to Analyze GEM Detector Signals." Available at: https://sbs.jlab.org/DocDB/0003/000358/001/4_Anuruddha_Rathnayake.pdf.

[148] S. Riordan, et al. "Measurements of the Electric Form Factor of the Neutron up to $Q^2 = 3.4$ GeV^2 using the Using the Reaction $^3\overrightarrow{\text{He}}(\overrightarrow{e},e'\overrightarrow{n})pp$," Phys. Rev. Lett., vol. 105, no. 26, pp. 262302, 2010.

[149] M.N. Rosenbluth *High Energy Elastic Scattering of Electrons on Protons*. Phys. Rev. 79, 615 (1950).

[150] E. Rutherford, "The Scattering of α and β Particles by Matter and the Structure of the Atom," *Philosophical Magazine*, vol. 21, 1911, pp. 669-688.

[151] R.G. Sachs, "High-Energy Behavior of Nucleon Electromagnetic Form Factors," *Phys. Rev.*, vol. 126, 1962, pp. 2256-2260.

[152] M. Satnik, "Some notes on GRINCH cuts for SBS9 and SBS8," Available at: https://sbs.jlab.org/DocDB/0005/000544/001/GRINCH%20cuts%20notes.pdf.

[153] M. Satnik, "GRINCH track-matching fits with Theta," GMn Analysis Update, Oct. 10, 2023. Available at: https://sbs.jlab.org/DocDB/0004/000448/002/GRINCH%20track-matching%20with%20theta1.pdf.

[154] F. Sauli, "GEM: A new concept for electron amplification in gas detectors," Nuclear Instruments and Methods in Physics Research Section A, vol. 386, p. 531, 1997.

[155] SBS Collaboration, "SBS-offline: Data analysis framework for the Super BigBite Spectrometer (SBS) experiments," GitHub repository, https://github.com/JeffersonLab/SBS-offline. Accessed on 2/25/24.

[156] SBS Collaboration, "SBS-replay: Replay and calibration scripts for SBS data," GitHub repository, https://github.com/JeffersonLab/SBS-replay. Accessed on 2/25/24.

[157] Jefferson Lab Hall A Collaboration, "Main Page," SBS wiki, https://sbs.jlab.org/wiki/index.php/Main_Page. Accessed on 2/25/24.

[158] J. Schwinger, "On Quantum Electrodynamics and the Magnetic Moment of the Electron," *Physical Review*, vol. 73, 1948, pp. 416-417.

[159] D. W. Scott, "Optimal and data-based histograms," *Biometrika*, vol. 66, no. 3, pp. 605–610, 1979.

[160] Sebastian Seeds, "HCal Crate Layout," Jefferson Lab Document Database, https://sbs.jlab.org/cgi-bin/DocDB/private/ShowDocument?docid=551. Accessed on 05/28/2024.

[161] Sebastian Seeds, "HCal Energy and Timing Calibration Report, Pass-2," https://sbs.jlab.org/cgi-bin/DocDB/private/ShowDocument?docid=441. Accessed on 5/25/24.

[162] JLab, "Document Database Page for Author Sebastian Seeds," https://sbs.jlab.org/cgi-bin/DocDB/private/ListBy?authorid=28. Accessed on 5/25/24.

[163] S. Seeds, "Equalizing Photoelectron Response Across Scintillators Employing Wavelength Shifting Fibers," Undergraduate Honors Thesis, University of Colorado Boulder, 2014. Available at: https://scholar.colorado.edu/concern/undergraduate_honors_theses/bn999731t.

[164] S. Seeds, "Hall A Analysis Software Farm Installation Guide," *Jefferson Lab SBS DocDB*, Document ID 423, https://sbs.jlab.org/cgi-bin/DocDB/private/ShowDocument?docid=423.

[165] Jefferson Lab, "SIMC in GFortran," GitHub repository, https://github.com/JeffersonLab/simc_gfortran. Accessed on 2/25/24.

[166] D. Gaskell and J. Arrington, "SIMC – Physics Monte Carlo for Hall C and Hall A," Hall A Analysis Meeting, December 14, 2009. Available at: https://hallaweb.jlab.org/data_reduc/AnaWork2009/simc_overview.pdf, accessed on May 18, 2024.

[167] Author(s), "SIMC Overview," Presentation at Jefferson Lab Analysis Workshop, December 14, 2009, https://hallaweb.jlab.org/collab/meeting/2009-winter/talks/Analysis%20Workshop%20--%20Dec%2014/simc_overview.pdf. Accessed on 2/25/24.

[168] O. Stern, "The Magnetic Moment of the Proton," *Physical Review*, vol. 50, 1936, pp. 851.

[169] H. A. Sturges, "The choice of a class interval," *Journal of the American Statistical Association*, vol. 21, no. 153, pp. 65–66, 1926.

[170] Holly Szumila-Vance, "Straight Track Analysis sbs4: Run 11611 with BB Field Off," https://sbs.jlab.org/DocDB/0001/000152/001/str_trk_sbs4.pdf.

[171] A. Tadepalli, "Dimensions of preshower and shower blocks used in the BigBite calorimeter." Available at: https://sbs.jlab.org/cgi-bin/DocDB/private/ShowDocument?docid=113.

[172] M. Tanabashi et al., "π^0 mass," Physical Review D, vol. 98, 2018.

[173] J.J. Thomson, "Cathode Rays," *Philosophical Magazine*, vol. 44, 1897, pp. 293-316.

[174] S. Tomonaga, "On a Relativistically Invariant Formulation of the Quantum Theory of Wave Fields," *Progress of Theoretical Physics*, vol. 1, 1946, pp. 27-42.

[175] T.N. Thorpe and S.E. Vahsen, "Avalanche gain and its effect on energy resolution in GEM-based detectors," Nuclear Instruments and Methods in Physics Research Section A: Accelerators, Spectrometers, Detectors and Associated Equipment, vol. 1045, pp. 167438, 2023, DOI: 10.1016/j.nima.2022.167438, URL: https://www.sciencedirect.com/science/article/pii/S0168900222007306.

[176] M. Ungaro, "Geant4 Updates - Hadronic Physics," ESA Space Workshop, December 2023. Jefferson Lab, Newport News, VA, USA. Available at: https://indico.esa.int/event/477/contributions/9186/attachments/5864/9781/

hadronic_physics_updates_space_workshop_dec_2023.pdf, accessed on May 18, 2024.

[177] L. Vidyaratne et al. *Deep Learning Based Superconducting Radio-Frequency Cavity Fault Classification at Jefferson Laboratory*. Frontiers in Artificial Intelligence, 4, (2022). DOI: 10.3389/frai.2021.718950

[178] M. Visser, "Feynman's iε prescription, almost real spacetimes, and acceptable complex spacetimes," Journal of High Energy Physics, vol. 2022, no. 8, Aug. 2022. Available at: http://dx.doi.org/10.1007/JHEP08(2022)129, DOI: 10.1007/jhep08(2022)129.

[179] N. V. Vlasov et al., "A Calorimeter for Detecting Hadrons with Energies of 10-100 GeV," Instruments and Experimental Techniques, vol. 49, pp. 41–55, 2006.

[180] R. C. Walker et al., *Measurements of the Proton Elastic Form Factors for* $1 \leq Q^2 \leq 3\,GeV^2$ *at SLAC*, Phys. Rev. D, 49(11):5671-5689, 1994. DOI: 10.1103/PhysRevD.49.5671

[181] W. Wang, "CEBAF Overview," HUGS 2010, Jefferson Lab, Newport News, VA, USA. Available at: https://www.jlab.org/hugs/archive/Schedule2010/slides/Wang.pdf, accessed on May 18, 2024.

[182] G. Warren, et al. "Measurement of the Electric Form Factor of the Neutron at $Q^2 = 0.5$ and 1.0 GeV^2," Phys. Rev. Lett., vol. 92, no. 4, pp. 042301, 2004.

[183] Z. Wertz, "Gain Match Update & Summary," July 2023. Available at: https://sbs.jlab.org/DocDB/0004/000408/001/GainMatch_Update.pdf.

[184] Zhihong Ye et al., "Proton and Neutron Electromagnetic Form Factors and Uncertainties," Phys. Lett. B, vol. 777, pp. 8–15, 2018.

[185] H. Yukawa, "On the Interaction of Elementary Particles I," *Proceedings of the Physico-Mathematical Society of Japan. 3rd Series*, vol. 17, 1935, pp. 48-57.

[186] A. Zec, "Compton Polarimetry for Neutral Weak Form Factor Measurements in ^{208}Pb and ^{48}Ca," PhD thesis, Jefferson Lab, 2024. Available at: https://misportal.jlab.org/ul/publications/view_pub.cfm?pub_id=16935.

[187] X. Zheng, *Precision measurement of neutron spin asymmetry An1 at large xBj using CEBAF at 5.7 GeV*, Ph.D. thesis, Massachusetts Institute of Technology, 2002. Available at: https://dspace.mit.edu/handle/1721.1/29310.

[188] G. Zweig, "An SU(3) Model for Strong Interaction Symmetry and its Breaking," *CERN Report No. 8419/TH.412*, 1964.

12 HCal Efficiency Map

Table 53: HCal x_{exp} efficiency map, SBS-8. Proton data from LH2 is used at both zero field and 70% field to generate these values. Each value in the "Overall Correction" column is the product of extracted efficiency from each field setting. All values are given for the indicated range in the quasielastic projection HCal x.

x_{exp}	Overall Correction	SBS field 70% Corr	SBS field 0% Corr
-1.53	1	1	1
-1.52	1	1	1
-1.51	0.974294	0.974294	1
-1.5	0.989517	0.989517	1
-1.49	1.01856	1.0225	0.99615
-1.48	1.0225	1.0225	1
-1.47	0.994591	0.994591	1
-1.46	0.890893	0.934165	0.953678
-1.45	1.02157	1.00836	1.01309
-1.44	1.01587	1.03015	0.986131
-1.43	0.981846	0.981846	1
-1.42	0.955842	0.986376	0.969044
-1.41	1.01012	0.999124	1.011
-1.4	1.02359	1.00072	1.02286
-1.39	1.02456	1.00608	1.01836
-1.38	0.961313	1.00904	0.952698
-1.37	1.02638	1.01357	1.01264
-1.36	0.981184	0.999379	0.981794
-1.35	0.985214	1.0017	0.98354
-1.34	1.01433	0.980539	1.03446
-1.33	0.985645	0.998023	0.987597
-1.32	0.972515	0.995417	0.976993
-1.31	1.01332	0.981191	1.03275
-1.3	1.00862	1.01057	0.998069
-1.29	0.962971	0.989517	0.973173
-1.28	0.982897	0.996341	0.986507
-1.27	0.997279	0.992074	1.00525
-1.26	0.997242	1.00004	0.997201
-1.25	1.01304	1.01057	1.00245
-1.24	1.00282	1.00768	0.995181
-1.23	0.991245	0.991367	0.999877
-1.22	0.998299	0.993194	1.00514
-1.21	1.01624	0.997525	1.01876
-1.2	1.00266	1.00358	0.999083
-1.19	0.979556	0.998834	0.980699
-1.18	0.985696	0.998277	0.987397
-1.17	1.00832	1.00623	1.00208
-1.16	1.01285	1.00162	1.01121
-1.15	1.00592	1.00169	1.00422
-1.14	0.973503	0.989704	0.98363
-1.13	1.00539	0.997018	1.0084
-1.12	1.00824	0.996354	1.01192
-1.11	0.9993	0.996773	1.00253
-1.1	1.01292	1.00764	1.00525
-1.09	1.03286	1.00898	1.02366
-1.08	1.01234	0.986251	1.02645
-1.07	0.97235	1.00377	0.968697
-1.06	1.01939	1.00908	1.01022
-1.05	0.995122	0.996091	0.999027
-1.04	1.01184	0.993397	1.01857
-1.03	1.0022	0.986866	1.01554
-1.02	1.00096	0.994297	1.0067
-1.01	1.00593	0.999275	1.00666
-1	1.02943	1.00943	1.01981

Continued on next page

Table 53 – continued from previous page

x_{exp}	Overall Correction	SBS field 70% Corr	SBS field 0% Corr
-0.99	1.02271	1.00488	1.01775
-0.98	0.993858	1.00551	0.988415
-0.97	1.02957	0.9998	1.02977
-0.96	0.990989	0.996074	0.994895
-0.95	1.01964	1.00087	1.01875
-0.94	1.00205	0.997801	1.00426
-0.93	0.986159	1.00195	0.984236
-0.92	1.00607	0.999055	1.00703
-0.91	1.00673	1.00133	1.0054
-0.9	0.99827	1.00324	0.995041
-0.89	0.977507	0.996642	0.980801
-0.88	0.997217	1.00877	0.988546
-0.87	0.977998	0.993257	0.984637
-0.86	0.993183	0.987108	1.00615
-0.85	0.999092	0.994119	1.005
-0.84	0.993407	0.992452	1.00096
-0.83	1.00504	0.987189	1.01808
-0.82	1.00088	0.994914	1.006
-0.81	0.970584	0.988058	0.982315
-0.8	0.949342	0.975004	0.97368
-0.79	0.937609	0.959167	0.977524
-0.78	0.944698	0.987689	0.956473
-0.77	0.929841	0.973466	0.955186
-0.76	0.927581	0.971977	0.954324
-0.75	0.915	0.95977	0.953353
-0.74	0.89008	0.960943	0.926257
-0.73	0.902312	0.980637	0.920128
-0.72	0.964552	0.987747	0.976517
-0.71	0.905048	0.967001	0.935933
-0.7	0.912708	0.9698	0.94113
-0.69	0.894229	0.976163	0.916065
-0.68	0.936875	0.97929	0.956688
-0.67	0.930953	0.989088	0.941224
-0.66	0.900202	0.966575	0.931332
-0.65	0.93608	0.974206	0.960865
-0.64	0.919464	0.972252	0.945705
-0.63	0.938621	0.986292	0.951666
-0.62	0.968803	0.989754	0.978832
-0.61	0.925074	0.981649	0.942367
-0.6	0.974173	0.987497	0.986507
-0.59	0.963347	0.989299	0.973767
-0.58	0.993302	1.00016	0.993142
-0.57	0.952464	0.993463	0.958731
-0.56	1.00492	0.994591	1.01038
-0.55	0.982287	0.997913	0.984341
-0.54	1.00555	0.995514	1.01008
-0.53	0.973503	0.97743	0.995982
-0.52	0.975459	0.996226	0.979154
-0.51	0.988118	0.993075	0.995008
-0.5	1.02192	1.01652	1.00531
-0.49	0.965909	0.993011	0.972707
-0.48	0.959873	0.981821	0.977646
-0.47	0.984447	0.986741	0.997675
-0.46	1.02925	1.00592	1.02319
-0.45	0.973041	1.00389	0.969268
-0.44	0.984201	1.00876	0.975651
-0.43	0.950563	0.993097	0.95717
-0.42	1.00976	1.01249	0.99731
-0.41	1.01881	0.999878	1.01893
-0.4	1.02277	1.01076	1.01188
-0.39	1.00063	1.00605	0.99462
-0.38	1.00204	0.988766	1.01343
-0.37	1.01627	1.00667	1.00954
-0.36	0.989103	1.00015	0.988954
-0.35	1.02919	1.00462	1.02446

Continued on next page

Table 53 – continued from previous page

x_{exp}	Overall Correction	SBS field 70% Corr	SBS field 0% Corr
-0.34	0.999273	1.0095	0.98987
-0.33	0.99952	1.0159	0.983872
-0.32	0.989055	0.999424	0.989625
-0.31	1.0031	1.00429	0.998822
-0.3	1.00797	1.0085	0.999477
-0.29	0.999747	1.00825	0.991568
-0.28	1.00367	1.00833	0.995377
-0.27	0.988339	0.996079	0.99223
-0.26	1.02995	1.01738	1.01236
-0.25	0.991765	0.996057	0.995691
-0.24	1.02102	1.00795	1.01297
-0.23	1.01103	1.00812	1.00288
-0.22	0.998981	0.99334	1.00568
-0.21	0.999878	1.00256	0.99733
-0.2	1.00329	1.00751	0.995812
-0.19	1.01298	1.01273	1.00025
-0.18	0.99433	1.00549	0.988898
-0.17	0.999812	0.995171	1.00466
-0.16	1.00383	1.00952	0.994371
-0.15	1.00185	1.0089	0.993011
-0.14	0.963595	0.999982	0.963612
-0.13	1.01511	1.01287	1.00221
-0.12	0.98653	0.997104	0.989395
-0.11	1.00745	1.01004	0.997436
-0.1	0.996367	1.00395	0.992444
-0.09	1.01537	1.00577	1.00954
-0.08	1.00094	1.00104	0.999902
-0.07	0.998331	1.01095	0.987518
-0.06	1.00567	1.00653	0.999148
-0.05	1.01608	1.00684	1.00918
-0.04	1.00182	1.0048	0.997031
-0.03	1.01875	1.00432	1.01438
-0.02	1.01619	1.00228	1.01388
-0.01	0.993538	0.99752	0.996008
0	0.968393	0.991724	0.976474
0.01	0.988574	0.99918	0.989385
0.02	1.00914	1.01707	0.992197
0.03	0.950182	1.00991	0.940855
0.04	0.985312	1.00586	0.979575
0.05	0.995607	1.0028	0.992829
0.06	0.979354	1.00215	0.977252
0.07	1.00263	0.994725	1.00795
0.08	0.989164	0.982513	1.00677
0.09	0.996086	0.99505	1.00104
0.1	0.999974	1.00223	0.997749
0.11	1.00192	0.992336	1.00966
0.12	0.981906	0.996994	0.984867
0.13	0.991509	0.994403	0.99709
0.14	0.981032	0.977888	1.00321
0.15	0.995489	0.981866	1.01388
0.16	0.965663	0.969525	0.996017
0.17	0.95645	0.957863	0.998525
0.18	0.9653	0.972634	0.99246
0.19	0.946449	0.969255	0.976471
0.2	0.965293	0.966418	0.998836
0.21	0.981183	0.972498	1.00893
0.22	0.953934	0.962131	0.99148
0.23	0.988985	0.972356	1.0171
0.24	0.956872	0.956849	1.00002
0.25	0.982125	0.962913	1.01995
0.26	0.987215	0.967933	1.01992
0.27	0.994692	0.969453	1.02603
0.28	0.981641	0.970274	1.01171
0.29	0.985446	0.98305	1.00244
0.3	0.966604	0.968242	0.998308

Continued on next page

Table 53 – continued from previous page

x_{exp}	Overall Correction	SBS field 70% Corr	SBS field 0% Corr
0.31	1.02258	0.991203	1.03165
0.32	0.980013	0.977154	1.00293
0.33	0.975394	0.988163	0.987078
0.34	0.983784	0.990382	0.993338
0.35	0.971215	0.989659	0.981363
0.36	0.990932	0.998023	0.992895
0.37	0.988033	0.996541	0.991462
0.38	0.97742	0.994119	0.983202
0.39	0.992425	0.99541	0.997001
0.4	1.01555	1.00901	1.00648
0.41	0.990212	1.00382	0.986446
0.42	0.988403	0.990197	0.998188
0.43	0.99811	0.993663	1.00448
0.44	0.965185	0.990359	0.974581
0.45	0.997568	0.988527	1.00915
0.46	0.990472	1.00472	0.985821
0.47	1.01644	1.01228	1.00412
0.48	1.00268	1.00446	0.998225
0.49	0.994516	1.00548	0.989096
0.5	0.988048	1.00223	0.985846
0.51	0.988924	1.00225	0.986706
0.52	0.969884	1.00267	0.967298
0.53	0.993801	0.989056	1.0048
0.54	0.9746	0.998571	0.975995
0.55	1.00006	1.00704	0.993075
0.56	0.994736	1.00613	0.988674
0.57	1.01096	1.00808	1.00286
0.58	0.992178	1.00413	0.988094
0.59	0.988001	0.994297	0.993668
0.6	0.986399	0.998729	0.987654
0.61	1.00408	0.996986	1.00711
0.62	0.996975	0.99661	1.00037
0.63	1.00354	1.00221	1.00132
0.64	0.987659	0.995373	0.99225
0.65	0.974054	0.996524	0.977452
0.66	0.986413	0.997913	0.988476
0.67	1.00938	1.00303	1.00634
0.68	1.00405	0.996741	1.00734
0.69	1.00854	1.00131	1.00722
0.7	1.00364	1.00688	0.996784
0.71	0.999635	0.994545	1.00512
0.72	0.989161	0.998385	0.990761
0.73	1.01705	0.993592	1.02361
0.74	1.01811	0.99601	1.02219
0.75	1.02495	0.997251	1.02777
0.76	1.01012	1.00444	1.00565
0.77	1.00564	0.994469	1.01123
0.78	1.00763	0.998927	1.00872
0.79	0.991158	1.00021	0.990948
0.8	0.995899	0.99297	1.00295
0.81	0.988349	0.988792	0.999552
0.82	1.02414	1.00816	1.01585
0.83	0.992737	0.990879	1.00188
0.84	1.01642	1.0062	1.01015
0.85	1.0239	1.00452	1.01928
0.86	1.0014	1.00006	1.00134
0.87	1.03256	0.999619	1.03296
0.88	1.0118	1.01178	1.00002
0.89	1.03197	1.00564	1.02618
0.9	1.00386	1.00636	0.99752
0.91	1.0179	1.00464	1.01321
0.92	1.02767	0.994764	1.03308
0.93	1.01525	1.00869	1.00651
0.94	1.02463	1.01267	1.01181
0.95	1.00173	0.995686	1.00607

Continued on next page

Table 53 – continued from previous page

x_{exp}	Overall Correction	SBS field 70% Corr	SBS field 0% Corr
0.96	1.01507	1.0081	1.00692
0.97	1.02077	1.00526	1.01543
0.98	0.999111	1.00163	0.997489
0.99	1.01063	0.998746	1.0119
1	0.986985	1.0078	0.979347
1.01	1.01796	1.01796	1
1.02	1.00271	1.00271	1
1.03	1.00031	1.00031	1
1.04	0.992419	0.992419	1
1.05	0.993004	0.993004	1
1.06	0.995981	0.995981	1
1.07	0.994508	0.994508	1
1.08	1.01016	1.01016	1
1.09	1.00367	1.00367	1
1.1	0.997996	0.997996	1
1.11	0.994784	0.994784	1
1.12	0.993782	0.993782	1
1.13	1.01031	1.01031	1
1.14	1.0048	1.0048	1
1.15	0.9977	0.9977	1
1.16	0.991144	0.991144	1
1.17	1.00236	1.00236	1
1.18	0.994436	0.994436	1
1.19	1.0033	1.0033	1
1.2	0.994309	0.994309	1
1.21	1.0062	1.0062	1
1.22	1.00264	1.00264	1
1.23	0.991492	0.991492	1
1.24	0.997566	0.997566	1
1.25	1.0038	1.0038	1
1.26	0.993971	0.993971	1
1.27	0.995816	0.995816	1
1.28	0.992336	0.992336	1
1.29	0.978751	0.978751	1
1.3	0.99583	0.99583	1
1.31	0.9867	0.9867	1
1.32	1.00374	1.00374	1
1.33	0.9867	0.9867	1
1.34	0.999639	0.999639	1
1.35	1.00341	1.00341	1
1.36	0.993444	0.993444	1
1.37	1.01433	1.01433	1
1.38	1.00506	1.00506	1
1.39	1.0025	1.0025	1
1.4	0.99541	0.99541	1
1.41	0.985404	0.985404	1
1.42	0.992886	0.992886	1
1.43	1.0037	1.0037	1
1.44	0.991491	0.991491	1
1.45	0.989072	0.989072	1
1.46	0.988738	0.988738	1
1.47	0.982175	0.982175	1
1.48	0.986756	0.986756	1
1.49	0.986726	0.986726	1
1.5	1.00869	1.00869	1
1.51	1	1	1

Table 54: HCal BNC Signal Cable Attenuation and Parameters

Module	Row	Col	Length (ft)	Signal Peak (mV)	Att
1	C	1	341	364	2.527
1	C	2	341	368	2.500
1	C	3	341	364	2.527
Continued on next page					

Table 54 – continued from previous page

Module	Row	Col	Length (ft)	Signal Peak (mV)	Att
1	C	4	341	360	2.556
1	C	5	341	360	2.556
1	C	6	341	364	2.527
1	C	7	341	356	2.584
1	C	8	341	360	2.556
1	C	9	341	364	2.527
1	C	10	341	360	2.556
1	C	11	341	364	2.527
1	C	12	341	360	2.556
1	C	13	341	360	2.556
1	C	14	341	356	2.584
1	C	15	341	360	2.556
1	C	16	341	360	2.556
1	D	1	341	348	2.644
1	D	2	341	356	2.584
1	D	3	341	356	2.584
1	D	4	341	348	2.644
1	D	5	341	360	2.556
1	D	6	341	360	2.556
1	D	7	341	360	2.556
1	D	8	341	356	2.584
1	D	9	341	352	2.614
1	D	10	341	348	2.644
1	D	11	341	352	2.614
1	D	12	341	352	2.614
1	D	13	341	356	2.584
1	D	14	341	348	2.644
1	D	15	341	352	2.614
1	D	16	341	352	2.614
2	A	1	341	344	2.674
2	A	2	341	356	2.584
2	A	3	341	352	2.614
2	A	4	341	348	2.644
2	A	5	341	352	2.614
2	A	6	341	344	2.674
2	A	7	341	352	2.614
2	A	8	341	340	2.706
2	A	9	341	352	2.614
2	A	10	341	348	2.644
2	A	11	341	348	2.644
2	A	12	341	348	2.644
2	A	13	341	348	2.644
2	A	14	341	348	2.644
2	A	15	341	336	2.738
2	A	16	341	352	2.614
2	B	1	341	344	2.674
2	B	2	341	344	2.674
2	B	3	341	344	2.674
2	B	4	341	352	2.614
2	B	5	341	348	2.644
2	B	6	341	344	2.674
2	B	7	346	304	3.026
2	B	8	341	348	2.644
2	B	9	341	348	2.644
2	B	10	341	352	2.614
2	B	11	341	344	2.674
2	B	12	341	352	2.614
2	B	13	341	356	2.584
2	B	14	341	344	2.674
2	B	15	341	348	2.644
2	B	16	341	348	2.644
2	C	1	341	348	2.644

Continued on next page

Table 54 – continued from previous page

Module	Row	Col	Length (ft)	Signal Peak (mV)	Att
2	C	2	341	368	2.500
2	C	3	341	372	2.473
2	C	4	341	364	2.527
2	C	5	346	352	2.614
2	C	6	341	368	2.500
2	C	7	336	368	2.500
2	C	8	341	364	2.527
2	C	9	341	360	2.556
2	C	10	341	364	2.527
2	C	11	341	356	2.584
2	C	12	341	356	2.584
2	C	13	341	356	2.584
2	C	14	341	352	2.614
2	C	15	336	348	2.644
2	C	16	341	352	2.614
2	D	1	341	348	2.644
2	D	2	341	348	2.644
2	D	3	341	348	2.644
2	D	4	341	348	2.644
2	D	5	341	348	2.644
2	D	6	341	348	2.644
2	D	7	341	344	2.674
2	D	8	341	348	2.644
2	D	9	341	352	2.614
2	D	10	341	352	2.614
2	D	11	341	352	2.614
2	D	12	341	348	2.644
2	D	13	341	352	2.614
2	D	14	341	348	2.644
2	D	15	341	348	2.644
2	D	16	341	352	2.614
3	A	1	341	348	2.644
3	A	2	341	352	2.614
3	A	3	341	352	2.614
3	A	4	341	348	2.644
3	A	5	341	348	2.644
3	A	6	341	348	2.644
3	A	7	341	352	2.614
3	A	8	341	352	2.614
3	A	9	336	348	2.644
3	A	10	341	348	2.644
3	A	11	341	348	2.644
3	A	12	341	352	2.614
3	A	13	341	356	2.584
3	A	14	341	352	2.614
3	A	15	341	352	2.614
3	A	16	341	352	2.614
3	B	1	341	368	2.500
3	B	2	341	356	2.584
3	B	3	341	352	2.614
3	B	4	336	360	2.556
3	B	5	341	348	2.644
3	B	6	341	348	2.644
3	B	7	336	360	2.556
3	B	8	341	356	2.584
3	B	9	341	352	2.614
3	B	10	341	356	2.584
3	B	11	341	360	2.556
3	B	12	336	352	2.614
3	B	13	341	360	2.556
3	B	14	341	352	2.614
3	B	15	341	356	2.584

Continued on next page

Table 54 – continued from previous page

Module	Row	Col	Length (ft)	Signal Peak (mV)	Att
3	B	16	341	360	2.556
3	C	1	341	352	2.614
3	C	2	341	356	2.584
3	C	3	341	360	2.556
3	C	4	341	360	2.556
3	C	5	336	356	2.584
3	C	6	341	364	2.527
3	C	7	341	356	2.584
3	C	8	341	356	2.584
3	C	9	341	364	2.527
3	C	10	341	360	2.556
3	C	11	341	360	2.556
3	C	12	330	352	2.614
3	C	13	341	360	2.556
3	C	14	336	356	2.584
3	C	15	341	348	2.644
3	C	16	341	356	2.584
3	D	1	341	348	2.644
3	D	2	341	352	2.614
3	D	3	341	352	2.614
3	D	4	341	352	2.614
3	D	5	341	352	2.614
3	D	6	336	348	2.644
3	D	7	341	352	2.614
3	D	8	341	352	2.614
3	D	9	356	324	2.840
3	D	10	356	328	2.805
3	D	11	356	324	2.840
3	D	12	356	328	2.805
3	D	13	356	328	2.805
3	D	14	356	324	2.840
3	D	15	356	328	2.805
3	D	16	356	324	2.840
4	A	1	356	332	2.771
4	A	2	356	328	2.805
4	A	3	356	324	2.840
4	A	4	356	324	2.840
4	A	5	356	324	2.840
4	A	6	356	328	2.805
4	A	7	356	324	2.840
4	A	8	356	328	2.805
4	A	9	356	328	2.805
4	A	10	356	324	2.840
4	A	11	356	328	2.805
4	A	12	356	328	2.805
4	A	13	356	328	2.805
4	A	14	356	328	2.805
4	A	15	356	328	2.805
4	A	16	356	328	2.805
4	B	1	356	320	2.875
4	B	2	356	320	2.875
4	B	3	356	316	2.911
4	B	4	356	320	2.875
4	B	5	356	320	2.875
4	B	6	356	320	2.875
4	B	7	356	320	2.875
4	B	8	356	316	2.911
4	B	9	356	328	2.805
4	B	10	356	328	2.805
4	B	11	356	324	2.840
4	B	12	356	324	2.840
4	B	13	356	324	2.840

Continued on next page

Table 54 – continued from previous page

Module	Row	Col	Length (ft)	Signal Peak (mV)	Att
4	B	14	356	328	2.805
4	B	15	356	324	2.840
4	B	16	356	324	2.840
4	C	1	351	328	2.805
4	C	2	356	320	2.875
4	C	3	356	320	2.875
4	C	4	356	320	2.875
4	C	5	351	320	2.875
4	C	6	356	320	2.875
4	C	7	356	320	2.875
4	C	8	351	324	2.840
4	C	9	356	324	2.840
4	C	10	356	324	2.840
4	C	11	356	324	2.840
4	C	12	356	324	2.840
4	C	13	356	324	2.840
4	C	14	356	324	2.840
4	C	15	356	324	2.840
4	C	16	356	324	2.840
4	D	1	356	320	2.875
4	D	2	356	320	2.875
4	D	3	356	320	2.875
4	D	4	351	316	2.911
4	D	5	356	320	2.875
4	D	6	356	324	2.840
4	D	7	356	324	2.840
4	D	8	356	324	2.840
4	D	9	356	324	2.840
4	D	10	356	324	2.840
4	D	11	356	320	2.875
4	D	12	356	324	2.840
4	D	13	356	324	2.840
4	D	14	356	324	2.840
4	D	15	356	324	2.840
4	D	16	356	320	2.875
5	A	1	341	352	2.614
5	A	2	341	348	2.644
5	A	3	341	348	2.644
5	A	4	341	352	2.614
5	A	5	341	352	2.614
5	A	6	341	348	2.644
5	A	7	341	348	2.644
5	A	8	341	348	2.644
5	A	9	341	344	2.674
5	A	10	341	344	2.674
5	A	11	341	344	2.674
5	A	12	336	344	2.674
5	A	13	341	344	2.674
5	A	14	341	344	2.674
5	A	15	341	340	2.706
5	A	16	341	344	2.674
5	B	1	356	336	2.738
5	B	2	356	336	2.738
5	B	3	356	336	2.738
5	B	4	356	336	2.738
5	B	5	356	336	2.738
5	B	6	356	332	2.771
5	B	7	356	328	2.805
5	B	8	356	324	2.840
5	B	9	341	296	3.108
5	B	10	341	344	2.674
5	B	11	341	348	2.644

Continued on next page

Table 54 – continued from previous page

Module	Row	Col	Length (ft)	Signal Peak (mV)	Att
5	B	12	341	344	2.674
5	B	13	341	348	2.644
5	B	14	341	344	2.674
5	B	15	341	344	2.674
5	B	16	341	344	2.674
5	C	1	336	344	2.674
5	C	2	341	344	2.674
5	C	3	341	340	2.706
5	C	4	341	344	2.674
5	C	5	336	344	2.674
5	C	6	341	344	2.674
5	C	7	341	344	2.674
5	C	8	341	344	2.674
5	C	9	356	324	2.840
5	C	10	356	324	2.840
5	C	11	356	324	2.840
5	C	12	356	324	2.840
5	C	13	356	324	2.840
5	C	14	356	324	2.840
5	C	15	356	324	2.840
5	C	16	356	324	2.840
5	D	1	356	328	2.805
5	D	2	356	324	2.840
5	D	3	356	324	2.840
5	D	4	356	324	2.840
5	D	5	356	328	2.805
5	D	6	356	328	2.805
5	D	7	356	324	2.840
5	D	8	356	320	2.875
5	D	9	356	324	2.840
5	D	10	356	324	2.840
5	D	11	356	320	2.875
5	D	12	356	324	2.840
5	D	13	356	320	2.875
5	D	14	356	324	2.840
5	D	15	356	320	2.875
5	D	16	356	320	2.875